AN APPROACH FOR EFFICIENT, CONCEPTUAL-LEVEL AEROSPACE STRUCTURAL DESIGN USING THE STATIC CONDENSATION REDUCED BASIS ELEMENT METHOD

A Dissertation
Presented to
The Academic Faculty

by

Mario A. Lee

In Partial Fulfillment
of the Requirements for the Degree
Doctor of Philosophy in the
School of Aerospace Engineering

Georgia Institute of Technology
December 2018

AN APPROACH FOR EFFICIENT, CONCEPTUAL-LEVEL AEROSPACE STRUCTURAL DESIGN USING THE STATIC CONDENSATION REDUCED BASIS ELEMENT METHOD

Approved by:

Professor Dimitri N. Mavris,
Committee Chair
School of Aerospace Engineering
Georgia Institute of Technology

Professor Daniel Schrage
School of Aerospace Engineering
Georgia Institute of Technology

Professor Graeme J. Kennedy
School of Aerospace Engineering
Georgia Institute of Technology

Doctor Neil Weston
School of Aerospace Engineering
Georgia Institute of Technology

Professor Sung Ha Kang
School of Mathematics
Georgia Institute of Technology

Date Approved: September 18^{th}, 2018

To my parents, Mr. Lowell Lee and Mrs. Sandra Lee

ACKNOWLEDGMENTS

I owe a great debt of gratitude to my advisor, Professor Dimitri Mavris. Because of his support, I was afforded the great privilege of pursing my PhD at one of the best technical universities in the world. He has never failed to provide his guidance, kindness, and patience throughout the years of my studies. It always amazes me that someone who is as distinguished and recognized as him in the aerospace industry will take a personal interest in the work of each and every one of his many students. Thank you for taking a chance on selecting me for your program all those years ago!

I would also like to thank the members of my PhD committee. This includes: Professor Graeme Kennedy, Professor Daniel Schrage, Professor Sung Ha Kang, and Dr. Neil Weston. In addition to taking the time to assess my PhD work, you all have never failed to make yourselves available for one-on-one consultations in order to provide your technical feedback on my work or to help me in my times on uncertainty and doubt. For this, I am incredibly grateful.

Throughout the course of my studies, I have met many wonderful peers from all over the world. Apart from my professional development during my tenure at Georgia Tech., getting to know you all has perhaps been the most rewarding experience during this time. There are too many to name individually, but I would like to thank the following for their technical and emotional support at one time or another during my studies. This includes: Sayan Ghosh, Ryan Jacobs, Justin Kizer, David Trawick, Alek Gavrilovski, Johanna Ceisel, Zilin "Elizabeth" Tang, Henry Schwartz, Ernesto Estrada, John Dykes, Chandrashekar Sundaresan and Aroua Gharbi.

On a personal note, I would like to thank my family, especially my parents, Mr. Lowell Lee and Mrs. Sandra Lee. From a very young age, you both instilled the

importance of obtaining a good education; both for personal development, as well as to improve the circumstances of my life and that of my family. Through your love and instilled discipline, I was afforded many privileges that my neighborhood friends and you yourselves were unfortunately not privy to while growing up. I am eternally grateful for the platform that was given to me from which I could start my adult life.

Lastly, and most importantly, I would like to thank God for the health and strength throughout my life. I credit my faith in Him for getting through some of the toughest times of my life throughout the course of my studies.

Contents

List of Tables

List of Figures

SUMMARY

In order to improve the energy efficiency and environmental compliance of future aircraft, the aviation industry has sought to investigate the inclusion of a variety of new technologies that are capable of enabling these goals. Among these technologies is a suite of structural technologies that are aimed at reducing airframe weight. At the conceptual level of aircraft design, the issues of vehicle weight and technology impact are of paramount importance. In aerospace engineering literature, there is a consensus that the finite element method (FEM) is the most accurate numerical method for determining the structural behavior and consequently, the weight of structural concepts that do not have vast empirical weight data. In the areas of conceptual and preliminary level design, the finite element method is often used in tandem with numerical optimization techniques to enable design space exploration and for finding suitable candidates that meet the requirements for the design problem. Unfortunately, the inclusion of detailed finite element analysis into conceptual level design environments has traditionally been prohibitive because of the associated computational expense.

Recently, there has been significant interest in the development of reduced order modeling strategies that are capable of expediting analyses performed by high fidelity simulations. Among these methods, a class of techniques known as Reduced Basis Approximation or Reduced Basis Methods has gained popularity because of their ability to replicate the accuracy of the higher fidelity analyses but at a very small fraction of the computational cost. In particular, a recently proposed approach known as the "*Static Condensation Reduced Basis Element (SCRBE) method*" is quite attractive because of its versatility of modeling a wide variety of final problem configurations

with a relatively small data set. This approach has been demonstrated on large-scale problems with physical problem domains that can be constructed from several repeated, underlying reference sub-domains or components. Unlike traditional reduced order modeling approaches, the SCRBE method performs the model reduction at the sub-domain level. This feature of the method enables the creation and analysis of a large variety of final problem domain configurations that can all be modeled with underlying physics.

The aim of this work is to develop an approach that uses the SCRBE method to enable conceptual-level, linear-static, structural design/optimization. While there has been extensive development in the SCRBE method since its inception, the author was unable to find many published, academic work that investigates the extension of this method to enable numerical optimization. Instead, most of the papers in literature focus on determining the state variable/ solution of the weak form of the underlying partial differential equation being modeled and then one or more outputs that depend on this solution. In the case of gradient-based optimization, one also needs the gradients of these outputs. For large-scale problems, numerical differentiation is not viable due to the computational expense associated with the "curse-of-dimensionality." This work presents an approach to estimate common, conceptual-level structural design metrics and their gradients under the SCRBE paradigm. This is so as to enable the structural optimization problem.

Another observation from the literature is that there tends to be a disparity between the computational time required to compose the equations to be solved in the SCRBE method and the time required to actually solve these equations. The literature recommends certain operational procedures that can be taken advantage of to tackle this overhead. This includes the use of repeated/ cloned sub-domains and interactive design. However, these methods may not be applicable during numerical optimization. Also, recall that numerical optimization is a "*many-query*" problem;

and as such, requires many calls of the simulator during the course of the optimization process. Admittedly, certain implementation strategies (such as the use of parallel computation) can be used to help to alleviate this overhead. This thesis proposes a technique that addresses this computational overhead and is perhaps most beneficial in situations where there are limited to moderate computational resources available. This technique leverages the matrix Discrete Empirical Interpolation Method (mDEIM) [1, 2].

The developments in this thesis are illustrated on a simple canonical problem of the strength design of a membrane-loaded, patched, variable-stiffness, composite plate. The findings of the experiments indicate that the SCRBE method, plus the techniques that are added to address the efficiency of the method have the potential to enable efficient conceptual-level structural design. It is anticipated that this approach can eventually be extended to conceptual-level studies of larger subsystems commonly featured in aerospace construction and forms an exciting avenue for future research.

Chapter I

INTRODUCTION

1.1 Motivation

Over the next 20 years, there is expected to be rapid growth in the aviation industry on both the domestic and international levels. According to the International Air Transport Association (IATA) [3], it is likely that passenger numbers will reach approximately 7.3 billion by 2034. This represents a 4.1% average annual growth in demand and air connectivity that will result in more than doubling the 3.3 billion passengers that travelled during 2014. In 20 years' time, it is projected that aviation will support around 105 million jobs and $6 trillion in GDP [3]. Unfortunately, accompanied with this promising economic development are concerns about the increased negative environmental impact associated with additional levels of aircraft activity. Aviation activity produces several pollutants; primarily, noise and gaseous pollutants (NOx, CO2 emissions etc.). Currently, aviation contributes approximately 2% of carbon dioxide emissions and an estimated 3% of all greenhouse gases [4]. However, due to the expected growth in air traffic volume over the next few decades, these contributions are expected to increase significantly in the absence of adequate intervention. As such, it is incumbent on aviation stakeholders to devote considerable attention to this area in order to stabilize and reduce said emissions. Furthermore, due to the capricious nature of oil prices, there is the need for energy-efficient aircraft so as to address not only the environmental concerns, but also the airline operators' direct operating costs.

There have been several regulatory initiatives aimed at addressing both the current levels and expected increases in deleterious gaseous emissions. In Europe, the EU

emissions trading system (EU ETS) was launched to establish policies to combat climate change [5]. Similarly, in the United States of America (USA), the American Clean Energy and Security Act (ACES) was proposed in 2009. Also, in the summer of 2009, the aviation industry announced its commitment to a global approach to mitigating aviation greenhouse gas emissions, adopting three high-level goals [6]:

- An average improvement in fuel efficiency of 1.5% per year from 2009 to 2020
- A cap on net aviation CO_2 emissions from 2020 (carbon-neutral growth)
- A reduction in net CO_2 emissions of 50% by 2050 relative to 2005 levels

In order to address these high-level goals, the aviation industry established a four-pillar strategy comprised of the following [7]:

- Investment into new technologies (more efficient airframe, engines and equipment, sustainable biofuels, new energy sources)
- Efficient operations (drive for maximum efficiency and minimum weight)
- Effective infrastructure (improved air routes, air traffic management and airport procedures)
- Positive economic measures (carbon offsets, global emissions trading)

The first of the four pillars, i.e. new technology, has been highlighted as potentially the most effective means of achieving these high-level goals [6]. In the USA, the National Aeronautics and Space Administration (NASA) embarked on an initiative known as the Environmentally Responsible Aircraft (E.R.A) Project. According to [8], the E.R.A. project aims to, "explore and document the feasibility, benefits and technical risk of vehicle concepts and enabling technologies to reduce aviation impact on the environment." In the initial phase of the project, a set of very aggressive but clear, quantitative targets were stipulated for key metrics associated with aircraft

Table 1: NASA system-level goals [9]

Technology benefits[a]	N+1 (2015)	N+2 (2020)	N+3 (2025)
Noise (cum. below stage 4)	-32 dB	-42 dB	-52 dB
LTO NOx (below CAEP6)	-60%	-75%	-80%
Cruise NOx[b]	-55%	-70%	-80%
Aircraft fuel burn[b]	-33%	-50%	-60%

[a]N+1 and N+3 values are referenced to a Boeing 737-800 with CFM56-7B engines, and N+2 values are referenced to a Boeing 777-200 with GE90 engines
[b]Relative to 2005 best in class

performance and emissions. Targets were stated for 5 year increments ranging from 2015 to 2025. These are summarized in table 1.

The E.R.A project seeks to identify and quantify the impact of a wide variety of technologies falling into the following categories [8]:

- Innovative Flow Control Concepts for Drag Reduction
- Advanced Composites for Weight Reduction
- Advanced UHB Engine Designs for Specific Fuel Consumption and Noise Reduction
- Advanced Combustor Designs for Oxides of Nitrogen Reduction
- Advanced Airframe and Engine Integration Concepts for Community Noise and Fuel Burn Reduction

Each of these technologies will affect at least one of the following aircraft metrics:

- Energy Conversion Efficiency (TSFC)
- Lift-to-drag ratio (L/D)
- Empty Weight (W_0)
- Aircraft Noise
- Combustion emissions

The impact of the first three metrics on fuel burn can be understood through the rearranged Breguet's range equation (1).

$$W_f = (W_{\text{pl}} + W_0)\left(\exp\left(\frac{R \times TSFC}{V \times {}^{L}/_{D}}\right) - 1\right) \tag{1}$$

As indicated, in order to minimize the fuel needed (W_f) to perform a mission with a stipulated flight range (R), velocity (V) and payload weight (W_{pl}), it is beneficial to minimize W_0 and TSFC; while maximizing the L/D of the aircraft.

The technologies under investigation that affect the airframe of new aircraft can be hierarchically decomposed in a bottom up fashion as: **Material Level**, **Structural Concepts Level** and **New Aircraft Concepts Level**. A brief overview of some of the concepts in these areas will be given in the following sections

1.2 Hierarchy Of New Structural Concepts

1.2.1 Material Level

Advanced composite materials have been identified as the new technology "S-curve" for achieving light-weight, structurally-efficient airframes [10]. Indeed, Nicolais [10] notes that the potential of aluminum alloys, (the traditional construction materials for high-subsonic speed aircraft) to improve the mechanical performance (i.e. strength and stiffness) of airframes has been explored exhaustively. This can be seen, for example, in the development of the aluminum-lithium alloys. The need for these alloys came in response to the competition created by composite materials. The goals to be met included, similar strength and stiffness characteristics to that of the 7075-T6 aluminum alloy, while having similar damage tolerance to 2024 aluminum alloys. However, despite attaining these improvements, composite airframe structures typically achieve a 25-35% saving in weight over those made from aluminum alloys [11].

Advanced composite materials are heterogeneous in nature. They feature high-strength, stiff fibers surrounded by a homogeneous resin (matrix). The fibers are responsible for the stiffness and tensile strength of these materials. There are several types of fibers used including, Aramid (Kevlar), fiber-glass, boron and graphite. In the context of aerospace structural design, graphite fibers are the most popular due to their overall superior mechanical characteristics. The purpose of the resin (matrix) used in composite materials is to bind together and protect the fibers, as well as to distribute the applied loads among them. The resin is responsible for the creep, compressive and shear strength characteristics of the material. In aerospace structures, thermoset resins, such as epoxy, are popular because of their good mechanical characteristics and suitability to manufacturing relative to thermoplastic resins. The fibers and resin are assembled into individual layers called *laminae* or *plies*; with the longitudinal axis of the fibers being the reference (0 deg) axis. These plies are stacked together into laminates as shown in figure 1. The number of plies, their orientations and individual thickness used in the laminate can be varied as desired.

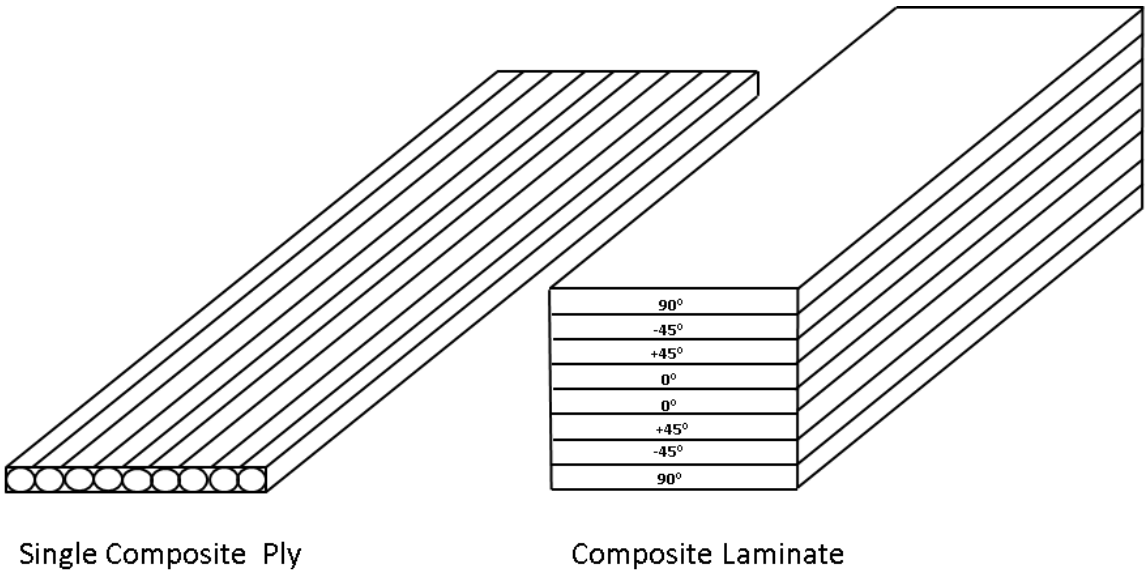

Figure 1: A single composite ply vs. a composite laminate

This versatility of composite materials allows for structural designers to tailor

them to specific loading scenarios so as to provide efficient load paths. Additional attractive features of composites include [12]:

- High stiffness and strength to weight ratios
- Reduced sensitivity to cyclic loads
- Improved corrosion resistance
- The capability of producing large parts without the need for the excessive joining of smaller parts (resulting in weight reduction)
- The capability of using highly-automated manufacturing processes so as to maintain high production efficiency and quality

Unfortunately, composites do have their associated disadvantages relative to aluminum alloys [11, 12]. These include:

- More susceptibility to impact damage
- Sensitivity to moisture absorptions and ultra-violet radiation. These cause reductions in the mechanical properties of these materials
- Significant manufacturing costs (non-recurring costs such as tooling investments and recurring costs such as material costs)
- High certification costs for the finished article

Recently, composite materials were incorporated into the primary structures of the wings and fuselage of large transport aircraft including the Boeing B787 and the Airbus A350. The empty weight of Boeing's B787 consists of 50% composites. According to Tenny et. al [13], the B787 is 40,000 lbs. lighter than airplanes of a similar size that are constructed from conventional materials. Furthermore, it is about 20% more fuel efficient and produces 20% fewer fuel emissions. Indeed, the use of composite materials in the airframe of new aircraft has great potential for addressing the need for fuel-efficiency, and thus, for the reduction of harmful gaseous emissions.

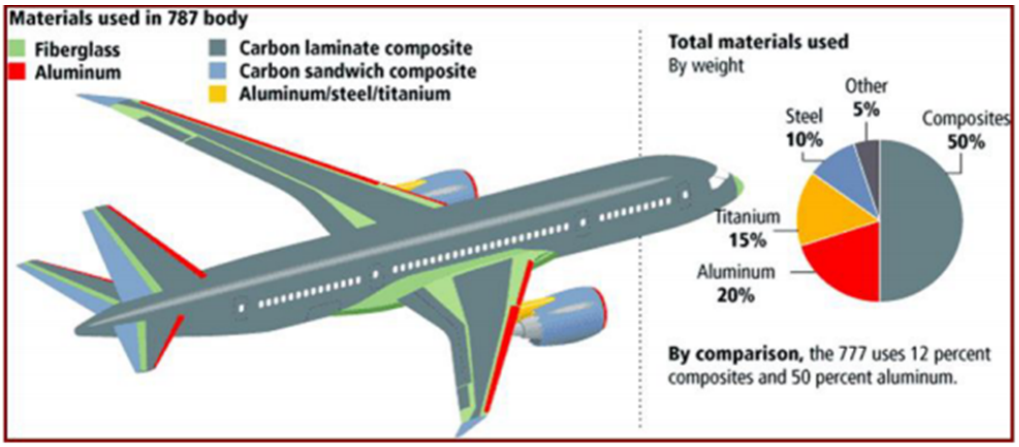

Figure 2: Composite utilization in the Boeing B-787 [13]

1.2.2 Structural Concept Level

A variety of novel structural concepts, featuring not only advanced composite materials, but also traditional aluminum alloys, have been developed with the aim of reducing the empty weight of airframe structures. They are meant to be used as novel construction techniques for the primary structures comprising the airframe of conventional tube and wing aircraft, as well as for new aircraft concepts such as the Blended Wing Body (BWB) aircraft. These structural concepts typically provide more efficient load paths and as a result, require less material for construction. This leads to lower empty weight. Figure 3 shows some of the new structural concepts being considered in the NASA ERA framework. A brief description will be given for a few of the pictured concepts. This is so as to stimulate an appreciation for the improvements provided by these concepts over traditional aerospace structural panel designs. For further details on omitted concepts, see [14].

Fiber Tow Steered Tailored Composites - Perhaps the simplest way of constructing a structural panel (curved or flat) made of composite materials is to use a constant laminate throughout its domain. However, in several references [15–18], it was shown

that varying the laminate construction throughout a panel is more structurally efficient than having a constant laminate all through the domain. In a variety of aerospace constructions, laminate variation is done by subdividing the domain of the panel into smaller "patches." The number of plies, their orientations and thicknesses are kept constant within each patch. On the other hand, the limiting case for the variable stiffness concept is to allow the fiber angles to vary continuously throughout the entirety of the panel rather than in a piecewise constant fashion. This is so as to achieve the maximum structural efficiency possible [19].

The Fiber Tow Steered Tailored Composites concept uses advanced tow-placement machines during manufacturing to lay the raw-material (often pre-preg tape) down in a fashion that is pre-determined to achieve high structural efficiency for a given application. This construction technique has received attention in several studies including [17, 20–22]. In terms of its potential use in airframe construction, the primary structures within the fuselage have been highlighted as an area of interest.

PRSEUS Concept - The PRSEUS panel concept has garnered considerable attention since the early 1990s [23]. It is a stiffened panel concept constructed of carbon warp-knit fabric, pultruded rods, foam core and stitched threads. The PRSEUS concept is shown in figure 3. Instead of using mechanical fasteners, simple co-curing (with no stitching) or paste bonding to attach the stiffeners and frames to the skins; they are stitched extensively through the thickness, forming a highly unitized structure. The design provides several benefits relative to traditional advanced composite stiffened panels. These include:

- Maintaining structural continuity by eliminating mechanical attachments, gaps, and mouse holes. This provides continuous load paths between the skin, stiffeners and frame components of the panels [24].
- Excellent damage arrestment characteristics. The extensive stitching helps to prevent inter-laminar resin failure, as well as to limit damage propagation within

bays of the panels, precluding catastrophic structural failure during operation. This has been demonstrated in several experimental studies [25–27]

- The formation of a rigid, self-supporting preform that obviates the need for interior mold tooling during manufacturing. The resin infusion and out-of-autoclave curing also aid in reducing recurring fabrication costs relative to conventional composite manufacturing [24].
- The use of high-modulus, carbon pultruded rods that not only aid in securing the connection between the stringers and frames, but also significantly increase the stability of the panel against buckling [28, 29].

The main application of interest for this concept is in the airframe of the BWB concept. Several studies consider the conceptual level design of BWB aircraft featuring this concept. These include [30–32].

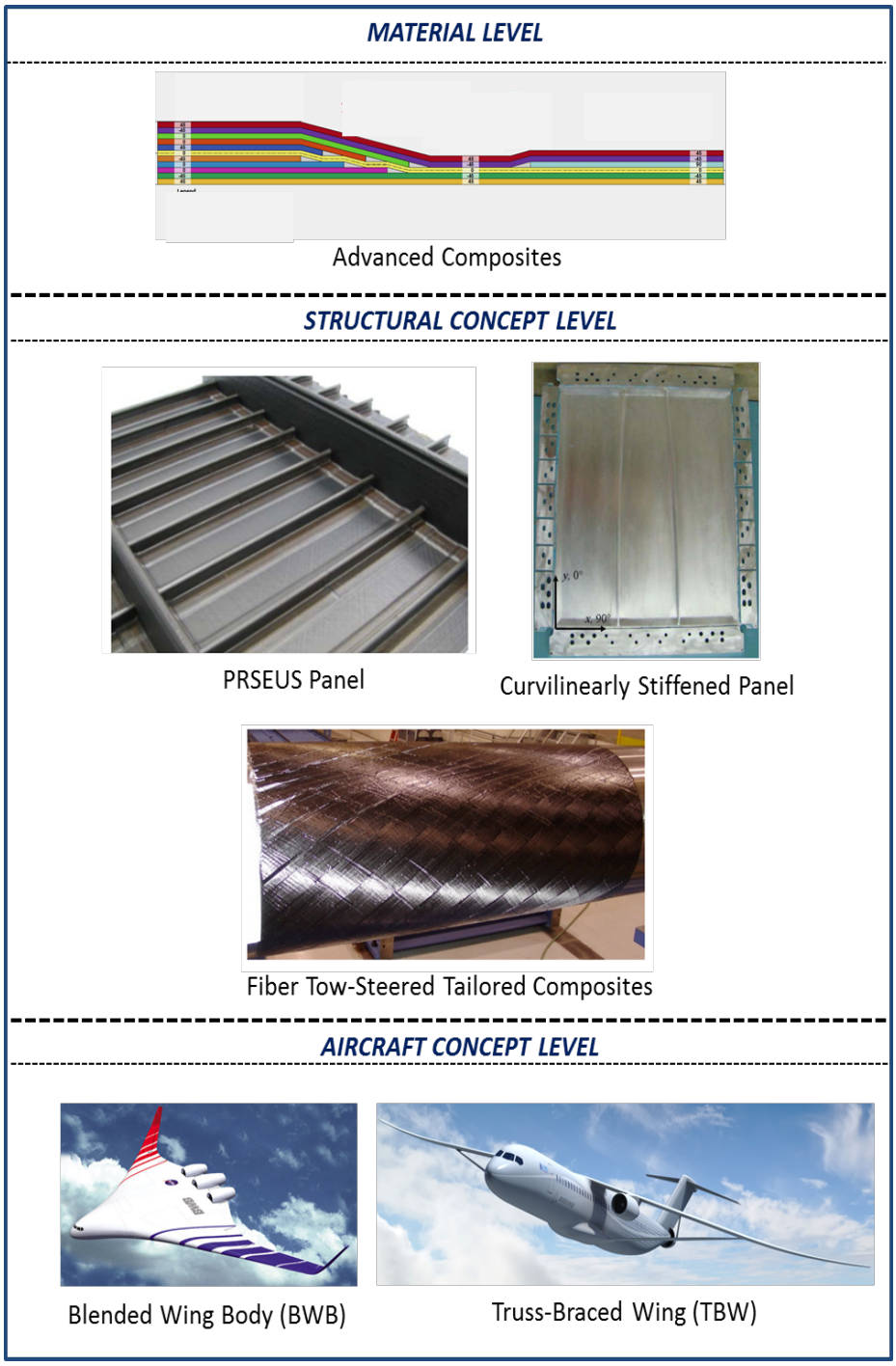

Figure 3: Hierarchy of structural technologies in the NASA ERA project. *Images:* **Material Level** - Advanced composites [33]. **Structural concept level** - PRSEUS panel [34], Curvilinear stiffened panel [35], Fiber tow-steered comp. [20]. **Aircraft concept level** - BWB [36], TBW [37]

1.2.3 Aircraft Concept Level

The highest level in the previously described hierarchy concerns new aircraft concepts. The external shape and design of these new concepts aim at producing significantly higher aerodynamic efficiency (lift-to-drag ratio) relative to conventional aircraft. For example, consider the truss-braced wing concept investigated during the Boeing-NASA SUGAR study [38]. Due to the structural support provided by the strut and jury in the configuration, very high aspect ratio wings are achievable. This significantly lowers the induced drag of the aircraft. Another example is the Blended Wing Body (BWB) concept. The BWB features an unconventional external shape which provides a lower wetted area relative to conventional tube-and-wing aircraft [39]. In turn, the lower wetted area allows for lower friction and thus profile drag.

The airframes of these aircraft are exposed to different loading scenarios relative to those of conventional aircraft designs. An example is in the fuselage design for the BWB as against a traditional tube-and-wing aircraft. The cabin of transport aircraft are pressurized at high altitudes so as to provide a safe and comfortable environment for the passengers and crew. When a traditional circular (or near circular) fuselage is subjected to this pressure, it is reacted efficiently by the fuselage skin in the form of membrane (hoop) tension [11]. In the case of the BWB, its center body section houses the passengers. It does not have a near circular shape and in fact, its longitudinal cross-sections are shaped like airfoils. This is so as to provide additional lift for the aircraft [39]. Unlike the fuselage skins in the tube-and-wing case, the outer shell of the BWB center-body section experiences an unfavorable interaction of pressure and bending loads [32]. This loading scenario requires special consideration in structural design.

Thus far, it has been highlighted that in order to achieve the aggressive targets set for fuel efficiency and the reduction of emissions, it is highly desirable to reduce

the empty weight of the new aircraft concepts being considered for introduction into service. As such, there is expected to be extensive use of advanced composite materials for the construction of the airframe of future aircraft. Furthermore, very efficient structural panel concepts are being considered for more efficient load paths, resulting in further weight reduction. These structural panel concepts are exposed to new, non-trivial loading scenarios that were not present in traditional aircraft. Therefore, all these factors require special attention during the aircraft design process.

1.3 Aircraft Design

The design of complex systems can be segmented into three major phases. These are, conceptual level design, preliminary level design and detailed design. Conceptual design concerns the initial formulation of candidate vehicles capable of performing the required mission(s). Here, a set of requirements - including those from the customer and those from regulations - are communicated to the designer. It is at the conceptual design level that questions of configuration arrangement, size, weight, and performance are addressed [40]. Major architectural decisions can be made, such as the number of engines to be used, the type of empennage arrangement (cruciform tail, conventional tail etc.), or perhaps the use of canards instead. After a suitable candidate design has been selected, preliminary design can begin. When the process enters the preliminary design level, major architectural changes are no longer permitted. It is at this stage that the disciplines (structures, aerodynamics, propulsion, stability and control, etc.) will focus on the analysis and design of their specific subdomains of interest on the selected candidate. As such, the aim of this stage is to design the system to such a level so that detailed design can begin. In the detailed design stage, the details relating to the actual fabrication of the aircraft are considered. This involves the development of rather intricate drawings or CAD files that facilitate the piecing together of the components of the aircraft. Additionally, there is extensive testing

of the fabricated structure in order to assess if it meets the necessary certification requirements.

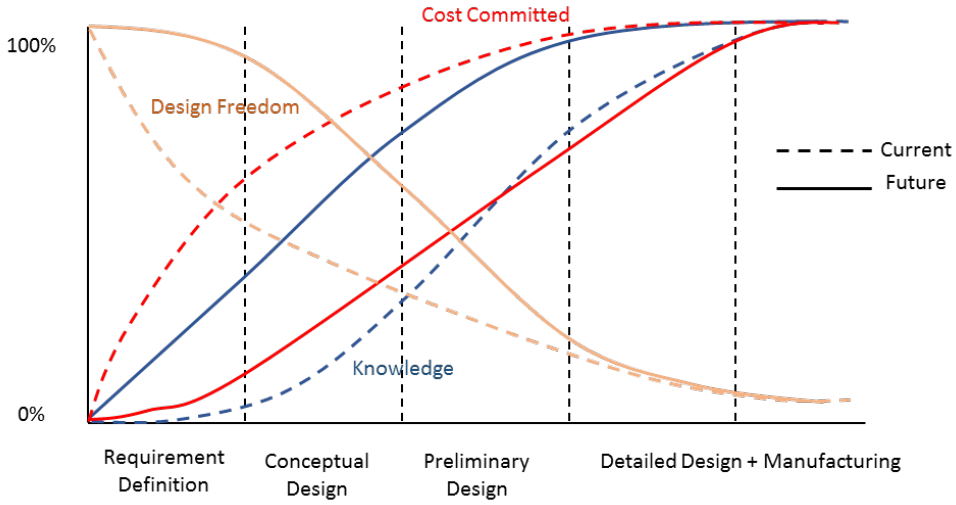

Figure 4: Progression of design knowledge, design freedom and cost committed throughout the stages of aircraft design

Figure 4 presents a notional plot depicting the distribution of design freedom, design knowledge and cost committed across the various phases of aircraft design. For traditional design (dashed curves), it can be seen that during the early stages there is a great deal of design freedom. Unfortunately, in this early phase there is little design information available and knowledge is typically accumulated as the design process progresses. By the end of the conceptual design phase, there is a significant commitment of cost and reduction in design freedom despite having little information about the system. Across the remaining design phases, further increases in design knowledge and cost commitment occur, while the design freedom continues to decrease.

There is a paradigm shift taking place in the way complex systems are being designed. The focus of design has shifted from design for performance to design for affordability [41, 42]. Consideration of additional issues - including life-cycle cost,

manufacturability, environmental compliance, safety, maintainability, etc. - has to take place earlier in the design process. This is due to more stringent requirements being placed upon designs. Additionally, it is extremely costly to make significant changes in the design if it is found to be deficient in any one of these areas at a later design stage. As such, it is desirable to increase the design knowledge during the conceptual level of design while keeping the design freedom open as long as possible and gradually committing cost (solid curves in figure 4). To meet these needs, new aircraft are increasingly being designed in Integrated Product Development (IPD) environments, and the work itself is carried out by Integrated Product Teams (IPT). In this approach, rather than sequentially designing each discipline of the aircraft, a concurrent design environment is created where representatives from each discipline are brought together to collectively design the aircraft. This includes disciplines that were typically ignored in conceptual design, such as manufacturing. The advantages of this approach include: fewer required engineering changes in production, reduced manufacturing costs and better product quality [40]. In order to gain an appreciation of the quantitative impact of these disciplines on the metrics of interest at the conceptual level, multi-disciplinary analysis and optimization (MDAO), modeling and simulation (M&S) environments are developed which are capable of capturing interactions among the disciplines. A typical MDAO M&S environment is an amalgamation of modules (each representing one or more disciplines) where the aim is to "size" the aircraft, while adhering to the strict requirements collected by the design team.

According to Raymer [40], the determination of weight is paramount to this sizing process, as it determines if the aircraft under consideration is capable of performing its intended mission(s). In the face of the paradigm shift in structural design, wherein new material systems, new structural concepts, and new aircraft are being investigated, there are at least two pertinent questions that can be asked. (1) What are the methods available to determine airframe empty weight at the conceptual/

early preliminary design level? (2) Of these methods, which ones are suitable for the new airframe technologies being considered? These questions will be examined in the following subsection.

1.3.1 Conceptual Level Weight Estimation

1.3.1.1 Criteria Used To Evaluate Weight Estimation Methods

Elham [43] provided criteria that a suitable conceptual level design, empty weight estimation method should satisfy. These criteria are:

- Design sensitivity (reflect features of the design under consideration)
- Very fast (computation time on order of seconds/minutes)
- Very accurate (error less than 5%)
- Largely based on physics, rather than statistics, such that innovative design solutions can also be addressed
- Suitable to support MDO studies
- Flexible enough to account for the inevitable difference in type and amount of data available at different design stages.

Elham [43] also provided a convenient categorization of popular methods available in aerospace literature for empty-weight estimation. These are Classes I-IV, with an intermediate class between classes II and III referred to as Class II &1/2. Class I-III methods are commonly used in the conceptual and preliminary levels of design, whereas class IV methods are typically used during the detailed design level and require an intricate understanding of the selected concept. Thus, class IV methods are not suitable for the initial formulation of concepts, nor are they suited for extensive design space exploration. Thus, class I-III methods will be described briefly in the following paragraphs.

1.3.1.2 Class I And II Methods

Both of these classes are based on the use of statistical methods. They leverage data gathered from the extensive development of aluminum alloy aircraft over the years. Unlike the remaining classes which focus on the specific subsystem being considered, class I methods provide an estimate for the empty weight of the entire aircraft. The weight regressions used are categorized based on aircraft class and function. They were derived by assessing the correlation between the empty weight and the takeoff gross weight of a large number of aircraft within a particular category. In the design of traditional aircraft configurations utilizing aluminum alloys, these methods are indeed convenient, as there is typically little design information available during their initial formulation. Class II methods on the other hand, carry out the empty weight estimation on the level of the major subsystems of the aircraft (wings, fuselage, empennage, landing gear system, etc.). They typically leverage many more design parameters than class I methods. For example, the estimate of wing weight may be a function of variables including wing area, thickness to chord ratio, and sweep. These methods are thus more design sensitive than class I methods, in that they are more reflective of the characteristics of the design being considered. Unfortunately, both of these classes of methods are not suitable for weight estimation of new airframes featuring new structural technologies, simply because the data for them do not exist. The extent to which composites are now being used in new designs is unprecedented. Furthermore, these methods provide no detailed knowledge of the internal structural designs of the aircraft (or its major components) so that a convenient transition into preliminary design can occur. Attempts have been made to quantify the weight savings achievable (such as Raymer [40]) when composite materials are employed, by the use of scaling or "fudge" factors. However, these generic scaling factors cannot capture the subtleties featured in the new designs and indeed, can only give crass estimates of the weight of these new concepts. Examples of class I and II methods

include work by Raymer [40], Roskam [44], Torenbeek [45], and Howe [46].

1.3.1.3 Class III Methods

Instead of relying on the use of statistical data, class III methods are aimed at performing the structural design of the primary structures within the airframe that satisfy various constraints, including: structural failure mechanisms, aeroelastic constraints, manufacturing constraints, etc. This problem is in essence one of optimization. There are many methods of various levels of fidelity available in this class. Some methods leverage convenient reductions in problem dimension while others aim to study the structural behavior of the three dimensional structure. The former methods are known as *Operational Model Order Reduction* methods [47]. Examples of methods within this category applied to weight estimation of the wingbox (a popular aircraft subsystem) is equivalent beam methods [48–51]. They are based on the observation that for high aspect ratio, thick wings, the approximation of their kinematic behavior with an equivalent beam model is reasonable. The stress and strain behavior of their cross-sections is approximated by thin-walled beam theory. For wing structures where the beam assumption becomes inappropriate - such as for thin, low aspect ratio wings - equivalent plate analysis (EPA) [52–61] methods become more attractive for use. In this approach, the wing is approximated by a thin plate. The kinematic behavior through the thickness is approximated by using the kinematic assumptions associated with popular plate theories such as Kirchhoff's plate theory or Mindlin's plate theory. Overall, the methods based on operational model order reduction struggle to capture detailed structural behaviors, such as the stress distributions in the presence of geometric discontinuities. Furthermore, they are incapable of determining the structural stability characteristics of the wing-box under study; thus, they are typically supplemented by analytical [62–66], and/or experimental [67–69], methods that provide approximate buckling and crippling criteria.

The rapid development of computational capabilities over the years has allowed for the development of increasingly complex simulations for studying the behavior of physical systems/processes. Perhaps the chief embodiment of this in the analysis of aerospace structures is the usage of finite element methods. Displacement based finite element analysis (FEA) discretizes a continuum structure into contiguous elements that are connected at vertices (nodes) and along edges and sides. The displacement behavior of the structure of interest is approximated by solving a sparse system of equations. The stress and strain behavior of the structure can then be recovered using post-processing techniques on the displacement data. Furthermore, if the model is of suitable fidelity, then the structural stability characteristics can be appropriately modeled. Unfortunately, the finite element method is well-known to be computationally burdensome; thus several simplifications or strategies are often leveraged to reduce the execution time for analysis. Popular methods proposed include multi-level analysis [70–72], cross-sectional smearing [73, 74], and multi-fidelity analysis [72, 75]. In the literature, there is a consensus that sufficiently detailed finite element analysis is preeminent in accuracy among the available numerical structural analysis methods [11, 12, 43, 48]; however, due to the associated computational expense, it has traditionally been viewed as inappropriate for the conceptual level of aircraft design. This is due to the fact that this stage features extensive design space exploration and optimization, requiring numerous evaluations of the parametric FEM analysis.

1.3.1.4 Class II &½ Methods

These methods feature the use of either analytical or numerical techniques for structural analysis from class III coupled with empirical weight estimation. They were born from the fact that there are components of the aircraft structure that are structurally non-critical and thus their weight cannot be estimated by means of structural analysis. These include the leading and trailing edge secondary structures, high-lift

devices, control surfaces etc. of a wing; the internal furnishing within a fuselage; and the control surfaces on the empennage. Additionally, estimates of non-optimum weights have to be included because the simplified mathematical models used to approximate the primary structures do not capture them. Fortifications necessitated by stress concentrations in the primary structure, as well the need for mechanical fastening of parts, are both examples of additional weight sources that cannot be captured by the analysis methods available during conceptual and preliminary level design. Examples of class II &1/2 methods include [76–78].

1.3.2 Structural Optimization

Thus far, we have seen that class III methods are the most suitable numerical means for determining the weight of structural concepts that do not have a vast empirical database. The underlying simulations arising from this class are often used in the context of structural or multidisciplinary optimization. When the underlying simulation is the finite element method, the problem falls into a general class of problems known as ***Partial Differential Equation (PDE) constrained optimization problems*** [79]. Optimization problems of this type takes the following form:

$$\text{Optimize :} \qquad J\left(u(\mu,x),\mu\right) \tag{2}$$

$$\text{With respect to :} \qquad \mu \in \mathbb{R}^p, \;\; x \in \Omega \tag{3}$$

$$\text{Subject to :} \qquad g_i\left(u(\mu,x),\mu\right) \leq 0, \;\; i = 1,\ldots,n \tag{4}$$

$$h_j\left(u(\mu,x),\mu\right) = 0, \;\; j = 1,\ldots,m \tag{5}$$

$$\mathcal{R}\left(u(\mu,x),\mu\right) = 0 \tag{6}$$

Where:

- $\mu \in \mathrm{R}^p$, design parameter vector of dimension p

- $u(\mu, x)$, the state variable of the problem (e.g. the displacement field for solid mechanics)
- Ω is the problem domain
- $J\left(u(\mu), \mu\right)$, the cost or objective function of the problem
- $g_i\left(u(\mu), \mu\right))$, the inequality constraints of the problem
- $h_j\left(u(\mu), \mu\right))$, the equality constraints of the problem
- $\mathcal{R}\left(u(\mu), \mu\right))$, the vector-valued residual defining the weak form of the PDE

In this context, the finite element model is used to determine a discrete approximation of the state variable, $u(\mu, x)$. The algebraic system associated with the FEM problem corresponds to the weak form of the governing partial differential equation. The vector valued residual of this algebraic system is represented as $\mathcal{R}\left(u(\mu), \mu\right))$. In the case of structural analysis, the state variable, $u(\mu, x)$, is often the displacement field of the structure being modeled. However, it is often the case where one is not directly interested in the state variable in and of itself, but on the various metrics that depend on it. These metrics include: the objective function, $\mathcal{J}\left(u(\mu), \mu\right)$; and the constraints, $g_i\left(u(\mu), \mu\right))$, $h_j\left(u(\mu), \mu\right))$. Examples of the objective function include: total mass, strain energy, and compliance of the structure. Whereas, examples of structural constraints include: material strength, structural stability, aeroelastic stiffness requirements, producibility and manufacturing costs. The goal of the optimization problem is to find a design that optimizes one or more prescribed objective functions, while satisfying the prescribed problem constraints.

In the literature for PDE constrained optimization, there are two common frameworks used to solve problems of this kind [79]. These are: (1) the *Nested Analysis And Design (NAND)* approach and; (2) the *Simultaneous Analysis And Design (SAND)* approach. In the former approach, the state variable is not considered explicitly in the optimization procedure; but instead, the weak form of the partial differential equation $\left(\mathcal{R}\left(u(\mu), \mu\right)\right) = 0)$ is solved exactly at each major iteration of the optimization

procedure. The state variable (and its derivative if used) is then used to calculate the cost and constraint functions (and their derivatives if necessary). On the other hand, in the latter method, the equality constraint formed by the partial differential equation is treated similarly to the other constraints. The optimizer is responsible for enforcing the satisfaction PDE equations as the procedure advances towards an optimum. In both cases, gradient-based optimization is preferable because it is better suited to handle the "curse of dimensionality".

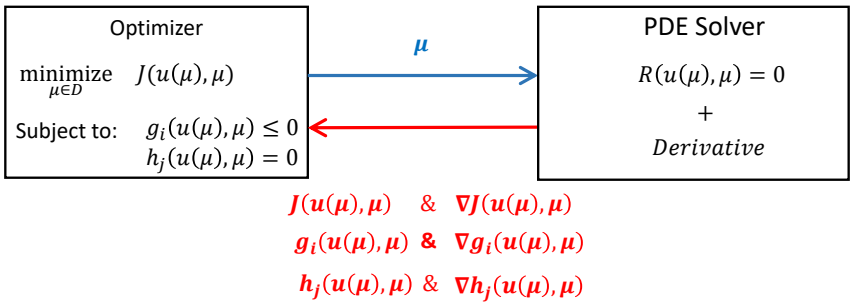

Figure 5: An illustration of the NAND framework

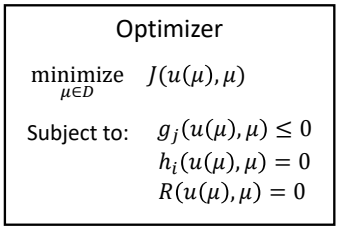

Figure 6: An illustration of the SAND framework

In practice, the solution of the underlying partial differential equation is computationally burdensome and often inhibits efficient optimization for large scale problems. At the conceptual level of aerospace design, it is desirable to have tools that are able to perform optimization and design in seconds to minutes, and not hours to

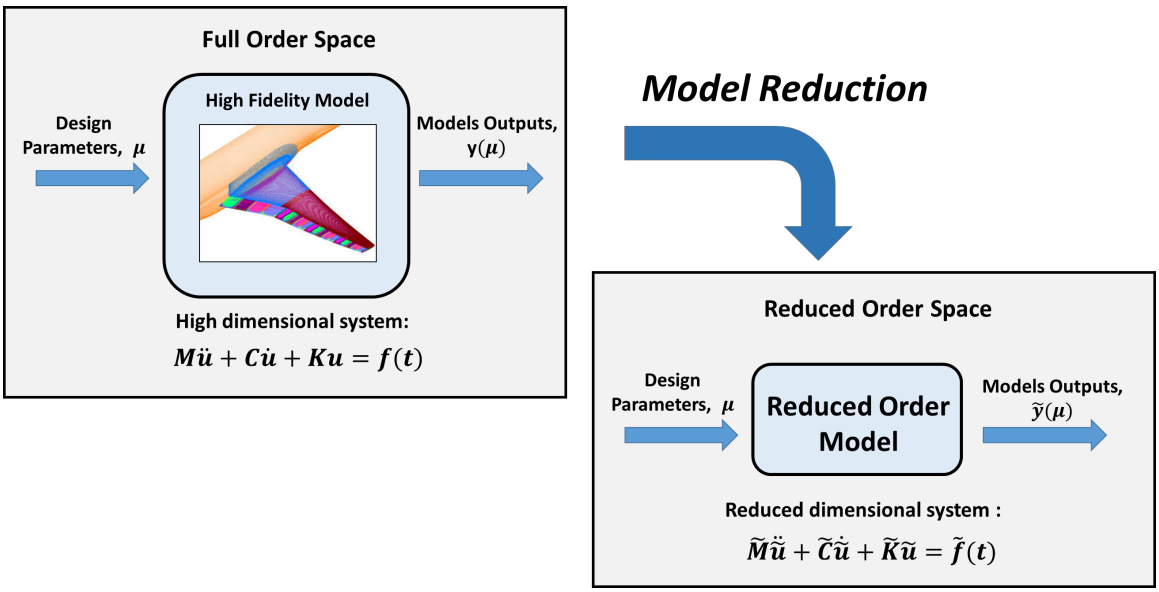

Figure 7: Main idea of reduced-order modeling. (Simulation image taken from [80])

days. To this end, a key enabler in mathematical, engineering and science literature is projection-based, reduced order models. These methods have been shown to drastically reduce the time required to perform PDE constrained optimization.

1.4 Reduced Order Modeling

In recent years there has been extensive development in the field of Galerkin projection-type Reduced Order Modeling (ROM) techniques. They are based on the realization that the solution of a typical finite element analysis is often more succinctly expressed by a subspace of the high-dimensional finite element approximation space. In fact, the associated finite element approximation spaces are often referred to as "unnecessarily rich". The basis functions in the associated reduced subspaces are empirically derived and have larger support than the nodal basis functions associated with the lower order polynomial finite element methods. They allow for the conversion of the sparse linear algebraic system associated with the standard FEM method into a dense but much smaller linear algebraic system. This allows for astounding speed-ups in computation times. Analyses that once took hours are now being done in seconds/minutes.

1.4.1 Major Limitations Of Traditional Projection-Based ROM For Conceptual Design

Indeed, projection-based ROM is an impressive tool that provides the opportunity to perform analyses on very large numerical problems, that were once computationally prohibitive at the conceptual and early preliminary levels of design. Unfortunately, the traditional approach is not without its limitations. One such limitation in the present context is the lack of versatility in the method when wholesale changes are made to the problem domain being analyzed. Projection-based ROM is empirical in nature. That is to say, a parametric finite element model has to be specified; from which data are extracted (often through a greedy sampling procedure) and then the reduced variant of the problem is created. Often, great care is taken in creating these finite element models in the first place. Subject-matter expertise is frequently required to assist in the creation of these models and to ensure that they behave adequately. This often requires significant time and effort for very large aircraft subsystems and systems. If major changes were to be made to the configuration being investigated - such as the discrete additional or removal of sub-regions in the configuration's physical domain - the model has to investigated again by personnel with the appropriate domain knowledge. This idea is illustrated in figure 8. The reduced order model is then recreated to reflect the updated configuration.

Another limitation in prescribing the reduced order model at the global level is associated curse of dimensionality associated with furnishing the snapshot data from which the empirical basis is created. Consider the structural wingbox illustrated in figure 11. Often with wingbox structures, each sub-region (illustrated with different colors) is equipped with parameters describing their local material system (many parameters for composites!) and their local geometric definition. The global parameter space/design vector is formed by the Cartesian product of these local subregions plus

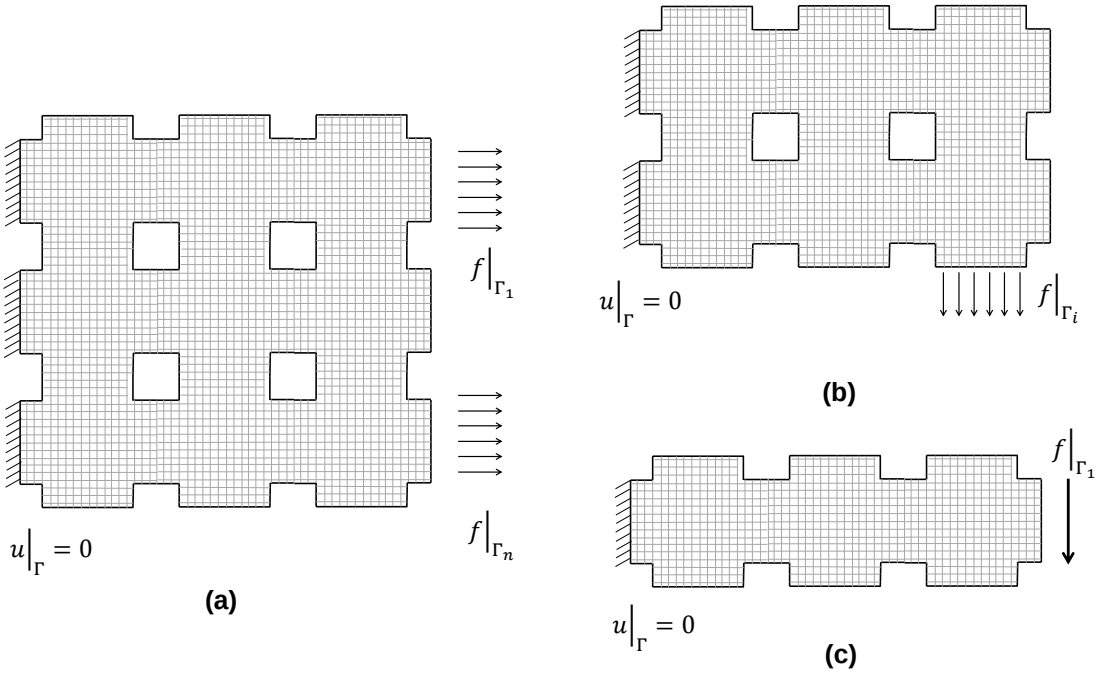

Figure 8: Examples of problem domains modeled with the finite element method that feature discrete addition and subtraction of sub-regions. (Inspired by an image presented in [81])

the parameters defined globally (such as load factor). Consequently, the global parameter space can perhaps venture into the 100's-1000's of parameters. Admittedly, there are greedy sampling algorithms available in the ROM literature that are able to address high dimensional problems [83]. However, they depend on using expensive optimization-based strategies, which further exacerbates the effort required to create the reduced order models in the first place. Even worse, information and time is lost when major configuration changes have to be made and the ROM has to be thrown out.

Recall that during the conceptual level of aerospace design, there is the most design freedom. Therefore, we are interested in investigating several, sometimes disparate concepts, that have the potential to meet the imposed requirements. In the area of structural design, this translates to having the ability to investigate a variety of

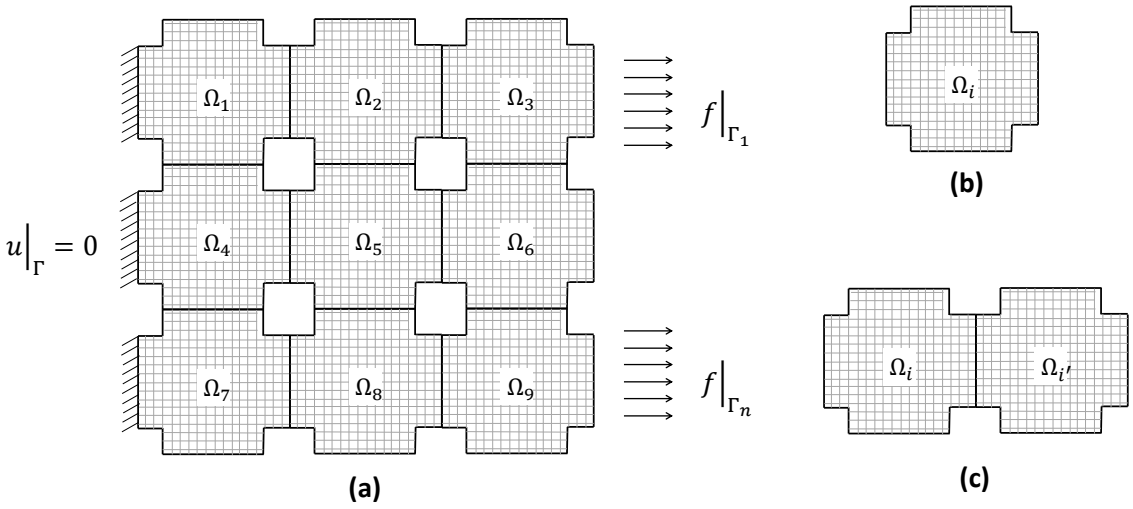

Figure 9: Decomposing the problem domain into repeated physical sub-domains. (a) Global problem domain. (b) Individual sub-domain. (c) A pair of sub-domains connected at a shared interface. (Inspired by an image presented in [81])

structural concepts in an efficient manner. A method that has been proposed recently in the ROM literature seems to have the potential to address these concerns. It is known as the Static Condensation Reduced Basis Element (SCRBE) Method.

1.4.2 Key Enabler: Static Condensation Reduced Basis Element Method (SCRBE)

The SCRBE method embraces a "bottom-up hierarchy" in creating problem domains. Under this paradigm, a library of reference, interoperable components are studied in isolation and in local neighborhoods of components. They are then used to create large problem domains. This idea is illustrated in figure 9. It is at the component level that the reduced order modeling is enabled. This method is aimed at expediting the familiar static condensation approach [84] to solving the finite element method. Static condensation is particularly suited for high-performance/parallel implementation. The SCRBE is most beneficial and perhaps only suitable for very large problems that consist of repeated sub-components. Aerospace structural design fits quite well into this paradigm. The resulting structures are often large and highly modular in

Figure 10: Aircraft configurations that might reuse the same structural building blocks [82]

nature and feature repeated sub-components with minor geometric variations among them. This premise has also been embraced in commercial structural analysis tools such as Collier Research's Hypersizer [33]. It leverages the fact that aerospace structures consist of a library of stringer-stiffened panels and that they can be used in a variety of configurations, thanks to the modularity of common structural designs. Note however, that there is no concern about redundancy in the approach; since Hypersizer is not meant to replace the finite element model, but is instead meant to post-process the results of the finite element procedure and provide estimates of structural constraints of interest. The SCRBE method on the other hand is meant to replace the FEM with a cheaper, but highly accurate surrogate model.

Another advantage of this type of approach is the capability to create and study subsystems (such as wings, fuselages, empennages) in isolation; and then join them together with ease. This modularity allows for collaborations from distributed teams and perhaps even help to reduce the design cycle time required for structural design.

Due to the promise of the method, it deserves further investigation. It should be

noted however, that a certain caveat has to be placed on the scope of said investigation. While it is desirable to eventually develop a sophisticated, conceptual level tool, equipped with parametric CAD for preprocessing the geometry of large-scale aircraft structural sub-systems and systems; the focus in this thesis will be placed on studying the underlying mathematics and procedures of the structural design problem. This desire further motivated the choice of the canonical problem used for investigation. The goal here is to understand the usage of the SCRBE method for the desired objective, first within a simple context. Further investigations for more complex problems - such as the one pictured in figure 11 - is left to future work.

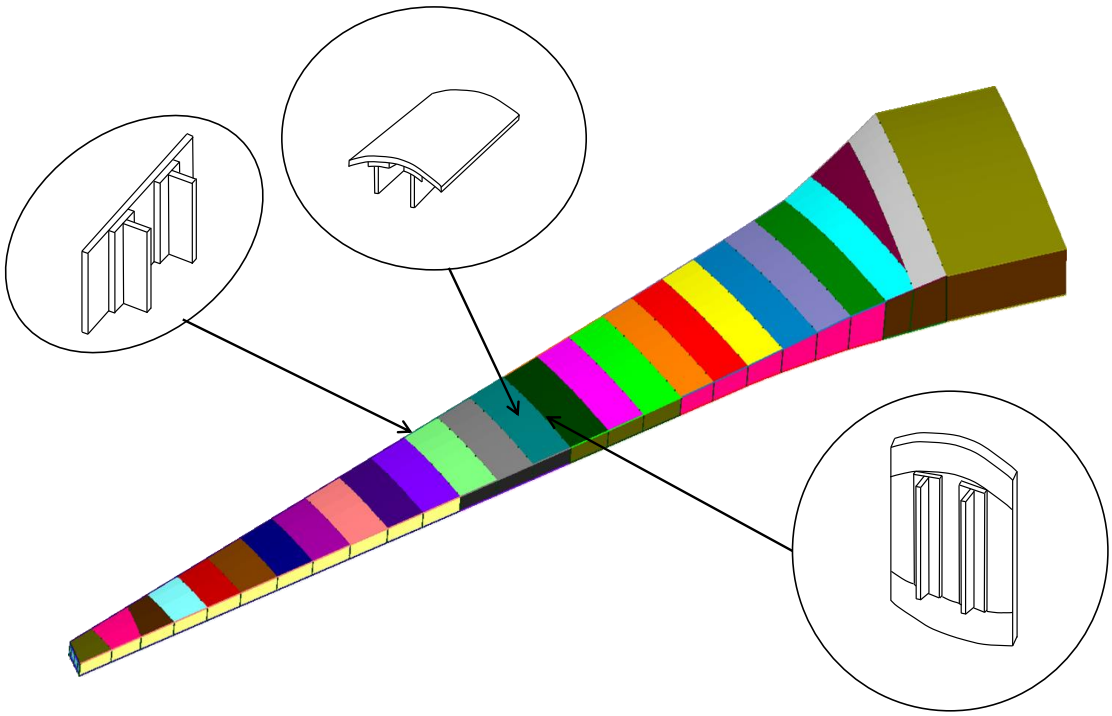

Figure 11: Modularity in aerospace structural design. Wingbox example

The remainder of this thesis is structured as follows:

- In chapter 2, a literature review of the use of projection-based ROM in optimization problems is provided. This is followed by a literature review of the

SCRBE method and the potential challenges its use potential use in optimization problems.

- In chapter 3, the problem being addressed in this thesis will be defined and the scope limitations will be specified
- In chapter 4, an overview will be given on the abstract finite element formulation; as well as the introduction of reduced basis approximation in order to expedite the simulation.
- In chapter 5, the abstract framework of the SCRBE framework is presented. It is further extended to facilitate the optimization procedure in the present context
- In chapter 6, a modified approach, built on the same elements presented for the SCRBE approach in chapter 5 will be presented. This is aimed at ameliorating one specific limitation presented in SCRBE literature, that is discussed in chapter 2
- In chapter 7, a canonical, structural design problem will be introduced. It is a simple, membrane plate design problem, that can help to foster an appreciation of how the methods described in this thesis can be applied to aerospace structural design problem that uses composite materials. Furthermore, it will serve as the numerical test-bed for the hypotheses developed during the course of this thesis.
- In chapter 8, the experimental results will be presented and analyzed
- In the final chapter, chapter 9, the conclusions and the limitations of this work will be presented. Areas for future work will also be highlighted

Chapter II

BACKGROUND AND LITERATURE REVIEW

2.1 Chapter Overview

In this chapter, a literature review is provided for the use of projection-based ROM in PDE-constrained optimization and also for the Static Condensation Reduced Basis Element Method (SCRBE). From the author's review of the available literature, some gaps and challenges will be highlighted regarding the potential use of the SCRBE method for performing aerospace, conceptual-level structural design. Finally, the research objective of this work will be stated.

2.2 Literature Review: Projection-Based Reduced Order Models In PDE-constrained Optimization

Projection-based reduced order models are an attractive alternative to solving the full, high fidelity models in many areas of science and engineering for "*many-query*" and "*real-time*" problems. PDE-constrained optimization falls into the many-query category. The use of projection-based reduced order models is aimed at drastically decreasing the computational cost associated with estimating the metrics that are normally determined by the underlying PDE.

The goal of RB methods is to carry out a Galerkin projection of the governing differential equation of the problem onto a lower dimensional subspace built upon the general numerical approximation space applied to the weak form of the problem. The finite element approximation space is commonly used in these types of problems. Using adequately chosen samples in the parameter space, various configuration snapshots are taken of the high fidelity simulation. They are then compressed with the Proper Orthogonal Decomposition (POD) procedure and used to form the required

lower dimensional approximation spaces. This results in linear algebraic systems that can be solved expeditiously due to their reduced sizes.

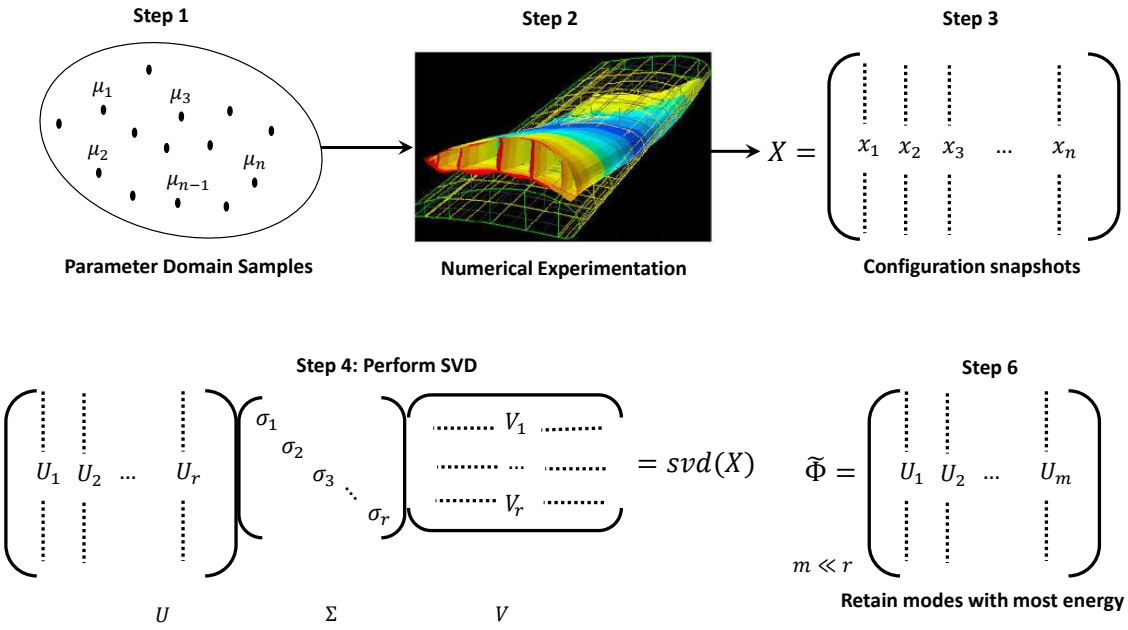

Figure 12: Illustration of the Proper Orthogonal Decomposition procedure

In the literature, the methods used to address PDE-constrained optimization with projection-based ROM typically fall into one of two broad categories. These are: (1) *Online-Offline* decomposition and (2) *Adaptive Framework* or *Progressively Constructed* reduced order models. The main features of the two methods are:

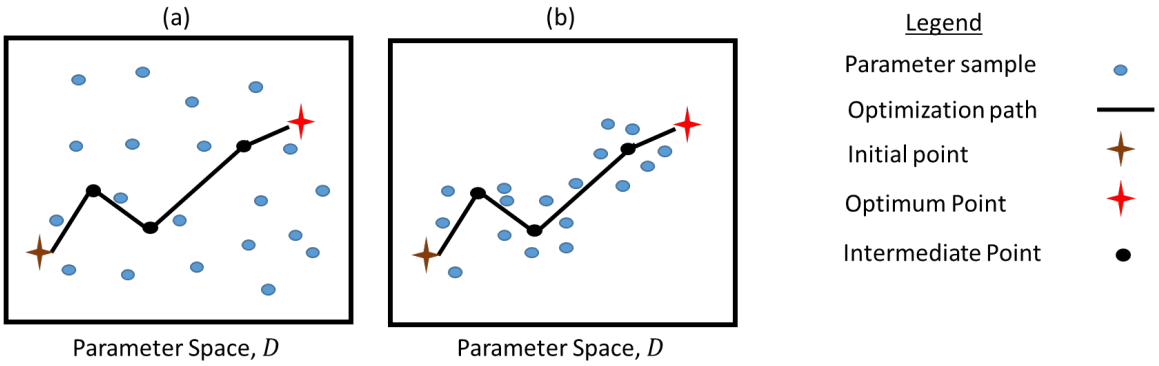

Figure 13: Two common schemes used in ROM assisted PDE-Optimization. (a) Online-offline decomposition (b) Progressively constructed

Online-Offline decomposition: In this approach, there is a clear distinction between the phases of the optimization procedure where the high-fidelity and reduced order models are queried. During the offline stage of the procedure, the key ingredients of the ROM models are built using data provided from the high-fidelity model. An adequately chosen greedy sampling technique is used to generate samples throughout the parameter space associated with the optimization problem. The associated configuration snapshots at these parameter settings are used to generate an empirical basis via POD. This empirical basis is then used to enable more concise Galerkin projections when the weak forms of the underlying PDEs are expressed.

On the other hand, during the online stage, the reduced order model is exclusively queried for the metrics of interest. A key requirement for the efficiency during the online stage is the "affine" or "separability" property. With this property, the operators in the problem can be written in the form: $A(\mu) = \sum_{q}^{Q} \theta_q(\mu) \bar{A}_q$. Here, the operator is written as the linear sum of parameter dependent coefficients ($\theta_q(\mu)$) and parameter independent terms $\left(\bar{A}_q\right)$. Using this decomposition, the projection operation of the Galerkin projection procedure can take place offline. Given an empirical basis $\tilde{\Phi}$, the projection of a stiffness matrix, for example, onto a low-dimensional subspace takes the form: $\tilde{\Phi}^T A(\mu) \tilde{\Phi} = \sum_{q}^{Q} \theta_q(\mu) \left(\tilde{\Phi}^T \bar{A}_q \tilde{\Phi}\right)$. During the offline phase, the parameter independent terms are created and stored; while during the online stage, the necessary operators can be efficiently assembled by first, evaluating the coefficients of the expansion ($\theta(\mu)'$s); then, by carrying out the linear sum shown above.

Such an approach has been used in the literature in the areas of: shape optimization [85–88]; inverse problems [89, 90]; multi-objective problems [91]; among others.

Adaptive Framework: In this approach, the high-fidelity model and reduced order model are used in tandem throughout the optimization procedure. These methods are very popular in the optimization literature for science and engineering problems. They are based on the observation that during the optimization procedure, the path

taken by the optimizer accounts for a very limited region of the design space. As such, proponents of this methods claim that when samples are taken globally over the entire design space, they are "wasted" because they give us information in areas of the design space that are not important to the optimization path. Consequently, the methods in this category seek to construct the empirical basis from the high-fidelity models in the neighborhood of the design point at each major iteration of the optimization procedure. This approach is often paired with a trust-region strategy (e.g. [92–95]). The trust-region takes into consideration the region of validity of the reduced order model and limits the strides that are taken during the iterations of the optimizer. Since the empirical basis generated by this procedure are created in the neighborhood of the current design point in the optimization procedure, it is likely to have smaller cardinality than an empirical basis generated for the entire design space.

The major disadvantage of using this approach is that the online stage is considerably more expensive than using the online-offline decomposition. This is due to the fact that the high fidelity model has to be queried during the online phase and the fact that the convenient affine property is less effective when the empirical basis has to be periodically updated. Some of the works in literature aim to reduce the overhead. Qian [94] used a certification procedure is used to determine if the reduced order model is accurate enough at the current design point and in its neighborhood. The reduced model is only recreated if this is not satisfied. This has the advantage of reducing the number of times the high-fidelity method has to be called during the online procedure. Carlberg [96, 97] used both the state variable and its derivatives to compute the empirical basis at a given design point. The latter can be cheaply obtained by using mathematical procedures aimed at solving linear algebraic systems with multiple right hand sides (such as back-solving after using LU or Cholesky decomposition with a direct solver; or by using an iterative solver with multiple right hand sides [98]).

2.3 High Level Overview Of Static Condensation

The merits of the SCRBE method were highlighted in chapter 1 and as such, this is the ROM approach of interest going forward. The literature for the SCRBE method can admittedly be abstract upon initial viewing. In order to provide an easier introduction for the reader who is unfamiliar with approaches of this kind; the static condensation method, as applied to the discrete finite element method, will be reviewed. Although there are some differences between the two methods (such as the Galerkin projection of the weak form), examining the static condensation approach is instructive for this case. The areas where the SCRBE is used to improve the efficiency of the static condensation will be identified during this presentation

2.3.0.1 *Overview Of The Static Condensation Method Applied To The Discrete Finite Element Problem*

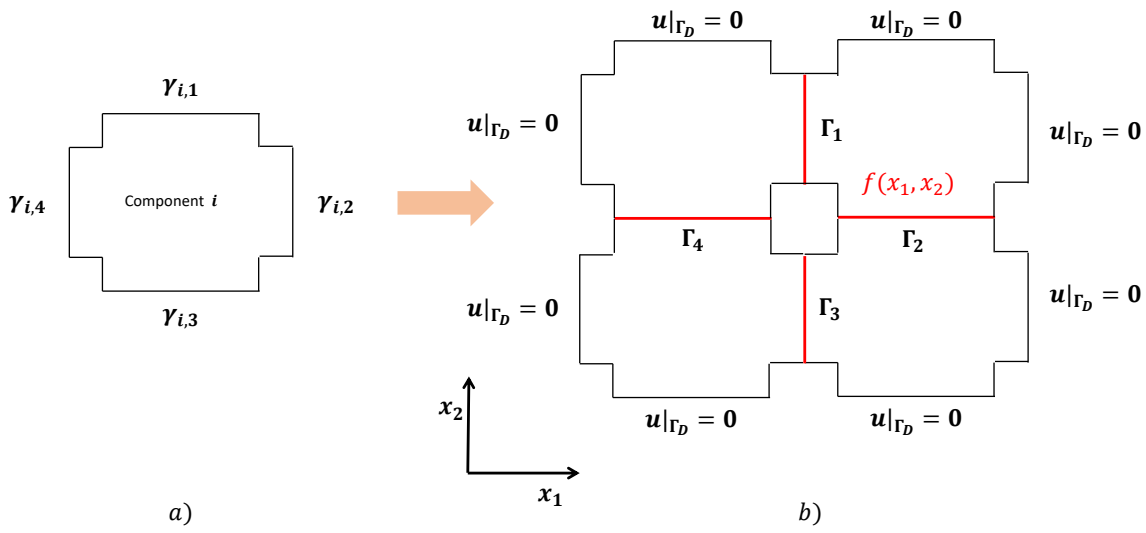

Figure 14: Illustration of a problem domain decomposed into four non-overlapping subdomains/ components (a) Individual component (b) Assembly of components. (Inspired by an image presented in [99])

Figure 14 shows a non-overlapping decomposition of a problem domain. It is assumed that there is a finite element mesh on this domain. For the global system, the discrete finite element linear algebraic equation is:

$$Ku = f \tag{7}$$

The stiffness matrix is represented as K; the displacement at the nodes is u; and finally, the force values on the nodes is f. If we consider the degrees of freedom on various regions of the problem domain, we have: b_i the degrees of freedom on the interior of component i (or *bubble space*); Γ_j, is the vector of displacements on the j^{th} interface between a pair of components; f_j, is the vector of force values on the j^{th} interface. For simplicity, the assumption is made that the forces on the interior of the component domains are zero. The solution and forces on the interfaces can each be collected and represented as $u_\Gamma = \{u_{\Gamma_1}, u_{\Gamma_2}, u_{\Gamma_3}, u_{\Gamma_4}\}$ and $f_\Gamma = \{f_{\Gamma_1}, f_{\Gamma_2}, f_{\Gamma_3}, f_{\Gamma_4}\}$, respectively. Using this partitioning, equation 7 can be decomposed as:

$$\begin{bmatrix} K_{b_1b_1} & 0 & 0 & 0 & K_{b_1\Gamma} \\ 0 & K_{b_2b_2} & 0 & 0 & K_{b_2\Gamma} \\ 0 & 0 & K_{b_3b_3} & 0 & K_{b_3\Gamma} \\ 0 & 0 & 0 & K_{b_4b_4} & K_{b_4\Gamma} \\ K_{b_1\Gamma}^T & K_{b_2\Gamma}^T & K_{b_3\Gamma}^T & K_{b_4\Gamma}^T & K_{\Gamma\Gamma} \end{bmatrix} \begin{Bmatrix} u_{b_1} \\ u_{b_2} \\ u_{b_3} \\ u_{b_4} \\ u_\Gamma \end{Bmatrix} = \begin{Bmatrix} 0 \\ 0 \\ 0 \\ 0 \\ f_\Gamma \end{Bmatrix} \tag{8}$$

The basic idea of the static condensation procedure is to use equation 8 to obtain a linear algebraic system that is written in terms of the degrees of freedom on the interfaces of the problem domain. This can be achieved by performing the multiplication on the left hand side of eq. 8, then by performing the steps of the block Gaussian elimination.

$$\begin{Bmatrix} K_{b_1b_1}u_{b_1} + K_{b_1\Gamma}u_\Gamma \\ K_{b_2b_2}u_{b_2} + K_{b_2\Gamma}u_\Gamma \\ K_{b_3b_3}u_{b_3} + K_{b_3\Gamma}u_\Gamma \\ K_{b_4b_4}u_{b_4} + K_{b_4\Gamma}u_\Gamma \\ \sum_{i=1}^{4} K_{b_i\Gamma}^T u_{b_i} + K_{\Gamma\Gamma}u_\Gamma \end{Bmatrix} = \begin{Bmatrix} 0 \\ 0 \\ 0 \\ 0 \\ f_\Gamma \end{Bmatrix} \tag{9}$$

The steps of the block Gaussian elimination are:

1. Perform the multiplication of the left hand side of equation 8. This is written as eq. 9.
2. From the first four rows, solve to obtain $u_{b_i} = K_{b_ib_i}^{-1} K_{b_i\Gamma} u_\Gamma$
3. Insert these solution into the equation corresponding to the last row. This results in equation 11
4. Solve the Schur complement equation, eq (12), for u_Γ
5. Using u_Γ, solve for u_{b_i} on each component by solving $u_{b_i} = K_{b_ib_i}^{-1} K_{b_i\Gamma} u_\Gamma$

Operation 3 above leads to:

$$\sum_{i=1}^{4} K_{b_i\Gamma}^T u_{b_i} + K_{\Gamma\Gamma}u_\Gamma = f_\Gamma \tag{10}$$

$$\left(\sum_{i=1}^{4} \left(K_{b_i\Gamma}^T K_{b_ib_i}^{-1} K_{b_i\Gamma} \right) + K_{\Gamma\Gamma} \right) u_\Gamma = f_\Gamma \tag{11}$$

$$K_{schur} u_\Gamma = f_{schur} \tag{12}$$

The resulting system that is formed in eq. (12) is known as the ***Schur complement***. In forming this system, the degrees of freedom on the interior of the components in the problem domain are "condensed" and written in terms of the degrees of freedom on the interfaces. There are several key takeaways from this procedure

- Each component's contribution to eq. 12 is independent of the contributions of other components; thus, invites parallelization

- The coefficient matrix of the Schur complement, K_{schur}, is denser than K and is of much smaller size
- If K is Symmetric and Positive Definite (SPD), then so is K_{schur} (see proof in [100]).

2.3.0.2 Application Of Reduced Order Modeling

The nodal-based finite element approximation space is used to solve the weak form of the PDE for many applications. A typical basis function in this scheme is illustrated in figure 15. The use of this type of basis function is very versatile in representing complex domains, as well as for refining the approximation in areas of interest in the problem domain. However, the associated linear algebraic systems are high dimensional and become computationally expensive to solve. The SCRBE approach identified areas where the static condensation procedure could be expedited. It addressed this by finding alternative ways of expressing the solutions on the various regions of the problem domain. The SCRBE method sought to find basis functions that: have larger support than the nodal basis functions; can be tailored to the specific problem at hand; and provide more concise linear algebraic systems to be solved. An example of an edge mode and a bubble space mode is shown in figures 16 and 17, respectively.

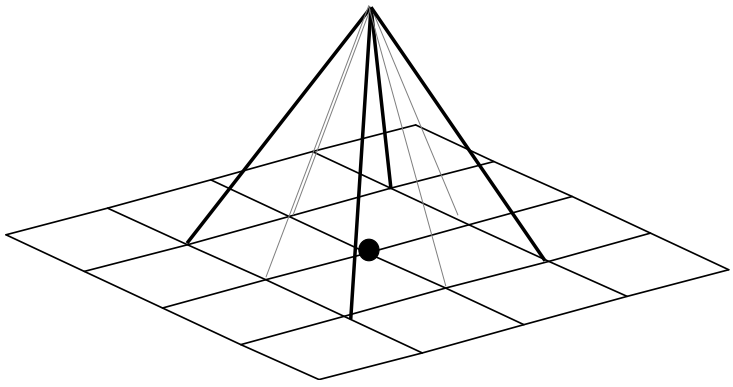

Figure 15: Illustration of a nodal basis function

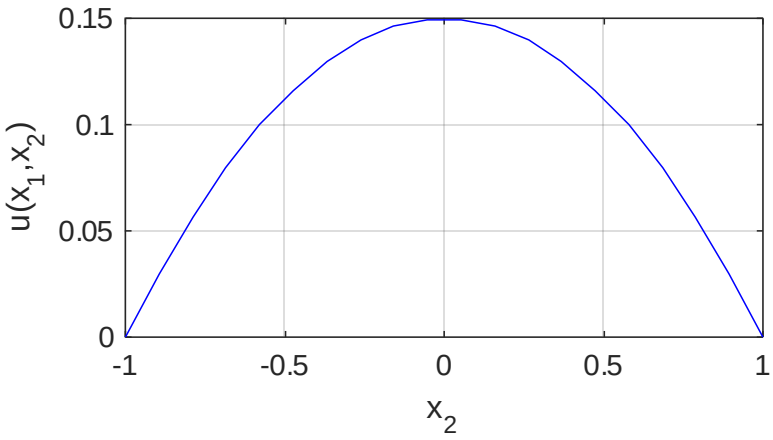

Figure 16: Example of an edge mode

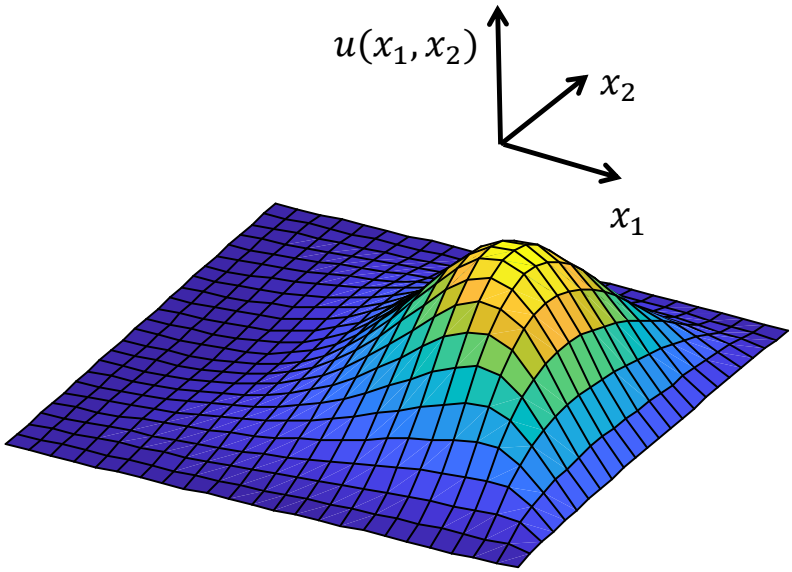

Figure 17: Example of a bubble mode

The use of bubble modes expedites step 2 of the block Gaussian elimination procedure; while the use of the edge space modes results in a Schur complement of much smaller size than using the nodal basis functions in step 4. This allows for faster solution times of the Schur complement.

2.4 Literature Review: SCRBE approach

Now that the main idea of what the SCRBE method addresses has been conveyed, the relevant literature will now be reviewed. The SCRBE method falls into the category of online-offline decomposition. The ingredients to the method are determined offline to enable a relatively efficient online stage.

Perhaps the earliest method that resembled the current Reduced Basis Element (RBE) method was developed by Lϕvgren et. al [101–103] and applied to problems in computational fluid dynamics. In these papers, the problem domain was decomposed into parametric components over which the RB method was applied. They were then "glued" together with a mortar-type, Lagrange multiplier method. The earliest papers describing the modern form of the SCRBE method, involving interoperable sub-domains (components) modeled through a combination of the RB method and static condensation, was by Huynh [104,105]. The SCRBE method is similar in flavor to the classical Component Mode Synthesis (CMS) method. In the CMS method, the first set of eigenvectors of the eigenvalue problem associated with the stiffness and mass matrices local to each component are determined. The solution of the weak form within each component is represented as a linearly scaled, truncated sum of the most significant eigenvectors. The static condensation method is then used to form a Schur complement system associated with the coupling modes on the interfaces between these components. The Schur complement system is normally of much smaller dimension that the original FEM problem. However, Kathrin [106] noted that the CMS approach suffers from rather slow convergence when an eigenmodal expansion is used to approximate the local solution on the interior of the components. On the other hand, the RB approximation can achieve an exponential rate of convergence [107]. As such, the SCRBE method uses the RB approximation instead of component mode synthesis to determine the local solution within each of the components. Huynh extended this approach to more complex problems for parametrized

complex Helmholtz partial differential equations [105] and three dimensional acoustic muffler analysis [108].

The computational efficiency of the SCRBE hinged, not only on the how concisely the solution on the interior of the components could be represented, but also on how concisely the coupling modes on the interfaces or *global ports* between components could be expressed. In Huynh's work, the solution on the interfaces was represented by an eigenfunction basis or more precisely, by the *Legendre polynomials* derived from the singular Sturm-Louville problem. Eftang et. al [81, 99, 109], later improved the SCRBE method by representing the solution on the interface using empirically derived modes. These empirical coupling modes are determined by the application of an algorithm that Eftang proposed. In this process, any two connectable components from a predetermined library of *archetype components* are paired together at the specific interface under study. The remaining non-shared interfaces are then subjected to random but smooth non-homogeneous Dirichlet boundary conditions. The solution over the shared interface is extracted and used to construct a snapshot set. After applying a proper orthogonal decomposition procedure to the retrieved data, a more concise basis for the coupling modes between components would then be available for online utility. This special variant of the SCRBE method was designated the Port Reduced Static Condensation Reduced Basis Element (PR-SCRBE) method. In the test problems considered, the use of empirical modes achieved much faster convergence than the eigenfunctions modes. Eftang proposed an aposteriori error certification with each of his contributions. However, Smetana [106] later made improvements in the sharpness of the solution and output bounds relative to Eftang's work. Smetna et al. also investigated optimal spaces for the port modes [110]. Here they proposed modes derived from a"transfer eigenproblem" and was shown to obtain rapid convergence.

Since the publication of these core set of papers, there have been other works in

literature that build upon this base. Vallaghé [111] investigated a mixed-mean conjugate heat exchanger modeling problem; solving symmetric eigenproblems [112] and parabolic PDE problems [113]. A limitation in the SCRBE literature was tackled by Bader et al. [114] when they studied Reynolds Lubrication problem. Previously, the interfaces between components within the problem domain were not allowed to intersect with each other. In their work, the authors pursued a space decomposition approach wherein the solution on the interfaces of the problem domain was represented by a combination of vertex and edge modes. However, the edge modes that they chose were not empirical, but eigenfunctions similar to the approach in the initial set of papers by Huynh. Other related methods in literature pursue combined domain decomposition and reduced empirical subspaces, adding in techniques from multiscale FEM for repeated grid structures [115, 116]. However, the focus of this thesis will be based on the work done under the SCRBE umbrella.

2.5 Challenges And Gaps In The Literature

After a review of the literature in this area, the author was unable to find any other published work that applied the SCRBE method to aerospace structural design i.e. structural optimization applied to an aerospace-type problem. In fact, most of the reviewed papers that build on the SCRBE approach focused on investigating the solution associated with a particular PDE and then evaluating the outputs that depend on it. The only paper found that references the SCRBE approach and performs numerical optimization was the work by Vidal-Codina et al. [116] for stochastic multiscale problems. In this work, they investigated the stochastic simulation and robust design of wave propagation through heterogeneous materials. The authors chose to use Lagrange polynomials distributed on Chebyshev nodes on the interfaces between the components. While this was an excellent piece of work, there are three main limitations with using this type of approximation space, particularly when dealing with

problem domains with geometrically complex, two dimensional interfaces in between the components.

- The Lagrange polynomial subspace is not hierarchical i.e. if it is enriched, it cannot reuse the same basis modes from the Lagrange polynomial subspaces of smaller cardinality. This provides some challenges that will be discussed later.
- Particularly for two dimensional interfaces (i.e. faces) between components, empirically-obtained subspaces lead to much faster convergence as the approximation is refined relative to other approximation approaches [81, 99, 109].
- It is difficult to find predetermined basis functions that are adaptable to complex, two dimensional interfaces between components. Admittedly, a piecewise approximation can be used on the interface, but this increases the dimensionality of the approximation. Empirical modes do not suffer from this limitation. An example of a complex geometrical interfaces in the context of aerospace structural design is illustrated in figure 18

In the case of gradient-based optimization, derivatives are needed for both the cost and constraint functions. Numerical differentiation is unsuitable to provide these quantities because problems using the SCRBE approach are likely to have very large parameter vectors and would require significant overhead to compute the required derivatives. As such, the *direct method* or *adjoint method* has to be used in order to calculate the derivatives of the metrics of interest. This requires approximations of the derivatives of the state variable or the Lagrange multipliers of the adjoint derivative problem, respectively, throughout the domain, including on the interfaces. The author was not able to find any works in the SCRBE literature that addressed the problem of determining empirical subspaces on the interfaces that are trained for the Lagrange multipliers of the adjoint problem or state variable derivatives.

From these observations, the first pair of gaps are:

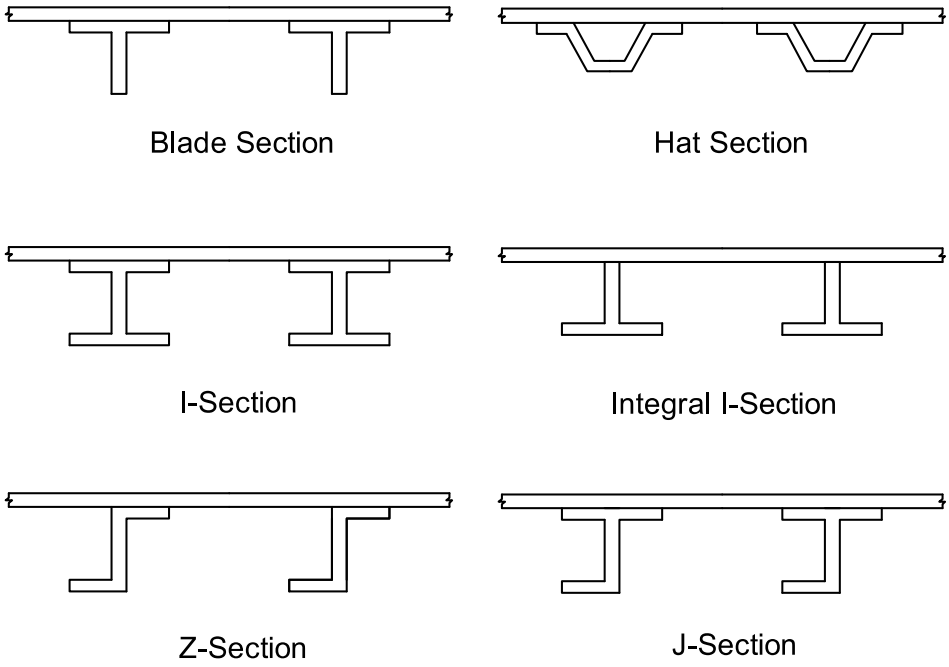

Figure 18: Examples of stiffened panels used in the wingbox

Gap 1.0: An approach is needed for performing conceptual level aerospace structural design with the SCRBE Method

Gap 2.0: An approach is needed to determine empirical subspaces on the interfaces between components that provide concise approximations of the state variable and its derivatives in the aerospace structural design context.

2.5.1 Computational Overhead With SCRBE Approach

A commonly highlighted issue in the SCRBE literature, is the computational overhead required to produce ingredients of the Schur complement when serial computing is used relative to the cost of solving the resulting system [105]. As an example of this disparity, consider an example from the literature. Bader [114] applied the SCRBE approach to a problem that was modeled with the Reynolds lubrication equations.

The global physical problem domain investigated consisted of 72 components. In their results, they noted that it required $3s$ to assemble the Schur complement while it only took $0.07s$ to solve it.

In the SCRBE literature, there are a few operational practices that are taken advantage of for reducing the impact of the overhead for large problem domains. These are:

- **Effective Components**: With this approach, it is noted that for the computational domain of many problems, there may be a significant quantity of components that are identical to one another. This is with regards to the component type and the current parameter settings on the component. With this knowledge, the local contribution to the Schur complement only has to be calculated for an "effective component," and used to fill the corresponding locations in the Schur complement matrix
- **Interactive Design**: With this design approach, there are no restrictions placed on the replication of components and their settings in the problem domain. However, with this approach, the parameter vector of only one component is updated at a time before resolving the Schur complement system. Using this approach, one only needs to update the portion of the Schur complement stiffness matrix that is affected by the modified component

In the case of gradient-based optimization, neither of these approaches are suitable because at each major iteration of the method, the entire global parameter vector for the problem is likely to change at each major iteration of the optimization procedure. This requires an update the local contribution of each component to the global Schur complement stiffness matrix and the associated systems required to furnish the gradients.

This brings us to the next gap:

Gap 3.0: An approach is needed to help to alleviate some of the computational overhead associated with furnishing the ingredients of the SCRBE method.

The expense in forming - in particular - the coefficient stiffness matrix is due to: (1) determining the solution on the interior of each component as a function of the degrees of freedom on its local interface i.e. the bubble solutions. (2) Using these bubble solutions to form the local component contribution to the coefficient stiffness matrix of the Schur complement system. In the SCRBE method, a single reduced basis is formed for each interface mode in order to expedite step (1). Alternative, but similar works to the SCRBE method in the ROM literature attempt to bypass the expense of step (1) by creating a single reduced bubble space that can accommodate a wide variety of local boundary conditions prescribed on the interfaces and interior of a component's domain. This reduced bubble space is formed by examining snapshots for the local solution defined on the interior of the component for several combinations of parameter settings and a variety of boundary conditions. As such, this only necessitates the solution of one linear algebraic system with multiple right hand sides when determining the bubble solutions. This approach is used by Ipichino et al. [117], Buhr et al. [115], and Vidal-Codina et al. [116]. However, these bubble spaces will inevitably be larger than any of the individual bubble spaces tailored specifically to a particular interface mode in the SCRBE method. This is due to the amalgamation of a large number of datasets that may be mutually correlated, but are not likely to completely overlap. Therefore, there is a trade-off between solving potentially many, small linear algebraic systems (Eftang [109] estimates a cardinality of 10 per basis) in the SCRBE method, versus solving one larger linear algebraic system with multiple right hand sides in the alternative methods. Recall that for a direct method, the expense of the solving linear algebraic system is $O(N^3 + N^2M)$ flops. Here, N and M are the size of the system and the number of right hand sides, respectively. This is likely to be applied due to the density of the ROM system.

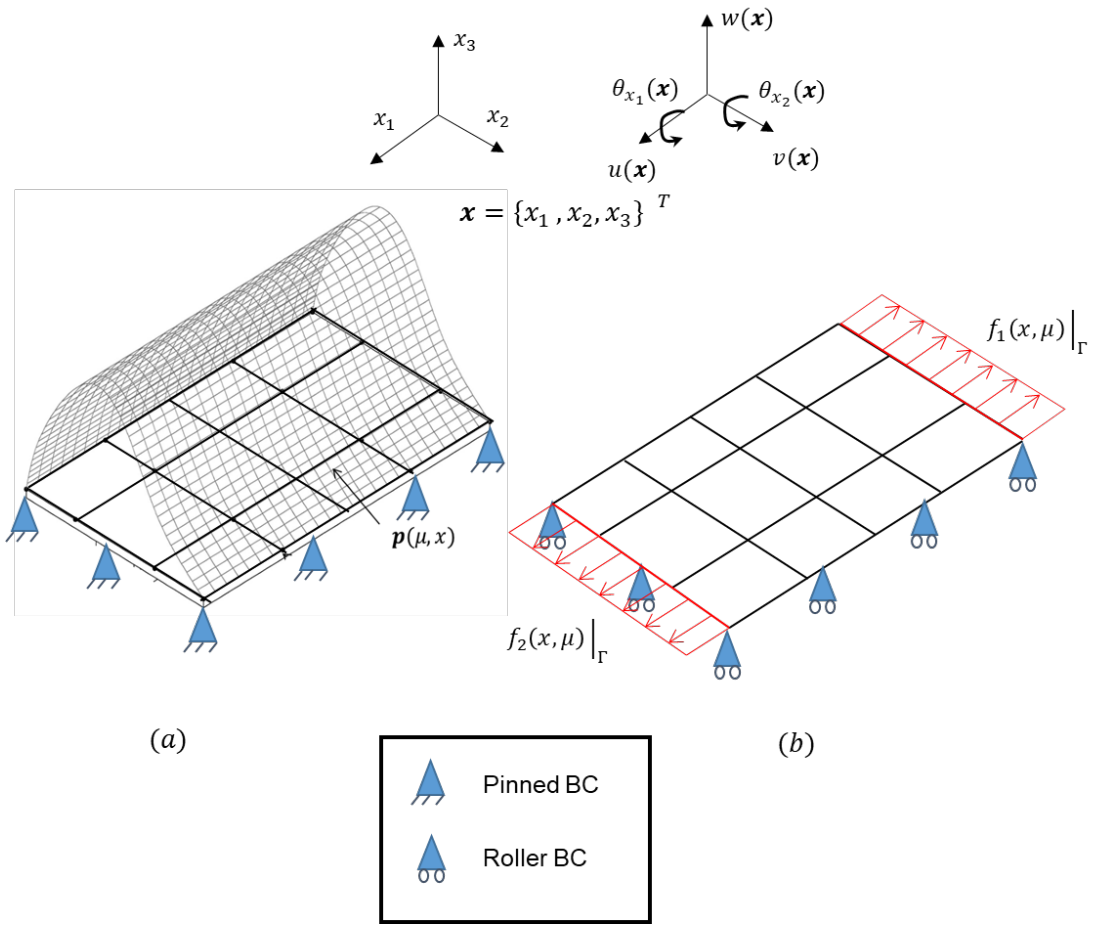

Figure 19: Shell subjected to two cases of boundary conditions. (a) Out of plane pressure loading, $p(\mu, x)$, with pinned boundary conditions. (b) In plane loading with roller boundary conditions

In the numerical experiments performed by the authors in the alternate methods, the problems were linear elliptical and featured solution fields that were scalar (e.g. temperature fields). In the case of solid mechanics, the solution fields are often vector fields. Depending on how the boundary conditions are applied, responses in certain degrees of freedom may not be elicited, making it difficult to find a single reduced basis that can accommodate a wide variety of bubble solutions. Consider the example shown in figure 19. Illustrated here is a plate subjected to two loading scenarios. For the plate, there are 5 degrees of freedom per node for this i.e. 3 orthogonal, translation d.o.f. and 2 (meaningful) rotational degrees of freedom. In the example shown, consider two sub-cases:

Case (a):

- Simply supported, pinned boundary conditions
- Application of an out-of-plane pressure field

Case (b):

- Roller boundary conditions
- Material and geometric symmetry of the plate's cross-section
- Application of in-plane boundary loads with no eccentricity

Case (a) will invoke out-of-plane displacement and rotations, with no in-plane displacements; whereas, case (b) will bring about the opposite. In-plane displacements, with no out-of-plane displacements or rotations. Thus, it can be seen that it is not straight-forward to create one global reduced bubble space that can accommodate various boundary conditions when a vector-field is being investigated. This challenge can perhaps be overcome by creating a separate empirical basis for the component of the state solution corresponding to each nodal degree of freedom and concatenating the various groups to form a global basis. However, this approach will increase the size of the overall basis.

The author acknowledges these other works in literature. However, in the present context, a method will be proposed in chapter 6 that attempts to bypass the calculation of the reduced bubble solutions and the need for performing step (2) during the online stage of the procedure. Instead, the proposed method works with terms that are dependent on the number of interface modes defined locally on each component within the problem domain. The performance of the proposed approach will only be compared to the SCRBE method.

2.5.2 Key Enabler: Parallel Computing

Besides the possible methods discussed above, the solution times can be expedited by the manner of implementation. As mentioned in chapter 1, the SCRBE method is very much patterned after the traditional static condensation approach for decomposing and solving the full finite element problem for very large systems. However, the introduction of reduced order modeling at the component level helps to expedite the calculations of the ingredients to the Schur complement stiffness matrix and to solving the Schur complement itself. In the literature for using high performance computing for large finite element systems, there are several frameworks that are presented to tackle this problem. Saad [100] provides an excellent overview of various algorithms available for the task of computing and solving the Schur complement in parallel. The purpose here is not to be exhaustive in listing all of the possible algorithms and rate their relative performance. Rather it is to state the observation that the task of calculating the local contributions to the Schur complement and its associated systems is "embarrassingly parallel." That is to say, they can be performed in parallel without any interdependencies between the tasks. In performing these tasks, the computational time is:

$$T_p = T_{\text{comp}} + T_{\text{comm}} \tag{13}$$

$$= \frac{T_s}{n} + T_{\text{comm}} \tag{14}$$

where:

- T_p represents the computational cost required to distribute, compute and collect the SCRBE ingredients in parallel
- T_{comp} represents the computational cost required to perform only the computation part of the SCRBE ingredients
- n is the number of processors
- T_s represents the computational cost required to compute the SCRBE ingredients serially
- T_{comm} is the overhead required to transmit data for the present problem. This overhead is heavily dependent the parallel computing architecture and the algorithm being used

There is some speedup afforded when solving the Schur complement using a parallel computing architecture; however, since this cost has been shown empirically to be a very small fraction of the overhead cost of the SCRBE method, the impact of parallel computing on it will not be addressed. From equation 14 we can see that provided the communication costs can be kept the same, we can reduce the parallel computation time provided that we can reduce the serial computation time required to produce the ingredients to the Schur complement.

Figure 20 further explores the impact of reducing the computational overhead at the component level to the overall efficiency of the method. Here we see that if the average overhead per component is cheaper than using another approach, then the impact of the time saving becomes more significant with an increased number of components being treated serially or in parallel on a single node.

2.6 Research Objective

The research objective will now be stated for the present work. It is meant to address the Gap 1.0. It is:

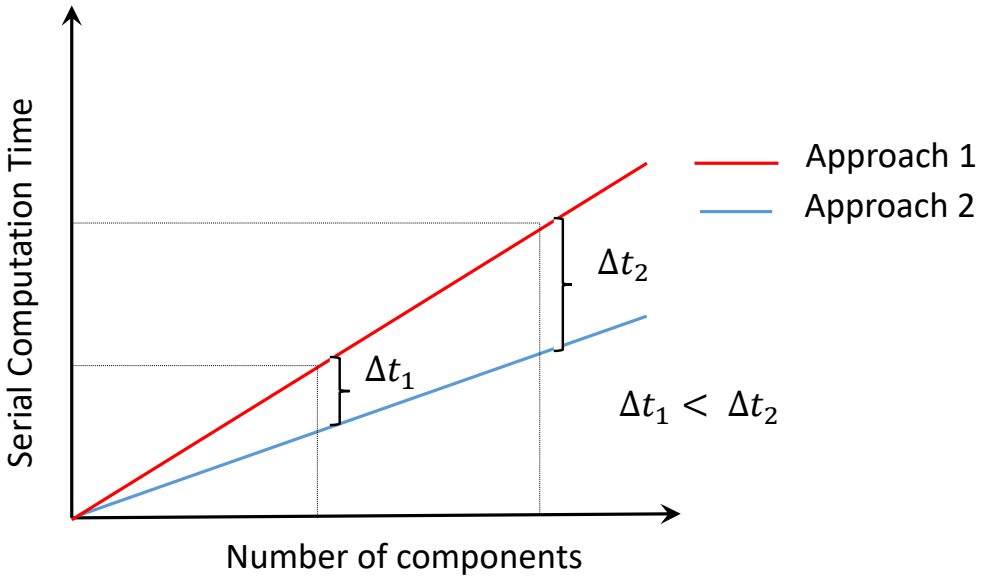

Figure 20: A notional plot of the serial time required vs number of components for two approaches. These approaches have different average times required to calculate their local Schur ingredients

Research Objective: To develop an approach that uses the Static Condensation Reduced Basis Element Method to enable efficient, conceptual-level, aerospace structural design

In the chapters that follow, the approach taken to address this research objective will be presented. Along the way, the gaps that have presented here will be addressed through the use of appropriate research questions, hypotheses, and then finally numerical experimentation

2.7 Chapter Summary

A literature review was performed for PDE constrained optimization and the SCRBE approach. This was followed by a highlight of a few challenges that the author identified when exploring the literature associated with the method. Several gaps were identified and then finally, the research objective that guides this research was officially stated.

Chapter III

PROBLEM DEFINITION

3.1 Chapter Overview

In this chapter, an overview will be provided for the problem that will be addressed in this thesis. Additionally, some limitations in the scope of the work will be stated. For convenience, the research objective presented at the end of chapter 2 will be restated here:

Research Objective: To develop an approach that uses the Static Condensation Reduced Basis Element Method to enable efficient, conceptual-level, aerospace structural design

3.2 Problem Statement And Scope Limitations

Aerospace structural design is a very complex field with many considerations required throughout the design phases. For the present problem, a list of the high level limitations and assumptions will be stated in order to provide a reasonable project scope. It is with the understanding that focus is on the conceptual and perhaps early preliminary levels of the aircraft design process.

1. **Class** III **Method**: A review of the categories of methods for weight estimation throughout the phases of aircraft design was presented in chapter 1. It was seen here that due to inherent lack of detailed component definition in the early phases of design, estimates made by numerical methods for primary weight have to be supplemented by empirical methods to furnish complete weight estimates. The work here is meant to enable the class III contribution to the class $II\&^1/_2$ category. However, estimating the weight of the secondary structures will not

be considered and the author defers to other work in literature.

2. **NAND Framework**: Since most of the ROM papers in literature seem to fall into the NAND framework, this approach is considered in this work.

3. **Single Disciplinary Analysis**: In aerospace design, many sub-disciplines are highly coupled with each other. This often necessitates the multi-objective optimization frameworks to capture the couplings and make necessary trade-offs. However, for simplicity, the focus will be placed on structural optimization as an individual discipline.

4. **Static, Linear Elasticity**: For this work, the focus will be placed on static, linear-elasticity problems.

5. **Mass Minimization**: The main focus of this work is to find the lightest, structurally admissible designs at the conceptual level. As such, the objective function selected for this work is the mass associated with the physical domain being considered.

6. **Structural Constraints**: There are many possible constraints to be considered in structural design. This includes manufacturing considerations (especially with the use of composite materials); production consideration; aeroelastic constraints; etc. However, only structural constraints will be considered here. Further details will be given regarding the assumptions for the structural constraints in section 3.2.2.

7. **Aposteriori Certification** Aposteriori error certification is an excellent feature described in the reduced basis approximation literature. With this tool, at any point in the parameter space (i.e. any combination of design variables) it gives an upper bound on the approximation error between the reduced order

model and the truth model from which the ROM was created. An error certification framework was not developed in this work, but instead was relegated to future work.

3.2.1 Statement Of The Optimization Problem Constrained By Schur Complement

Now that the scope of the present work has been specified. The structural optimization problem that is addressed will now be specified. It is:

$$\text{Optimize :} \qquad m\left(\mu\right) \tag{15}$$

$$\text{w.r.t :} \qquad \mu \in \mathcal{D}, \;\; x \in \Omega \tag{16}$$

$$\text{Subject to :} \qquad \mathcal{R}\left(u(\mu), \mu\right) = 0 \tag{17}$$

$$g_\ell\left(u(\mu, x), \mu\right) \leq 0 \;\text{ for }\; 1 \leq \ell \leq n_g \tag{18}$$

Here:

- μ - the parameter vector (design variables) of the entire domain
- x - the location in the physical domain Ω
- u - the state variable of the problem. In this case, it is the displacement field
- m - the total mass associated with the physical domain
- $\mathcal{R}\left(u(\mu), \mu\right)$ - The residual of the discretized, weak form of the PDE
- g_ℓ - the ℓ^{th} inequality constraint that depends on the state variable

Note that equality constraints are not explicitly considered here. In this optimization statement, the inequality constraints are dependent on the state variable, u. According to the NAND framework, the weak form of the PDE is treated as a black-box. Consequently, this black-box needs to provide estimates of the constraints, g_ℓ, and their derivatives whenever needed.

3.2.2 Conceptual Level Structural Inequality Constraints

Aerospace structural subsystems are normally composed of stiffened panels. This type of construction normally features thin, stiffened components, that typically have high stiffness-to-strength ratios relative to other types of constructions. An overview of typical aerospace structural design, particularly in the case of a wingbox, is given in appendix A.3.

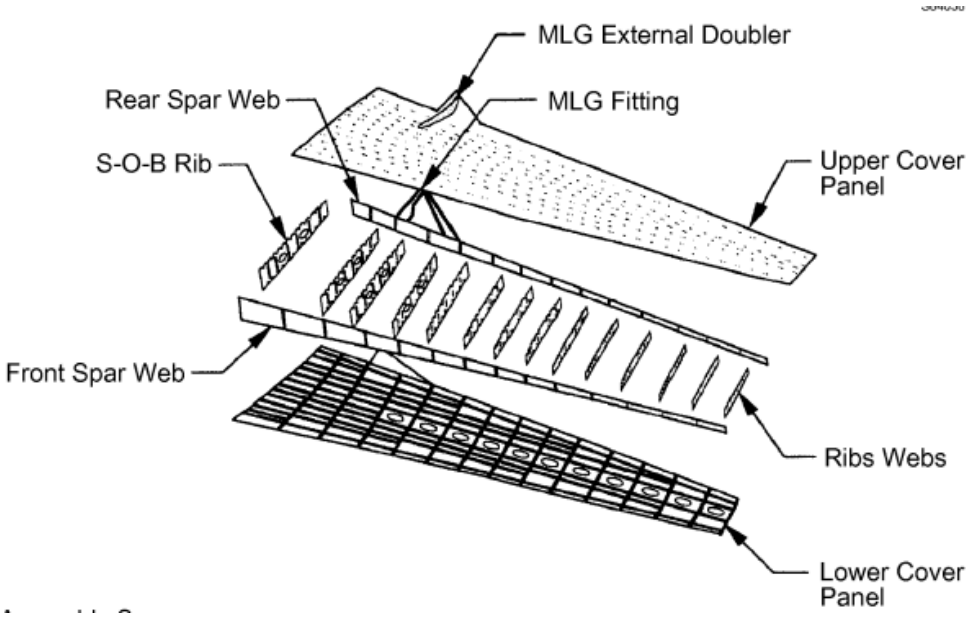

Figure 21: Exploded Isometric View of a Conventional Transport Aircraft Wing [118]

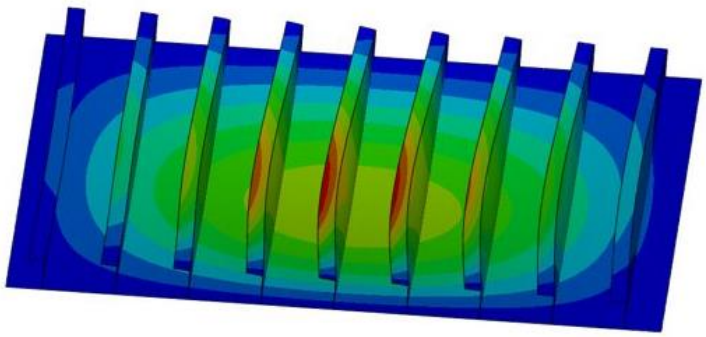

Figure 22: An example of a stiffened panel undergoing panel buckling [33]

When stiffened panels are loaded, they are vulnerable to certain types of failures

which render their use limited or even results in catastrophic failure. Kassapoglou [12] provided a detailed description of these potential failure mechanisms. They can be placed into two broad categories. These are: (1) material failure and (2) structural instability when compressive loads/stresses are present. In the former category, the material comprising the components fail because the local stresses and/or strains that develop exceed the material strengths. The second category of failures involve either the loss of structural stability of each stiffened panel as a whole or the localized instability of any of its constituents. Localized instability includes, skin buckling between stiffeners; stiffener crippling; skin-stiffener separation; stiffener inter-rivet buckling; and stiffener column buckling. It is incumbent on the structural designer to not only ensure that all these failure modes are precluded during aircraft operation, but to also sequence them such that if one should occur, it is one that will not result in catastrophic failure of the entire aircraft.

3.2.2.1 Material Failure

The first type of structural failure can be described as a bound constraint. The associated inequality constraints, $g_\ell = g_\ell\left(u(\mu, x), \mu\right), \;\; 1 \leq j \leq n_g$, form nonlinear functionals that vary over the problem domain, Ω. The condition: $\max \;\; g = g_\ell(u(\mu, x^*), \mu) \leq 0$ where $x^* = \text{argmax}_x \, g_\ell(u(\mu, x), \mu)$ has to be satisfied by the optimization procedure; however, the location of x^* varies with parametric changes to the problem. Since the state variable $u(\mu)$ (and hence g_ℓ) is not calculated analytically, it is difficult to determine where $\max \;\; g = g_\ell(u(\mu, x^*), \mu)$ occurs in the problem domain. Early works in literature attempted to address this problem by checking the constraint of the finite element mesh in various locations (perhaps even element by element). However, this presents two main challenges in the present context, (1) A strict tenet of the SCRBE approach and of reduced basis approximation approaches in general is, the underlying finite element model should not be queried during the online stage

of the procedure. (2) The maximum values produced in this fashion do not enable continuous derivatives of the constraint to be found, as is needed by the optimization procedure.

To address this problem, several *constraint aggregation techniques* have been proposed in the literature of structural optimization. The constraint aggregate takes the form of:

$$c(g,\rho) = \max\ g + r(g,\rho) \tag{19}$$

where: $c(g,\rho)$ is the constraint aggregate approximation of $g(u(\mu,x^*),\mu)$; ρ is the aggregation parameter that controls the functional approximation; and, $r(g,\rho)$ is the residual term. The approximation must have the following behavior

$$\lim_{\rho\to\infty} c(g,\rho) = \max\ g \tag{20}$$

This form now gives a smooth estimate to the quantity of interest.

Several constraint aggregate functionals have been proposed including: the Kreisselmeier Steinhauser (KS) functional [119]; the p−norm functional; and the induced aggregation functional [120, 121]. Kennedy et. al [120], carried out a convergence study on the convergence behavior among these functionals. They noted, that the accuracy of the discrete forms of both the KS and p−norm functionals diminished as the underlying finite element mesh was refined; whereas, the induced functional displayed mesh-independent convergence behavior. The finite element meshes that are used in Reduced Basis Approximation applications tend to be quite refined. Due to the favorable, mesh-independent properties of the discrete version of the induced aggregation functional, it was selected for this work.

The particular choice of induced aggregate functional selected for this work is the induced exponential functional and the continuous version takes the form:

$$c_{IE}(g_\ell,\rho) = \frac{\int_\Omega g_\ell(x) e^{\rho g_\ell(x)} d\Omega}{\int_\Omega e^{\rho g_\ell(x)} d\Omega} \tag{21}$$

where Ω in this context is the physical domain. This functional is evaluated by the use of numerical integration. Additionally, the value of ρ and the order of the numerical integration have to be determined in a heuristic fashion in order to minimize $r(g, \rho)$ for a given application. In this work, although $r(g, \rho)$ might not be zero in a practical setting, the inequality constraints estimated with this approach is still treated as the truth model. It is expected that the practitioner will make sufficient refinements to the problem in order to get the estimates to within suitable tolerances.

3.2.2.2 Structural Instability

While the use of reduced order modeling allows one to capture the behavior of quite detailed finite element models, the partial differential equation selected for this thesis does not capture the structural stability (global or local buckling) of problem domain and its components. This normally involves the solution of the eigenvalue problem:

$$K\psi = \lambda K_G \psi \tag{22}$$

Where: λ is the eigenvalue; ψ is the eigenmode; and K and K_G are the small deflection and geometric stiffness matrices of the structure, respectively, associated with the buckling problem.

An alternative method that is commonly used in conceptual level structural design, is *global-local* analysis. With this type of approach, the global finite element model corresponding to the linear static structural problem is first solved for the displacement field and reaction stresses/forces. Semi-analytical models (e.g. [122–125]); detailed finite element models (e.g. [126, 127]); or experimental-data based analysis ([128–130]) can then be used to determine whether or not the local regions within the model are above some threshold for structural stability. Although the use of the detailed finite element method for solving the buckling eigenproblem is prohibitive at the conceptual level due to the computational cost, there are maturing reduced order

modeling approaches that seek to expedite this type of analysis. Such an example is the work by Vallaghé et al. [112] and Horger et al. [131]

These localized models often require as input, the displacement or internal forces acting on the boundaries of the sub-regions. In the case of structural instabilities, this often takes the form of the averages of the load distributions on the boundaries. This idea is illustrated in figure 24.

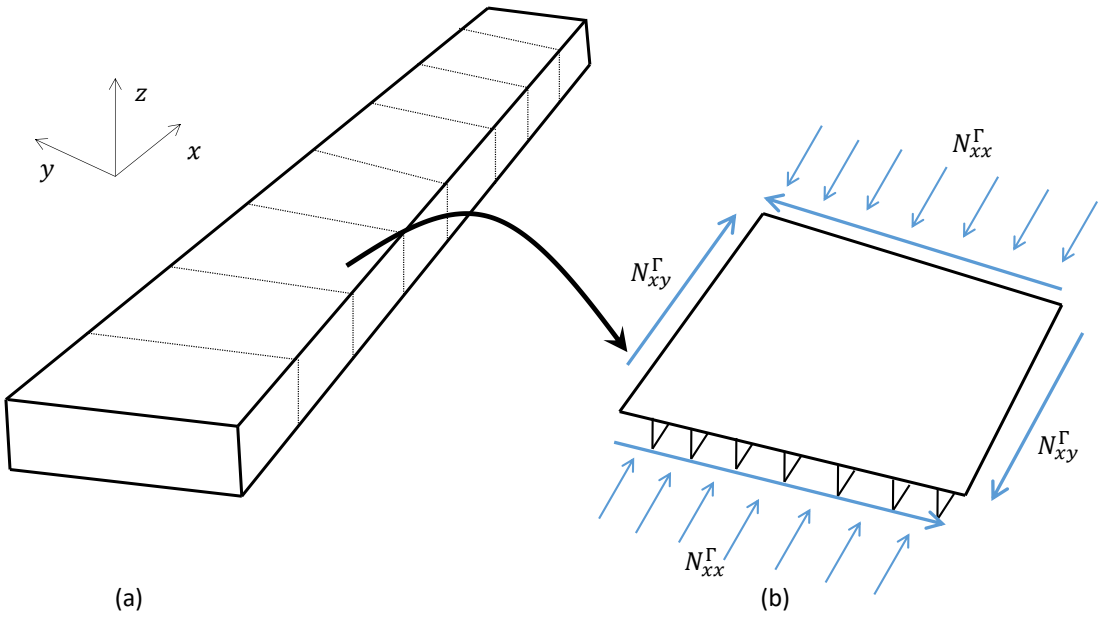

Figure 23: An illustration of a global local-analysis. (a) Global model (b) Local model

Consequently, estimates of these average loads need to be supplied whenever these constraints are required. The boundary loads take the functional form: $N^{\Gamma}_{xx}(u(\mu),\mu)$, $N^{\Gamma}_{yy}(u(\mu),\mu)$, $N^{\Gamma}_{xy}(u(\mu),\mu)$. Here N^{Γ}_{xx} and N^{Γ}_{yy} are the normal stress resultants on the edges of the constituent thin plates, while N^{Γ}_{xy} is the shear stress resultant. If other quantities are needed for the buckling analysis, such as moment resultants or part stresses, they can be furnished in a similar manner. The key take-away is the functional dependence on the approximate solution of the PDE, $u(\mu)$, and the

parameter set μ. The averages of the above-listed quantities are:

$$N^{\Gamma}_{xx,\text{avg}} = \frac{\int_{\Gamma} N^{\Gamma}_{xx}\left(u(\mu),\mu\right) d\Gamma}{\int_{\Gamma}(1) d\Gamma} \tag{23}$$

$$N^{\Gamma}_{yy,\text{avg}} = \frac{\int_{\Gamma} N^{\Gamma}_{yy}\left(u(\mu),\mu\right) d\Gamma}{\int_{\Gamma}(1) d\Gamma} \tag{24}$$

$$N^{\Gamma}_{xy,\text{avg}} = \frac{\int_{\Gamma} N^{\Gamma}_{xy}\left(u(\mu),\mu\right) d\Gamma}{\int_{\Gamma}(1) d\Gamma} \tag{25}$$

Here Γ corresponds to the local, physical domain boundary segment of interest. Since these quantities will have to be determined with the finite element method, they have to be calculated on the finite elements in the vicinity of the local boundary. As such, area weighted averages are often used in order to estimate the average loads [33]. Denoting the collective area of the finite element mesh in the vicinity of a particular local boundary as A_s, the updated averages are:

$$N^{\Gamma}_{xx,\text{avg}} \approx \frac{\int_{A_s} N_{xx}\left(u(\mu),\mu\right) dA_s}{\int_{A_s}(1) dA_s} \tag{26}$$

$$N^{\Gamma}_{yy,\text{avg}} \approx \frac{\int_{A_s} N_{yy}\left(u(\mu),\mu\right) dA_s}{\int_{A_s}(1) d\Gamma} \tag{27}$$

$$N^{\Gamma}_{xy,\text{avg}} \approx \frac{\int_{A_s} N_{xy}\left(u(\mu),\mu\right) dA_s}{\int_{A_s}(1) dA_s} \tag{28}$$

The terms are dependent on the displacement solution in the vicinity of the local boundary next to which A_s is defined. In order to avoid overly querying the underlying finite element model, these area-weighted integrals will be approximated by the Gaussian quadrature approach. These average values are fed into the approach used to calculate the various forms of structural stability constraints. This takes the form: $\mathbf{BC}\left(N^{\Gamma}_{xx,\text{avg}}, N^{\Gamma}_{yy,\text{avg}}, N^{\Gamma}_{xy,\text{avg}}, \mu\right) \leq 0$.

Depending on the level of abstraction required, these averages loads may not be calculated on entire local boundary, but on non-overlapped sub-regions of the boundary.

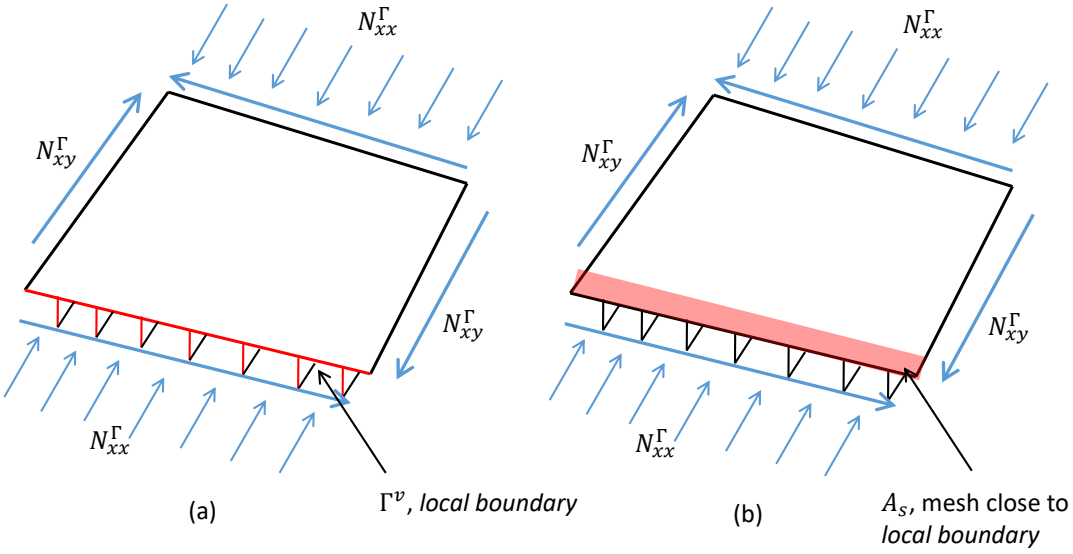

Figure 24: Evaluating the average edge loads (a) on local boundary (b) on mesh in the vicinity of a local boundary

These choices for dealing with the constraints offer a compromise for the requirement of not querying the underlying FEM model. Although the FEM model will be queried, it will be at a very small number of sampling points on the problem domain and as such, should not prove to be overbearing in the overall scheme.

3.3 Presentation Of Research Questions

Research questions have been generated in response to the gaps identified in chapter 2 and are presented below. For ease of reference, the relevant gap is paired with the associated research question.

3.3.1 Research Question 1

Gap 2.0: An approach is needed to determine empirical subspaces on the interfaces between components that provide concise approximations of the state variable and its derivatives in the aerospace structural design context.

RQ 1.0: What is a suitable approach for determining empirical interface subspaces that can concisely represent the constraints and their derivatives as the fidelity of the model is refined?

3.3.2 Research Questions 2 and 3

Gap 3.0: An approach is needed to help to alleviate some of the computational overhead associated with furnishing the ingredients of the SCRBE method.

RQ 2.0: What is an alternative approach for generating the ingredients of the SCRBE procedure that will help to alleviate the computational overhead, for similar levels of approximation error?

RQ 3.0: How do the SCRBE method and its surrogate compare in an optimization setting?

The hypotheses that will be raised in response to these research questions presented in chapter 2 will be stated in chapters 5 and 6. Finally, numerical experiments

will be performed to address the hypotheses in chapter 8.

3.4 Chapter Summary

In this chapter, the major assumptions and limitations of the this work were presented. This was followed by the statement of the research questions that appear throughout out the rest of the work.

Chapter IV

THE FINITE ELEMENT PROBLEM AND REDUCED BASIS APPROXIMATION

4.1 Chapter Overview

In this chapter, a presentation is given for the strong form of the governing partial differential equation associated with the linear elastostatic problem. This is followed by the development of the abstract finite element problem. The chapter is rounded out by a presentation of the use of reduced basis approximation to expedite the finite element problem. The development in chapter 5 builds upon the material presented here. Therefore, a proper understanding of the material in this section is fundamental for the remaining work.

4.2 Linear Elasticity: Strong Form and Weak Form

4.2.1 Strong Form Of The Linear Elastostatic Problem

Consider a generic solid as shown in figure 25. It has a domain $\Omega \subset \mathbb{R}^d$ (where $d = \{1, 2, 3\}$), with a Lipschitz boundary, Γ. The domain is subjected to a body force, f; homogeneous displacement boundary conditions on the boundary segment $\Gamma^D \subset \Gamma$; and surface traction, g_N, on the boundary segment $\Gamma^N = \Gamma \setminus \Gamma^D$. The linear elliptic partial differential equation (PDE) governing the stress and displacement behavior

throughout the solid can be written as follows [1]

$$-\nabla \cdot \sigma = f, \quad \text{in } \Omega \tag{29}$$

$$\sigma_{ij} = C_{ijkl}\epsilon_{kl}, \quad \text{in } \Omega \tag{30}$$

$$u = 0, \quad \text{on } \Gamma_D \tag{31}$$

$$\sigma \cdot e^n = g_N^n, \quad \text{on } \Gamma_N \tag{32}$$

$$\sigma \cdot e^t = g_N^t, \quad \text{on } \Gamma_N \tag{33}$$

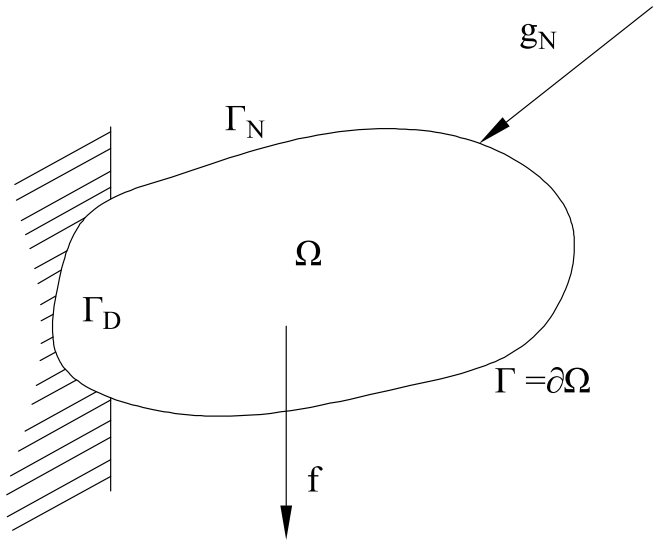

Figure 25: Illustration of an arbitrary solid with domain Ω subjected to a body force f, a traction force g_N and homogeneous displacement boundary conditions.

Equation (29) is known as Cauchy's equilibrium equation. In component form it can be written as [2]:

$$-\frac{\partial \sigma_{ij}}{\partial x_j} = f_i \tag{34}$$

[1] Note that g_N is used to describe a boundary traction in this context and not a constraint on the optimization problem as used in other chapters.

[2] Note that Einstein's summation convention is used here.

Here σ is the second-order stress tensor. The terms in the stress tensor, σ_{ij}, represent the force per unit area in direction x_i on a surface with unit normal along the direction x_j. As such, the diagonal elements, σ_{ii}, are direct stresses and the off-diagonal elements, σ_{ij} $(i \neq j)$, are shear stresses. In the absence of concentrated moments, the principle of conservation of angular momentum shows that the stress tensor is symmetric. Thus, there are only 6 independent terms in the tensor.

The displacement field of the solid is represented by $u = u(x)$, for $x \in \Omega$. Specifically, for an individual particle, the displacement from its initial position, x_0, to its final position, x, is given by $u(x) = x - x_0$. Assuming small displacement gradients, the strain of the solid is measured with the second-order, linearized strain tensor, ϵ. The stain tensor is given by

$$\epsilon = \frac{1}{2}(\nabla u + \nabla u^T) \tag{35}$$

or in component form

$$\epsilon_{ij} = \frac{1}{2}\left(\frac{\partial u_i}{\partial x_j} + \frac{\partial u_j}{\partial x_i}\right) \tag{36}$$

A critical assumption in the linearized case is that the point-wise rotations are small. The diagonal terms, ϵ_{ii}, represent the change in length in the x_i direction, while the off-diagonal terms, ϵ_{ij} $(i \neq j)$, represent the first order change in the angle between two initially orthogonal directions, x_i and x_j. The constitutive relationship equation (30), relates the stress to strain in the material. In the linear elastic case it is known as Hooke's law, with the fourth order *elastic tensor*, $C = C_{ijkl}$. In the most general form, C has 36 independent components; however, for certain classes of materials, it can be greatly simplified. Consider for example, C for an isotropic solid. The tensor C_{ijkl} is given by

$$C_{ijkl} = \frac{\nu}{(1+\nu)(1-2\nu)}\delta_{ij}\delta_{kl} + \frac{1}{2(1+\nu)}(\delta_{ik}\delta_{jl} + \delta_{il}\delta_{jk}), \qquad 1 \leq i,j,k,l \leq d \tag{37}$$

This results in a sparse tensor with few non-zero terms. In general, utilizing the

symmetry property of C_{ijkl}, equation (30) can be written in the form

$$\sigma_{ij} = C_{ijkl}\frac{\partial u_k}{\partial x_l}, \qquad 1 \leq i,j,k,l \leq d \tag{38}$$

Therefore, the strong form of the equation governing the displacement of the solid can be restated by substituting equation (38) into equation (29) resulting in the following linear, second order elliptic PDE

$$-\nabla \cdot (C\nabla u) = f \tag{39}$$

or in component form

$$-\frac{\partial}{\partial x_j}(C_{ijkl}\frac{\partial u_k}{\partial x_l}) = f_i, \qquad 1 \leq i,j,k,l \leq d \tag{40}$$

Along sections of the boundary, Γ, certain displacement and traction boundary conditions are specified. Along the portion, Γ_D, Dirichlet boundary conditions are prescribed. These are applied directly to $u(x)$. In the case shown in Figure 25, $u|_{\Gamma_D} = 0$, as stated in equation (31). Along the portion of the boundary, Γ_N, tractions forces (concentrated or distributed) are applied. Traction forces apply Neumann boundary conditions i.e. they specify boundary values on the first derivative of $u(x)$. The traction forces can be resolved into two components, one tangential to the surface (g_N^t) and the other normal (g_N^n). Using equation (38), the Neumann boundary conditions (equations (32) and (33)) can be restated as:

$$\left(C_{ijkl}\frac{\partial u_k}{\partial x_l}\right) \cdot e_j^n = g_N^n e_i^n, \qquad 1 \leq i,j,k,l \leq d \tag{41}$$

$$\left(C_{ijkl}\frac{\partial u_k}{\partial x_l}\right) \cdot e_j^t = g_N^t e_i^t, \qquad 1 \leq i,j,k,l \leq d \tag{42}$$

4.2.2 Parametrization Of The Problem

To describe more general situations, the problem domain, Ω; the elastic tensor (C_{ijkl}); and the forces (f and g_N); can be made to be parametric. These quantities are parametrized by the parameter vector $\mu \in \mathcal{D} \subset \mathbb{R}^p$. This vector consists of p elements,

each of which has a finite and closed domain. $\mathcal{D}$ represents the Cartesian product of all of the parameter domains belonging to the elements of μ. For convenience, the vector μ can be decomposed as $\mu = \left\{\mu^E, \mu^f, \mu^{g_N}, \mu^{geo}\right\}$. Here μ^E relates to the mechanical properties of the material (e.g. Young's modulus: E, Poisson's ratio: ν); μ^f and μ^{g_N} relate to the forces; and μ^{geo} relate to the parametrization of the problem domain. C_{ijkl}, f and g_N can also vary spatially. As an example of the representation of the spatial and parameter dependence, C_{ijkl} can be written as $C_{ijkl} = C_{ijkl}\left(x, \mu^E\right)$.

4.2.3 Weak Form Of The Linear Elastostatic Problem

It is rather difficult to solve the system of equations stated in equation (29)- (33) directly for complex domains and complex boundary conditions. Thus, the finite element method is often leveraged to provide an approximate solution. The weak form of the finite element method, applied specifically to the second order elliptic PDE discussed thus far, will be now presented. The development of the equations will be with respect to a *reference* domain, $\hat{\Omega}$ (with boundary $\hat{\Gamma}$), and not the *actual* problem domain, Ω. Steps to relate the problem solved over the actual domain to that over the reference domain will be presented in section 4.2.7. In what follows, quantities with the $\{\hat{\cdot}\}$ symbol will correspond to their representation in the reference domain, while quantities without it correspond to the actual problem domain

To commence, two important vector spaces will be introduced. The first is the $L^2(\hat{\Omega})$ vector space. It is a Hilbert space[3] that satisfies the following criterion

$$L^2(\hat{\Omega}) = \{\bar{v} : \hat{\Omega} \to \mathbb{R} : \int_{\bar{\Omega}} |\hat{v}|^2 \mathrm{d}\hat{\Omega} < \infty\} \tag{43}$$

[3]A Hilbert space is a vector space equipped with an inner product and where all Cauchy sequences converge i.e. complete.

It is equipped with an inner product and an induced norm defined respectively as

$$< \hat{v}, \hat{w} >_{L^2(\hat{\Omega})} = \int_{\hat{\Omega}} \hat{v}\bar{\hat{w}} \mathrm{d}\hat{\Omega} \tag{44}$$

$$\|\hat{v}\|_{L^2(\hat{\Omega})} = \sqrt{< \hat{v}, \hat{v} >_{L^2(\hat{\Omega})}} = \left(\int_{\hat{\Omega}} |\hat{v}|^2 \mathrm{d}\hat{\Omega} \right)^{\frac{1}{2}} \tag{45}$$

The second important function space in this context is the Sobolev space, $H^1\left(\hat{\Omega}\right)$. This Sobolev space is defined as follows

$$H^1\left(\hat{\Omega}\right) = \left\{ \hat{v} \in L^2(\hat{\Omega}) : \nabla \hat{v} \in \left(L^2(\hat{\Omega}) \right)^d \right\} \tag{46}$$

In this case, both the function itself and its weak derivative are bounded. An important subspace of $H^1\left(\hat{\Omega}\right)$ is the following

$$H_0^1\left(\hat{\Omega}\right) = \left\{ \hat{v} \in H^1\left(\hat{\Omega}\right) : \hat{v}|_{\hat{\Gamma}} = 0 \right\} \tag{47}$$

Here, homogeneous Dirichlet boundary conditions are applied to the entire boundary of the problem domain. For many problems, only one or a few sections of the boundary are subjected to Dirichlet boundary conditions. This can be represented by, X, an infinite dimensional space such that $\left(H_0^1\left(\hat{\Omega}\right) \right)^d \subset X \subset \left(H^1\left(\hat{\Omega}\right) \right)^d$. X is endowed with inner product $\langle \cdot, \cdot \rangle_X$ and norm $\| \cdot \|_X = (\langle \cdot, \cdot \rangle_X)^{\frac{1}{2}}$. It is now appropriate to introduce the bilinear functional $\hat{a}(\cdot, \cdot; \mu) : X \times X \times \mathcal{D} \to \mathbb{R}$ and linear functional $\hat{f}(\cdot; \mu) : X \times \mathcal{D} \to \mathbb{R}$. The weak form of the governing equation can now be derived. Multiplying equation (34) by an arbitrary test function, $\hat{w} \in X$, and integrating over the domain $\hat{\Omega}$

$$-\int_{\hat{\Omega}} \hat{w}_i \frac{\partial \hat{\sigma}_{ij}}{\partial \hat{x}_j} \mathrm{d}\hat{\Omega} = \int_{\hat{\Omega}} \hat{w}_i \hat{f}_i \mathrm{d}\hat{\Omega} \qquad \forall \hat{w} \in X\left(\hat{\Omega}\right) \tag{48}$$

Integrating the left hand side by parts and applying the divergence theorem gives

$$-\int_{\hat{\Omega}} \hat{w}_i \frac{\partial \hat{\sigma}_{ij}}{\partial \hat{x}_j} \mathrm{d}\hat{\Omega} = -\int_{\hat{\Gamma}} \hat{w}_i \hat{\sigma}_{ij} \hat{e}_j \mathrm{d}\hat{\Gamma} + \int_{\hat{\Omega}} \frac{\partial \hat{w}_i}{\partial \hat{x}_j} \hat{\sigma}_{ij} \mathrm{d}\hat{\Omega} \tag{49}$$

Substituting equation (49) into equation (48) and applying equation (32) and equation (33) yields

$$\int_{\Omega} \frac{\partial w_i}{\partial x_j} \sigma_{ij} \mathrm{d}\Omega = \int_{\Omega} w_i f_i \mathrm{d}\Omega + \int_{\Gamma} w_i g_N^n \hat{e}_i^n \mathrm{d}\Gamma + \int_{\Gamma} w_i g_N^t \hat{e}_i^t \mathrm{d}\Gamma \tag{50}$$

Using equation (40)

$$a\left(u,w;\mu\right)=f\left(w;\mu\right)\qquad\forall w\in X\left(\Omega\right) \tag{51}$$

Where

$$a\left(u,w;\mu\right) = \int_{\Omega}\frac{\partial w_i}{\partial x_j}C_{ijkl}\frac{\partial u_k}{\partial x_l}\mathrm{d}\Omega \tag{52}$$

$$f\left(w;\mu\right) = \int_{\Omega}w_i f_i\mathrm{d}\Omega+\int_{\Gamma}w_i g_N^n\hat{e}_i^n\mathrm{d}\Gamma+\int_{\Gamma}w_i g_N^t\hat{e}_i^t\mathrm{d}\Gamma \tag{53}$$

Equation 51 is known as the *weak form* or alternatively as the *variational formulation*. Often times, we are interested in some output that is a function that is dependent on the state variable and the problem parameters. This takes the form: $s\left(u\left(\mu\right),\mu\right)$.

4.2.4 "Truth" Finite Element Approximation

At this point the finite element approximation can be introduced. A finite, but high dimensional space, $X^h\subset X$, known as the *"truth"* approximation space, is used to replace X in the weak form equation (51). This subspace inherits the inner product and induced norm from the functional space X, that were previously presented. The truth finite element approximation is thus: $\forall\mu\in\mathcal{D}\subset\mathbb{R}^p$, evaluate one or more outputs of interest of the form:

$$s^h\left(\mu\right)=s\left(u^h\left(\mu,x\right),\mu\right) \tag{54}$$

Where $u^h\left(\mu,x\right)$ satisfies

$$a\left(u^h,v;\mu\right)=f\left(v,\mu\right)\qquad\forall v\in X^h \tag{55}$$

Normally, the approximation space X^h is sufficiently refined so that $u(\mu,x)$ and $u^h(\mu,x)$ are almost indistinguishable. Thus, why X^h is often referred to as the "*truth*" approximation space to X.

4.2.5 Well-Posedness Of The Weak Form

The solution given by equation (51) and equation (55) can be shown to be unique by using the Lax-Milgram theorem [132]. However, this is contingent on the bilinear functional, $a(\cdot,\cdot;\mu)$, satisfying two important properties. These are that $a(\cdot,\cdot;\mu)$ must both be *coercive* and *continuous*. In addition, the linear functional $f(\cdot;\mu)$ has to be continuous. First, the coercive constants for the bilinear functional are defined as:

$$\alpha(\mu) = \inf_{w\in X} \frac{a(w,w;\mu)}{\|w\|_X^2} \tag{56}$$

$$\alpha^h(\mu) = \inf_{w\in X^h} \frac{a(w,w;\mu)}{\|w\|_X^2} \tag{57}$$

Provided that the finite element approximation space is conforming, the coercive requirement is as follows:

$$\exists \alpha_0 \in \mathbb{R}^+ : \quad 0 < \alpha_0 \leq \alpha(\mu) \leq \alpha^h(\mu)$$

The continuity constants can also be defined as:

$$\gamma(\mu) = \sup_{v\in X}\sup_{w\in X} \frac{a(v,w;\mu)}{\|v\|_X^2\|w\|_X^2} \tag{58}$$

$$\gamma^h(\mu) = \sup_{v\in X^h}\sup_{w\in X^h} \frac{a(v,w;\mu)}{\|v\|_X^2\|w\|_X^2} \tag{59}$$

Thus the continuity requirement can be stated as:

$$\exists \gamma_0 \in \mathbb{R}^+ : \quad \gamma^h(\mu) \leq \gamma(\mu) \leq \gamma_0 < \infty \qquad \forall \mu \in D$$

The functional $f(\cdot;\mu)$ can be shown to be continuous in a similar fashion.

4.2.6 Affine Parameter Dependence

In order to achieve computational efficiency in the RB method, a crucial requirement, especially for the bilinear functional, is the *affine* or *separable* property relative to the parameter μ. The affine property for bilinear functional can be expressed:

$$a(w,v;\mu) = \sum_{q=1}^{Q_a} \Theta_a^q(\mu) a^q(w,v) \qquad \forall w,v \in X^h, \ \forall \mu \in \mathcal{D} \tag{60}$$

The linear functional $f(\cdot;\mu)$ can also be expressed in this fashion as:

$$f(v;\mu) = \sum_{q=1}^{Q_f} \Theta_f^q(\mu) f^q(v) \qquad \forall v \in X^h, \ \forall \mu \in \mathcal{D} \tag{61}$$

The functions $\Theta_a^q(\mu) : \mathcal{D} \to \mathbb{R}$ and $\Theta_f^q(\mu) : \mathcal{D} \to \mathbb{R}$ are typically very smooth functions dependent only on μ. On the other hand, the functions $f^q(\cdot) : X \to \mathbb{R}$ and $a^q(\cdot,\cdot) : X \times X \to \mathbb{R}$ are independent μ. It is desirable for Q_a and Q_f to be small numbers so as to aid in the computational efficiency of the RB computation.

4.2.7 Parametric Problem Domain And The Weak Form

The development of the weak form thus far considers a reference problem domain, $\hat{\Omega}$, that is independent of geometric parameters. As highlighted in section 4.2.2, more general problem considerations require Ω to be parametric. Furthermore, additional versatility is offered by representing Ω as a set of non-overlapping sub-domains, Ω^k, each equipped with its own set of parameters, μ_k. This can be stated precisely as

$$\Omega = \cup_{k=1}^{K_{dom}} \Omega^k(\mu_k) \tag{62}$$

With **open** component sub-domain Ω^k, $1 \le k \le K_{dom}$, that satisfy and $\Omega^k \cap \Omega^{k'} = \emptyset$, $1 \le k < k' \le K_{dom}$. An example of this type of decomposition is illustrated in figure 26. Each of these K_{dom} sub-domains is related to the reference domain by $\hat{\Omega}^k = \Omega^k(\mu_{\text{ref}}^{geo})$, where μ_{ref} are the parameters that recover the reference domain.

The weak form, equations (51) and (55), are defined with respect to the reference domain; thus, it is necessary to relate problem (actual) domain to the reference domain. This is typically done by the use of an affine geometric map that relates points in the reference domain to the points in the problem domain. This map takes the form of

$$\Omega^k(\mu) = \mathcal{T}^{\text{aff},k}\left(\hat{\Omega}^k; \mu_k^{geo}\right), 1 \le k \le K_{dom}; \tag{63}$$

The map must be individually invertible, collectively continuous and bijective. These

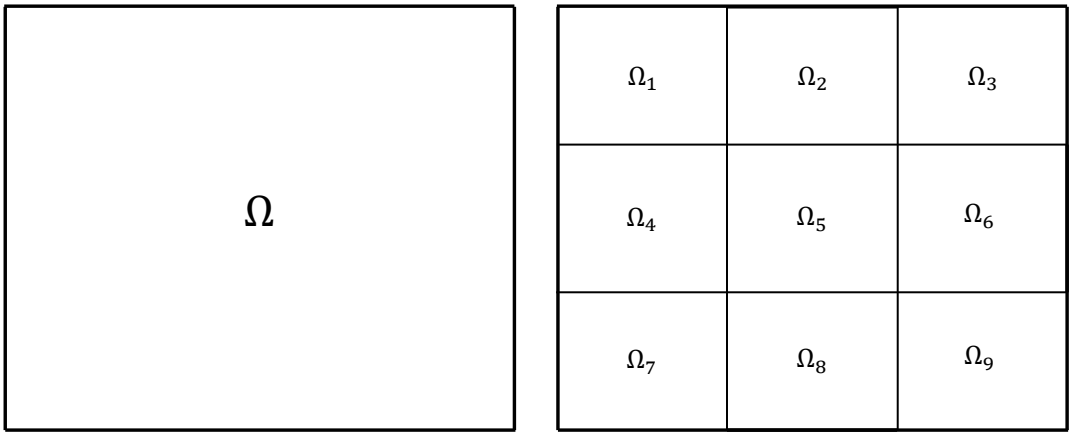

Figure 26: Decomposition of the problem domain Ω into 9 non-overlapping sub-regions

requirements can be represented mathematically as

$$\mathcal{T}^{\text{aff},k}\left(\hat{x};\mu_k^{geo}\right) = \mathcal{T}^{\text{aff},k'}\left(\hat{x};\mu_{k'}^{geo}\right) \qquad \forall \hat{x} \in \bar{\hat{\Omega}}^k \cap \bar{\hat{\Omega}}^{k'}, \quad 1 \leq k \leq K_{dom} \tag{64}$$

The affine map takes the form

$$\mathcal{T}_i^{\text{aff},k}\left(\hat{x};\mu_k^{geo}\right) = C_i^{\text{aff},k}\left(\mu_k^{geo}\right) + \sum_{j=1}^{d} G_{ij}^{\text{aff},k}\left(\mu_k^{geo}\right)\hat{x}_j \qquad 1 \leq i \leq d \tag{65}$$

Here $C_i^{\text{aff},k}(\mu) : D \to \mathbb{R}^d$ represents a translation vector and $G_{ij}^{\text{aff},k}(\mu) : D \to \mathbb{R}^{d\times d}$ represents a transformation matrix. Typical operations of the latter include, rotation, scaling and/or shear. An important feature of affine maps is that they are invertible and result in a positive mapping Jacobian. The global map that links the problem domain to the reference domain can be defined as

$$\mathcal{T}^{\text{aff},k}(\cdot;\mu) : \hat{\Omega} \to \Omega(\mu) \quad \text{, where } \mathcal{T}^{\text{aff}}(\hat{x};\mu) = \mathcal{T}^{\text{aff},k}(\hat{x};\mu),$$
$$k = \min_{k' \in \{1\cdots K_{dom}\} | x \in \Omega_{k'}} k' \tag{66}$$

Rozza [86] describes a variety of sub-domain shapes and parametrizations that can be used in this context. This includes, standard, elliptic and curvy triangles. Veroy

Table 2: Mappings for common planar, elementary transformations

Transformation	Figure	$G_i^{\text{aff},k}(\mu_k^{geo})$	$C_i^{\text{aff},k}(\mu_k^{geo})$
Horizontal and vertical stretch	27 (b), (c)	$\begin{bmatrix} \frac{t_1}{\hat{t}_1(\mu_k^{geo})} & 0 \\ 0 & \frac{t_2}{\hat{t}_2(\mu_k^{geo})} \end{bmatrix}$	$\begin{Bmatrix} 0 \\ 0 \end{Bmatrix}$
Horizontal Shear	27 (d)	$\begin{bmatrix} 1 & -\tan(\alpha) \\ 0 & 1 \end{bmatrix}$	$\begin{Bmatrix} 0 \\ 0 \end{Bmatrix}$
Rotation	27 (e)	$\begin{bmatrix} \cos(\alpha) & \sin(\alpha) \\ -\sin(\alpha) & \cos(\alpha) \end{bmatrix}$	$\begin{Bmatrix} 0 \\ 0 \end{Bmatrix}$

[133] presented several elementary transformations that can be used to morph the domain. These are presented in figure 27. For the mappings shown, the associated transformations are presented in table 2. For more complex geometric transformations that do not admit affine parametrization, one can employ the use of the discrete empirical interpolation method [134] to provide an approximation for efficient system assembly.

In section 4.2.3 the weak form was developed for the reference domain. The weak form developed for a general problem domain can be related to the reference domain. The bilinear operator with respect to the actual domain is

$$a\left(w, v; \mu\right) = \sum_{k=1}^{K_{dom}} a\left(w|_{\Omega^k}, v|_{\Omega^k}; \mu_k\right) \tag{67}$$

Applying the geometric map, $\mathcal{T}^{\text{aff},k}\left(x; \mu\right)$, yields

$$a\left(w, v; \mu\right) = \sum_{k=1}^{K_{dom}} \hat{a}_k\left(w|_{\Omega^k} \circ \mathcal{T}^{\text{aff},k}\left(x; \mu\right), v|_{\Omega^k} \circ \mathcal{T}^{\text{aff},k}\left(x; \mu\right); \mu_k\right) \tag{68}$$

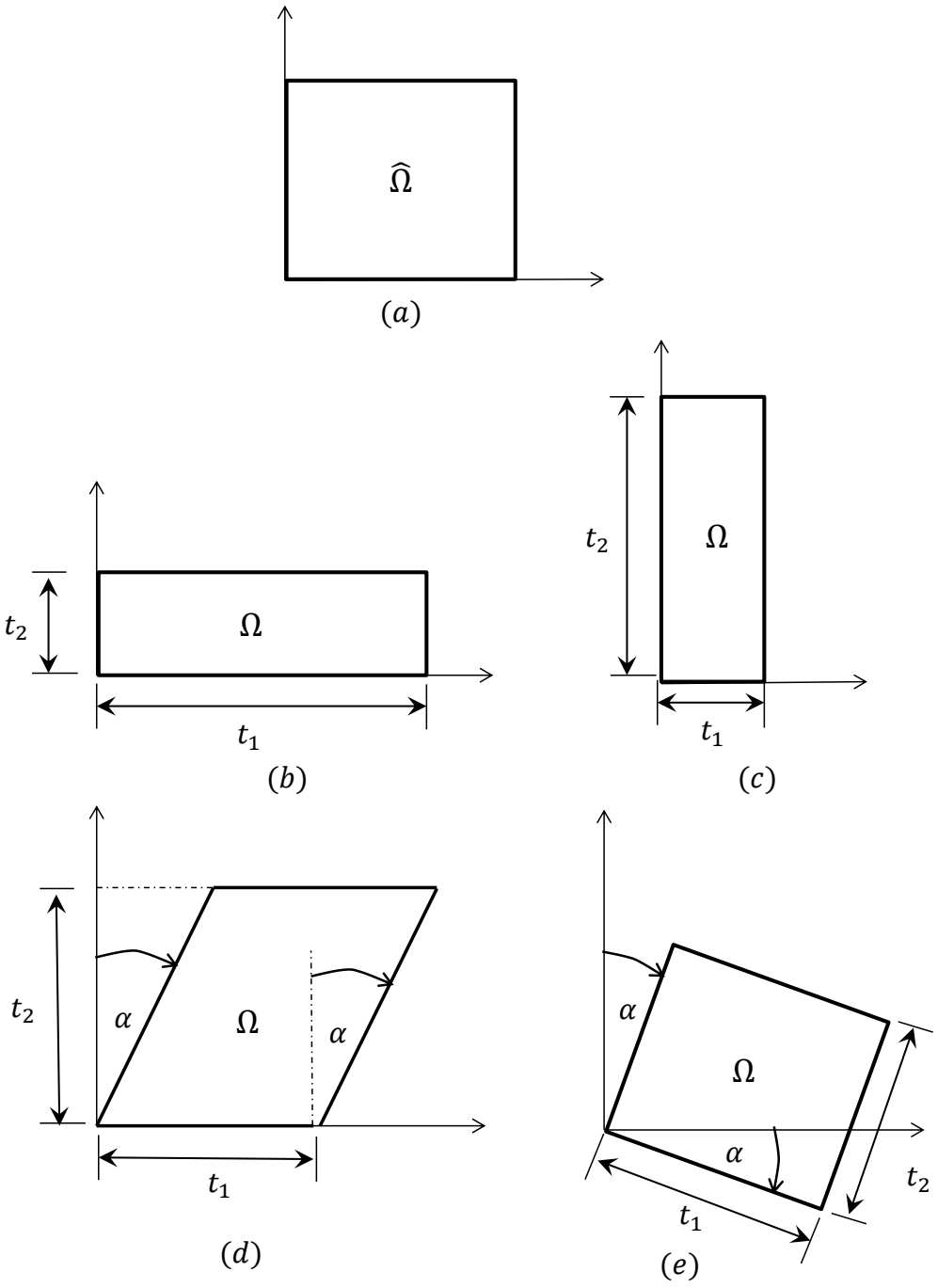

Figure 27: Examples of elementary, planar transformations. (a) Reference domain (b) Horizontal stretching (c) Vertical stretching (d) Horizontal shear (e) Rotation

Similarly the linear functional $f(\cdot;\mu)$ can be defined as

$$f(v;\mu) = \sum_{k=1}^{K_{dom}} \hat{f}_k \left(v|_{\Omega^k} \circ \mathcal{T}^{\text{aff},k}(x;\mu); \mu_k \right) \quad \forall v \in X \tag{69}$$

Thus the general problem statement becomes. Evaluate

$$s(u(\mu);\mu) \tag{70}$$

where $u(\mu) \in X(\mu)$ satisfies

$$a(u(\mu), v;\mu) = f(v), \quad \forall v \in X(\mu) \tag{71}$$

Here $\left(H_0^1(\Omega)\right)^d \subset X \subset \left(H^1(\Omega)\right)^d$. Also, the bilinear and linear functionals need to satisfy, $a(\cdot,\cdot;\mu) : X \times X \to \mathbb{R}$ and $f(\cdot;\mu) : X \to \mathbb{R}$, respectively.

4.3 Mathematical Overview Of The Reduced Basis Method

4.3.1 RB Approximation Space

As mentioned in section 1.4, X^h is unnecessarily rich and indeed, the solution is likely to lie on a manifold of much smaller dimension than the full truth subspace. Based on this important observation, the task is now to identify a suitable set of N points on this low-dimensional manifold so that a new solution, $u(\mu|_{new})$, can be represented as a linear combination of the solutions precomputed at these N known points (or "*snapshots*"), i.e. $u^h(\mu|_n)$, $1 \leq n \leq N$. It is desirable that $N \ll \mathcal{N}$ so as to achieve significant speed-ups in computations. In the literature, the Greedy sampling algorithm [107] is typically used to determine the sample points, $\mu|_n \in S_N$, $1 \leq n \leq N$. The Greedy sampling algorithm tries to find the smallest set of N points in the domain $\mathcal{D}$ that minimizes $\|u_h(\mu) - u_N^h(\mu)\|_X$, where $u_N^h(\mu)$ is the RB approximation to the true FE solution $u_h(\mu)$. Through this procedure, a sequence of hierarchical subspaces of X^h is sought that takes the form W_N, $1 \leq N \leq N_{max}$. The hierarchical requirement simple means that $W_1 \subset W_2 \subset \cdots \subset W_{N_{max}} \subset X^h$. The set of sample points from the parameter manifold are

$$S_N = \{\mu|_1, \mu|_2, \ldots, \mu|_N\}, \quad \text{where } \mu|_i \in \mathcal{D}, \ 1 \leq N \leq N_{max} \tag{72}$$

The sequence of sample sets for increasing N are also hierarchical i.e. $S_1 \subset S_2 \subset \cdots \subset S_{N_{max}}$. The resulting global reduced basis space is

$$W_N^u = \text{span}\left\{u^h\left(\mu|_n\right),\ \ 1 \leq n \leq N,\ \ 1 \leq N \leq N_{max}\right\} \tag{73}$$

Here $u^h\left(\mu|_n\right) \in X^h$ and $\mu|_n \in S_N$. By construction, W_N^u is hierarchical for increasing N. Unfortunately, as the number of retained snapshots increases (i.e. as N increases), the latter elements in the set become increasingly co-linear. The is due to the fact that if the first n snapshots allow rapid convergence in approximating $u\left(\mu|_{new}\right)$, then the $n+1^{th}$ snapshot onward will be linearly dependent on the first n snapshots. To remedy this, a QR factorization technique such as the modified Gram-Schmidt or the Householder transformation [135] can be used to extract an orthonormal basis from W_N^u. The result is a new global reduced basis space

$$W_N^\zeta = \text{span}\left\{\zeta_n,\ \ 1 \leq n \leq N,\ \ 1 \leq N \leq N_{max}\right\} \tag{74}$$

Where $\left\langle \zeta_n, \zeta_m \right\rangle_X = \delta_{nm}$. Rozza [86] noted the significant improvement in the condition number of the coefficient matrix of the linear algebraic system associated with the RB method in numerical problems.

An alternative approach for generating the reduced basis is to generate samples in the parameter domain with sampling techniques, such as random or Latin-Hypercube sampling. The hierarchical, empirical basis is then generated by applying the Proper Orthogonal Decomposition procedure to the associated snapshots of the solution evaluated at these sampled locations.

4.3.1.1 Galerkin Projection To The RB subspace

The analysis now has to be represented with respect to the new approximation space $W_N^\zeta \subset X^h$. To do this, a Galerkin projection is carried out using W_N^ζ as both the test and trial space. The displacement solution, $u\left(x;\mu\right)$, projected onto W_N^ζ is

$$u_N\left(\mu\right) = \sum_{j=1}^{N} u_{N,j}\left(\mu\right)\zeta_j = ZU_N \tag{75}$$

Where $Z \in \mathbb{R}^{\mathcal{N}\times N}$ is a matrix whose columns are the elements of W_N^ζ i.e. column j is $\zeta_j \in \mathbb{R}^{\mathcal{N}}$. $U_N(\mu) \in \mathbb{R}^N$ is a column vector whose elements are the unknown weighting coefficients used to scale the elements of W_N^ζ so as to achieve an approximation of $u(x;\mu)$. The weak form of the problem can be represented in this new subspace

$$a(u_N(\mu), v; \mu) = f(v), \qquad \forall v \in W_N^\zeta \tag{76}$$

Substituting equation (75) into equation (76) gives

$$a\left(\sum_{j=1}^{N} u_{N,j}(\mu)\,\zeta_j, \zeta_i; \mu\right) = f(\zeta_i), \qquad \forall \zeta_i \in W_N^\zeta \tag{77}$$

Expanding gives

$$\sum_{j=1}^{N} u_{N,j}(\mu)\, a(\zeta_j, \zeta_i; \mu) = f(\zeta_i), \qquad 1 \le i \le N \tag{78}$$

This can be represented as an equivalent linear algebraic system

$$A_N(\mu)\, U_N(\mu) = F(\mu) \tag{79}$$

After solving this system, the output can be evaluated as

$$s_N = s_N(U_N(\mu), \mu) \tag{80}$$

Where $A_N(\mu) \in \mathbb{R}^{N\times N}$ is the stiffness matrix with respect to the subspace W_N^ζ and $U_N(\mu), F(\mu) \in \mathbb{R}^N$ are the vector of weighting coefficients and forces (relative to W_N^ζ), respectively. The task is now to relate the problem developed in the physical finite element space (equation (71)) to that in W_N^ζ (equation (79)). Since $\zeta_i \in W_N^\zeta \subset X^h$, it can be represented with the Lagrangian basis elements (ϑ_m associated with X^h). Thus

$$\zeta_i = \sum_{m=1}^{\mathcal{N}} \zeta_i^m \vartheta_m \tag{81}$$

Inserting this representation into equation (77) gives

$$\sum_{j=1}^{N} u_{N,j}(\mu)\, a\left(\sum_{m=1}^{\mathcal{N}} \zeta_i^m \vartheta_m, \sum_{k=1}^{\mathcal{N}} \zeta_j^k \vartheta_k; \mu\right) = f\left(\sum_{k=1}^{\mathcal{N}} \zeta_i^k \vartheta_k\right), \qquad \forall i,j \in \{1,\cdots,N\} \tag{82}$$

Using the bilinearity and linearity of $a(\cdot,\cdot;\mu)$ and $f(\cdot;\mu)$, respectively, gives

$$\sum_{j=1}^{N} u_{N,j}(\mu) \sum_{m=1}^{\mathcal{N}} \sum_{k=1}^{\mathcal{N}} \zeta_i^m \zeta_j^k a(\vartheta_m, \vartheta_k; \mu) = \sum_{k=1}^{\mathcal{N}} \zeta_i^k f(\vartheta_k), \qquad \forall i, j \in \{1, \cdots, N\} \quad (83)$$

This results is equivalent to the linear algebraic system derived in equation (79). $A_N(\mu)$ can be represented more concisely as

$$A_N(\mu) = Z^T A_{\mathcal{N}}(\mu) Z \quad (84)$$

While $F_N(\mu)$ takes the form

$$F_N(\mu) = Z^T F_{\mathcal{N}}(\mu) \quad (85)$$

Where $A_{\mathcal{N}}(\mu) \in \mathbb{R}^{\mathcal{N}\times\mathcal{N}}$ and $F_{\mathcal{N}}(\mu) \in \mathbb{R}^{\mathcal{N}}$ respectively represent the *stiffness matrix* and *load vector* relative to the finite element space, X^h. $Z \in \mathbb{R}^{\mathcal{N}\times N}$ is a linear transformation which allows a change of basis from those in X^h to those in W_N^ζ. Thus, equation (84) and equation (85) are the representations of $A_{\mathcal{N}}(\mu)$ and $F_{\mathcal{N}}(\mu)$ in W_N^ζ, respectively. Early efforts with the RB method sought to first assemble $A_{\mathcal{N}}(\mu)$ and $F_{\mathcal{N}}(\mu)$ and then project them into W_N^ζ in the real time context [86]. This was followed by solving the associated linear algebraic system equation (79) to determine $U_N(\mu)$. This approach resulted in only moderate speedups over solving equation (55) directly, primarily due to the expense of computing equation (84). Fortunately, thanks to the affine decomposition of $a(\cdot,\cdot;\mu)$ and $f(\cdot;\mu)$, these computation of can be avoided in a real time context. Leveraging the affine property (equations (60)-(61)) and starting from equation (83), the relationship between $A_{\mathcal{N}}(\mu)$ and $A_N(\mu)$ can be determined in a more convenient fashion. To wit

$$\sum_{j=1}^{N} u_{N,j}(\mu) \sum_{m=1}^{\mathcal{N}} \sum_{k=1}^{\mathcal{N}} \zeta_i^m \zeta_j^k \left[\sum_{q=1}^{Q_a} \Theta_a^q(\mu) a^q(\vartheta_m, \vartheta_k; \mu) \right] = \sum_{k=1}^{\mathcal{N}} \zeta_i^k \left[\sum_{q=1}^{Q_f} \Theta_f^q(\mu) f^q(\vartheta_k) \right], \quad \forall i, j \in \{1, \cdots, N\} \quad (86)$$

Rearranging gives

$$\sum_{j=1}^{N} u_{N,j}(\mu) \sum_{q=1}^{Q_a} \Theta_a^q(\mu) \sum_{m=1}^{\mathcal{N}} \sum_{k=1}^{\mathcal{N}} \zeta_i^m \zeta_j^k a^q(\vartheta_m, \vartheta_k; \mu) = \sum_{q=1}^{Q_f} \Theta_f^q(\mu) \sum_{k=1}^{\mathcal{N}} \zeta_i^k f^q(\vartheta_k), \quad \forall i, j \in \{1, \cdots, N\} \quad (87)$$

This can be represented more concisely as

$$\sum_{j=1}^{N} u_{N,j}(\mu) \sum_{q=1}^{Q_a} \Theta_a^q(\mu) \left(Z^T A_{\mathcal{N}}^q Z\right) = \sum_{q=1}^{Q_f} \Theta_f^q(\mu) \left(Z^T F_{\mathcal{N}}^q\right), \quad \forall i, j \in \{1, \cdots, N\} \quad (88)$$

Which leads to

$$\sum_{j=1}^{N} u_{N,j}(\mu) \sum_{q=1}^{Q_a} \Theta_a^q(\mu) A_N^q = \sum_{q=1}^{Q_f} \Theta_f^q(\mu) F_N^q, \quad \forall i, j \in \{1, \cdots, N\} \quad (89)$$

Where $A_N^q = Z^T A_{\mathcal{N}}^q Z \in \mathbb{R}^{N \times N}$ and $F_N^q = Z^T F_{\mathcal{N}}^q \in \mathbb{R}^{N \times 1}$ are parameter independent terms in the affine decomposition. Equation (89) is fully equivalent to equation (79). It provides a result that is critical for the efficiency of RB computations in real time. Notice that $A_N(\mu)$ is found by first finding the product of each parameter dependent scalar, $\Theta_a^q(\mu) \in \mathbb{R}$, and the associated parameter independent matrix, A_N^q, for $1 \leq q \leq Q_a$. This is followed by summing the Q_a products in order to form $A_N(\mu)$. $F_N(\mu)$ can be found in a similar fashion.

4.3.2 Online/Offline Problem Decomposition

This convenient result allows for the separation of the RB procedure into two convenient stages. First, a very expensive offline process that involves calculating the parameter independent terms, A_N^q and f_N^q, is carried out. It is important to note that this procedure is performed only once. The second step involves an inexpensive online procedure where the approximation to the field variable, $U_N(\mu)$ is sought. Unlike the

offline step, the online step is carried out many times and is especially suitable to the "*many-query*" and "*real-time*" problems. The computations performed in each of the two steps, as well as their computation costs are

- *Offline*: This step involves determining the N_{max} sample points $\mu_n \in S_N \subset \mathcal{D}$ on the parameter manifold, followed by calculating the associated *snapshots* $u^h(\mu_n)$ via a full finite element model representing the problem. After orthonormalizing W_N^u to form W_N^ζ, the parameter independent terms in (equation (89)) can be determined by first assembling the parameter independent terms in the affine representation associated with the full FE model, $A_\mathcal{N}^q$ and $F_\mathcal{N}^q$, and then by performing the computations (equation (84))-(equation (85)).

- *Online:* The steps involves assembling the terms $A_N(\mu) = \sum_{q=1}^{Q_a} \Theta_a^q(\mu) A_N^q$ and $F_N(\mu) = \sum_{q=1}^{Q_f} \Theta_f^q(\mu) F_N^q$ leveraging the parameter independent terms determined in the offline step. The linear algebraic system (equation (79)) can then be solved, followed by the determination of the output of the problem $s_N = s_N(U_N(\mu), \mu)$.

A very important result of this problem decomposition is that the online steps are completely independent of dimension of the original FE problem, $\mathcal{N}$. Thus, regardless of how refined the FE mesh is, the RB method's performance is only contingent on Q_a, Q_f, and N. The operation count involved in carrying out the online computation includes

- *Assembly:* $O(Q_a N^2) + O(Q_f N)$
- *Solving the linear system:* In lieu of using an iterative method, the linear system (equation (79)) can be solved in $O(2/3 N^3)$ steps
- *Memory storage:* The online storage cost is $O(Q_a N_{max}^2) + O(Q_f N_{max})$

Thus, it is apparent that the number of retained snapshots, N, plays a crucial role

in determining the efficiency of the online phase of the RB procedure. As such, it is desirable to have a small set W_N^{ζ} that rapidly converges in approximating u^h.

4.3.3 A-Posteriori Error Estimation

In section 4.3.2 the importance of selecting a small number of retained snapshots, N, was highlighted; as this is paramount to the efficiency of the online performance of the RB method. One of the powerful additions to the RB Method framework is the a-posteriori error estimation. The a-posteriori error estimation not only addresses the issue of *efficiency*, but also provides a rigorous upper bound for the error of the output, $s_N\left(u_N\left(x;\mu\right),\mu\right)$, and the field solution, $u_N\left(x;\mu\right)$, from the RB approximation relative to the corresponding quantities from the finite element "*truth*" approximation. Thus, the a-posteriori error estimation establishes the *reliability* of the RB approximation of these quantities. To satisfy the requirements of efficiency and reliability, the following error estimates can be introduced

$$\Delta_N^{en}\left(\mu\right) \approx \left\|u^h\left(\mu\right)-u_N^h\left(\mu\right)\right\|_X \tag{90}$$

$$\Delta_N^{s}\left(\mu\right) \approx \left|s^h\left(\mu\right)-s_N\left(\mu\right)\right| \tag{91}$$

Where $\Delta_N^{en}\left(\mu\right)$ and $\Delta_N^{s}\left(\mu\right)$ are the error estimators for the energy norm and output, respectively. Also, u_N^h is the representation of u_N in the Lagrangian basis associated with X. The remaining quantities are as previously defined. The requirements for these error estimators are that they need to be *reliable*, *sharp*, and *inexpensive* to compute. Further, the effectivities of these error estimators can be defined as

$$\eta_N^{en}\left(\mu\right) = \frac{\Delta_N^{en}\left(\mu\right)}{\left\|u^h\left(\mu\right)-u_N^h\left(\mu\right)\right\|_X} \tag{92}$$

$$\eta_N^{s}\left(\mu\right) = \frac{\Delta_N^{s}\left(\mu\right)}{\left|s^h\left(\mu\right)-s_N\left(\mu\right)\right|} \tag{93}$$

Leveraging $\eta_N^{en}\left(\mu\right)$ and $\eta_N^{s}\left(\mu\right)$ the reliability and sharpness requirements can be quantified. This is done, for example with $\eta_N^{en}\left(\mu\right)$ as

$$1 \leq \eta_N^{en}\left(\mu\right) \leq \rho \tag{94}$$

Where $\rho \approx 1$. There rigor and reliability requirement is ensured by enforcing that the effectivities are greater than 1, while the sharpness is enforced by seeking an upper bound, ρ, that is close to 1; thus, not grossly over-predicting the error. In online usage, the error estimators are useful for determining the minimum number of retained snapshots that are needed for a certain level of accuracy. Thus, the problem can be stated as, find the minimum number of retained snapshots, N_{min}, such that

$$\Delta_N^s \leq \epsilon_{max}^s \tag{95}$$

$$\Delta_N^{en} \leq \epsilon^e n_{max} \tag{96}$$

Where ϵ_{max}^s and ϵ_{max}^{en} are suitably chosen error limits for the output and field variable, respectively. Veroy [133] derives expedient error estimators that were leveraged for linear elasticity problems.

4.4 Chapter Summary

In this chapter, the abstract finite element problem was presented for the linear elasto-static solid mechanics problem. This was followed by the inclusion of reduced basis approximation for expediting the analysis. The work in the rest of this thesis builds upon the fundamental platform laid out in this chapter.

Chapter V

SCRBE APPROACH FOR GENERATING CONSTRAINTS

5.1 Chapter Overview

The purpose of this chapter is to provide the development of the SCRBE approach. First, a high level overview of how the SCRBE method is used in the optimization procedure is given. This is so as to facilitate an easier transition into the more demanding mathematical content associated with the SCRBE method. After this, the mathematical details in using the SCRBE method in evaluating the constraints of interest and their sensitivities are presented. Furthermore, an approach is proposed for determining empirical subspaces that can approximate the state variable and its derivatives on the interfaces of the problem domain. Finally, the detailed offline and online procedures of the method are highlighted.

5.2 High Level Overview Of The SCRBE approach

The optimization problem of focus was presented in chapter 3. The main steps involved in addressing this problem are presented in figure 28. The procedure begins with the prescription and assembly of the global, physical problem domain. As mentioned in chapter 1, the physical problem domain is made up of several sub-domains that are each formed from an *archetype* or *reference* component coming from a library. The basic idea of this approach is presented in figures 30 and 31. After the problem domain has been assembled, boundary conditions can be specified and applied. These can include tractions (such as pressure fields) and imposed displacements on the boundary of the model. These boundary conditions can be parametric in order

to reflect various scenarios of interest to the designer. After these ingredients have been specified, the optimization procedure can be performed.

A simplified illustration of the numerical optimization procedure is shown in figure 29. Under the NAND paradigm, at each step of the optimization procedure, a vector of parameters, μ, is passed into the function call module. This function call module in turn returns snapshots of the objective function, the constraints and their gradients corresponding to the parameter set. In the present context, the former is the mass of the assembled domain. The inner working of the function module is shown graphically in figure 30. The parameter vector, μ, is used to update the problem domain (e.g. geometry and/or material properties) and the boundary conditions. The mass of the updated physical problem domain and its gradient are determined and passed to the optimizer. Both the updated physical problem domain and boundary conditions are then passed to the constraint evaluation module so that the constraints and their gradients can be determined.

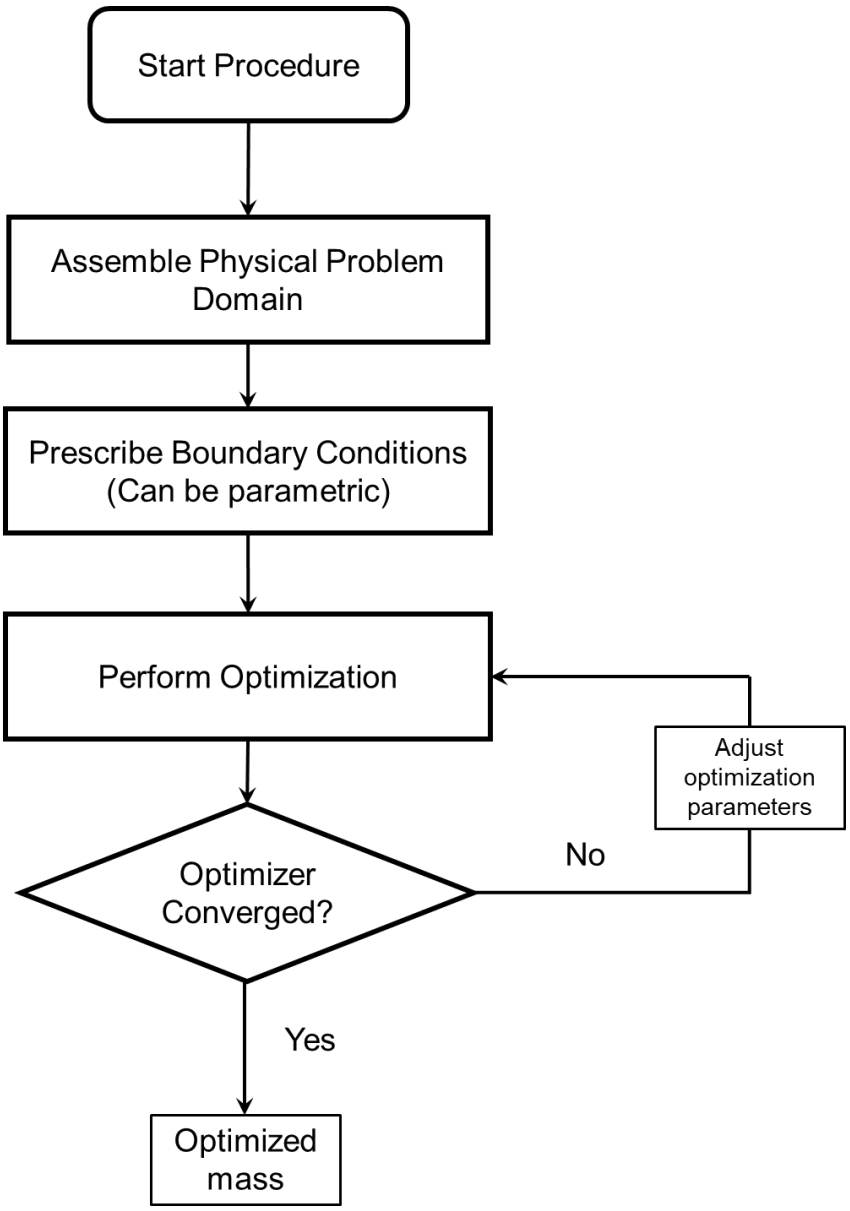

Figure 28: Flowchart for the optimization problem

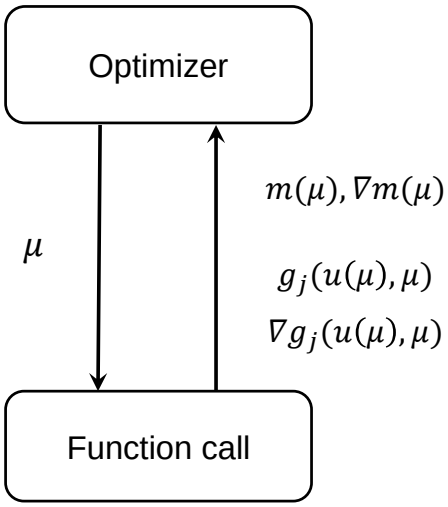

Figure 29: A simplified illustration of a function call during optimization

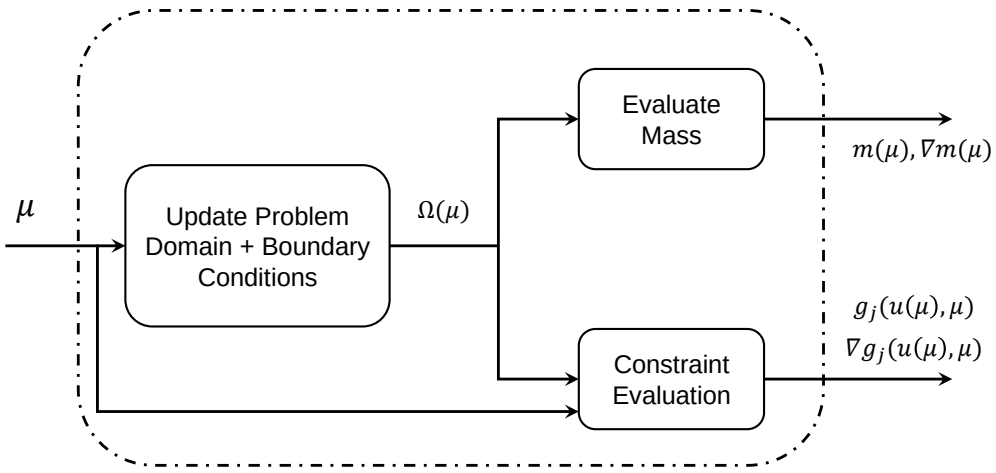

Figure 30: The operations associated with a function call

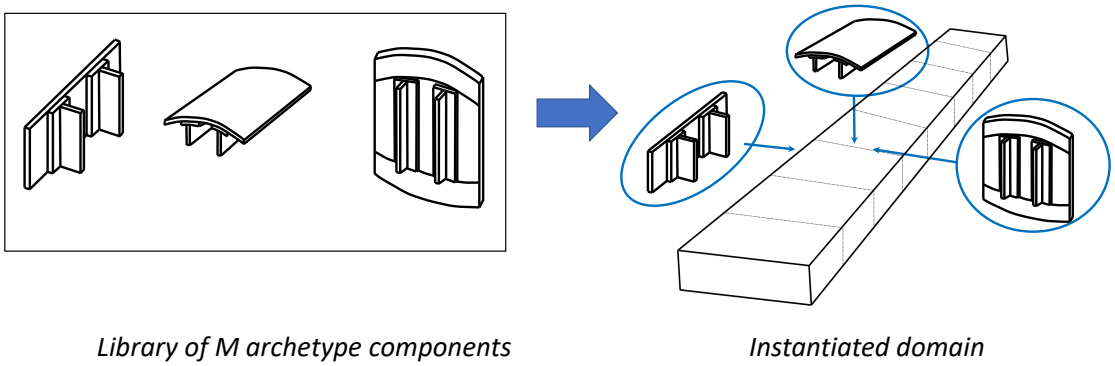

Figure 31: The use of archetype components to construct a problem domain for a wingbox example

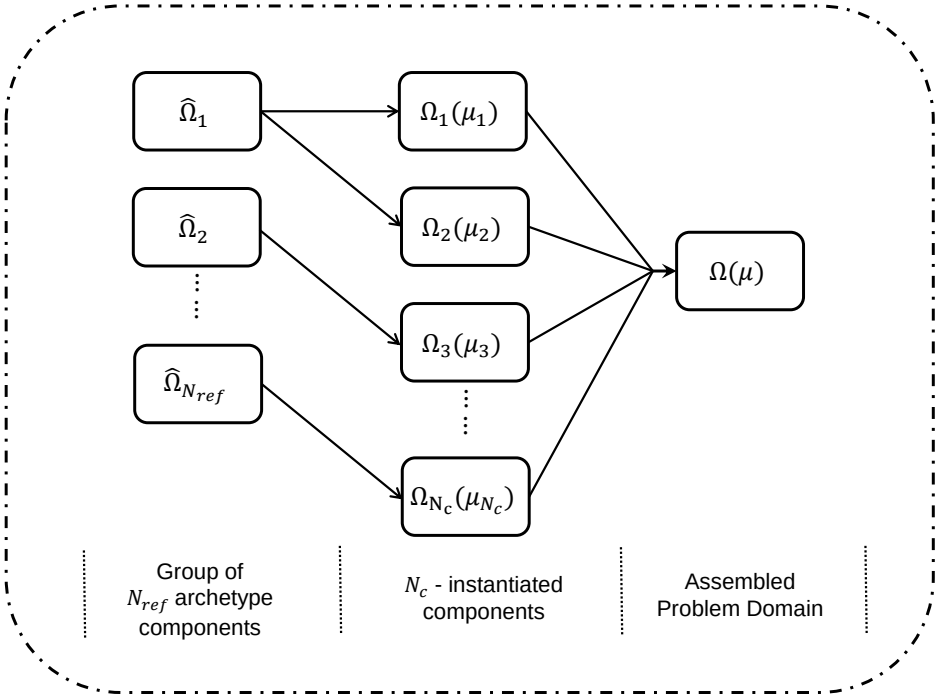

Figure 32: Domain assembly procedure

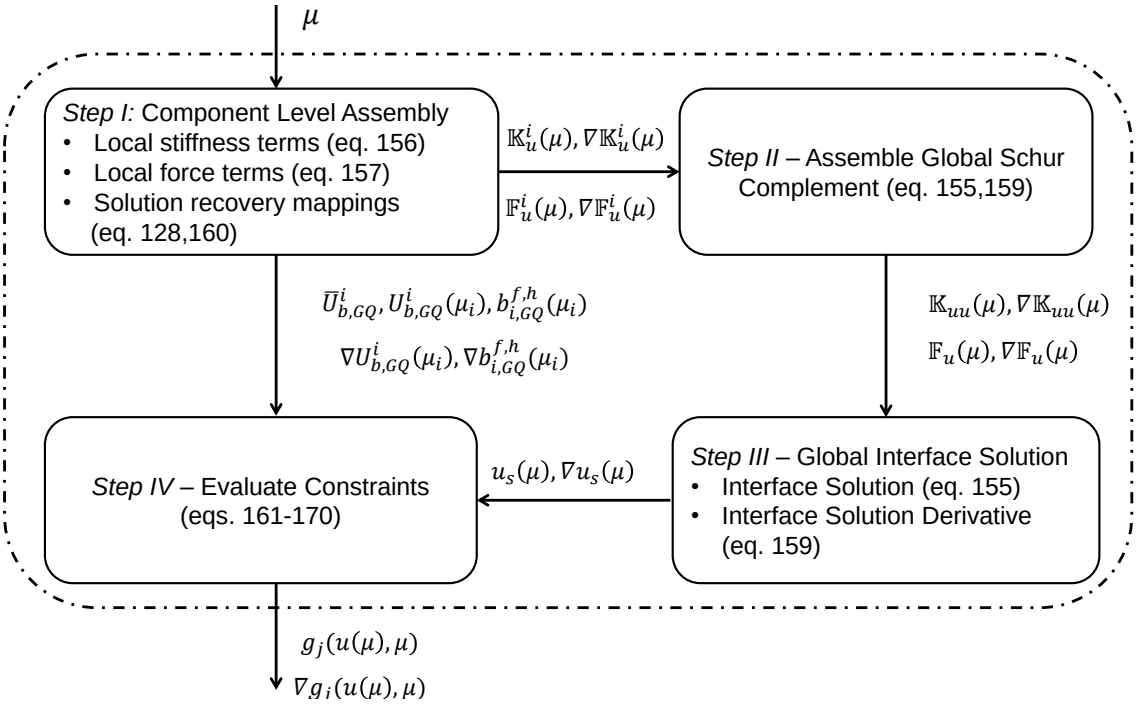

Figure 33: The procedure with the Constraint Evaluation module

The main structure of the constraint evaluation module, along with references to the associated equations are presented in figure 33. Within this module, there are four major steps that are performed. Steps I and IV occur at the local component level; while steps II and III occur at the global level of the interconnected system. Step I is concerned with the calculation of the local contributions to the Schur complement linear algebraic system, as well as the terms required to recover the state variable on each component. For the former case, these are the contributions to the coefficient stiffness matrix, as well as to the right-hand side of the system. For the latter, these are certain mappings that work in tandem with the state variable on the interface between the components to recover the solution on their interior. In step II, the global Schur complement system is formed from the contributions collected from the individual components in the problem domain. The connectivity of the linear algebraic system is reflected by the connectivity of the components through their interfaces. Step III follows. Here, the state variable and its gradient prescribed

on the interfaces between the components are determined. The resulting interface solution fields are then passed along with the solution recovery mappings (from step I) to the procedure in step IV in order to evaluate the constraints and their derivatives on the problem domain.

5.3 Static Condensation Applied To A System Of Components

Now that the high level overview of the procedure has been presented, the mathematical development will now be given in detail. The presentation in this section builds upon the work presented by Eftang [81, 109]. As such, this includes shared notation and sequencing of the development; particularly in subsections 5.3.1 through 5.3.5.

5.3.1 System of Components And Interfaces

5.3.1.1 Reference Components

The SCRBE approach begins with the prescription of a set of unique components that can be copied, modified and then configured into a wide variety of final, physical problem domains. The resulting global, physical problem domains all share the same underlying mathematical model; and some behavior of interest can simulated therein. These components are referred to as "*reference*" or "*archetype*" components. The reduced order models are specified at the level of the reference components and are created during a laborious offline process. The behavior of each of these components is studied both individually and in local neighborhoods of interacting components.

The quantity of archetype components studied during the offline stage will be denoted by N_{ref}. Each of these archetype components has a reference physical domain, $\hat{\Omega}_m \in \mathbb{R}^d$ where $d \in \{2, 3\}$. The boundary of an archetype component's physical domain is represented as $\partial\hat{\Omega}_m$. It is formed by a set of $n_m^e \in \mathbb{N}$ *local edges* $\left(\text{if } \partial\hat{\Omega}_m \in \mathbb{R}^1\right)$ or *local faces* $\left(\text{if } \partial\hat{\Omega}_m \in \mathbb{R}^2\right)$. In what follows, both component boundary types will be referred to as *edges* for simplicity of notation. Each local edge is represented as

$\hat{e}_{m,j} \subseteq \partial\hat{\Omega}_m$, $1 \leq j \leq n_m^e$. On each archetype component, pairs of adjacent local edges meet at a local vertex, i.e. $\bar{\hat{e}}_{m,j} \cap \bar{\hat{e}}_{m,j'} \neq \emptyset$[1] for $1 \leq j, j' \leq n_m^e$, and further, $\partial\hat{\Omega}_m = \bigcup_{j=1}^{n_m^e} \bar{\hat{e}}_{m,j}$. A local vertex that is formed from the intersection of two adjacent local edges, $\bar{\hat{e}}_{m,j}$ and $\bar{\hat{e}}_{m,j'}$ is denoted by $\hat{v}_{m,j,j'}$. Finally, each archetype component has a set of parameters (or design variables), $\hat{\mu}_m \in \mathcal{D}_m \subset \mathbb{R}^{P_m}$, for $1 \leq m \leq N_{\text{ref}}$.

5.3.1.2 Instantiation Of Components And Physical Problem Domains

During the online stage of the method, a system of components is *instantiated* from the set of reference components. The quantity of instantiated components is denoted as N_c. Each of these instantiated components can be uniquely mapped to an archetype component. This is denoted by the mapping $\mathcal{G} : \{1, ..., N_c\} \rightarrow \{1, ..., N_{\text{ref}}\}$. This type of mapping is often used in the SCRBE literature and is repeated here. During the instantiation procedure, a local parameter vector, μ_i, is used to update the properties of the associated component, i.e. component i. This can include the parameterization of a domain mapping applied to its local physical domain. This takes the form of: $\Omega_i = \mathcal{T}_i\left(\hat{\Omega}_{\mathcal{G}(i)}\right)$, $e_{i,j} = \mathcal{T}_i\left(\hat{e}_{\mathcal{G}(i),j}\right)$ and $v_{i,j,j'} = \mathcal{T}_i\left(\hat{v}_{\mathcal{G}(i),j,j'}\right)$, $1 \leq i \leq N_c$. The geometric mappings, $\mathcal{T}_i$, were already discussed in section 4.2.7.

Using these instantiated components as building blocks, the complete physical domain, Ω, can now be represented as $\overline{\Omega} = \bigcup_{i=1}^{N_c} \overline{\Omega}_i$. In words, as the non-overlapping intersection of the instantiated components' physical domains. The underlying components are connected to each other at the local edges, $e_{i,j}$, and/or at local vertices, $v_{i,j,j'}$. When the instantiated components are connected by their local edges, the local collection is referred to as a *global edge*, E_p, $1 \leq p \leq n_0^E$. The set of all the global edges is designated as: $\boldsymbol{E} = \{E_1, \ldots E_{n_0^E}\}$. Two convenient mappings discussed in [104,105], will now be introduced. The first corresponds to the connectivity of global edges and is represented as the connectivity map, π_p^E, $1 \leq p \leq n_0^E$. A global edge formed by the

[1]The notation $\bar{\cdot}$ is used to represent the "*closure*" of the physical domain

meeting of two local edges, $e_{i,j}$ and $e_{i',j'}$ $1 \leq i, i' \leq N_c$, $1 \leq j \leq n^e_{\mathcal{G}(i)}$, $1 \leq j' \leq n^e_{\mathcal{G}(i')}$, can be represented by $\pi^E_p = \{(i,j),(i',j')\}$. Similarly, a global edge with only one local edge can be represented as $\pi^E_p = \{(i,j)\}$. This mapping can be trivially extended to situations wherein more than three congruent, local edges meeting at a global edge; however, for simplicity, this is not represented explicitly in this work. A subset of these global edges, $n^E \leq n^E_0$, are those upon which Dirichlet boundary conditions are *not* imposed. These make up the edges on the interior of the system's problem domain, as well the parts of the domain's periphery on which tractions can be applied or that are left free. The second is: for each instantiated component, i, $1 \leq i \leq N_c$, a local-to-global map $\mathcal{C}_i$ is applied to a local edge j, $1 \leq j \leq n^e_{\mathcal{G}(i)}$. This map then links a local edge, $e_{i,j}$ to a global edge, E_p, as $\mathcal{C}_i(j) = p$.

As mentioned previously, the edges in the problem domain are allowed to intersect. The global vertices are designated by V_z, $1 \leq z \leq n_{V,0}$, where n^V_0 is the total number of global vertices in the assembled domain, Ω. In a similar fashion to the global edges, the set of all the global vertices is designated as: $\boldsymbol{V} = \{V_1, \ldots V_{n^V_0}\}$. A subset of the vertices, $n^V \leq n^V_0$, are those that do not belong to the boundary segment $\partial\Omega_D$ i.e. the region where known Dirichlet boundary conditions are applied. The global edges that meet at an individual global vertex, V_z, can be identified through the use of connectivity maps, π^V_z. As an example, consider a global vertex which is formed by the intersection of the closure of four global edges (see figure 35), i.e. $V_z = \bar{E}_p \cap \bar{E}_{p'} \cap \bar{E}_{p''} \cap \bar{E}_{p''}$. The connectivity map in this case can be represented as, $\pi^V_z = \{p, p', p'', p'''\}$ for $1 \leq z \leq n^V$ and $1 \leq p, p', p'', p''' \leq n^E_0$. Illustrations of an archetype component, followed by its instantiation and inclusion into a working system is shown in figures 34 and 35. The key idea of the instantiation of reference components and their inclusion in the formation of the global physical problem domain is illustrated in both figures 30 and 31.

The global parameter or design variable vector of the entire system, μ, is made

up of the parameter domains defined on the each of the local components and auxiliary parameters (such as those defining boundary tractions or parametric Dirichlet boundary conditions). The auxiliary parameters are designated as: $\mathcal{D}_{\text{aux}} \in \mathbb{R}^{p_{\text{aux}}}$ with $p_{\text{aux}} \in \mathbb{N}$. Using this designation, the global parameter domain defined for the global problem can be defined as: $\mathcal{D} \subseteq \mathcal{D}_{\mathcal{G}(1)} \times \mathcal{D}_{\mathcal{G}(2)} \times \cdots \times \mathcal{D}_{\mathcal{G}(N_c)} \times \mathcal{D}_{\text{aux}}$.

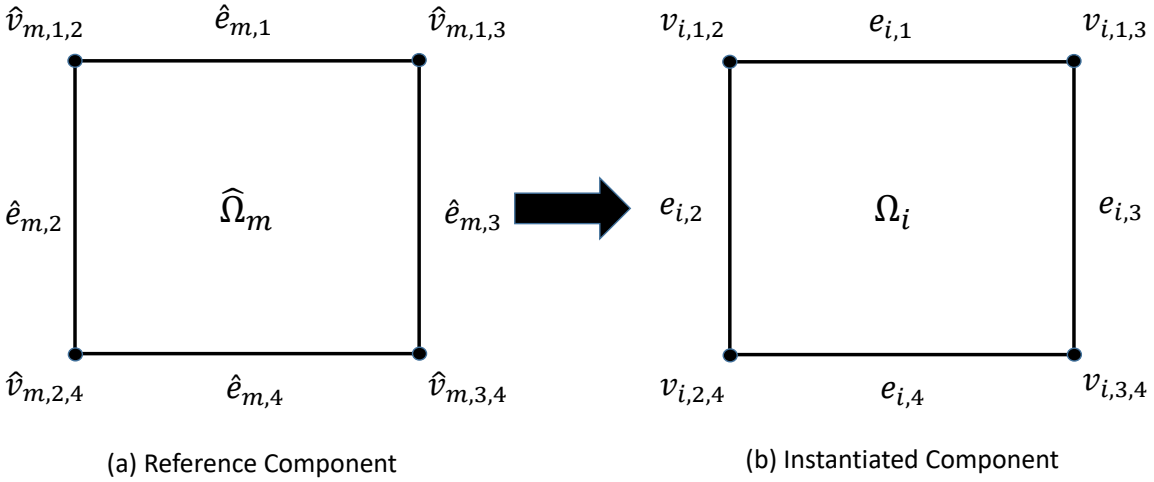

Figure 34: An illustration of an archetype component followed by its instantiation

5.3.2 Billinear Form, Linear Functional And Finite Element Space

Each of the N_{ref} components has a parameter-dependent, affine billinear form, $\hat{a}_m(\cdot,\cdot;\mu_m)$: $\left(H^1(\hat{\Omega}_m)\right)^d \times \left(H^1(\hat{\Omega}_m)\right)^d \times \mathcal{D}_m \to \mathbb{R}$ for $(d = \{1,2,3\})$, and a linear functional, $\hat{f}_m(\cdot;\mu_m) : \left(H^1(\hat{\Omega}_m)\right)^d \times \mathcal{D}_m \to \mathbb{R}$, prescribed over its domain. An important property for both the billinear and linear functionals is that they should possess the *affine* or *separable* property. This takes the form:

$$\begin{aligned} \hat{a}_m(\cdot,\cdot;\mu_m) &= \sum_{q=1}^{Q_a} \theta_q^a(\mu_m)\hat{a}_m(\cdot,\cdot) \\ \hat{f}_m(\cdot;\mu_m) &= \sum_{q=1}^{Q_f} \theta_q^f(\mu_m)\hat{f}_m(\cdot) \end{aligned} \tag{97}$$

In this type of decomposition, there are parameter independent terms ($\hat{a}_m(\cdot,\cdot)$ and $\hat{f}_m(\cdot)$) that are scaled by parameter dependent scalars $\left(\theta_q^a(\mu_m)\right.$ and $\left.\theta_q^f(\mu_m)\right)$ to form

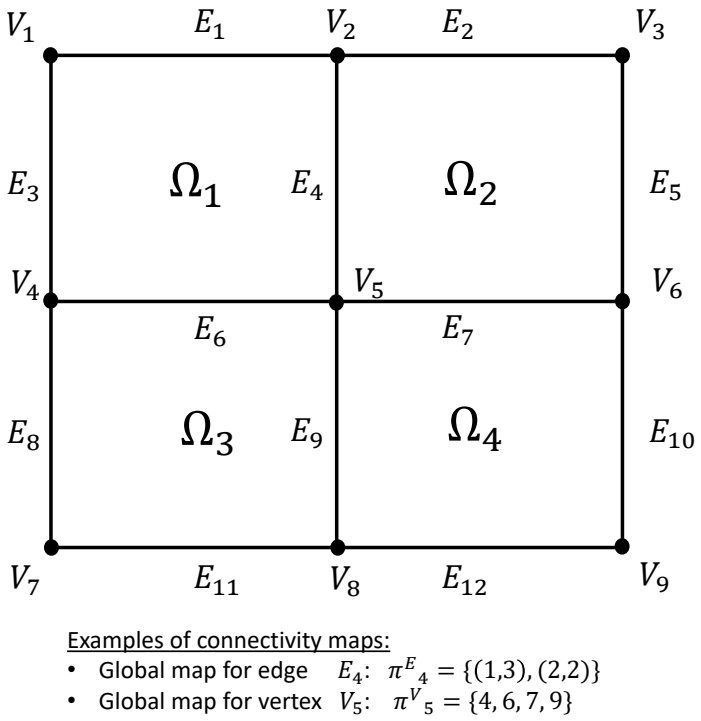

Figure 35: An illustration of an assembled problem domain using the components from figure 34

their respective output functional. This allows for a separation of the offline and online stages of the Reduced Order Modeling (ROM) and has been shown to considerably increase the efficiency of "many-query" or "real-time" problems. If this is not satisfied, then the Discrete Empirical Interpolation Method (DEIM) [134] approach is often used in literature to create an approximation of the desired form.

The local, high-dimensional, discrete finite element space, $\hat{X}^h_m$ of size $\mathcal{N}_m$, is now introduced as the function space used to provide an approximation of the solution within the m^{th} component. The trace of this finite element function space, restricted to the closed domain of an edge, is referred to here as the *edge space* and is defined as, $\hat{P}^h_{m,j} \equiv \hat{X}^h_m\Big|_{\bar{\hat{e}}_{m,j}}$, $1 \leq j \leq n^e_m$, and is of dimension $\mathcal{N}_{m,j}$. The designation of the trace space and the associated basis was used in [109]. The basis functions for each

edge space are denoted by $\{\hat{\chi}_{m,j,k}\}_{k=1}^{\mathcal{N}_{m,j}}$. Expanded, it is written as:

$$\hat{P}^h_{m,j} = \text{span}\left\{\hat{\chi}_{m,j,1}, ..., \hat{\chi}_{m,j,\mathcal{N}_{\mathcal{G}(i),j}}\right\} \tag{98}$$

The local finite element space defined for an instantiated component mapped to the FE space defined over the corresponding reference domain is

$$X^h_i = \text{span}\left\{\mathcal{T}^{rot}_i\left(v \circ \mathcal{T}^{-1}_i\right),\ \ v \in \hat{X}^h_{\mathcal{G}(i)}\right\}; \tag{99}$$

Similarly, the basis elements in the edge space, $P^h_{i,j}$, on an instantiated component can be mapped to the corresponding reference edge space, $\hat{P}^h_{\mathcal{G}(i),j}$, as

$$\chi_{i,j,k} = \mathcal{T}^{rot}_i\left(\hat{\chi}_{\mathcal{G}(i),j,k} \circ \mathcal{T}^{-1}_i\right),\ \ 1 \le j \le n^e_{\mathcal{G}(i)},\ \ 1 \le i \le N_c,\ \ 1 \le k \le \mathcal{N}_{\mathcal{G}(i),j}; \tag{100}$$

Thus, the discrete edge space on an instantiated component can be represented as

$$P^h_{i,j} = \text{span}\left\{\chi_{i,j,1}, ..., \chi_{i,j,\mathcal{N}_{i,j}}\right\} \tag{101}$$

Here, $[\cdot] \circ \mathcal{T}^{-1}_i$ is similar to the geometric map discussed in section 4.2.7. The map $\mathcal{T}^{rot}_i(\cdot)$ is applied to reference component to properly orient it for "docking" to a global edge [81].

Congruency is enforced on the global interfaces between components. For the edges interfacing at a global edge, E_p, we have:

$$P^h_{i,j} = P^h_{i',j'} \tag{102}$$

Here, the indices are governed by the connectivity map associated with the global edge, i.e. π^E_p. In other words, the underlying finite element discretization must "match" at the each global edge. Similarly, for the global edges interfacing at a global vertex, V_z, we must have congruency of the associated edge spaces at the vertex. In the event that the problem domain is planar, this is trivially satisfied because the interfacing edges all intersect at a single node.

The bilinear form and linear functionals for the system can be introduced $\forall v, w \in (H^1(\Omega))^d$ as

$$a(w, v; \mu) = \sum_{i=1}^{N_c} \hat{a}_{\mathcal{G}(i)} \left(\left(\mathcal{T}_i^{rot}\right)^{-1} \left(v|_{\bar{\Omega}_i} \circ \mathcal{T}_i \right), \left(\mathcal{T}_i^{rot}\right)^{-1} \left(w|_{\bar{\Omega}_i} \circ \mathcal{T}_i \right); \mu_i \right) \tag{103}$$

and

$$f(w; \mu) = \sum_{i=1}^{N_c} \hat{f}_{\mathcal{G}(i)} \left(\left(\mathcal{T}_i^{rot}\right)^{-1} \left(w|_{\bar{\Omega}_i} \circ \mathcal{T}_i \right); \mu_i \right) \tag{104}$$

The global space, $X(\Omega)$, discussed in section 4.2.4 is reused here. To this point, it is assumed that the domain is suitably constrained so that the bilinear operator remains coercive over $X(\Omega)$. The global finite element approximation space can now be expressed as

$$X^h(\Omega) = \oplus_{i=1}^{N_c} X_i^h(\Omega_i) \cap X(\Omega) \tag{105}$$

The size of this space is $\mathcal{N}$. The intersection is included so as to "preserve the boundary conditions and the global continuity of $X(\Omega)$" [81].

5.3.2.1 Global Finite Element Problem

Finally, the global finite element problem to be solved can be stated as: $\forall \mu \in \mathcal{D}$, find $u^h(\mu, x) \in X^h(\Omega)$ such that

$$a\left(u^h(\mu, x), v; \mu\right) = f\left(v; \mu\right), \quad \forall v \in X^h(\Omega); \tag{106}$$

with the outputs of interest:

- Constraints: $g_\ell(u^h(\mu, x), \mu)$ for $1 \leq \ell \leq n_g$.

Here n_g is the number of constraints that are dependent on the state variable.

5.3.3 Static Condensation - Edge and Vertex Modes

In the static condensation procedure, the global finite element problem is written in terms of the degrees of freedom on the interfaces between the components on the problem domain; i.e. the union of all the global edges and global vertices. The degrees of freedom corresponding to the state variable on the interior of the component

domains are first *condensed* and written in terms of the solution on the interfaces. Consequently, the discrete global finite element space, $X^h(\Omega)$, is decomposed into, bubble spaces, defined on the interior of each component and, interface spaces, defined on the edges and vertices.

In the initial set of papers in the SCRBE literature, the component domains were assembled in such a way that the global edges did not intersect with each other. Consequently, modes from the edge space $P^h_{i,j}$ - defined on each component boundary - could be selected without the need for special modifications. In order to remove this limitation, later papers (Bader [114]) pursued a space decomposition approach and allowed the global edges to intersect. This type of space decomposition approach is commonly used in domain decomposition FEM approaches [136]. The state variable was expressed on the interfaces with a combination of *vertex modes* and *edge modes*. The vertex modes chosen were the hat functions defined on the coarse grid formed by the component boundaries. These modes have a non-zero value at the vertex about which they are defined and a value of zero at all other vertices. They also have a linear variation over the edges that are coincident with the vertex. On the other hand, the edge modes were chosen to have support[2] over the open domain of each edge, and would vanish at the global vertices bounding the edge. These two mode types are illustrated in figure 36.

For the present work, a similar decomposition of the interface solution will be pursued. These modes come from the edge spaces, $P^h_{i,j}$, and share the same support as the modes already defined in this section.

For each global edge, E_p, the edge modes are represented as:

$$\chi^E_{p,k}, \;\; 1 \leq k \leq \mathcal{N}_{E_p} \tag{107}$$

Where $\mathcal{N}_{E_p}$ is the number of modes used to represent the solution on the global edge

[2]The support of a function, f(x), is defined as: $\text{supp}(f) = \{x \in \bar{\Omega} : f(x) \neq 0\}$

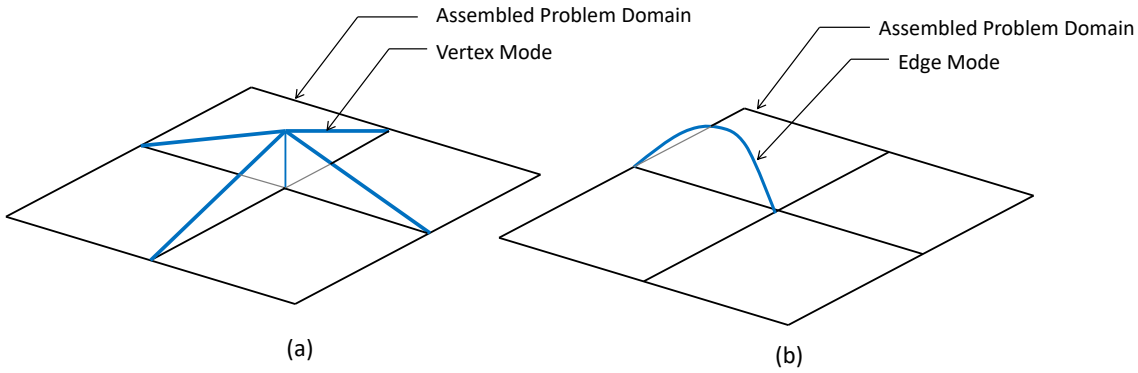

Figure 36: An illustration of the vertex modes and edge modes used to express the solution on the interfaces

E_p. To enable model reduction, we require that the edge modes come from a subspace of the edge space, $P^h_{i,j}$. This subspace should be hierarchical and allow for rapid convergence to approximation of the state variable on the interface as the number of modes is increased. An approach to furnish an empirical subspace satisfying these properties is provided in section 5.4.1.

For each global vertex, V_z, the vertex modes are defined as:

$$\chi^V_{z,k'}, \;\; 1 \leq k' \leq \mathcal{N}_{V_z} \tag{108}$$

Here $\mathcal{N}_{V_z}$ is the number of modes used to represent the solution on the global vertex V_z.

5.3.4 Static Condensation - Interface Mode Extensions And Bubble Solutions

The process of static condensation begins by the specification of the bubble spaces on each of the archetype components. They are defined as:

$$\hat{B}^h_{m;0} = \left\{ v \in \hat{X}^h_m : v|_{\hat{e}_{m,j}} = 0, \;\; 1 \leq j \leq n^e_m \right\}; \tag{109}$$

The elements of $\hat{B}^h_{m;0}$ vanish on the local edges of each component. An example of a bubble function defined on the interior of a component is illustrated in figure 37.

The analogous bubble space defined on an instantiated component i is $B^h_{\mathcal{G}(i);0}$.

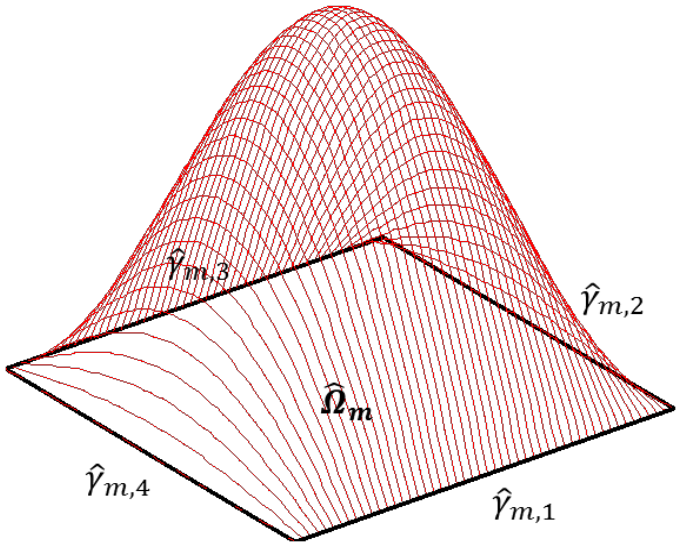

Figure 37: An illustration of a bubble space function

Now that the bubble space has been defined, the next task to define the *extension* of each edge and vertex mode into the interior of the neighboring components. In the initial set of papers in the SCRBE literature, the interface modes were "lifted" into interior of the component such that weak form of the Laplacian PDE was satisfied by the extension on the component domain. This was referred to as the *harmonic extension*. The literature suggests that one is free to chose the elliptical partial differential equation that is used to determine the extension of the interface mode into the interior of the component. As such, the approach taken by [115] will be used because of convenience. The extension of a particular edge mode, $\chi^E_{p,k}$, into the interior of the components that surround the global edge will be referred to as: $\Psi^{E,h}_{p,k}$. For each component adjacent to the edge, Ω_i, the local extension into its interior is designated as: $\Psi^{E,h}_{p,k}\Big|_{\bar{\Omega}_i}$. The local extension $\Psi^{E,h}_{p,k}\Big|_{\bar{\Omega}_i}$ must satisfy:

$$a_{\mathcal{G}(i)}\left(\Psi^{E,h}_{p,k}\Big|_{\bar{\Omega}_i}, v; \bar{\mu}\right) = -a_{\mathcal{G}(i)}\left(\chi^E_{p,k}\big|_{\bar{\Omega}_i}, v; \bar{\mu}\right), \quad \forall v \in B^h_{\mathcal{G}(i);0} \tag{110}$$

Here, $\bar{\mu}$ is a randomly chosen, but fixed value in the parameter space of the local

component. In a similar fashion, the extension of a vertex mode, $\chi^V_{z,k'}$, into the interior of the adjacent components will be denoted to as: $\Psi^{V,h}_{z,k'}$. The local extension into component, Ω_i is found by solving:

$$a_{\mathcal{G}(i)}\left(\Psi^{V,h}_{z,k'}\Big|_{\bar{\Omega}_i}, v; \bar{\mu}\right) = -a_{\mathcal{G}(i)}\left(\chi^V_{z,k'}|_{\bar{\Omega}_i}, v; \bar{\mu}\right), \quad \forall v \in B^h_{\mathcal{G}(i);0} \tag{111}$$

The global extension of the edge modes can be written concisely as:

$$\Psi^{E,h}_{p,k} = \bigcup_{i \in \pi^E_p} \Psi^{E,h}_{p,k}\Big|_{\bar{\Omega}_i} \tag{112}$$

Similarly, the global extension for the vertex modes is written as:

$$\Psi^{V,h}_{z,k} = \bigcup_{i \in \pi^V_z} \Psi^{V,h}_{z,k}\Big|_{\bar{\Omega}_i} \tag{113}$$

The extensions for both the edge and vertex modes are calculated during the once and for all during the offline stage of the procedure.

The static condensation approach seeks to remove the degrees of freedom corresponding the state variable expressed on the interior of the component domains. As such, these solutions are expressed in terms of the degrees of freedom on the interface. For each interface mode, we desire to find the bubble solution on a component that is induced from a unit perturbation of the mode. The bubble solution induced by a global extension mode, $\Psi^{E,h}_{p,k}$, is designated as, $b^{E,h}_{p,k}$. The corresponding local terms defined on a component, Ω_i, are: $\Psi^E_{p,k}|_{\bar{\Omega}_i}$ and $b^{E,h}_{p,k}\Big|_{\bar{\Omega}_i}$, respectively. The bubble solution, $b^{E,h}_{p,k}\Big|_{\bar{\Omega}_i}$, is obtained by solving the following equation:

$$a_{\mathcal{G}(i)}\left(b^{E,h}_{p,k}\Big|_{\bar{\Omega}_i}, v; \mu\right) = -a_{\mathcal{G}(i)}\left(\Psi^{E,h}_{p,k}\Big|_{\bar{\Omega}_i}, v; \mu\right), \quad \forall v \in B^h_{\mathcal{G}(i);0} \tag{114}$$

using the linearity of the system, we have:

$$a_{\mathcal{G}(i)}\left(\Psi^{E,h}_{p,k}\Big|_{\bar{\Omega}_i} + b^{E,h}_{p,k}\Big|_{\bar{\Omega}_i}, v; \mu\right) = a_{\mathcal{G}(i)}\left(\Phi^{E,h}_{p,k}\Big|_{\bar{\Omega}_i}, v; \mu\right) = 0, \quad \forall v \in B^h_{\mathcal{G}(i);0} \tag{115}$$

The term $\Phi^{E,h}_{p,k}\Big|_{\bar{\Omega}_i}$ is referred to as the *fundamental solution* defined on the interior of a component Ω_i. The analagous bubble solution $b^{V}_{z,k'}\big|_{\bar{\Omega}_i}$ induced by the extension of the vertex mode extension, $\Psi^{V,h}_{z,k'}$, is determined by:

$$a_i\left(b^{V,h}_{z,k'}\Big|_{\bar{\Omega}_i}, v; \mu\right) = -a_i\left(\Psi^{V,h}_{z,k'}\Big|_{\bar{\Omega}_i}, v; \mu\right), \quad \forall v \in B^h_{\mathcal{G}(i);0} \tag{116}$$

with the associated fundamental solution determined by

$$a_{\mathcal{G}(i)}\left(\Psi^{V,h}_{z,k'}\Big|_{\bar{\Omega}_i} + b^{V,h}_{z,k}\Big|_{\bar{\Omega}_i}, v; \mu\right) = a_{\mathcal{G}(i)}\left(\Phi^{V,h}_{z,k'}\Big|_{\bar{\Omega}_i}, v; \mu\right) = 0, \quad \forall v \in B^h_{\mathcal{G}(i);0} \tag{117}$$

The global fundamental solution corresponding to an edge mode is:

$$\Phi^{E,h}_{p,k} = \bigcup_{i \in \pi^E_p} \Phi^{E,h}_{p,k}\Big|_{\bar{\Omega}_i} \tag{118}$$

for components i defined on the map, π^E_p. Similarly for the vertex mode,

$$\Phi^{V,h}_{z,k} = \bigcup_{i \in \pi^V_z} \Phi^{V,h}_{z,k}\Big|_{\bar{\Omega}_i} \tag{119}$$

Using these elements, we now define the following function subspaces that will be used later on during the Galerkin and Petrov-Galerkin stages for the static condensation procedure. These subspace groups are:

$$\begin{aligned}
\mathcal{S}^E_{\text{asymm}}(\Omega) &\equiv \left\{\Psi^{E,h}_{p,k},\ \ 1 \le p \le n^E,\ \ 1 \le k \le \mathcal{N}_{E_p}\right\} \\
\mathcal{S}^V_{\text{asymm}}(\Omega) &\equiv \left\{\Psi^{V,h}_{z,k'},\ \ 1 \le z \le n^V,\ \ 1 \le k' \le \mathcal{N}_{V_z}\right\} \\
\mathcal{S}_{\text{asymm}}(\Omega) &\equiv \left\{v : v \in \mathcal{S}^E_{\text{asymm}}(\Omega) \cup \mathcal{S}^V_{\text{asymm}}(\Omega)\right\}
\end{aligned} \tag{120}$$

and

$$\begin{aligned}
\mathcal{S}^E_{\text{sym}}(\Omega) &\equiv \left\{\Phi^{E,h}_{p,k},\ \ 1 \le p \le n^E,\ \ 1 \le k \le \mathcal{N}_{E_p}\right\} \\
\mathcal{S}^V_{\text{sym}}(\Omega) &\equiv \left\{\Phi^{V,h}_{z,k'},\ \ 1 \le z \le n^V,\ \ 1 \le k' \le \mathcal{N}_{V_z}\right\} \\
\mathcal{S}_{\text{sym}}(\Omega) &\equiv \left\{v : v \in \mathcal{S}^E_{\text{sym}}(\Omega) \cup \mathcal{S}^V_{\text{sym}}(\Omega)\right\}
\end{aligned} \tag{121}$$

The final ingredient that has to be developed before we are able to express the global solution of the problem is bubble solution that is induced when traction is

applied directly on the interior of the component domain (e.g. a pressure field). Given a traction defined directly on the interior of the component domain, the bubble solution $b_i^{f,h}$ is obtained by solving:

$$a_{\mathcal{G}(i)}\left(b_i^{f;h}(\mu), v; \mu\right) = f_{\mathcal{G}(i)}\left(v; \mu\right), \qquad \forall v \in B^h_{\mathcal{G}(i);0} \tag{122}$$

5.3.5 The Schur Complement

Using these fundamental solutions and the traction-induced bubble solutions, the global solution is now defined as:

$$u^h(\mu) = \sum_{p=1}^{n^E}\sum_{k=1}^{\mathcal{N}^{E_p}} \mathbb{U}_{p,k}\left(\mu\right)\Phi^{E,h}_{p,k} + \sum_{z=1}^{n^V}\sum_{k'=1}^{\mathcal{N}^{V_z}} \mathbb{U}_{z,k'}\left(\mu\right)\Phi^{V,h}_{z,k'} + \sum_{i=1}^{N_c} b_i^{f,h} \tag{123}$$

Notice that with the exception of the traction-induced bubble solution, the global state variable is written in terms of the degrees of freedom on the interfaces i.e. $\mathbb{U}_{p,k}\left(\mu\right)$ and $\mathbb{U}_{z,k'}\left(\mu\right)$ defined on the global edges and vertices respectively. This global solution is also referred to as the *trial solution*.

The task is now to determine the state variable on the interfaces of the problem domain. In the literature for SCRBE, there are two approaches used to determine the unknowns degrees of freedom. The most common approach is to use the subspace $\mathcal{S}_{\text{sym}}\left(\Omega\right)$ as the test space in the Galerkin projection procedure. The resulting system takes the form:

$$a\left(\Phi^h(\mu), v; \mu\right) u_s(\mu) = f\left(v; \mu\right) - \sum_{i=1}^{N_c} a\left(b_i^{f;h}(\mu), v; \mu\right), \quad \forall v \in \mathcal{S}_{\text{sym}}\left(\Omega\right) \tag{124}$$

where $\Phi^h(\mu) \in \mathcal{S}_{\text{sym}}\left(\Omega\right)$. Switching from the abstract form of the global system, the discrete version of the system can be written as:

$$\mathbb{K}_{uu}(\mu)\mathbb{U}_s(\mu) = \mathbb{F}_u(\mu) \tag{125}$$

and is of dimension $\mathcal{N}_{sc}$. Here $\mathbb{K}_{uu}(\mu)$[3] represents the global stiffness matrix; $\mathbb{U}_s(\mu)$

[3]The Schur complement stiffness matrix is represented here as $\mathbb{K}_{uu}(\mu)$ instead of $\mathbb{A}_{uu}(\mu)$ as is often

represents the vector of unknown coefficients for the interface state variable; $\mathbb{F}_u(\mu)$ represents the sum of the global force vector consisting of traction applied directly to the interfaces in the problem domain and the induced forces on the interfaces due to traction-induced bubble solutions $b_i^f(\mu)$ (i.e. $\sum_{i=1}^{N_c} \mathbb{K}_{ub}(\mu) b_i^f(\mu)$). The elements of the Schur complement are formed at the component level and then assembled into the global system by use of the *Direct Stiffness Method* [137]. At the component level, we have:

$$\mathbb{K}^i_{uu,((m,k),(m',k'))}(\mu) = a_i\left(\Phi^{g,h}_{m,k}\Big|_{\bar{\Omega}_i}, \Phi^{g',h}_{m',k'}\Big|_{\bar{\Omega}_i}; \mu\right) \tag{126}$$

$$\mathbb{F}^i_{u,(m',k')}(\mu) = f\left(\Phi^{g',h}_{m',k'}\Big|_{\bar{\Omega}_i}; \mu\right) - a\left(b_i^{f;h}(\mu), \Phi^{g',h}_{m',k'}\Big|_{\bar{\Omega}_i}; \mu\right) \tag{127}$$

Here, $\Phi^{g,h}_{m,k}$, $\Phi^{g',h}_{m',k'} \in \mathcal{S}_{\text{sym}}(\Omega)$ are used generically to refer to either of the fundamental solutions induced by the edge or vertex modes.

A less commonly used approach is to select the function subspace $\mathcal{S}_{\text{asymm}}$ and perform the Petrov-Galerkin procedure instead of the Galerkin procedure when creating the weak form of the PDE. This approach was developed by Eftang [81]. Using this approach leads to the following system.

$$a\left(\Phi^h(\mu), v; \mu\right)\mathbb{U}_s(\mu) = f(v;\mu) - \sum_{i=1}^{N_c} a_i\left(b_i^{f;h}(\mu), v; \mu\right), \quad \forall v \in \mathcal{S}_{\text{asymm}}(\Omega) \tag{128}$$

The discrete system takes a similar form to equation 125 except for the fact that the coefficient matrix $\mathbb{K}_{uu}(\mu)$ is not symmetric. This can be seen by examining the contributions to the Schur complement at the component level

$$\mathbb{K}^i_{uu,((m,k),(m',k'))}(\mu) = a_i\left(\Phi^{g,h}_{m,k}\Big|_{\bar{\Omega}_i}, \Psi^{g',h}_{m',k'}\Big|_{\bar{\Omega}_i}; \mu\right) \tag{129}$$

$$\mathbb{F}^i_{u,(m',k')}(\mu) = f\left(\Psi^{g,h}_{m',k'}\Big|_{\bar{\Omega}_i}; \mu\right) - a\left(b_i^{f;h}(\mu), \Psi^{g,h}_{m',k'}\Big|_{\bar{\Omega}_i}; \mu\right) \tag{130}$$

The lack of symmetry was handled by performing the following operation to recover

done in Reduced Basis Approximation literature. This was done to cater to a structural/aerospace design audience

symmetry:

$$\mathbb{K}^i_{uu,((m,k),(m',k'))}(\mu) = \frac{1}{2}a_i\left(\Psi^{g,h}_{m,k}\Big|_{\bar{\Omega}_i}, \Phi^{g',h}_{m',k'}\Big|_{\bar{\Omega}_i}; \mu\right) + \frac{1}{2}a_i\left(\Phi^{g,h}_{m,k}\Big|_{\bar{\Omega}_i}, \Psi^{g',h}_{m',k'}\Big|_{\bar{\Omega}_i}; \mu\right) \tag{131}$$

The Petrov-Galerkin procedure is advantageous for the following reasons:

- Less computational time is required to assemble the Schur complement contributions during the online stage
- There is less memory overhead when storing the associated affine matrices
- Less computational time is required to create the underlying components during the offline stage of the procedure

For these reasons, the Schur complement furnished by the Petrov-Galerkin procedure will be used for the remainder of this section.

5.3.6 Recovering The State Variable On The Interior Of The Components

A pair of mappings will now be defined in order to conveniently recover the state variable on the interior of each component. These mappings are:

$$U^i_b: \quad \mathcal{D}_{\mathcal{G}(i)} \times \mathbb{R}^{\mathcal{N}_{sc}} \rightarrow \mathbb{R}^{\mathcal{N}_{b_i}} \tag{132}$$

$$\bar{U}^i_b: \quad \mathbb{R}^{\mathcal{N}_{sc}} \rightarrow \mathbb{R}^{\mathcal{N}_{b_i}} \tag{133}$$

Here $\mathcal{N}_{b_i}$ corresponds to the number of degrees of freedom used to represent the state variable on the interior of the domain Ω_i. The columns of the first mapping, $U^i_b(\mu_i) \in \mathbb{R}^{\mathcal{N}_{b_i} \times \mathcal{N}_{sc}}$, correspond to the bubble solutions that are induced by the extension of each interface mode defined on the component's boundary; i.e. $b^{E,h}_{p,k}\Big|_{\bar{\Omega}_i}$ and $b^{V,h}_{z,k'}\Big|_{\bar{\Omega}_i}$. Similarly, the columns of $\bar{U}^i_b \in \mathbb{R}^{\mathcal{N}_{b_i} \times \mathcal{N}_{sc}}$ are formed from the extensions of the interface modes defined on the component's boundary; i.e. $\Psi^{E,h}_{p,k}\Big|_{\bar{\Omega}_i}$ and $\Psi^{V,h}_{z,k'}\Big|_{\bar{\Omega}_i}$. The column that each entry is placed in is governed by the location of the associated degree of freedom in the vector, $\mathbb{U}_s$. Clearly, both mappings are sparse since only a small fraction of the interface degrees of freedom will correspond to the bubble solutions and extensions of a given component. This is especially true for large problem

domains containing many components.

Using these mappings; the traction induced bubble solution, $b_i^{f;h}(\mu)$; and, the global interface solution, $\mathbb{U}_s(\mu)$; the complete solution on the interior of a component, $U(\mu)|_{\bar{\Omega}_i}$, can be recovered as:

$$U(\mu)|_{\bar{\Omega}_i} = \left[\bar{U}_b^i + U_b^i(\mu_i)\right] \mathbb{U}_s(\mu) + b_i^{f;h}(\mu) \tag{134}$$

5.3.7 Inequality Constraints On Each Component

In this section, an overview will be given on how the inequality constraints are treated under the present framework. The constraints are defined locally on each of the components in the problem domain. Thus, the material strength and structural stability constraints are all evaluated on the component's physically domain Ω_i

5.3.7.1 Bound Constraints

Consider an arbitrary inequality constraint, $g = g(U(\mu, x)|_{\bar{\Omega}_i}, \mu)$, defined on the interior of a generic component's physical domain, Ω_i. The continuous, induced exponential constraint-aggregation functional applied to this constraint takes the form:

$$c_{IE}(\rho, g) = \frac{\int_{\Omega_i} g \mathrm{e}^{\rho g} d\Omega_i}{\int_{\Omega_i} \mathrm{e}^{\rho g} d\Omega_i} \tag{135}$$

Since the inequality constraint is not available in an analytical form, the functional has to be approximated by the use of numerical integration. In particular, by the use of the Gaussian quadrature. The discrete form can be expressed as:

$$\widetilde{c}_{IE}(\rho, g) = \frac{\sum_{\wp=1}^{n} \frac{w_\wp}{w_s} g|_\wp \mathrm{e}^{\rho(g|_\wp - \max(g|_\wp))}}{\sum_{\wp=1}^{n} \frac{w_\wp}{w_s} \mathrm{e}^{\rho(g|_\wp - \max(g|_\wp))}} \tag{136}$$

Where:

- $w_\wp$ is the Gaussian quadrature weight at node j
- w_s is the sum of the Gaussian quadrature weights, $w_s = \sum_{\wp=1}^{n} w_\wp$
- ρ is the aggregation parameter that controls the functional approximation

- $g|_{\wp}$ is the inequality constraint evaluated at node $\wp$

The argument of the exponential function is shifted in order to avoid numerical ill-conditioning as $g_{\wp} \to \infty$. With this formulation, the constraint only needs to be evaluated in the vicinity of the Gaussian quadrature nodes on the component domain. This is illustrated in figure 38.

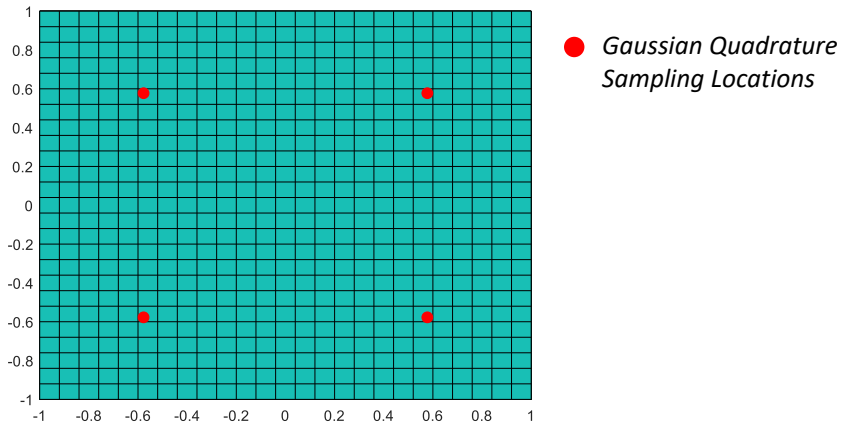

Figure 38: Sampling points for the Gaussian quadrature on the finite element mesh using 2 sampling points in each direction

In the context of aerospace structural analysis, it is very common to discretize the problem domain with triangular or quadrilateral finite elements and use a lower order polynomial approximation subspace with Lagrangian basis functions. In this work, consideration is restricted to approximation spaces of this kind. In this context, in order to determine the discrete constraint aggregate, we only need the state variable on the nodes in the vicinity of the quadrature sampling points. These values are then used to calculate the inequality constraints at the quadrature sampling points, and then ultimately, used to calculate the discrete constraint aggregate. Consequently, the induced constraint aggregate can be represented as:

$$\widetilde{c}_{IE} = \widetilde{c}_{IE}\left(\rho, g\left(U(\mu)|_{\Omega_{i,GQ}}\right), \mu\right) \tag{137}$$

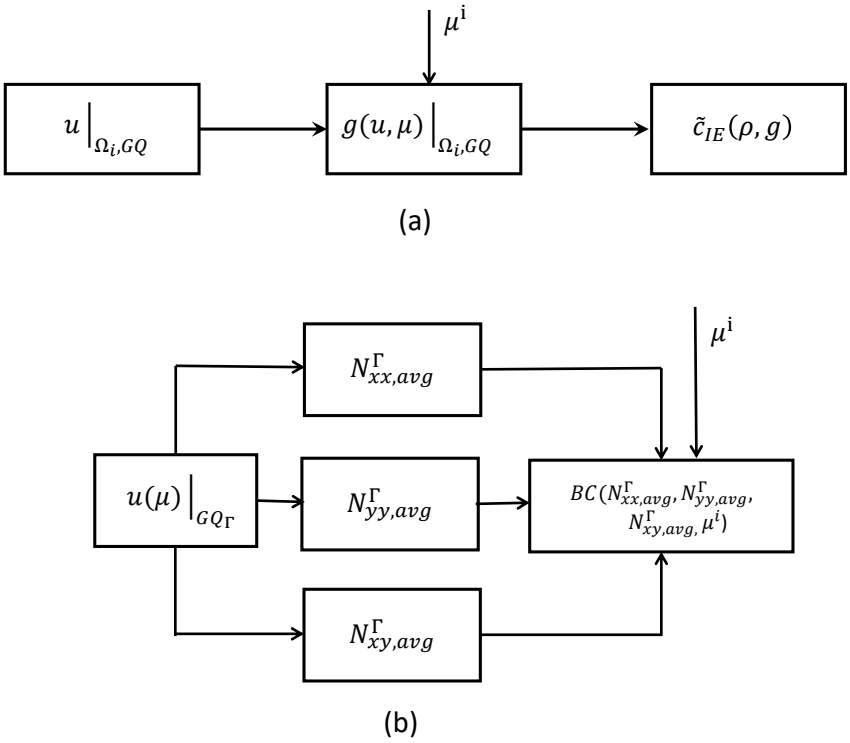

Figure 39: Use of the state variable to furnish an approximation of the constraints. (a) Constraint aggregate (b) Buckling Constraint

where $U(\mu)|_{\Omega_{i,GQ}}$ is used to restrict the state variable to the nodes in the vicinity of the Gaussian quadrature sampling points. Using this restriction, the expression for the state variable on the interior of the components can be similarly restricted as:

$$U(\mu)|_{\Omega_{i,GQ}} = \left[\bar{U}^i_{b,GQ} + U^i_{b,GQ}(\mu_i)\right] \mathbb{U}_s(\mu) + b^{f;h}_{i,GQ}(\mu) \tag{138}$$

5.3.7.2 Structural Stability Inequality Constraints

The average boundary loads are determined with the Gaussian quadrature in a similar fashion the bound-constraint. The approximate integration takes the form.

$$N_{xx,\text{avg}}^{\Gamma_v} \approx \frac{1}{A_s^v} \sum_{\wp=1}^{n} w_\wp N_{xx,\wp}^{\Gamma_v} \left(U(\mu)|_{\Omega_{i,GQ}}^{\Gamma_v}, \mu_i \right) \tag{139}$$

$$N_{yy,\text{avg}}^{\Gamma_v} \approx \frac{1}{A_s^v} \sum_{\wp=1}^{n} w_\wp N_{yy,\wp}^{\Gamma_v} \left(U(\mu)|_{\Omega_{i,GQ}}^{\Gamma_v}, \mu_i \right) \tag{140}$$

$$N_{xy,\text{avg}}^{\Gamma_v} \approx \frac{1}{A_s^v} \sum_{\wp=1}^{n} w_\wp N_{xy,\wp}^{\Gamma_v} \left(U(\mu)|_{\Omega_{i,GQ}}^{\Gamma_v}, \mu_i \right) \tag{141}$$

Here Γ_v is the local boundary being considered on the problem domain, Ω_i. The Gaussian quadrature sampling locations are not the same as those for the bound-constraints. Here, the sampling points are located in the vicinity of the local boundary being investigated. This is illustrated in figure 40.

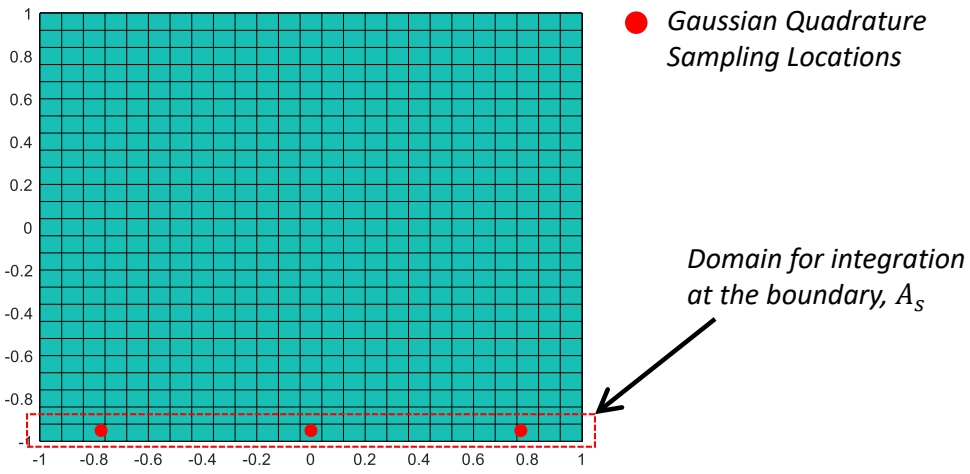

Figure 40: Sampling points for the Gaussian quadrature on the finite element mesh in the vicinity of a local boundary

In order to have more concise equations, the state variable restricted at the Gaussian quadrature sampling points will be denoted simply as $U(\mu)|_{\Omega_{i,GQ}}$ for both cases.

5.3.8 Calculating The Sensitivity Of The Inequality Constraint

For gradient-based optimization, estimates are needed for the constraints and their derivatives. Based on the discussion in section 2.5, using numerical differentiation

to provide estimates of the constraint derivatives is not viable because it only exacerbates the concerns about the computational overhead of the SCRBE approach. Consequently, the use of direct method or adjoint method are the only viable options for efficiency. Initial attempts were made by the author to use the adjoint method. However, with the choice of constraint aggregation functionals to represent the inequality constraints, this led to peaked/non-smooth functions on the interior of the components and on the global edges. The peaks were centered around the points were the constraints were sampled on the finite element mesh. This made it difficult to determine concise empirical subspaces that could approximate both the state variable and the Lagrange multipliers on the problem domain. For this reason, only the direct method will be considered for providing estimates of the derivatives.

Consider and arbitrary variable $\mu^r \in \mathbb{R}$ that belongs to the global parameter set μ. Taking the derivative of eq. 137 yields:

$$\frac{d\widetilde{c}_{IE}}{d\mu^r} = \frac{\partial \widetilde{c}_{IE}}{\partial \mu^r} + \frac{\partial \widetilde{c}_{IE}}{\partial\, U(\mu)|_{\Omega_{i,GQ}}} \frac{\partial\, U(\mu)|_{\Omega_{i,GQ}}}{\partial \mu^r} \tag{142}$$

and similarly, the sensitivity of the edge loads are:

$$\frac{dN^{\Gamma_v}_{xx,\text{avg}}}{d\mu^r} = \frac{\partial N^{\Gamma_v}_{xx,\text{avg}}}{\partial \mu^r} + \frac{\partial N^{\Gamma_v}_{xx,\text{avg}}}{\partial\, U(\mu)|_{\Omega_{i,GQ}}} \frac{\partial\, U(\mu)|_{\Omega_{i,GQ}}}{\partial \mu^r} \tag{143}$$

$$\frac{dN^{\Gamma_v}_{yy,\text{avg}}}{d\mu^r} = \frac{\partial N^{\Gamma_v}_{yy,\text{avg}}}{\partial \mu^r} + \frac{\partial N^{\Gamma_v}_{yy,\text{avg}}}{\partial\, U(\mu)|_{\Omega_{i,GQ}}} \frac{\partial\, U(\mu)|_{\Omega_{i,GQ}}}{\partial \mu^r} \tag{144}$$

$$\frac{dN^{\Gamma_v}_{xy,\text{avg}}}{d\mu^r} = \frac{\partial N^{\Gamma_v}_{xy,\text{avg}}}{\partial \mu^r} + \frac{\partial N^{\Gamma_v}_{xy,\text{avg}}}{\partial\, U(\mu)|_{\Omega_{i,GQ}}} \frac{\partial\, U(\mu)|_{\Omega_{i,GQ}}}{\partial \mu^r} \tag{145}$$

where:

$$\frac{\partial\, U(\mu)|_{\Omega_{i,GQ}}}{\partial \mu^r} = \left[\bar{U}^i_{b,GQ} + U^i_{b,GQ}(\mu_i)\right] \frac{\partial \mathbb{U}_s(\mu)}{\partial \mu^r} + \frac{\partial U^i_{b,GQ}(\mu_i)}{\partial \mu^r} \mathbb{U}_s(\mu) + \frac{\partial b^{f;h}_{i,GQ}(\mu)}{\partial \mu^r} \tag{146}$$

The sensitivity of the constraints with respect to μ^r is dependent on: $\mathbb{U}_s(\mu)$, $\Psi^{E,h}_{p,k}$, $\Psi^{V,h}_{z,k'}$, $b^{E,h}_{p,k}$, $b^{V,h}_{z,k'}$, $b^{f;h}_{i,GQ}(\mu)$, and their derivatives. However, recall that $\Psi^{E,h}_{p,k}$ and $\Psi^{V,h}_{z,k'}$ are parameter independent. The terms $b^{E,h}_{p,k}$, $b^{V,h}_{z,k'}$, and their derivatives are only dependent on the local parameters defined on the components. In addition to these

local parameters, $b_{i,GQ}^{f;h}(\mu)$ and its derivative are also dependent on the parameters pertaining to the boundary traction. The interface solution, $\mathbb{U}_s(\mu)$ and its derivative are dependent on all the parameters in the set μ. To determine the derivatives, we solve the following equations. For $\dfrac{\partial \mathbb{U}_s(\mu)}{\partial \mu^r}$, we take the derivative of equation (125):

$$\mathbb{K}_{uu}(\mu)\frac{\partial \mathbb{U}_s(\mu)}{\partial \mu^r} = \frac{\partial \mathbb{F}_u(\mu)}{\partial \mu^r} - \frac{\partial \mathbb{K}_{uu}(\mu)}{\partial \mu^r}\mathbb{U}_s(\mu) \tag{147}$$

For $b_{p,k}^{E,h}(\mu_i)$ and $b_{z,k'}^{V,h}(\mu_i)$, we take the derivative of equations (114) and (116), respectively:

$$a_i\left(\frac{\partial b_{p,k}^{E,h}\Big|_{\bar{\Omega}_i}}{\partial \mu^r}, v; \mu_i\right) = -\frac{\partial a_i}{\partial \mu^r}\left(b_{p,k}^{E,h}\Big|_{\bar{\Omega}_i}, v; \mu_i\right) - \frac{\partial a_i}{\partial \mu^r}\left(\Psi_{p,k}^{E,h}\Big|_{\bar{\Omega}_i}, v; \mu_i\right), \quad \forall v \in B_{i;0}^h \tag{148}$$

and

$$a_i\left(\frac{\partial\, b_{z,k'}^{V,h}\Big|_{\bar{\Omega}_i}}{\partial \mu^r}, v; \mu_i\right) = -\frac{\partial a_i}{\partial \mu^r}\left(b_{z,k'}^{V,h}\Big|_{\bar{\Omega}_i}, v; \mu_i\right) - \frac{\partial a_i}{\partial \mu^r}\left(\Psi_{z,k'}^{V,h}\Big|_{\bar{\Omega}_i}, v; \mu_i\right), \quad \forall v \in B_{i;0}^h \tag{149}$$

For $b_i^{f;h}(\mu)$, we take the derivative of equations (122):

$$a_i\left(\frac{\partial b_i^{f;h}(\mu)}{\partial \mu^r}, v; \mu\right) = -\frac{\partial a_i}{\partial \mu^r}\left(b_i^{f;h}(\mu), v; \mu\right) + \frac{\partial f_i(v;\mu)}{\partial \mu^r}, \quad \forall v \in B_{\mathcal{G}(i);0}^h \tag{150}$$

There are several things to note about underlying terms, $\dfrac{\partial \mathbb{K}_{uu}(\mu)}{\partial \mu^r}$ and $\dfrac{\partial \mathbb{F}_u(\mu)}{\partial \mu^r}$:

- Provided that μ^r does not come from the auxiliary parameter set, the contributions from each local component to these terms are non-zero only when the derivative is taken with respect to one of the component's local parameters.
- If this is not the case, then $\dfrac{\partial \mathbb{F}_u(\mu)}{\partial \mu^r}$ has contributions from all components on which the boundary traction is applied, while the term $\dfrac{\partial \mathbb{K}_{uu}(\mu)}{\partial \mu^r}$ vanishes.
- The contribution from each local component to $\dfrac{\partial \mathbb{K}_{uu}(\mu)}{\partial \mu^r}$ is dependent on $\dfrac{\partial\, b_{p,k}^{E,h}\Big|_{\bar{\Omega}_i}}{\partial \mu^r}$ and $\dfrac{\partial\, b_{z,k'}^{V,h}\Big|_{\bar{\Omega}_i}}{\partial \mu^r}$.

In the case where the traction applied to the component during a given function call is not parametric, each component produces $\mathbb{K}^i_{uu}(\mu_i)$, $\mathbb{F}^i(\mu_i)$ and $p_{\mathcal{G}(i)}$ pairs of derivatives, $\frac{\partial \mathbb{K}^i_{uu}(\mu_i)}{\partial \mu^r}$ and $\frac{\partial \mathbb{F}^i(\mu_i)}{\partial \mu^r}$. Recall that $p_{\mathcal{G}(i)}$ is the number of parameters on component i. If the traction is parametric, then there are the additional terms for $\frac{\partial \mathbb{F}(\mu)}{\partial \mu^r}$ corresponding to the number of auxiliary parameters defining the traction.

5.4 Model Order Reduction Applied To Static Condensation Procedure

The novelty of the SCRBE procedure is that it took the traditional static condensation procedure and expedited it. This was achieved by finding subspaces of the function spaces already introduced that provide more concise linear algebraic systems to be solved locally and also globally. In this context, one seeks to find approximation subspaces that can concisely represent the state variable and its derivative on the global interfaces and on the interior of the components. In this work, we seek function subspaces that are hierarchical and can represent the state variable and its derivatives with the same orthonormal basis. The hierarchical property is important because it facilitates varying the fidelity of the approximations so that trade-offs can be made between solution accuracy and computational cost.

The process by which the edge modes, $\chi^E_{p,k}$, are determined will be described in section 5.5. We now seek to determine the reduced bubble solution corresponding to each of the global interface mode extensions into the interior of each component domain. The dimension of the original finite element space on the interior of each component, $\mathcal{N}_{b_i}$, is expected to be very large and does not facilitate efficient computation. In the original papers in the SCRBE literature, empirical bubble subspaces were developed to represent the state variable induced by each of the mode extensions into the interior of each of the component domains. For the present work, we seek bubble subspaces that can represent both the state variable and its derivative induced

by each interface mode extension on the interior of component i. We refer to these bubble subspaces as: $\widetilde{B}^E_{p,k}\Big|_{\bar{\Omega}_i}$ and $\widetilde{B}^V_{z,k'}\Big|_{\bar{\Omega}_i}$ for the global edge mode extensions and global vertex extensions, respectively. The manner in which these bubble spaces will be produced is described in section 5.5.0.7.

Using these bubble spaces, we redefine the state equations ((114) and (116)) as:

$$a_i\left(\widetilde{b}^{E,h}_{p,k}\Big|_{\bar{\Omega}_i}, v; \mu\right) = -a_i\left(\Psi^{E,h}_{p,k}\Big|_{\bar{\Omega}_i}, v; \mu\right), \quad \forall v \in \widetilde{B}^E_{p,k}\Big|_{\bar{\Omega}_i} \tag{151}$$

$$a_i\left(\widetilde{b}^{V,h}_{z,k'}\Big|_{\bar{\Omega}_i}, v; \mu\right) = -a_i\left(\Psi^{V,h}_{z,k'}\Big|_{\bar{\Omega}_i}, v; \mu\right), \quad \forall v \in \widetilde{B}^V_{z,k'}\Big|_{\bar{\Omega}_i} \tag{152}$$

and their derivatives ((148) and (149)) as:

$$a_i\left(\frac{\partial \widetilde{b}^{E,h}_{p,k}\Big|_{\bar{\Omega}_i}}{\partial \mu^r}, v; \mu_i\right) = -\frac{\partial a_i}{\partial \mu^r}\left(\widetilde{b}^{E,h}_{p,k}\Big|_{\bar{\Omega}_i}, v; \mu_i\right) - \frac{\partial a_i}{\partial \mu^r}\left(\Psi^{E,h}_{p,k}\Big|_{\bar{\Omega}_i}, v; \mu_i\right), \ \forall v\ \widetilde{B}^E_{p,k}\Big|_{\bar{\Omega}_i} \tag{153}$$

$$a_i\left(\frac{\partial\, \widetilde{b}^{V,h}_{z,k'}\Big|_{\bar{\Omega}_i}}{\partial \mu^r}, v; \mu_i\right) = -\frac{\partial a_i}{\partial \mu^r}\left(\widetilde{b}^{V,h}_{z,k'}\Big|_{\bar{\Omega}_i}, v; \mu_i\right) - \frac{\partial a_i}{\partial \mu^r}\left(\Psi^{V,h}_{z,k'}\Big|_{\bar{\Omega}_i}, v; \mu_i\right), \ \forall v \in \widetilde{B}^V_{z,k'}\Big|_{\bar{\Omega}_i} \tag{154}$$

These equations lead to the modified fundamental solutions:

$$\widetilde{\Phi}^E_{p,k}\Big|_{\bar{\Omega}_i} = \Psi^E_{p,k}|_{\bar{\Omega}_i} + \widetilde{b}^{E,h}_{p,k}\Big|_{\bar{\Omega}_i} \tag{155}$$

$$\widetilde{\Phi}^V_{z,k'}\Big|_{\bar{\Omega}_i} = \Psi^V_{z,k'}|_{\bar{\Omega}_i} + \widetilde{b}^{V,h}_{z,k}\Big|_{\bar{\Omega}_i} \tag{156}$$

5.4.0.1 Model Reduced Schur Complement

Using the reduced bubble spaces (eqs. (151) and (152)) and reduced fundamental solutions ((155) and (156)), we can now define the reduced global solution:

$$\widetilde{u}(\mu) = \sum_{p=1}^{n^E}\sum_{k=1}^{\mathcal{N}^{E_p}} \widetilde{\mathbb{U}}_{p,k}(\mu)\,\widetilde{\Phi}^E_{p,k} + \sum_{z=1}^{n^V}\sum_{k'=1}^{\mathcal{N}^{V_z}} \widetilde{\mathbb{U}}_{z,k'}(\mu)\,\widetilde{\Phi}^V_{z,k'} + \sum_{i=1}^{N_c}\widetilde{b}^f_i \tag{157}$$

Using the global solution and $\mathcal{S}_{\text{asymm}}$ to perform the Petrov-Galerkin procedure to define the updated global equations:

$$a\left(\widetilde{\Phi}(\mu),v;\mu\right)\widetilde{u}_s(\mu)=f\left(v;\mu\right)-\sum_{i=1}^{N_c}a_i\left(\widetilde{b}_i^f(\mu),v;\mu\right),\quad\forall v\in\mathcal{S}_{\text{asymm}}\left(\Omega\right)\tag{158}$$

with the discrete form being:

$$\widetilde{\mathbb{K}}_{uu}(\mu)\widetilde{\mathbb{U}}_s(\mu)=\widetilde{\mathbb{F}}_u(\mu)\tag{159}$$

where

$$\widetilde{\mathbb{K}}^i_{uu,((m,k),(m',k'))}(\mu_i)=\frac{1}{2}a_i\left(\widetilde{\Psi}^g_{m,k}\Big|_{\bar{\Omega}_i},\Phi^{g',h}_{m',k'}\Big|_{\bar{\Omega}_i};\mu_i\right)+\frac{1}{2}a_i\left(\widetilde{\Phi}^g_{m,k}\Big|_{\bar{\Omega}_i},\Psi^{g',h}_{m',k'}\Big|_{\bar{\Omega}_i};\mu_i\right)\tag{160}$$

$$\widetilde{\mathbb{F}}^i_{u,(m',k')}(\mu_i)=f\left(\Psi^{g,h}_{m',k'}\Big|_{\bar{\Omega}_i};\mu_i\right)-a\left(\widetilde{b}_i^f(\mu_i),\Psi^{g,h}_{m',k'}\Big|_{\bar{\Omega}_i};\mu_i\right)\tag{161}$$

The derivative of the Schur complement takes the form:

$$\widetilde{\mathbb{K}}_{uu}(\mu)\frac{\partial\widetilde{\mathbb{U}}_s(\mu)}{\partial\mu^r}=\frac{\partial\widetilde{\mathbb{F}}_u(\mu)}{\partial\mu^r}-\frac{\partial\widetilde{\mathbb{K}}_{uu}(\mu)}{\partial\mu^r}\widetilde{\mathbb{U}}_s(\mu)\tag{162}$$

Note that in addition to the terms that $\widetilde{\mathbb{K}^i}_{uu}(\mu)$ depends on, $\dfrac{\partial\widetilde{\mathbb{K}^i}_{uu}(\mu)}{\partial\mu^r}$ also depends on $\dfrac{\partial\widetilde{b}^E_{p,k}}{\partial\mu^r}$ and $\dfrac{\widetilde{b}^V_{z,k'}}{\partial\mu^r}$.

5.4.0.2 Reduced versions of the constraints and their derivative

Using the reduced versions of the bubble solutions induced by interface mode extensions, the reduced parametric mappings for expressing the state variable on the interior a component i can be represented as:

$$\widetilde{U}^i_b:\ \mathcal{D}_{\mathcal{G}(i)}\times\mathbb{R}^{\mathcal{N}_{sc}}\rightarrow\mathbb{R}^{\mathcal{N}_{b_i}}\tag{163}$$

Using this mapping (eq. 163); the parameter independent mapping (eq. 133); and the reduced Schur complement solution, $\widetilde{\mathbb{U}}_s$; the solution on the interior of the component can be represented as:

$$\widetilde{U}(\mu)\Big|_{\Omega_{i,GQ}}=\left[\bar{U}^i_{b,GQ}+\widetilde{U}^i_{b,GQ}(\mu_i)\right]\widetilde{\mathbb{U}}_s(\mu)+\widetilde{b}^f_{i,GQ}(\mu)\tag{164}$$

The reduced order variant of the bound constraints can then be represented as:

$$\widetilde{\widetilde{c}}_{IE} = \widetilde{\widetilde{c}}_{IE}\left(\rho, g\left(\widetilde{U}(\mu_i)\Big|_{\Omega_{i,GQ}}\right), \mu\right) \tag{165}$$

while the reduced edge loads are:

$$\widetilde{N}^{\Gamma_v}_{xx,\text{avg}} = \widetilde{N}^{\Gamma_v}_{xx,\text{avg}}\left(\widetilde{U}(\mu_i)\Big|_{\Omega_{i,GQ}}, \mu\right) \tag{166}$$

$$\widetilde{N}^{\Gamma_v}_{yy,\text{avg}} = \widetilde{N}^{\Gamma_v}_{yy,\text{avg}}\left(\widetilde{U}(\mu_i)\Big|_{\Omega_{i,GQ}}, \mu\right) \tag{167}$$

$$\widetilde{N}^{\Gamma_v}_{xy,\text{avg}} = \widetilde{N}^{\Gamma_v}_{xy,\text{avg}}\left(\widetilde{U}(\mu_i)\Big|_{\Omega_{i,GQ}}, \mu\right) \tag{168}$$

The derivatives of the bound constraint is:

$$\frac{d\widetilde{\widetilde{c}}_{IE}}{d\mu^r} = \frac{\partial\widetilde{\widetilde{c}}_{IE}}{\partial\mu^r} + \frac{\partial\widetilde{\widetilde{c}}_{IE}}{\partial\,\widetilde{U}(\mu)\Big|_{\Omega_{i,GQ}}}\frac{\partial\,\widetilde{U}(\mu)\Big|_{\Omega_{i,GQ}}}{\partial\mu^r} \tag{169}$$

and for the edge loads, the derivatives are:

$$\frac{d\widetilde{N}^{\Gamma_v}_{xx,\text{avg}}}{d\mu^r} = \frac{\partial\widetilde{N}^{\Gamma_v}_{xx,\text{avg}}}{\partial\mu^r} + \frac{\partial\widetilde{N}^{\Gamma_v}_{xx,\text{avg}}}{\partial\,\widetilde{U}(\mu)\Big|_{\Omega_{i,GQ}}}\frac{\partial\,\widetilde{U}(\mu)\Big|_{\Omega_{i,GQ}}}{\partial\mu^r} \tag{170}$$

$$\frac{d\widetilde{N}^{\Gamma_v}_{yy,\text{avg}}}{d\mu^r} = \frac{\partial\widetilde{N}^{\Gamma_v}_{yy,\text{avg}}}{\partial\mu^r} + \frac{\partial\widetilde{N}^{\Gamma_v}_{yy,\text{avg}}}{\partial\,\widetilde{U}(\mu)\Big|_{\Omega_{i,GQ}}}\frac{\partial\,\widetilde{U}(\mu)\Big|_{\Omega_{i,GQ}}}{\partial\mu^r} \tag{171}$$

$$\frac{d\widetilde{N}^{\Gamma_v}_{xy,\text{avg}}}{d\mu^r} = \frac{\partial\widetilde{N}^{\Gamma_v}_{xy,\text{avg}}}{\partial\mu^r} + \frac{\partial\widetilde{N}^{\Gamma_v}_{xy,\text{avg}}}{\partial\,\widetilde{U}(\mu)\Big|_{\Omega_{i,GQ}}}\frac{\partial\,\widetilde{U}(\mu)\Big|_{\Omega_{i,GQ}}}{\partial\mu^r} \tag{172}$$

where:

$$\frac{\partial\,\widetilde{U}(\mu)\Big|_{\Omega_{i,GQ}}}{\partial\mu^r} = \left[\bar{U}^i_{b,GQ} + \widetilde{U}^i_{b,GQ}(\mu_i)\right]\frac{\partial\widetilde{\mathbb{U}}_s(\mu)}{\partial\mu^r} + \frac{\partial\widetilde{U}^i_{b,GQ}(\mu_i)}{\partial\mu^r}\widetilde{\mathbb{U}}_s(\mu) + \frac{\partial\widetilde{b}^f_{i,GQ}(\mu)}{\partial\mu^r} \tag{173}$$

5.4.1 Empirical Mode Training - Research Question 1 (RQ1)

Attention is now turned to the task of determining edge subspaces that can concisely represent the state variable and its derivatives on the interfaces of the problem

domain. In previous work in the SCRBE literature, the focus has been on approximating the state variable of a problem and then calculating the outputs that depend on it. However, the general reduced order modeling literature suggests that an empirical subspace trained specifically for the state variable of a problem is not sufficient to also represent its derivatives when the direct method is used to calculate them [138, 139]. This then leads to the first research question.

Research Question 1.0 (RQ1.0): What is a suitable method for determining empirical edge subspaces that can concisely approximate the state variable and its derivatives on the component interfaces?

5.5 Empirical Modes For Edge Spaces

5.5.0.1 Overview

The "configuration agnostic" feature of the SCRBE method provides great versatility when modeling a wide variety of problem domains with only a handful of reference components. However, with this feature comes the difficulty of anticipating the possible state variables that will have to approximated on the component interfaces for a wide variety of problem setups. To address this problem, Eftang [81,99,109] proposed a heuristic algorithm to simulate various scenarios that a global interface might be exposed to when it is included into configurations. The procedures in this section follow this type of approach. There is the need to simulate the state variable and its derivatives on an interface within a generic assembly of components and then to determine an empirical subspace to approximate them.

5.5.0.2 Testing Apparatus

Figures 41 and 42 illustrate the testing domains that will be considered. However, note that we are not restricted to global domains of the type shown in figure 41 (i.e. a simple rectangular grid). The figure's purpose is merely to illustrate an example

of how the testing domains can be extracted from large scale systems. Other possible testing domains can be devised depending on the anticipated connectivity of components in a local sense.

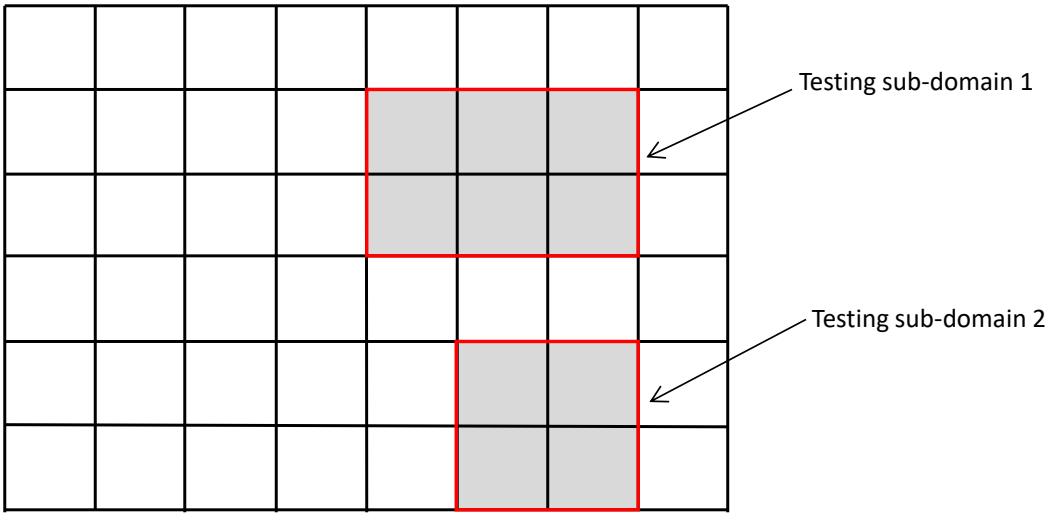

Figure 41: Testing subdomains within the global problem domain

The testing domains are comprised of components that are compatible with each other at their interfaces. Each component has its own parameter set μ_i. For the testing domains considered in this problem, the global edge that is of interest, E, is highlighted for clarity. The boundary of the testing domain is subjected to arbitrary Dirichlet boundary conditions and consistent with the work of Eftang, this is done by using Legendre polynomials as the basis for the arbitrary displacement specification. Modifications have to be made for more complex, two dimensional boundaries (i.e. faces) with complex geometry. This takes the form:

$$u_k(\mu) = \sum_{\varphi=1}^{n_\alpha} \alpha_\varphi(\mu)\phi_\varphi(\Gamma) \tag{174}$$

where $\{\phi_1(\Gamma), \phi_2(\Gamma), \phi_3(\Gamma), \dots\}$ are the Legendre polynomials prescribed on the boundary segment of interest, Γ. Similar to the work of Eftang, the coefficients of the expansion, $\alpha_\varphi(\mu)$, are chosen as the controlling parameters of the approximation of the

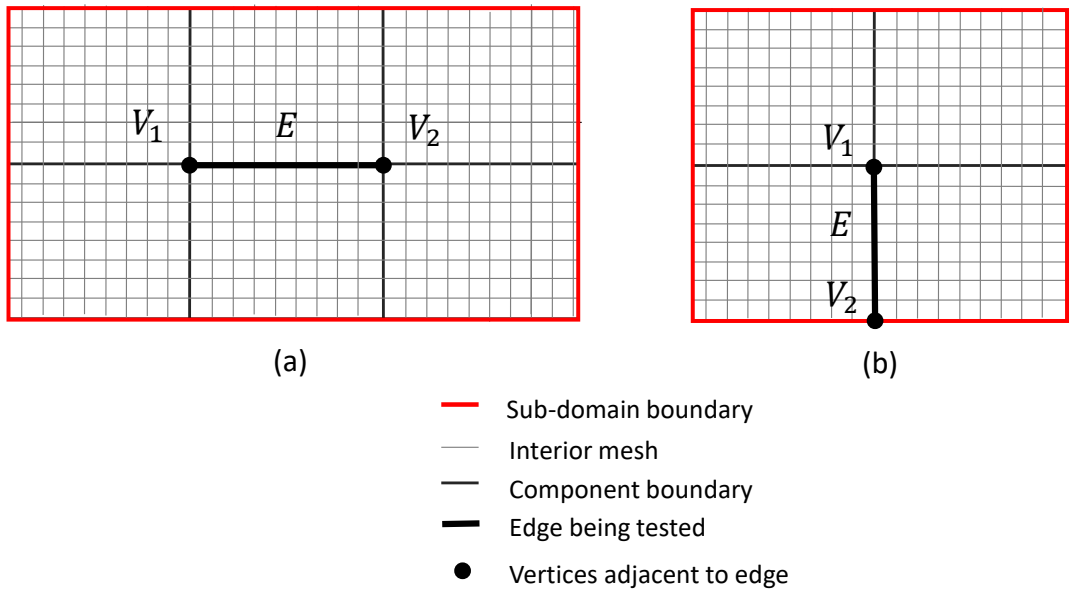

Figure 42: Testing subdomains for the empirical edge modes

Dirichlet boundary condition. The maximum absolute value allowed for each coefficient is lowered as $\wp$ increases. This is done to bias the approximation to the first few modes of the linear expansion.

Depending on the problem being solved, suitable traction forces can also be applied to the interior of the problem domain. Using both of these sources of inhomogeneity to the underlying partial differential equation, we seek to simulate state variable and its derivatives that will be on the identified edge in a general application. Note that we not only have to simulate the derivatives of the state variable with respect to the local parameters, but also with respect to the parameters beyond the testing domain.

5.5.0.3 Linear Algebraic System - State Variable

The linear algebraic system to be solved for the state variable on the global problem domain is:

$$Ku = f \tag{175}$$

Here, K corresponds to the stiffness matrix of the entire problem domain, u is the discrete version of the state variable and f is the vector of forces applied to global problem domain. It should be noted that static condensation is not used here. The blocked linear algebraic system associated with the general global problem domain is:

$$\begin{bmatrix} K_{uu} & K_{uk} \\ K_{ku} & K_{kk} \end{bmatrix} \begin{Bmatrix} u_u \\ u_k \end{Bmatrix} = \begin{Bmatrix} f_u \\ f_k \end{Bmatrix} \tag{176}$$

The subscript u is used to represent the degrees of freedom on the interior of the test domain, while the degrees of freedom on the boundary of the the test domain and beyond are represented with the subscript k. It is assumed that u_k on the boundary of the test domain is known and is approximated by smooth test functions. Using this information, the stiffness matrix can be decomposed for an equation to solve for u. This is:

$$K_{uu}u_u + K_{uk}u_k = f_u \tag{177}$$

Rearranged we have:

$$K_{uu}u_u = f_u - K_{uk}u_k \tag{178}$$

Note that the terms K_{uu} and K_{uk} in equation (178) are only dependent on the parameters defined on the components within the testing domain, while f_u depends on parameters coming from the auxiliary parameters set. Using this setup, we can simulate the state variable induced for a variety of parameter settings on the interior of the test domain and Dirichlet boundary conditions on the boundary.

5.5.0.4 Linear Algebraic System - State Variable Derivatives

Except for the prescription of an optional traction on the interior of the test domain, f_u, the setup in the previous subsection is similar to the work proposed by Eftang. Attention is now turned to building on this platform to provide the data required to estimate the derivatives of the state variable. The process begins by taking the

derivative of equation 178:

$$\begin{bmatrix} K_{uu} & K_{uk} \\ K_{ku} & K_{kk} \end{bmatrix} \begin{Bmatrix} \dfrac{\partial u_u}{\partial \mu^r} \\ \dfrac{\partial u_k}{\partial \mu^r} \end{Bmatrix} = \begin{Bmatrix} \dfrac{\partial f_u}{\partial \mu^r} \\ \dfrac{\partial f_k}{\partial \mu^r} \end{Bmatrix} - \begin{bmatrix} \dfrac{\partial K_{uu}}{\partial \mu^r} & \dfrac{\partial K_{uk}}{\partial \mu^r} \\ \dfrac{\partial K_{ku}}{\partial \mu^r} & \dfrac{\partial K_{kk}}{\partial \mu^r} \end{bmatrix} \begin{Bmatrix} u_u \\ u_k \end{Bmatrix} \tag{179}$$

Similar to determining the state variable, it is assumed that u_k and $\dfrac{\partial u_k}{\partial \mu^r}$ are both known and can be approximated separately. Again, the choice of approximation is the use of Legendre polynomials with smoothness constraints at points where there are sharp changes in the boundary's topology (e.g. corners). Extracting the rows of equation (179) corresponding to these degrees of freedom $\dfrac{\partial u_u}{\partial \mu^r}$ and rearranging leads to:

$$K_{uu}\frac{\partial u_u}{\partial \mu^r} = \frac{\partial f_u}{\partial \mu^r} - \frac{\partial K_{uu}}{\partial \mu^r}u - \frac{\partial K_{uk}}{\partial \mu^r}u_k - K_{uk}\frac{\partial u_k}{\partial \mu^r} \tag{180}$$

In this equation, K_{uu}, K_{uk}, $\dfrac{\partial K_{uu}}{\partial \mu^r}$ and $\dfrac{\partial K_{uk}}{\partial \mu^r}$ only depend on the local parameters of the components within the testing domain. $\dfrac{\partial f_u}{\partial \mu^r}$ will only depend on auxiliary parameters coming from the set, $\mathcal{D}_{\text{aux}}$. As such, all of these terms vanish when the derivative is calculated with respect to parameters outside of the test domain. However, the term $\dfrac{\partial u_k}{\partial \mu^r}$ also depends on the far field components' parameters. Since the configuration outside of the test domain can be arbitrarily specified, the term $\dfrac{\partial u_k}{\partial \mu^r}$ will be treated as such.

5.5.0.5 Equations To Provide Simulation Data

Thanks to the linearity of equations (178) and (180), we define the following equations:

$$\text{SC1}: \quad K_{uu}\left(\mu|^{\text{dom}}\right) u_{s_1} = \quad -K_{uk}\left(\mu|^{\text{dom}}\right) u_k\left(\mu|^{\text{bnd}}\right) \tag{181}$$

$$\text{SC2}: \quad K_{uu}\left(\mu|^{\text{dom}}\right) u_{s_2} = \quad f_u\left(\mu|^{\text{aux}}\right) \tag{182}$$

$$\text{DC1}: \quad K_{uu}\left(\mu|^{\text{dom}}\right) \frac{\partial u_{d_1}}{\partial \mu^r} = \quad -\frac{\partial K_{uu}\left(\mu|^{\text{dom}}\right)}{\partial \mu^r} u_u - \frac{\partial K_{uk}\left(\mu|^{\text{dom}}\right)}{\partial \mu^r} u_k\left(\mu|^{\text{bnd}}\right) \tag{183}$$

$$\text{DC2}: \quad K_{uu}\left(\mu|^{\text{dom}}\right) \frac{\partial u_{d_2}}{\partial \mu^r} = \quad -K_{uk}\left(\mu|^{\text{dom}}\right) \frac{\partial u_k\left(\mu|^{\text{bnd}}\right)}{\partial \mu^r} \tag{184}$$

$$\text{DC3}: \quad K_{uu}\left(\mu|^{\text{dom}}\right) \frac{\partial u_{d_3}}{\partial \mu^r} = \quad \frac{\partial f_u\left(\mu|^{\text{aux}}\right)}{\partial \mu^r} \tag{185}$$

Here there parameter dependence of the known terms have been expressed. The parameters are:

- $\mu|^{\text{dom}}$ - The parameters corresponding to the components in the testing domain
- $\mu|^{\text{bnd}}$ - The parameters controlling the Dirichlet boundary conditions
- $\mu|^{\text{aux}}$ - The parameters controlling the force inhomogeneity applied to the domain

Correspondingly, the parameter domains associated with these parameters are, $\mathcal{D}|^{\text{dom}}_{\text{test}}$, $\mathcal{D}|^{\text{bnd}}_{\text{test}}$, and $\mathcal{D}|^{\text{aux}}_{\text{test}}$, respectively. These spaces have cardinality, p_{dom}, p_{bnd} and p_{aux}, respectively. In any of the algorithms that follow, the parameter sample set that is used for empirical mode training will be designated as Ξ. It consists of parameter samples taken from the Cartesian product of the test parameters spaces. For example, a parameter sample set defined as: $\Xi \in \mathcal{D}|^{\text{dom}}_{\text{test}} \times \mathcal{D}|^{\text{bnd}}_{\text{test}}$ simply means parameter samples formed by combining parameter samples taken from the subspaces $\mathcal{D}|^{\text{dom}}_{\text{test}}$ and $\mathcal{D}|^{\text{bnd}}_{\text{test}}$.

Using these five cases expressed in equations (181) to (185), we seek to find an empirical subspace for the state variable and its derivatives on the identified global edge. Since the same approximation approach is used for both u_k and $\dfrac{\partial u_k}{\partial \mu^r}$, the cases SC1 and DC2 should yield the same snapshot set. Thus, going forward, only one of these two cases will be used.

Finally, combining the state variable and its derivatives is a non-trivial task. Much of the literature that seek to combine the state variable and its derivatives seem to rely on heuristic methods [96, 97, 138, 139]. For the present problem, the approach taken by Schmidt et al. [138] will be used. In this paper, the data sets are scaled by a scaling approach and then using the weighted Proper Orthogonal Decomposition approach [140], an empirical basis is found for the data. We would like that each of the four remaining sample sets be represented well by the resulting empirical modes.

5.5.0.6 Edge Mode Training Algorithm

Algorithms will now be presented for determining the empirical subspace associated with the highlighted edge in the test domains. Before this, the Proper Orthogonal Decomposition (POD) procedure will be highlighted, as this is the basis for finding all of the empirical subspaces found throughout this work. The algorithm for performing the proper orthogonal decomposition is presented in algorithm 1.

Algorithm 1: Proper Orthogonal Decomposition (POD)

input : S, η_{tol}
output : X, η_{refine}
begin

- Perform SVD on the snapshot set: $[U, \Sigma, V] = \text{svd}(S)$
- Find $n : \text{argmin}_n \dfrac{\sigma_n}{\sigma_1} \leq \eta_{\text{tol}}$
- Get the empirical modes, $X = \{U_1, U_2, \ldots, U_n\} \subset U$
- Retain the normalized singular values for global tolerance refinement procedure, $\eta_{\text{refine}} = \{{}^{\sigma_1}/_{\sigma_1}, {}^{\sigma_2}/_{\sigma_1}, \ldots, {}^{\sigma_n}/_{\sigma_1}\}$

end

Often the choice for the tolerance function in literature for the POD procedure is $n : \text{argmin}_n \dfrac{\sum_{i=1}^{n} \sigma_i^2}{\sum_{i=1}^{n_s} \sigma_i^2} \geq 1 - \eta_{\text{tol}}$, where n_s is the number of snapshots used. This can be used as an alternative to the choice used in algorithm 1. Algorithm 2 corresponds

to extracting the portions of the state variable or its derivative on a given global edge, that need to approximated by the edge function space. This is done simply by realizing that the representation of the vertex modes must be equal to the state variable at V_1 and V_2, while the representation by the empirical edge modes should vanish at both locations.

Algorithm 2: Remove Vertex Mode Contributions (**RVMC**)

input : $u_{\bar{E}}, \left\{\chi^V_{1,1}, \ldots, \chi^V_{1,\mathcal{N}_{V_1}}\right\}, \left\{\chi^V_{2,1}, \ldots, \chi^V_{2,\mathcal{N}_{V_2}}\right\}$

output : u_{out}

begin

$$u_{\text{out}} = u_{\bar{E}} - \sum_{k=1}^{\mathcal{N}_{V_1}} \left\langle u_{\bar{E}}|_{V_1} \, , \, \chi^V_{1,k}\big|_{V_1} \right\rangle \chi^V_{1,k}\big|_{\bar{E}} - \sum_{k'=1}^{\mathcal{N}_{V_2}} \left\langle u_{\bar{E}}|_{V_2} \, , \, \chi^V_{2,k'}\big|_{V_2} \right\rangle \chi^V_{2,k'}\big|_{\bar{E}}$$

end

Algorithm 3: State Solution 1 Sample (**SS1S**)

input : $\Xi \in \mathcal{D}|^{\text{dom}}_{\text{test}} \times \mathcal{D}|^{\text{bnd}}_{\text{test}}$

output : S_1

begin

Initialize: $S_1 = \emptyset$;

foreach $\mu \in \Xi$ **do**

- Solve eq. (181)
- Extract the solution on the tested edge, i.e. $u_{\bar{E}} = u_{s1}|_{V_1 \bigcup E \bigcup V_2}$
- $S_1 = \{S_1 \bigcup u_{\bar{E}}\}$

end

end

The next step is to furnish the data required to determine the empirical subspaces on the global edges. Algorithms 3 through 6 are used to provide the snapshot data needed to create the empirical modes. The weighted Proper Orthogonal Decomposition is then used to combine the snapshot sets. This is algorithm 7. The weights, $\boldsymbol{W} = \{w_1, w_2, \ldots, w_n\}$ are such that $w_i \in [0, 1]$. In the work of Schmidt et al. [138], they noted that the w_i's are chosen by the experimenter and can be used to take into

Algorithm 4: State Solution 2 Sample (**SS2S**)

input : $\Xi \in \mathcal{D}|_{\text{test}}^{\text{dom}} \times \mathcal{D}|_{\text{test}}^{\text{aux}}$
output : S_2
begin
  Initialize: $S_2 = \emptyset$;
  foreach $\mu \in \Xi$ **do**
    - Solve eq. (182)
    - Extract the solution on the tested edge i.e. $u_{\bar{E}} = u_{s2}|_{V_1 \bigcup E \bigcup V_2}$
    - $S_2 = \{S_2 \bigcup u_{\bar{E}}\}$
  end
end

consideration that the gradient of the state variable is a function of the state variable itself. With this realization, w_i can be set to $w_i < 1$, if desired.

For the case where the state solution is vector valued field one empirical subspace is created for each degree of the freedom in the vector field. For example, in a planar solid mechanics problem, the in-plane displacement field $u = \{u_1, u_2\}$ is vector valued. Separate empirical subspaces are created for u_1 and for u_2. The number of degrees of freedom in the vector valued field is d.

Finally, algorithms 1 through 7 are then used in algorithm 8 to create the empirical edge subspace for the global edge being investigated.

5.5.0.7 Bubble Space Training Approach

We now examine the bubble spaces found through the various steps of the model reduction formulation. As mentioned in section 5.4, the empirical subspaces will be built for both the bubble spaces and their derivatives on each local component. To this end, three algorithms are provided for creating the empirical subspaces associated with the bubble solutions of the problem. A parameter sample set is generated for the archetype component being tested. The archetype component is instantiated and

Algorithm 5: Derivative Solution 1(a)(**DSS1A**)

input : $\Xi \in \mathcal{D}|_{\text{test}}^{\text{dom}} \times \mathcal{D}|_{\text{test}}^{\text{aux}} \times \mathcal{D}|_{\text{test}}^{\text{bnd}} \times \mathcal{D}|_{\text{test}}^{\text{bnd}}$

output : $\{S_3, S_4, \ldots, S_{p_{\text{dom}}+2}\}$

begin

  for $r \leftarrow 1$ ***To*** p_{dom} **do**

    Initialize: $S_{r+2} = \emptyset$;

    foreach $\mu \in \Xi$ **do**

- Decompose: μ as $\left\{\mu|^{\text{dom}}, \mu|^{\text{aux}}, \mu|_1^{\text{bnd}}, \mu|_2^{\text{bnd}}\right\}$
- Using $\mu|^{\text{dom}}, \mu|^{\text{aux}}$ and $\mu|_1^{\text{bnd}}$, solve eq. (178) for u_u
- Using $\mu|^{\text{dom}}, \mu|_2^{\text{bnd}}$ and u_u solve eq. (183)
- Extract the sensitivity on the tested edge i.e. $\dfrac{\partial u_{\bar{E}}}{\partial \mu^r} = \left.\dfrac{\partial u_{d_1}}{\partial \mu^r}\right|_{V_1 \bigcup E \bigcup V_2}$
- $S_{r+2} = \left\{ S_{r+2} \bigcup \dfrac{\partial u_{\bar{E}}}{\partial \mu^r} \right\}$

    end

  end

end

the parameter sample set is represented as $\Xi \in \mathcal{D}_{\text{test}}^i$.

The first two algorithms, algorithm 9 and 10, correspond to training the subspaces for the interface mode extensions into the interior of the components. For a given component i, we consider the interface mode extensions for edges and vertices that are coincident to the boundary of the component.

The third algorithm, algorithm 11, corresponds to determining the empirical subspaces associated with the bubble solutions induced by tractions applied directly to the interior of the component. The algorithm is:

5.5.1 Empirical Mode Training - Hypothesis 1 (HYP1)

The work in the previous subsection leads to the following hypothesis.

Algorithm 6: Derivative Solution 1(b)(**DSS1B**)

input : $\Xi \in \mathcal{D}|_{\text{test}}^{\text{dom}} \times \mathcal{D}|_{\text{test}}^{\text{aux}}$
output : $\left\{S_{p^{\text{dom}}+3}, S_{p^{\text{dom}}+4}, \ldots, S_{p^{\text{dom}}+p^{\text{aux}}+2}\right\}$
begin
  for $r \leftarrow 1$ ***To*** p_{aux} **do**
    Initialize: $S_{p^{\text{dom}}+2+r} = \emptyset$;
    foreach $\mu \in \Xi$ **do**
      - Solve eq. 185
      - Extract the sensitivity on the tested edge i.e. $\dfrac{\partial u_{\bar{E}}}{\partial \mu^r} = \left.\dfrac{\partial u_{d_2}}{\partial \mu^r}\right|_{V_1 \bigcup E \bigcup V_2}$
      - $S_{p^{\text{dom}}+r+2} = \left\{ S_{p^{\text{dom}}+r+2} \bigcup \dfrac{\partial u_{\bar{E}}}{\partial \mu^r} \right\}$
    end
  end
end

HYP 1.0: Relative to the underlying finite element mesh, the use of the empirical edge subspaces and the associated empirical bubble spaces should lead to fast convergence of the estimated constraints and their derivatives as the model is refined.

5.6 Computational Procedures

The procedures for the offline and online computations required by the SCRBE approach will be highlighted in this section.

5.6.1 Offline Computational Procedures

The very first step in the SCRBE procedure is the creation of the empirical modes on the interfaces of the problem domain and on the interior of the constituent components. The procedure to create these modes are based on the algorithms that were already presented in sections 5.5.0.6 and 5.5.0.7.

Algorithm 7: Weighted Proper Orthogonal Decomposition (**wPOD**)

input : $\left\{S_1, S_2, \ldots, S_{p^{\text{dom}}+p^{\text{aux}}+2}\right\}$, $\boldsymbol{W} = \left\{w_1, w_2, \ldots, w_{p^{\text{dom}}+p^{\text{aux}}+2}\right\}$, η_{tol}
output : X, η_{tol}
begin
  Initialize: $S_{\text{comb}} = \emptyset$;
  for $i \leftarrow 1$ ***To*** $(p^{dom} + p^{aux} + 2)$ **do**
    weight $= 0$;
    for $j \leftarrow 1$ ***To*** $|S_i|$ **do**
      weight $=$ weight $+ \|S_{i,j}\|$
    end
    $S_{\text{comb}} = \left\{ S_{\text{comb}} \bigcup \frac{w_i |S_i|}{weight} S_i \right\}$;
  end
  $X = \textbf{POD}(S_{\text{comb}}, \eta_{\text{tol}})$
end

5.6.1.1 Offline Step 1 - Creation Of Empirical Modes

As previously stated, the edge modes are used in tandem with vertex modes to provide the approximations on the interfaces of the problem domain. The vertex modes of choice are the hat function that were described in section 5.3.3. For this work, a unique edge subspace is determined for each unique combination of component types surrounding a particular global edge, rather than combining them to form a singular edge subspace. Admittedly this approach leads to more storage overhead; however, it allows for terse subspaces tailored to a particular component configuration. For each unique combination of components surrounding a type of global edge, the test subdomains illustrated in figure 42 are created and subjected to algorithm 8.

The empirical edge subspaces and vertex modes are then used to create the interface mode extensions into the interior of the components adjacent to each global edge. This is represented by eq. (114) and (116), respectively. This procedure is carried out once for each combination of interface mode and archetype component that are incident to a global edge. Using the resulting interface mode extensions, the tailored

Algorithm 8: Get Edge Modes (**GetEdgeModes**)

input : $\{S_1, S_2, \dots\}, \boldsymbol{W}, \eta_{\text{tol}}, \left\{\chi^V_{1,1}, \dots, \chi^V_{1,\mathcal{N}_{V_1}}\right\}, \left\{\chi^V_{2,1}, \dots, \chi^V_{2,\mathcal{N}_{V_2}}\right\}$

output : X_{edge}, $1 \leq i \leq d$

begin

Initialize: $X_{\text{edge}} = \emptyset$;

for $i \leftarrow 1$ ***To*** d **do**

- Extract pure edge terms:
  - $S^i = \text{RVMC}\left(\{S^i_1, S^i_2, \dots\}, \left\{\chi^V_{1,1}, \dots, \chi^V_{1,\mathcal{N}_{V_1}}\right\}, \left\{\chi^V_{2,1}, \dots, \chi^V_{2,\mathcal{N}_{V_2}}\right\}\right)$
- $out = \boldsymbol{wPOD}(S^i, \boldsymbol{W}, \eta_{\text{tol}})$
- $\widetilde{X}_{\text{edge}} = X_{\text{edge}} \bigcup out$

end

end

bubble spaces for the bubble solution and its derivative are created for each interface mode defined on each global edge. The associated algorithms are 9 and 10. Finally, the empirical bubble spaces corresponding to the traction applied to the interior of each component is found by using algorithm 11.

5.6.1.2 Offline Step 2 - Creation Of Affine Components

The vertex modes, the empirical edge modes, and associated bubble subspaces are now used to create the affine matrices and vectors that are called during the online stage of the procedure. In order to facilitate understanding, the discrete versions of the equations developed in this chapter will be used.

5.6.1.3 Schur Complement: Coefficient Matrix And Interface Forces

We begin by writing the discrete for the coefficient matrix for the Schur complement:

$$\begin{Bmatrix} \boldsymbol{\Psi}|^{\text{bnd}}_{\bar{\Omega}_i} \\ \boldsymbol{\Psi}|^{\text{int}}_{\bar{\Omega}_i} \end{Bmatrix}^T \begin{bmatrix} K^i_{ee} & K^i_{eb} \\ K^{i,T}_{eb} & K^i_{bb} \end{bmatrix} \begin{Bmatrix} \boldsymbol{\Psi}|^{\text{bnd}}_{\bar{\Omega}_i} \\ \boldsymbol{\Psi}|^{\text{int}}_{\bar{\Omega}_i} + \boldsymbol{b}(\mu)|_{\bar{\Omega}_i} \end{Bmatrix} =$$

$$\underbrace{\begin{Bmatrix} \boldsymbol{\Psi}|^{\text{bnd}}_{\bar{\Omega}_i} \\ \boldsymbol{\Psi}|^{\text{int}}_{\bar{\Omega}_i} \end{Bmatrix}^T \begin{bmatrix} K^i_{ee} & K^i_{eb} \\ K^{i,T}_{eb} & K^i_{bb} \end{bmatrix} \begin{Bmatrix} \boldsymbol{\Psi}|^{\text{bnd}}_{\bar{\Omega}_i} \\ \boldsymbol{\Psi}|^{\text{int}}_{\bar{\Omega}_i} \end{Bmatrix}}_{\text{term 1}} + \underbrace{\begin{Bmatrix} \boldsymbol{\Psi}|^{\text{bnd}}_{\bar{\Omega}_i} \\ \boldsymbol{\Psi}|^{\text{int}}_{\bar{\Omega}_i} \end{Bmatrix}^T \begin{bmatrix} K^i_{ee} & K^i_{eb} \\ K^{i,T}_{eb} & K^i_{bb} \end{bmatrix} \begin{Bmatrix} 0 \\ \boldsymbol{b}(\mu)|_{\bar{\Omega}_i} \end{Bmatrix}}_{\text{term 2}} \tag{186}$$

The term K^i corresponds to the stiffness matrix defined on the finite element mesh of the component. The subscripts e and b represent the degrees of freedom on the interface and interior of component i, respectively. $\boldsymbol{\Psi}|_{\bar{\Omega}_i}$ is used to represent the collection of interface mode extensions that are incident to component i. Consequently, $\boldsymbol{\Psi}|^{\text{bnd}}_{\bar{\Omega}_i}$ and $\boldsymbol{\Psi}|^{\text{int}}_{\bar{\Omega}_i}$ are used to refer to the restriction of the extensions to the boundary and the interior of component i, respectively. Finally, $\boldsymbol{b}(\mu)|_{\bar{\Omega}_i}$ is used to refer to all of the bubble solutions that are induced by the interface mode extensions, $\boldsymbol{\Psi}|_{\bar{\Omega}_i}$.

Term 1 in the representation has a simple parametric relationship. The interface mode extensions for the component are used to transform the parameter independent terms in the affine representation for the component's stiffness matrix. The resulting reduced, parameter-independent affine matrices need to calculated only once and stored. It should also be noted that several of affine terms are symmetric. This can and should be taken advantage of for concise offline storage and expedient online assembly.

Term 2 is a little more challenging. It depends on the bubble solutions induced by the interface mode extensions. These bubble solutions do not have affine parametric dependence and must be solved each time there is a parametric change for the component. This is done by solving the discrete versions of eq. (151) and eq. (152) (and eq. (153) and (154) for the derivative, respectively). If bubble solutions were to be determined by the use of the finite element bubble space defined on the component,

then the equation to be solved would take the form:

$$K^i_{bb}\,\boldsymbol{b}(\mu)|_{\bar{\Omega}_i} = -K^i_{bb}\,\boldsymbol{\Psi}|^{\text{int}}_{\bar{\Omega}_i} - K^i_{be}\,\boldsymbol{\Psi}|^{\text{bnd}}_{\bar{\Omega}_i} \tag{187}$$

However, in the SCRBE approach, instead of solving eq. (187) in one step, a reduced bubble subspace is created for each mode in the set $\boldsymbol{\Psi}|_{\bar{\Omega}_i}$ in order to expedite the solution. Using the reduced bubble spaces, $\widetilde{X}^{b,E}_{p,k}\Big|_{\bar{\Omega}_i}$ and $\widetilde{X}^{b,V}_{z,k'}\Big|_{\bar{\Omega}_i}$, we have the following set of equations corresponding to eqs (151) - (154):

$$\left(\widetilde{X}^{b,E}_{p,k}\Big|_{\bar{\Omega}_i}{}^T K^i_{bb}\,\widetilde{X}^{b,E}_{p,k}\Big|_{\bar{\Omega}_i}\right)\widetilde{b}^{E,h}_{p,k}\Big|_{\bar{\Omega}_i} = -\widetilde{X}^{b,E}_{p,k}\Big|_{\bar{\Omega}_i}{}^T K^i_{bb}\,\Psi^{E,h}_{p,k}\Big|^{\text{int}}_{\bar{\Omega}_i} - \widetilde{X}^{b,E}_{p,k}\Big|_{\bar{\Omega}_i}{}^T K^i_{be}\,\Psi^{E,h}_{p,k}\Big|^{\text{bnd}}_{\bar{\Omega}_i} \tag{188}$$

and

$$\left(\widetilde{X}^{b,V}_{z,k'}\Big|_{\bar{\Omega}_i}{}^T K^i_{bb}\,\widetilde{X}^{b,V}_{z,k'}\Big|_{\bar{\Omega}_i}\right)\widetilde{b}^{V,h}_{z,k'}\Big|_{\bar{\Omega}_i} = -\widetilde{X}^{b,V}_{z,k'}\Big|_{\bar{\Omega}_i}{}^T K^i_{bb}\,\Psi^{V,h}_{z,k'}\Big|^{\text{int}}_{\bar{\Omega}_i} - \widetilde{X}^{b,V}_{z,k'}\Big|_{\bar{\Omega}_i}{}^T K^i_{be}\,\Psi^{V,h}_{z,k'}\Big|^{\text{bnd}}_{\bar{\Omega}_i} \tag{189}$$

The associated derivatives are, respectively:

$$\begin{aligned}\left(\widetilde{X}^{b,E}_{p,k}\Big|_{\bar{\Omega}_i}{}^T K^i_{bb}\,\widetilde{X}^{b,E}_{p,k}\Big|_{\bar{\Omega}_i}\right)\frac{\partial\,\widetilde{b}^{E,h}_{p,k}\Big|_{\bar{\Omega}_i}}{\partial\mu^r} = &-\left(\widetilde{X}^{b,E}_{p,k}\Big|_{\bar{\Omega}_i}{}^T \frac{\partial K^i_{bb}}{\partial\mu^r}\,\widetilde{X}^{b,E}_{p,k}\Big|_{\bar{\Omega}_i}\right)\widetilde{b}^{E,h}_{p,k}\Big|_{\bar{\Omega}_i} \\ &-\widetilde{X}^{b,E}_{p,k}\Big|_{\bar{\Omega}_i}{}^T \frac{\partial K^i_{bb}}{\partial\mu^r}\,\Psi^{E,h}_{p,k}\Big|^{\text{int}}_{\bar{\Omega}_i} - \widetilde{X}^{b,E}_{p,k}\Big|_{\bar{\Omega}_i}{}^T \frac{\partial K^i_{be}}{\partial\mu^r}\,\Psi^{E,h}_{p,k}\Big|^{\text{bnd}}_{\bar{\Omega}_i}\end{aligned} \tag{190}$$

and

$$\begin{aligned}\left(\widetilde{X}^{b,V}_{z,k'}\Big|_{\bar{\Omega}_i}{}^T K^i_{bb}\,\widetilde{X}^{b,Z}_{z,k'}\Big|_{\bar{\Omega}_i}\right)\frac{\partial\,\widetilde{b}^{V,h}_{z,k'}\Big|_{\bar{\Omega}_i}}{\partial\mu^r} = &-\left(\widetilde{X}^{b,V}_{z,k'}\Big|_{\bar{\Omega}_i}{}^T \frac{\partial K^i_{bb}}{\partial\mu^r}\,\widetilde{X}^{b,V}_{z,k'}\Big|_{\bar{\Omega}_i}\right)\widetilde{b}^{V,h}_{z,k'}\Big|_{\bar{\Omega}_i} \\ &-\widetilde{X}^{b,V}_{z,k'}\Big|_{\bar{\Omega}_i}{}^T \frac{\partial K^i_{bb}}{\partial\mu^r}\,\Psi^{V,h}_{z,k'}\Big|^{\text{int}}_{\bar{\Omega}_i} - \widetilde{X}^{b,V}_{z,k'}\Big|_{\bar{\Omega}_i}{}^T \frac{\partial K^i_{be}}{\partial\mu^r}\,\Psi^{V,h}_{z,k'}\Big|^{\text{bnd}}_{\bar{\Omega}_i}\end{aligned} \tag{191}$$

Due to the convenience of the affine representations, we only need to calculate and store the affine terms:

- $\widetilde{X}^{b,E}_{p,k}\Big|_{\bar{\Omega}_i}{}^T K^{i,q}_{bb}\,\widetilde{X}^{b,E}_{p,k}\Big|_{\bar{\Omega}_i}$
- $\widetilde{X}^{b,E}_{p,k}\Big|_{\bar{\Omega}_i}{}^T K^{i,q}_{bb}\,\Psi^{E,h}_{p,k}\Big|^{\text{int}}_{\bar{\Omega}_i} + \widetilde{X}^{b,E}_{p,k}\Big|_{\bar{\Omega}_i}{}^T K^{i,q}_{be}\,\Psi^{E,h}_{p,k}\Big|^{\text{bnd}}_{\bar{\Omega}_i}$
- $\widetilde{X}^{b,V}_{z,k'}\Big|_{\bar{\Omega}_i}{}^T K^{i,q}_{bb}\,\widetilde{X}^{b,Z}_{z,k'}\Big|_{\bar{\Omega}_i}$

- $\widetilde{X}^{b,V}_{z,k'}\Big|_{\bar{\Omega}_i}{}^T K^{i,q}_{bb}\ \Psi^{V,h}_{z,k'}\Big|^{\text{int}}_{\bar{\Omega}_i} + \widetilde{X}^{b,V}_{z,k'}\Big|_{\bar{\Omega}_i}{}^T K^{i,q}_{be}\ \Psi^{V,h}_{z,k'}\Big|^{\text{bnd}}_{\bar{\Omega}_i}$

Where index q is used to represent the q^{th} parameter independent term in the affine expansion of the component's stiffness matrix. The next set of quantities that need to be determined are those in term 2. Written with respect to the bubble solutions coming from the truth space of the component, this is:

$$\left(\boldsymbol{\Psi}|^{\text{int}^T}_{\bar{\Omega}_i} K^i_{bb} + \boldsymbol{\Psi}|^{\text{bnd}^T}_{\bar{\Omega}_i} K^{i,T}_{be}\right) \boldsymbol{b}(\mu)|_{\bar{\Omega}_i} \tag{192}$$

Using the model order reduction on the bubble spaces, the equations to be solved are:

$$\left(\boldsymbol{\Psi}|^{\text{int}^T}_{\bar{\Omega}_i} K^i_{bb} + \boldsymbol{\Psi}|^{\text{bnd}^T}_{\bar{\Omega}_i} K^{i,T}_{be}\right) \widetilde{X}^{b,E}_{p,k}\Big|_{\bar{\Omega}_i} \tag{193}$$

and

$$\left(\boldsymbol{\Psi}|^{\text{int}^T}_{\bar{\Omega}_i} K^i_{bb} + \boldsymbol{\Psi}|^{\text{bnd}^T}_{\bar{\Omega}_i} K^{i,T}_{be}\right) \widetilde{X}^{b,V}_{z,k'}\Big|_{\bar{\Omega}_i} \tag{194}$$

The affine terms that need to be stored are:

- $\left(\boldsymbol{\Psi}|^{\text{int}^T}_{\bar{\Omega}_i} K^{i,q}_{bb} + \boldsymbol{\Psi}|^{\text{bnd}^T}_{\bar{\Omega}_i} K^{i,q,T}_{be}\right) \widetilde{X}^{b,E}_{p,k}\Big|_{\bar{\Omega}_i}$
- $\left(\boldsymbol{\Psi}|^{\text{int}^T}_{\bar{\Omega}_i} K^{i,q}_{bb} + \boldsymbol{\Psi}|^{\text{bnd}^T}_{\bar{\Omega}_i} K^{i,q,T}_{be}\right) \widetilde{X}^{b,V}_{z,k'}\Big|_{\bar{\Omega}_i}$

Calculating the derivative of the coefficient matrix of the Schur complement can be trivially achieved by using the affine parametric dependence of the terms listed above.

In terms of the force term that is applied to the Schur complement, it is assumed that this term can be represented in an affine form, $f^i(\mu) = \sum_{q=1}^{Q_f} \theta^f(\mu)\bar{f}^{i,q}$. Using this representation, the forces on the interfaces can be represented as:

$$\boldsymbol{\Psi}|^{\text{int}^T}_{\bar{\Omega}_i} f^i_b(\mu) + \boldsymbol{\Psi}|^{\text{bnd}^T}_{\bar{\Omega}_i} f^i_e(\mu) = \sum_{q=1}^{Q_f} \theta^f_q(\mu) \left(\boldsymbol{\Psi}|^{\text{int}^T}_{\bar{\Omega}_i} f^{i,q}_b(\mu) + \boldsymbol{\Psi}|^{\text{bnd}^T}_{\bar{\Omega}_i} f^{i,q}_e(\mu)\right) \tag{195}$$

The terms $\left(\boldsymbol{\Psi}|^{\text{int}^T}_{\bar{\Omega}_i} f^{i,q}_b(\mu) + \boldsymbol{\Psi}|^{\text{bnd}^T}_{\bar{\Omega}_i} f^{i,q}_e(\mu)\right)$ are calculated and stored offline.

5.6.1.4 *Traction Induced Bubble Solution Terms*

The next set of terms to be determined are those that correspond to the traction induced bubble solutions on component i. The discrete form of eq. (122) is:

$$K_{bb} b^f = f_b^i; \tag{196}$$

The model reduced version, written with respect to the appropriate reduced order modes, $\widetilde{X}^{b,f}\Big|_{\bar{\Omega}_i}$, is:

$$\left(\widetilde{X}^{b,f}\Big|_{\bar{\Omega}_i}{}^T K_{bb}^i \widetilde{X}^{b,f}\Big|_{\bar{\Omega}_i} \right) \widetilde{b}^f = \widetilde{X}^{b,f}\Big|_{\bar{\Omega}_i}{}^T f_b^i \tag{197}$$

The affine terms that need to be calculated and stored are:

- $\left(\widetilde{X}^{b,f}\Big|_{\bar{\Omega}_i}{}^T K_{bb}^{i,q} \widetilde{X}^{b,f}\Big|_{\bar{\Omega}_i} \right)$
- $\widetilde{X}^{b,f}\Big|_{\bar{\Omega}_i}{}^T f_b^{i,q}$

The derivatives of the bubble solution, $\dfrac{\partial \widetilde{b}^f}{\partial \mu^r}$, are calculated using these same ingredients.

These bubble solutions also have a contribution to the inhomogeneity of the Schur complement equation. This takes the form:

$$\left(\boldsymbol{\Psi}|_{\bar{\Omega}_i}{}^T K_{be}^i{}^T \right) \widetilde{b}^f \tag{198}$$

Using the reduced bubble space associated with this bubble solution, the terms that need to be created and stored offline are:

$$\left(\boldsymbol{\Psi}|_{\bar{\Omega}_i}{}^T K_{be}^{i,q T} \right) \widetilde{X}^{b,f}\Big|_{\bar{\Omega}_i} \tag{199}$$

5.6.1.5 *Solution Recovery On The Interior Of The Component*

Finally, the retrieval of the state variable on the interior of each component is enabled by the two mappings (eq. (132) and (133)):

$$\begin{aligned} \bar{U}_b^i &= \boldsymbol{\Psi}|_{\bar{\Omega}_i} \\ U_b^i &= \boldsymbol{b}(\mu)|_{\bar{\Omega}_i} \end{aligned} \tag{200}$$

and by $b^{i,f}$. After introducing the model order reduction and the restriction operation to the nodes in the vicinity of the Gaussian quadrature points, the terms that need to be created and stored are: $\boldsymbol{\Psi}|_{\bar{\Omega}_i,GQ}$, $\widetilde{X}^{b,E}_{p,k}\Big|_{\Omega_i,GQ}$, $\widetilde{X}^{b,V}_{z,k'}\Big|_{\Omega_i,GQ}$, and $\widetilde{X}^{b,f}\Big|_{\Omega_i,GQ}$. The designation $\cdot|_{GQ}$ simply means that the corresponding terms are restricted to the aforementioned nodes close to the Gaussian integration points.

5.6.2 Online Computational Procedures And Computational Complexity

5.6.2.1 Refinement For Edge And Bubble Subspaces

The convenient feature about using hierarchical bases for the empirical edge and bubble subspaces is that smaller subspaces of these spaces can be formed by using a subset of the basis modes without the need for special modification. This is particularly convenient when it is desired to refine the sizes of the terms used in reduced model. In a similar fashion to the approach used by Eftang [109], the basis used for each empirical subspace will be segmented into active modes and inactive modes. The former modes consist of modes arising from the POD procedure that possess the most energy; whereas, the latter set of modes are the remaining modes used to round out the subspace. Using this decomposition, the model reduced terms can be partitioned to reflect this approach. As an example, consider the contribution of component i to the coefficient matrix of the Schur complement. The partitioning becomes:

$$\mathbb{K}^i_{uu} = \begin{bmatrix} \mathbb{K}^{i,AA}_{uu} & \mathbb{K}^{i,AI}_{uu} \\ \mathbb{K}^{i,IA}_{uu} & \mathbb{K}^{i,II}_{uu} \end{bmatrix} \tag{201}$$

A similar decomposition can be performed for the other terms depending on the edge modes and those depending on the bubble space modes. For the terms considered during the online procedures, only the entries that only correspond to the active modes need to be formed. For this work, the singular values obtained from the POD procedure are used to determine the number of active modes used for the approximations. To whit, two "fidelity parameters" are defined to globally control the number

of active modes. These are η_{edge} and η_{b}. These correspond to the tolerance for all of the edge and bubble spaces, respectively. The tolerances are based on the one defined in the POD algorithm; in that for each subspace, the minimum number of modes needed to satisfy the tolerance are retained.

5.6.2.2 Overview Of The Online Procedure

The terms described in the offline computational procedure allows for an efficient online procedure. These terms are mostly independent of the finite element mesh. The exception is evaluating the constraint constraints. However, due to the use of lower-order Gaussian quadrature, this should not be an overbearing concern. The following sections describe the steps that need to be taken during the online stage of the method. Throughout the presentation, a time complexity analysis is presented for each major step. In order to enable this analysis, the following terms are defined:

- $\mathcal{N}_E^{\max}$ - is the maximum number of edge mode degrees of freedom on any single global edge in the problem domain after the edge space refinement
- $\mathcal{N}_V^{\max}$ - is the maximum number of vertex mode degrees of freedom on any single global vertex in the problem domain
- n_b - is the maximum number of bubble modes associated with any single interface mode extensions used throughout the problem domain after the bubble space refinement
- n_b^f - is the maximum number of bubble modes associated with the traction induced bubble solution for any component in the problem domain after the bubble space refinement
- Q_K - The number of terms in the affine representation for K
- N_c - The number of components in the assembled problem domain
- $n_{\mu_i,\max}$ - The maximum number of parameters defined on any component in the problem domain.

For simplicity, it is assumed that each component has 4 local edges and 4 local vertices. Modifications can be trivially made in cases where this is not so. As such, for brevity, the term $\mathcal{N}_{\text{interface}} = 4(\mathcal{N}_E^{\max} + \mathcal{N}_V^{\max})$ is now introduced for more concise complexity analysis terms. This is the maximum number of interface modes defined on any component in the problem domain.

5.6.2.3 Online Step 1 - Schur Complement: Core Affine Matrices

As described in section 5.6.1.3, the formation of the coefficient matrix of the Schur complement can be performed in two major steps. Correspondingly, there are two terms (expressed in in eq. (186)) which need to be determined. During the online stage, term 1 can be expeditiously assembled for the coefficient matrix of the Schur complement and its derivative by using the associated affine decomposition. The computational complexity associated with this step is $O\left(N_c(n_{\mu_i,\max}+1)\left[Q_K\mathcal{N}_{\text{interface}}^2\right]\right)$.

5.6.2.4 Online Step 2 - Schur Complement: Solving For The Local Bubble Solutions

The first step in producing term 2 in equation (186) is to solve for $b_{p,k}^{E,h}\Big|_{\bar{\Omega}_i}$, $b_{z,k'}^{V,h}\Big|_{\bar{\Omega}_i}$ and their derivatives. These terms are also used in the parameter dependent mapping to recover the solution on the interior of each component (eq. 163) and its derivatives. The bubble solutions and their derivatives are found by solving equations (188) through (191) for each degree of freedom on each interface entity on each component. In solving for the bubble solution and its derivatives in each case, a single LU decomposition is performed on the shared coefficient matrix. This is followed by back-solving for the terms of interest using the right-hand sides. The overall computational complexity for this procedure is $O\left(N_c\mathcal{N}_{\text{interface}}\left[{}^2\!/_3 n_b^3 + Q_K(n_{\mu_i,\max}+1)n_b^2\right]\right)$.

5.6.2.5 *Online Step 3 - Schur Complement: Adding In The Bubble Solutions To Schur Complement*

Using the bubble solutions and their derivatives determined in the previous step, the model reduced version term 2 can now be computed. This is done with the aid of equations (193), (194) and their derivatives. The overall time complexity for performing this operation is $O\left(N_c(n_{\mu_i,\max}+1)\left[Q_K n_b \mathcal{N}^2_{\text{interface}}\right]\right)$.

The model reduced versions of terms 1, 2 and their derivatives are used to create asymmetric versions of the coefficient matrix of the Schur complement matrix and its derivatives. The symmetric versions are created by using the operation in eq. (131). The forces on the interface and their derivatives are determined by assembling the terms in eq. (195).

5.6.2.6 *Online Step 4 - Traction Induced Bubble Solutions*

The traction induced bubble solution and its derivatives are determined by eq. (197) and the appropriate derivatives of this equation. In the similar fashion to section 5.6.2.4, an LU decomposition is preformed for the coefficient stiffness matrix, followed by the back-solving procedure for the various right-hand sides required for calculating the bubble solution and its derivatives. The inhomogeneity introduced into the Schur complement is recovered by using eq. (198). The associated inhomogeneity for the derivative of the Schur complement can be trivially solved using these ingredients. The overall time complexity for solving for the bubble solution and its derivatives is: $O\left(N_c\left[{}^2\!/_3 n_b^{f\,3}+(n_{\mu_i,\max}+1)\left(Q^K n_b^{f\,2}+Q^f n_b^f\right)\right]\right)$. The overall time complexity for determining the inhomogeneities is: $O\left(N_c(n_{\mu_i,\max}+1)\left[Q_K n_b^f \mathcal{N}_{\text{interface}}\right]\right)$

5.6.2.7 *Online Step 5 - Schur Complement: Solving For The Schur Complement Solution And Its Derivatives*

The terms produced in Online steps 3 and 4 are used to produce equations (159) and (162). Since the coefficient matrix is the same in both equations, this allows for

the use of a technique that can solve linear algebraic systems with multiple right-hand sides for the same coefficient matrix. The coefficient matrix for the global Schur complement is sparse. This allows the use methods such as: (1) sparse LU decomposition of the coefficient matrix with back-solving for the multiple cases on the right-hand side. (2) The use of an indirect method that is adapted to solving multiple right-hand sides (e.g. [98]). Both approaches allow for cheaply determining the derivatives of the Schur complement solution. For this work, approach (1) was selected.

5.6.2.8 Online Step 6 - Recovering The Constraints and Their Derivatives

The final step in the online procedure is to recover the constraints and their derivatives over the problem domain. Before this can be done, the state variable and its derivatives have to be recovered on the interior of each component in the vicinity of the Gaussian quadrature sampling points. Using the outcomes provided in section 5.6.1.5, the state variable and its derivatives defined on the interior of the component domains can be approximated. The resulting terms are then used to estimate the constraints and their derivatives.

5.6.2.9 Overall Time Complexity For The Online Steps Associated With The Overhead

The overall computational complexity is:

$$O\left(N_c\left\{\mathcal{N}_{\text{interf.}}\left[{}^2\!/_3 n_b^3 + Q_K(n_{\mu_i,\max}+1)n_b^2\right] + \left[{}^2\!/_3 {n_b^f}^3 + (n_{\mu_i,\max}+1)\left(Q_K {n_b^f}^2 + Q_f n_b^f\right)\right]\right.\right.$$
$$\left.\left.+(n_{\mu_i,\max}+1)\left[Q_K n_b \mathcal{N}^2_{\text{interface}}\right] + (n_{\mu_i,\max}+1)\left[Q_K n_b^f \mathcal{N}_{\text{interface}}\right]\right\}\right) \quad (202)$$

The time complexity can be made to be more concise; however, it is left in this format so that the contributions from the various online sub-steps can be identified. This time complexity is very similar to the version presented by Huynh [104]. The main differences are the following:

- The factor $(n_{\mu_i,\max}+1)$ to account for the inclusion of the derivatives
- The first bracketed term above has an additional term, $Q_K(n_{\mu_i,\max}+1)n_b^2$, that is associated with solving for the derivative of the reduced bubble solutions.
- The third bracketed term, $(n_{\mu_i,\max}+1)Q_K n_b \mathcal{N}^2_{\text{interface}}$, is reduced by a factor of n_b because of the Petrov-Galerkin projection of the system's PDE.
- The inclusion of the terms that are dependent on the bubble solution induced by direct tractions

We can see from this time complexity that the overhead scales poorly when :

- The number of interface modes grows i.e. $\mathcal{N}_{\text{interface}} \to \infty$
- The affine representation of the bilinear operator are not concise $(Q_K \to \infty)$
- Bubble subspaces with large cardinalities $(n_b,\ \ n_b^f \to \infty)$.

5.7 Chapter Summary

In this chapter, the details of using the SCRBE method to estimate the constraints and their derivatives of the problem of interest were provided. This was followed by the proposal of an algorithm to determine edge subspaces for the concise approximation of the state variable and its derivatives on the interfaces. A summary of the steps during the offline and online procedures were also provided.

Algorithm 9: Empirical Bubble Spaces For The Edge Modes

input : $\Xi,\ \Psi_{p,k}^{E,h}\Big|_{\bar{\Omega}_i},\ \boldsymbol{W},\ \eta_{\text{tol}}$

output : $\widetilde{X}_{p,k}^{b,E}\Big|_{\bar{\Omega}_i},\ \ \eta_{\text{refine}}$

begin

Initialize: $S_1 = \emptyset$;

foreach μ *in* Ξ **do**

- Solve equation (114)
- $S_1 = \left\{ S_1 \bigcup b_{p,k}^{E,h}\Big|_{\bar{\Omega}_i} \right\}$

end

for $r \leftarrow 1$ ***To*** $p_{\mathcal{G}(i)}$ **do**

Initialize: $S_{r+1} = \emptyset$;

foreach μ *in* Ξ **do**

- Solve equation (148)
- $S_{r+1} = \left\{ S_{r+1} \bigcup \dfrac{\partial b_{p,k}^{E,h}\Big|_{\bar{\Omega}_i}}{\partial \mu^r} \right\}$

end

end

$[\widetilde{X}_{p,k}^{b,E}\Big|_{\bar{\Omega}_i}, \eta_{\text{refine}}] = \boldsymbol{wPOD}\left(\{S_1, S_2, \dots\}, \boldsymbol{W}, \eta_{\text{tol}}\right)$;

end

Algorithm 10: Empirical Bubble Spaces For The Vertex Modes

input : $\Xi,\ \Psi^{V,h}_{z,k'}\Big|_{\bar{\Omega}_i},\ \boldsymbol{W},\ \eta_{\text{tol}}$

output : $\widetilde{X}^{b,V}_{z,k'}\Big|_{\bar{\Omega}_i},\ \ \eta_{\text{refine}}$

begin

Initialize: $S_1 = \emptyset$;

foreach μ *in* Ξ **do**

- Solve equation (116)
- $S_1 = \left\{ S_1 \bigcup b^{Z,h}_{z,k'}\Big|_{\bar{\Omega}_i} \right\}$

end

for $r \leftarrow 1$ ***To*** $p_{\mathcal{G}(i)}$ **do**

Initialize: $S_{r+1} = \emptyset$;

foreach μ *in* Ξ **do**

- Solve equation (149)
- $S_{r+1} = \left\{ S_{r+1} \bigcup \dfrac{\partial b^{V,h}_{z,k}\Big|_{\bar{\Omega}_i}}{\partial \mu^r} \right\}$

end

end

$[\widetilde{X}^{b,V}_{z,k'}\Big|_{\bar{\Omega}_i}, \eta_{\text{refine}}] = \boldsymbol{wPOD}\left(\{S_1, S_2, \dots\}, \boldsymbol{W}, \eta_{\text{tol}}\right)$;

end

Algorithm 11: Empirical Bubble Spaces For Component Traction

input : Ξ, $\boldsymbol{W}$

output : $\widetilde{X}^{b,f}\Big|_{\bar{\Omega}_i}$, η_{refine}

begin

Initialize: $S_1 = \emptyset$;

foreach $\mu \in \Xi$ **do**

- Solve equation (122)
- $S_1 = \left\{ S_1 \bigcup b_i^{f;h}\Big|_{\bar{\Omega}_i} \right\}$

end

for $r \leftarrow 1$ ***To*** $p_{\mathcal{G}(i)}$ **do**

Initialize: $S_{r+1} = \emptyset$;

foreach $\mu \in \Xi$ **do**

- Solve equation (150)
- $S_{r+1} = \left\{ S_{r+1} \bigcup \dfrac{\partial b_i^{f;h}\Big|_{\bar{\Omega}_i}}{\partial \mu^r} \right\}$

end

end

$[\widetilde{X}^{b,f}\Big|_{\bar{\Omega}_i}, \eta_{\text{refine}}] = \boldsymbol{wPOD}(\{S_1, S_2, \dots\}, \boldsymbol{W}, \eta_{\text{tol}})$;

end

Chapter VI

SCRBE-DEIM APPROACH FOR GENERATING CONSTRAINTS

6.1 Chapter Overview

This chapter is concerned with addressing research questions 2 and 3. This is done by identifying places where adjustments can be made in the SCRBE procedure, in order to reduce the computational overhead associated with the method. For ease of reference, the research questions are restated here:

RQ 2.0: What is an alternative approach for generating the ingredients of the SCRBE procedure that will help to alleviate the computational overhead, while not drastically increasing the approximation error?

RQ 3.0: How do the SCRBE method and its surrogate compare in an optimization setting?

6.2 Identification Of Bottlenecks In The SCRBE Procedure

In chapter 5, a formulation was presented for determining typical, state-variable dependent, inequality constraints and their derivatives on a component using the SCRBE method. It was shown there that in furnishing these quantities, there is a certain level of independence among the components comprising the problem domain. In section 5.6.2.2, an overview was given for the computational complexity associated with the online stage of the SCRBE method, it was shown that in cases where the number of affine terms is not small (i.e. $Q \to \infty$) and when the cardinality of the bubble spaces are large, the overhead associated with SCRBE method is exacerbated.

Clearly, the overhead of the method comes from calculating the terms required from each component to calculate the Schur complement system and the outputs.

In this chapter, we will be examining the static condensation terms produced by only using the reduced modes on the interfaces in the static condensation procedure i.e. before model reduction is applied to the bubble spaces. These are the terms described in sections 5.3.5, 5.3.6 and 5.3.8. As such, the key terms that have to be provided by the components in the problem domain are:

- Stiffness matrix components: $\mathbb{K}^i_{uu}(\mu_i)$ and $\dfrac{\partial \mathbb{K}^i_{uu}(\mu_i)}{\partial \mu^r}$
- Force terms: $\mathbb{F}^i_u(\mu)$ and $\dfrac{\partial \mathbb{F}^i_u(\mu)}{\partial \mu^r}$
- Parameter-dependent solution recovery: $U^i_{b,GQ}(\mu_i)$ and $\dfrac{\partial U^i_{b,GQ}(\mu_i)}{\partial \mu^r}$
- Bubble solution due to traction on the interior of the component: $b^{f;h}_{i,GQ}(\mu)$ and $\dfrac{\partial b^{f;h}_{i,GQ}(\mu)}{\partial \mu^r}$

These terms are all nonlinear and have nonaffine parametric dependence. All terms are dependent on the local parameter set defined on the component. The force terms are also dependent on the auxiliary parameter set. All these terms readily accommodate the edge mode refinement procedure by the addition or deletion the relevant rows and/or columns from the matrices as described in section 5.6.2.1. In order to calculate these terms, there were several intermediate system solves and operations that were required to get the final desired form. It would be convenient to have a more direct approach to furnish these terms.

6.2.0.1 Dealing with the nonaffine parametric dependence of the nonlinear terms

In the general case, while the affine parametric dependence of the underlying bilinear and linear functionals associated with the weak form of the underlying PDE is a key

requirement for efficiency in reduced basis approximation, this is sometimes not possible with certain problems. This is the case for the terms described above. There are two common approaches in literature that address efficiently approximating ROMs in such cases in many-query or real-time problems. These are: (1) Methods that seek to perform direct interpolation among adjacent reduced order models that are precalculated at various points in the design space. (2) Methods belonging to a growing area of research known as "hyper-reduction." In what follows, a brief literature review will be provided for both of these methods.

6.3 Key Enablers: ROM Interpolation and Hyper-reduction

6.3.0.1 ROM Interpolation

This category of methods was perhaps the earlier of the two types of approaches to be developed. In this case, the ROM is first determined at various points in the parameter space. Some methods (e.g. [141–143]) seek to interpolate among these ROMs in the original space in which the matrices are defined. In the associated papers, the entries of the nonlinear matrix (i.e. $A_{ij}(\mu)$) were interpolated by the use of cubic splines. These authors noted that they obtained "good results" relative to other, more sophisticated interpolation schemes. An inherent limitation of this type of interpolation scheme is that there is no guarantee that certain properties of the nonlinear term are inherited at interpolated points in the design space. For example, if the coefficient matrix in a linear algebraic system (e.g. a stiffness matrix) is non-singular, symmetric and positive definite (SPD), it is desirable to maintain these properties at design points evaluated outside of the sampling set in the parameter domain. While it is easy to ensure symmetry, it is not as easy to ensure positive definiteness. For imposed constraints like this, other methods sought to first project the sampled ROM into adjacent matrix spaces; perform interpolation in these spaces; and then map the product back to the original space that the ROM is defined in.

Such an approach is pursed in the following works [142, 143]. This approach ensures that estimates produced by these methods possess the desired properties. However, the underlying exponential and logarithmic mappings of the matrix ($\mathbf{expm}(X)$ and $\mathbf{logm}(X)$, respectively) induce some computational overhead. These mappings have an additional computational complexity of $O(qN^3)$ [144]. Here, q is not necessarily small, such as in the case of an LU or Cholesky decomposition of an operator (i.e. $q = 2/3$ and $q = 1/3$, respectively).

6.3.0.2 Hyper-reduction

Methods of this type are becoming increasingly popular in science and engineering applications that feature nonlinear PDEs. These areas include: nonlinear solid mechanics, computational fluid dynamics, etc. The key idea of this method is to determine an approximate affine relationship for nonlinear operators that have nonaffine parameter dependence:

$$A(\mu) \approx A_m(\mu) = \sum_{q=1}^{Q} \theta(\mu)_q \bar{A}_m^q \tag{203}$$

Note that the use of θ here is not to be confused with the use in scaling parameters used in the weighted POD algorithm in section 5.5.0.6. With this decomposition, parameter independent terms are first determined during a laborious offline procedure; whereas, the parameter dependent coefficients are calculated during the online stage of the procedure.

There are many sub-categories of methods that address the problem shown in eq. 203. Although they go by different names in the literature, their end goal is aimed at producing the form shown. These methods include: Empirical Interpolation Method(EIM) [145, 146], Discrete EIM (DEIM) [147], Matrix DEIM (MDEIM) [1, 2, 148, 149], Missing point estimation [150], gappy POD [151]. However, with the exception of MDEIM, Negri [1] and Bonomi [2] both note that these procedures have

an "extensive, problem-specific pre-processing phase" that has to be carried out in order to obtain the desired parametric form. On the other hand, the MDEIM has been shown to admit an "efficient and algebraic structure". It is for this reason why this type of approximation is pursued.

6.4 Overview Of The MDEIM Approach

Before identifying the areas where the hyper-reduction procedure can be applied to the SCRBE approach, as well as the modifications made for this work, an overview will be given on MDEIM. The MDEIM approach is built upon the $DEIM$ method and is meant to approximate nonlinear, nonaffine matrices (particularly operators). However, the DEIM approach is aimed at approximating vectors $f(\mu)$ rather than matrices. As such, the first step is normally to convert the nonlinear matrix with nonaffine parameter dependence, $A(\mu) \in \mathbb{R}^{n\times m}$ into a vector. This is enabled by the $vec(\cdot)$ operator. This function simply stacks the column of the operator into a large vector, i.e. $A(\mu) \in \mathbb{R}^{(n\times m)} \rightarrow vec(A(\mu)) \in \mathbb{R}^{(nm\times 1)}$. The reverse of this operation is designated as $vec_r(\cdot)$. With these operations in tow, the main offline and online steps of the MDEIM will now be presented.

6.4.0.1 MDEIM Offline - Determining The Parameter Independent Terms, $\bar{A}_q$

The parameter independent terms are determined through the following procedure:

1. Generate samples n_s in the parameter domain, $\mathcal{D}$ i.e. $\mathcal{D}_{\text{test}} \in \mathcal{D} : |\mathcal{D}_{\text{test}}| = n_s$
2. Evaluate the nonlinear operator snapshots at these points, i.e. $S = \{vec(A(\mu)) : \mu \in \mathcal{D}_{\text{test}}\}$
3. Perform POD on the snapshot sample set to determine a concise basis to represent, S. This takes the form: $\Phi = POD(S, \varepsilon_{tol})$

Here $\Phi \in \mathbb{R}^{nm\times N}$ are the N empirical modes that are used to concisely approximate $vec(A(\mu))$ at any point in the parameter domain. A key requirement to approximating the coefficients $\boldsymbol{\theta}$ is the formation of the recovery matrix $\Phi_{\mathcal{I}} \in \mathbb{R}^{N\times N}$.

This matrix is formed by using the DEIM procedure. The algorithm associated with the DEIM procedure will not be stated here, but instead, the author defers to [134]. The main take away is that using a greedy sampling procedure, N indices in the vector $vec(A(\mu))$ that help to provide the best approximation of the coefficients $\boldsymbol{\theta}$ are determined. These indices are denoted as $\mathcal{I} \subset \{1, \ldots, nm\}$, $|\mathcal{I}| = N$. Using these indices, the DEIM procedure also produces an operator $\Phi_{\mathcal{I}} \in \mathbb{R}^{N \times N}$ that is used to recover the coefficients needed to produce the approximation $A_m(\mu)$. $\Phi_{\mathcal{I}} \in \mathbb{R}^{N \times N}$ is built using the rows in Φ corresponding to the indices, $\mathcal{I}$. This recovery will be described in the following section.

6.4.0.2 MDEIM Online - Recovering The Approximation, $A_(\mu)$

Using this empirical basis, an approximation of the nonlinear operator at the parameter value μ can be obtained by performing the operation: $A(\mu) = vec_r(\Phi\boldsymbol{\theta}(\mu))$. The coefficients, $\boldsymbol{\theta}(\mu) = \{\theta_1, \theta_2, \ldots, \theta_N\}$ in this linear expansion are obtained by performing the following procedure:

1. For a given parameter value of μ, evaluate the term $vec(A(\mu))$ at the indices $\mathcal{I}$. This takes the form: $vec(A(\mu))_{\mathcal{I}}$.
2. Using operator $\Phi_{\mathcal{I}}$, approximate the coefficients $\boldsymbol{\theta}$ by solving the equation, $\Phi_{\mathcal{I}}\boldsymbol{\theta} = vec(A(\mu))_{\mathcal{I}}$
3. The approximation of the nonlinear operator is: $A(\mu) = vec_r(\Phi\boldsymbol{\theta}(\mu))$

Thus, using this procedure, the operator can be estimated at any point in an affine manner.

6.4.0.3 Challenges With The Stated Interpolation Approach

One key observation in the online procedure is the sampling of the nonlinear operator required at the indices $\mathcal{I}$. The indices correspond to the nodal values on the underlying finite element mesh used to solve the PDE problem. Both Negri [1] and Bonomi [2]

note the efficiency of the sampling technique for the nonlinear operator that they explored. These operators are large, sparse and built upon lower-order, polynomial finite elements. Thus, getting the element-wise contributions to $vec(A(\mu))_{\mathcal{I}}$ is trivial and can be done efficiently. However in the case of the SCRBE technique, sampling at an element in the vectorized matrices involves considerably more work. The underlying calculations include solving the bubble space problem for extensions of the interface modes. Solving for these bubble solutions on the underlying finite element mesh is expensive. Alternatively, if the reduced bubble spaces are used to facilitate the computation, there is added approximation error introduced in order to gain the desired expediency. Additionally, in order to recover the coefficients $\boldsymbol{\theta}$, one has to solve the associated linear algebraic system. Since $\Phi_{\mathcal{I}}$ is dense, this is a $O(N^3)$ calculation.

6.5 Application Of Hyper-Reduction + Interpolation To The SCRBE Approach

The SCRBE procedure readily admits an interpolation formulation of this type, because as previously noted, the entries arising from each component are only dependent on the local parameter vectors associated with it. This allows an offline study of each archetype component that would create ingredients available for online utility. Going forward, this method will be referred to as the Static Condensation Reduced Basis Element − Discrete Empirical Interpolation Method (SCRBE-DEIM). The steps taken in this modeling procedure will be described in the following sections.

6.5.1 Selection Of An Alternative Interpolation Procedure

While the application of the MDEIM method to the SCRBE approach should be relatively efficient, there are the aforementioned issues raised about the overhead during interpolation. In the present case, we are not comparing performance to the High Fidelity Model (HFM), but instead we are comparing to an ROM (i.e. the SCRBE approach), which should be relatively fast. It is desirable to obtain

an alternative approach to the SCRBE method that can achieve as much relative efficiency as possible. For these reasons, the decision was made to estimate the coefficients in the linear expansion with *surrogate models*. The particular choice of surrogate model should be amenable to nonlinear approximations, while not having overbearing overhead.

In order to meet the desired objectives, *feed-forward, multi-layer, artificial neural network* surrogate modeling is chosen to interpolate the N coefficients in the approximation.

6.5.1.1 Overview Of Neural Network Surrogate Modeling

An artificial neural network (ANN) mathematical model - when used in a regression setting - tries to approximate the functional relationship between one or more parameters, μ, to corresponding output(s) $y = f(\mu)$ i.e. an approximate mapping of the form $\tilde{f} : \mu \rightarrow \tilde{f}(\mu)$. The neural network has a hierarchical structure with several layers of interconnected nodes. There is an input layer, one of more hidden layers, and an output layer of nodes. In the feed-forward variant of the neural network, data is communicated from the input layer through to one or more nodes in the hidden layers and then out to the output layer. The contributions of each of nodes in a given layer are weighted before passing each node in the succeeding layer. Each of the hidden nodes is equipped with an activation function. Common choices for these activation functions are the hyperbolic tangent and exponential functions, linear functions etc. For a more detailed review of artificial neural network for regression purposes, please see [152].

For the present work, the attractive feature of the ANN is the computational complexity associated with its use. For example, if there are two hidden layers with N_{w_1} and N_{w_2} nodes, respectively; the computational complexity associated with generating the N surrogate models is: $O\left(N\left(N_{w_2}N_{w_1} + N_{w_1}|\mu|\right)\right)$. If N_{w_1} and N_{w_2} are on the

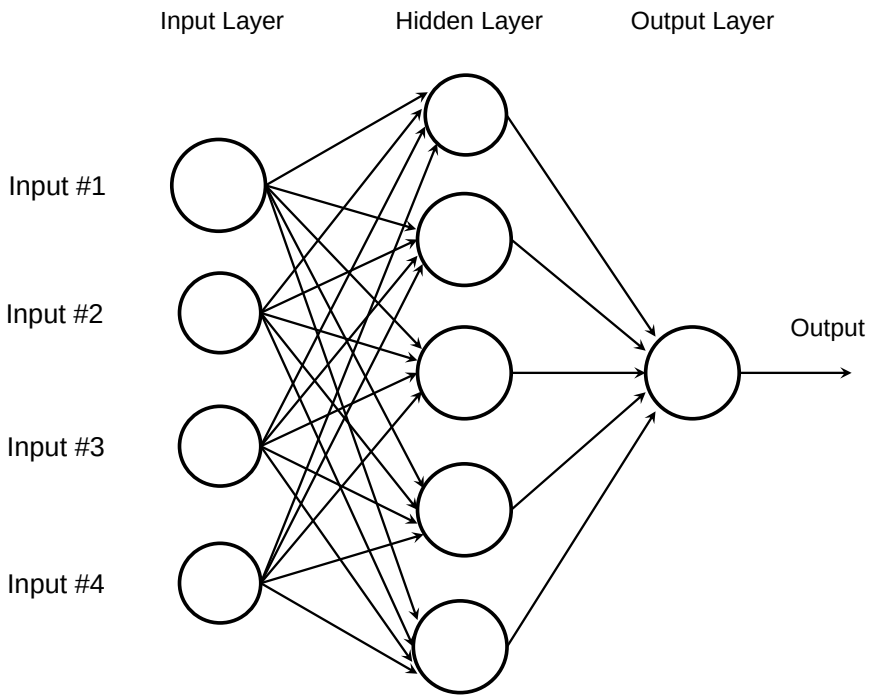

Figure 43: An illustration of an artificial neural network

order of the reduced bubble space cardinality and the number of approximation coefficients, N, then there can be a considerable advantage in using the neural network regression purely from an efficiency point of view.

6.5.2 Treatment Of The Elements Of The SCRBE

Now that the high level idea has been given for the approximation procedure, attention is now turned to the details of the SCRBE procedure in this context. In section 6.2, the main elements that have to be provided for each component were listed. For the stiffness matrices, $\mathbb{K}^i_{uu}(\mu)$, and $\dfrac{\partial \mathbb{K}^i_{uu}(\mu)}{\partial \mu^r}$, in order to ensure symmetry during the approximation, only the lower triangular part each matrix is modeled explicitly. To enable this, the lower triangular part of the relevant stiffness matrix is first extracted, then each column from the lower triangular regions is stacked into a vector. This

is done with the mapping $vec^{LT}(\cdot)$, with reverse operation $vec_r^{LT}(\cdot)$. For the mapping of the parameter-dependent interior solution map, $U^i_{b,GQ}(\mu_i)$, and $\dfrac{\partial U^i_{b,GQ}(\mu_i)}{\partial \mu^r}$, the regular $vec(\cdot)$ and $vec_r(\cdot)$ operators can be applied.

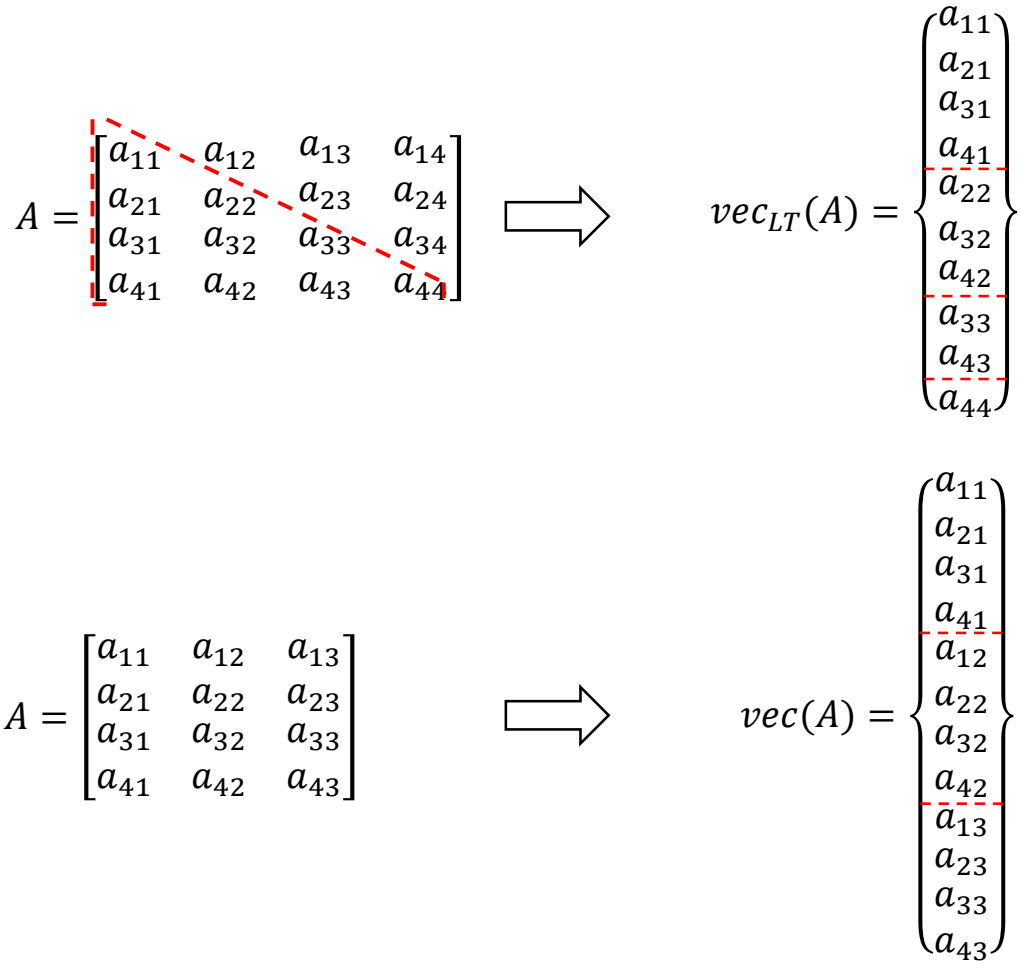

Figure 44: Illustration of the vector mappings

Finally, the remaining terms present a bit more of a challenge. These include: the force terms, $\mathbb{F}^i_u(\mu)$ and $\dfrac{\partial \mathbb{F}^i_u(\mu)}{\partial \mu^r}$; and the traction induced bubble solutions, $b^{f;h}_{i,GQ}(\mu)$ and $\dfrac{\partial b^{f;h}_{i,GQ}(\mu)}{\partial \mu^r}$. This is due to the fact that in addition to the parameters defined for the component, they also depend on prescribed boundary tractions applied to the component. Recall the force term for the Schur complement equation shown

in equation (158). The instantiated component can be placed at many different locations in the final physical problem domain. As such, the current approach can only be applied if the restriction of the term $f(\cdot, \mu)$ to an instantiated component i.e. $(f(\cdot, \mu)|_{\Omega_i})$, is independent of where this component is located in the physical problem domain. If this requirement is not satisfied, then the development presented in section 5.6.2.6 can be used instead.

6.5.2.1 Notes About The Coefficient Schur Complement Matrix

Among these terms, special mention has to be made about the terms entering the Schur complement coefficient matrix, i.e. $\mathbb{K}^i_{uu}(\mu_i)$. It would be beneficial to have a guarantee that these terms are positive definite; particularly when an indirect solver is used to solve the system. The challenge that arises is that there is an overhead associated with the aforementioned mappings when interpolation techniques that enforce positive definiteness are used. Encouraged by the work of Degroote et al. [141], where they successfully performed the interpolation in the original matrix space, the positive definiteness requirement will not be strictly enforced so as to get the best efficiency from the method. In a similar manner, Negri [1] and Bonomi [2] did not enforce the positive definiteness requirement in the MDEIM case. If positive-definiteness is absolutely required for robustness sake, then interpolation can be performed in the appropriate tangent matrix spaces. Note that the overall approach should still be efficient and that it is only one of a group of terms that need to be estimated by the SCRBE approach for each component.

6.5.3 Updated Offline Procedure

The algorithms associated with the offline stage of the SCRBE-DEIM method can now be presented. Algorithm 5.1 is the procedure that is responsible for determining the empirical modes for approximating the nonlinear matrices arising from the SCRBE procedure, as well as the surrogate models of the interpolation coefficients.

The algorithm takes the inputs; the parameter domain sample, $\mathcal{D}_{\text{test}}$; the snapshots generated at these points, $S = \{f(\mu) : \mu \in \mathcal{D}_{\text{test}}\}$; and the convergence tolerance for the POD procedure, ϵ_{tol}. The algorithm produces the outputs: the empirical basis, Φ; the surrogate coefficients for the approximation coefficients, $\tilde{\boldsymbol{\theta}}$.

Algorithm 12: SCRBE DEIM Offline

input : S, $\epsilon_{\boldsymbol{tol}}$, X
output : Φ, $\boldsymbol{\theta}_{ANN}$
begin

- Determine the empirical basis associated with the snapshots: $\Phi = \boldsymbol{POD}(S, \epsilon_{\text{tol}})$
- Create the testing data to create the ANN surrogates: $\boldsymbol{\theta}_{test} = \Phi^T S$
- Create the ANN surrogates for the coefficients with the data: $\boldsymbol{\theta}_{test} = \Phi^T S$
- The coefficients are: $\boldsymbol{\theta}_{ANN}$

end

6.5.4 Updated Online Procedure

Using the elements produced during to the offline procedure (Φ and $\boldsymbol{\theta}_{ANN}$), we can now recover estimates for the SCRBE terms ($f(\mu)$) at any given point in the parameter space, $\mu \in \mathcal{D}$. The control parameter for the edge fidelity, η_{edge} is also included to help to refine the approximation. The associated algorithm is:

Algorithm 13: SCRBE-DEIM Online

input : Φ, $\boldsymbol{\theta}_{ANN}$, μ, η_{edge}
output : $\tilde{f}(\mu)$
begin

- Evaluate the surrogates at μ: $\tilde{\boldsymbol{\theta}} = \boldsymbol{\theta}_{ANN}(\mu)$
- Retain the relevant rows and/or columns of the empirical basis, Φ, corresponding to the control parameter, η_{edge}
- Recover the approximation for $f(\mu)$ as $\widetilde{f}(\mu) = \Phi\widetilde{\boldsymbol{\theta}}$

end

The output $\widetilde{f}(\mu)$ can be reshaped by the appropriate reverse operator and then included in the SCRBE procedure.

6.5.5 Online Complexity Analysis

Attention is now turned to analyzing the computational complexity associated with assembling the ingredients for the problem domain. The relevant terms required to perform the complexity analysis are restated here:

6.5.5.1 Definition Of Terms

- $\mathcal{N}_E^{\max}$ - is the maximum number of edge mode degrees of freedom on any single global edge in the problem domain after the edge space refinement
- $\mathcal{N}_V^{\max}$ - is the maximum number of vertex mode degrees of freedom on any single global vertex in the problem domain
- $\mathcal{N}_{\text{interface}} = 4(\mathcal{N}_E^{\max} + \mathcal{N}_V^{\max})$
- N_c - the number of components in the assembled problem domain
- n_{μ_i} - the maximum number of parameters among all of the components
- $Q_{K^{\text{emp}}}$ - the maximum number of terms required for the approximate affine representation of $\mathbb{K}_{uu}^i(\mu)$ and $\dfrac{\partial \mathbb{K}_{uu}^i(\mu)}{\partial \mu^r}$ among all of the components
- Q_u - the maximum number of terms required for the approximate affine representation of $U_{b,GQ}^i(\mu_i)$ and $\dfrac{\partial U_{b,GQ}^i(\mu_i)}{\partial \mu^r}$ among all of the components
- Q_{b_f} - the maximum number of terms required for the approximate affine representation of $b_{i,GQ}^{f;h}(\mu_i)$ and $\dfrac{\partial b_{i,GQ}^{f;h}(\mu_i)}{\partial \mu^r}$ among all of the components
- τ_{surr} - The maximum number of operations required to evaluate any of the surrogates for the problem coefficients

6.5.5.2 Complexity Analysis Of Each Major Term

Using these terms, the online time complexity for the major steps are:

Terms	Time Complexity
$\mathbb{K}^i_{uu}(\mu_i),\ \dfrac{\partial \mathbb{K}^i_{uu}(\mu_i)}{\partial \mu^r}$	$O\left(N_c\left(n_\mu+1\right)Q_{K^{\text{emp}}}\left(\tau_{surr}+\mathcal{N}^2_{\text{interface}}\right)\right)$
$\mathbb{F}^i_u(\mu),\ \dfrac{\partial \mathbb{F}^i_u(\mu)}{\partial \mu^r}$	$O\left(N_c\left(n_\mu+1\right)Q_f\left(\tau_{surr}+\mathcal{N}_{\text{interface}}\right)\right)$
$U^i_{b,GQ}(\mu_i),\ \dfrac{\partial U^i_{b,GQ}(\mu_i)}{\partial \mu^r}$	$O\left(N_c\left(n_\mu+1\right)Q_u\left(\tau_{surr}+\mathcal{N}_{\text{interface}}\right)\right)$
$b^{f;h}_i(\mu),\ \dfrac{\partial b^{f;h}_i(\mu)}{\partial \mu^r}$	$O\left(N_c\left(n_\mu+1\right)Q_{b_f}\tau_{surr}\right)$

6.5.5.3 Overall Complexity Analysis

This leads to an overall time complexity of:

$$O\left(N_c\left(n_\mu+1\right)\left[Q_{K^{\text{emp}}}\left(\tau_{surr}+\mathcal{N}^2_{\text{interface}}\right)+Q_f\left(\tau_{surr}+\mathcal{N}_{\text{interface}}\right)+Q_u\left(\tau_{surr}+\mathcal{N}_{\text{interface}}\right)+Q_{b_f}\tau_{surr}\right]\right) \tag{204}$$

6.5.5.4 Comparison To The SCRBE Approach

Here we see that computational time is not dependent on the cost of solving bubble solutions on the problem domain. Instead, to form the ingredients of the static condensation problem, we are only required to do an affine summation for each term. Furthermore, the largest multiplicative factor of the $\mathcal{N}^2_{\text{interface}}$ terms is $Q_{K^{\text{emp}}}$, as opposed to $n_b Q_K$ in the case of the SCRBE method. The latter scales poorly with affine representations for the bilinear operator that are not concise ($Q_K \to \infty$) and bubble spaces with large cardinalities $n_b \to \infty$. For efficiency, it is critical to keep the values of $Q_{K^{\text{emp}}}$, Q_{K_b}, Q_u, Q_{b_f} and τ_{surr} as low as possible.

6.6 Chapter Summary

In this chapter, an alternative method was presented to provide the ingredients of the SCRBE approach. The approach leverages a modified version of the Matrix Discrete Empirical Interpolation approach. It was shown through a time complexity

analysis that the SCRBE-DEIM approach should have a competitive advantage from an efficiency point of view relative to the SCRBE approach. The relative accuracy is yet unclear and will have to be tested.

The hypotheses corresponding to the research questions will now be stated.

Hypothesis 2.0: Based on a time complexity analysis, the SCRBE-DEIM approach should help to alleviate some of the computational overhead of the SCRBE approach. However, a reduction is accuracy is expected due to the use of interpolation techniques in multiple places

Hypothesis 3.0: The SCRBE-DEIM approach should help to alleviate some of the computational overhead during the optimization procedure. However, its suitability as a replacement to the SCRBE method is contingent on its accuracy along the optimization paths.

Chapter VII

CANONICAL PROBLEM

7.1 Chapter Overview

In this chapter, the pair of canonical problems that were studied for this work is presented. This includes: a description of the use of archetype components; the underlying finite element mesh; the choice of component parametrization and the treatment of the state variable dependent constraints.

7.2 Introduction Of The Design Problem

For the canonical problem, it was desired to select a representative, yet simple aerospace design problem for application of the methods examined in this work. Due to the increased use of composite materials in aerospace structural design over the years, a canonical problem centered around their use was coveted. As such, the problem chosen was the membrane strength design of a patched, variable stiffness composite plate. Figure 45 illustrates a patched, variable stiffness composite plate. With this type of design, the entire problem domain is segmented into subregions. Within each subregion, the laminate lay-up (i.e. number of plies, their orientations and overall laminate thickness) is uniform throughout its local, physical domain; but is allowed to differ from adjacent subregions. This type of design has been shown to provide superior structural performance relative to constant stiffness designs; wherein, the entire structure has a consistent laminate throughout its physical domain [153].

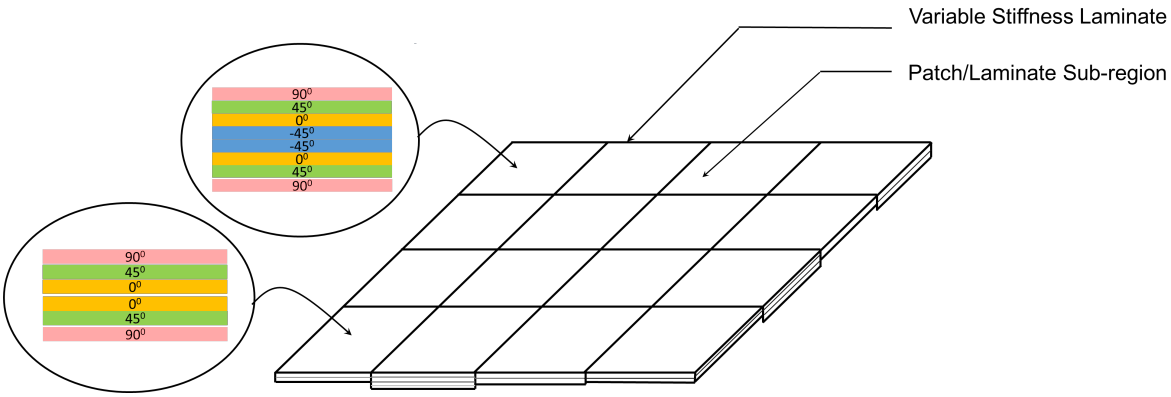

Figure 45: Illustration of a variable stiffness plate

The patched, variable stiffness composite design fits well into the paradigm of the SCRBE method. Each or a group of the sub-regions can be treated as a component under the SCRBE paradigm. As such, these components naturally inherit the material and geometric parametrization from the individual or group of variable stiffness sub-regions. For this work, each sub-region will be treated as a component.

7.3 Description Of The Two Canonical Problems

Two canonical problem variants that will be used to perform the numerical experiments in the following chapter. Variant 1 was created for the purpose of investigating research questions 1 and 2; whereas variant 2 was created in order to investigate research question 3 i.e. for the optimization problem. Although the SCRBE and SCRBE-DEIM methods allow for the direct application of boundary tractions to the periphery of the problem domain, the implementation by the author was performed in an ad-hoc fashion for the application of Dirichlet boundary conditions. The approximation spaces used on the boundaries for the test problems were Lagrange polynomials distributed on Chebyshev nodes. This is similar to the approach used by Vidal-Codina et al. [116] for a one dimensional interface/boundary. A space decomposition approach of the type described in section 5.3.3 could have been used. However, since Dirichlet boundary conditions are prescribed and are not modulated,

the simpler approximation space was chosen in order to reduce the required experimental effort in training the empirical edge spaces on the periphery.

The displacement field applied in the normal direction of the top and bottom boundaries are parabolic, with the maximum value occurring in the middle of the boundary and zero at either bounding vertex. In the lateral directions along these boundaries, the displacement are constrained. On the left and right boundaries, homogeneous Dirichlet boundary conditions are applied.

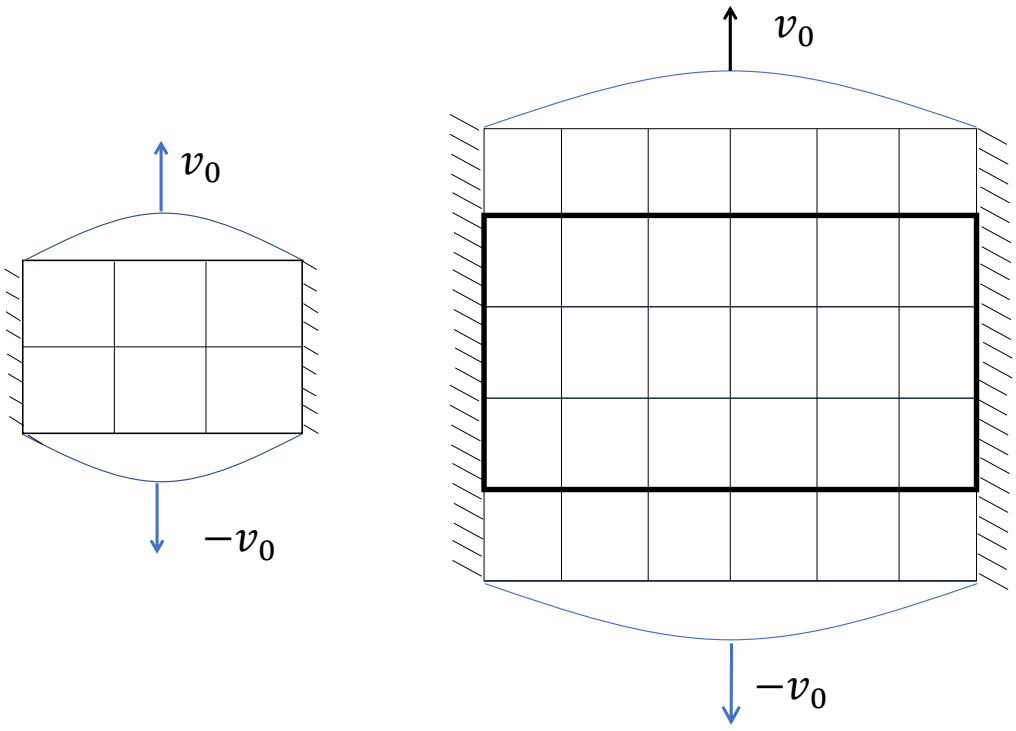

Figure 46: The two variants of the canonical problem. *Left:* problem domain variant 1. *Right:* problem domain variant 2

For variant 2, the extra rows of components were added in order to mimic the application for boundary tractions on the 3 interior rows of components. This was done by first fixing the material parameters in the domain and then by applying the prescribed Dirichlet boundary conditions to the periphery. The resulting internal

forces developed on the upper and lower highlighted edges were kept fixed and used during the optimization procedure for experiment 2. It should be noted that the Lagrange polynomial basis (with a fixed number of modes) was also used for the boundary of the interior domain. Therefore, only the interfaces on the interior of the highlighted physical problem domain feature an empirical basis.

7.3.0.1 Choice Of Laminate Parametrization

Kennedy and Martins [154] provided a thorough review of the methods that are available in the composite structural design literature for laminate parametrization. The two major category of methods identified are: *direct methods* and *indirect methods*. For indirect methods, rather than working with the physical parameters that directly describe the laminates; intermediate variables which are functions of the physical parameters are used. The primary manifestation of this approach in the literature is with the use of *lamination parameters*. They were initially introduced by Tsai and Pagano [155]. Lamination parameters were chosen for the canonical problems described in this section. They provide the opportunity to create relatively concise, affine relationships for the requisite stiffness matrices and do not scale poorly when a large number of plies are used to construct the composite laminate.

The main challenges with using lamination parameters are: (1) recovering physically realizable laminates from the found optimum designs and (2) properly identifying the feasible design/parameter space for which they are meaningful. Regarding limitation (1), a commonly used approach in addressing this problem is to use a multilevel optimization approach [153]. In this approach, the lamination parameters are first used to design the laminate for some objective (such as mass minimization, compliance, etc). Subsequently; another optimization routine is used to obtain a detailed ply-by-ply laminate definition that meets manufacturing and certification requirements. The author defers to the work in literature for this post-processing step.

Limitation number 2 will be addressed in section 7.3.3.

In chapter 4, the strong and weak forms of the linear-static elasticity problem were presented. In appendix A, the constitutive model of a general, anisotropic composite laminate using shell theory is presented. This is followed by the inclusion of lamination parameters and material invariants for an affine representation of the stiffness matrix.

7.3.0.2 Design Rules For The Canonical Problem

The following are the major design rules that were imposed on the problem:

- Symmetry and balance of the laminate is enforced in each component
- Each component contains at least one ply with one of the following orientations: $\{0^0, -45^0, 45^0, 90^0\}$. This is to enable stress calculations.
- Blending will not be enforced between adjacent sub-regions on the problem domain.

7.3.1 Assembly Of The Archetype Components Into The Problem Domain

For the present work, there are nine archetype components. They are each built upon the same finite element mesh (figure 48); and use the same constitutive relationship and parameter spaces. The difference among them lies in the choice of edge and vertex modes (including transformations) used to form the local boundaries. The nine archetype components form the basis of the problem domains considered in this section. Figure 47 shows the two problem domains and the use of archetype components as building blocks for their creation. Each unique archetype component is illustrated with a unique color.

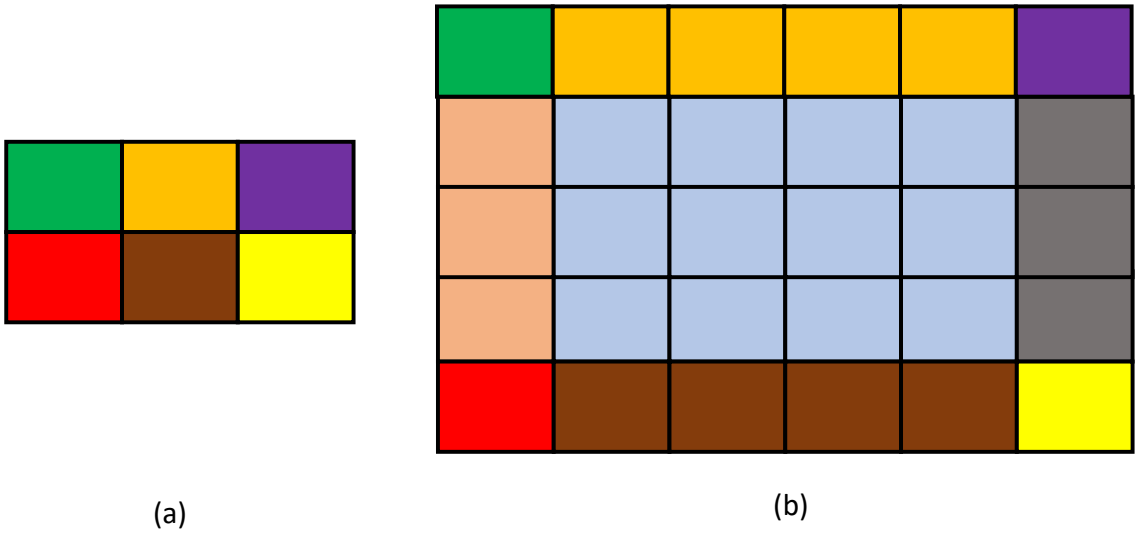

Figure 47: Assembly of template components into the problem domain. (*left*) Problem domain 1. (*right*) Problem domain 2

7.3.2 Finite Element Subspace Chosen For The Components

Both the SCRBE and SCRBE-DEIM methods are built upon the finite element approximation space. A finite element approach had to be chosen that is compatible with the shell theory used to model the composite plate. For this purpose, the flat shell approach [156] was chosen for the present work. This approach avoids several types of "*locking*" [1] that often plague shell finite element implementations.

Figure 48 shows the finite element mesh that is used to model each component in the variable stiffness composite plate's domain. The mesh has 25 bilinear elements (26 nodes) along each of the four local boundaries and features a two-way bias towards

[1]Locking can be defined as *the presence of artificial stresses in a finite element formulation.* There are four common types of locking, including, (1) Transverse shear locking; caused by incorrect transverse forces under bending; (2) In-plane shear locking in plates and shells; (3) Membrane locking that occurs in curved beams and shells; (4) Volumetric locking that occurs with Poisson ratio, $\nu \approx 0.5$

the vertices of the domain. The direct application of Dirichlet boundary conditions to the boundaries of the plate in the various directions during the training procedures led to a somewhat non-smooth displacement field in the peripheral regions of the plate. The use of the mesh bias was found to quickly diminish this pattern as one moved away from the periphery of the domain. In total, there are 3456 degrees of freedom on the mesh.

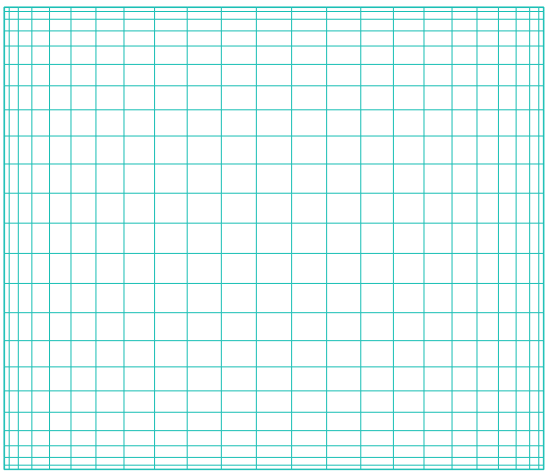

Figure 48: Finite element mesh on a template component

This finite element mesh was used for the following tasks:

- The creation of the components used within the truth model. The truth model was used for validation purposes.
- The creation of the testing domains used for the edge space and bubble space training procedures described in section 5.5.
- The creation of the SCRBE stiffness matrices and solution recovery mappings used in the SCRBE-DEIM approach.

The truth models corresponding to the canonical problems were created and validated against similar models created in the commercial Finite Element software, **ABAQUS** [157]. There was good agreement between the corresponding models for

displacement estimations and the slight differences ($< 1\%$) were attributed by the author to the differences in finite element formulations.

7.3.3 Stiffness Matrix Parametrization For Each Component

Based on the presentation in appendix A, the stiffness matrix for a general, anisotropic composite laminate can be described by a combination of: the laminate thickness, lamination parameters and lamina invariant terms. The laminate thickness and lamination parameters are used to create the affine coefficients for the stiffness matrix; whereas the lamina invariant terms, along with the finite element truth space, is used to create the parameter independent terms. The resulting affine representation for the stiffness matrix for component i is:

$$K^i = hK^{A_0} + \sum_{q=1}^{4} h\xi_q^A K^{A_q} + \sum_{q=1}^{4} h^2\xi_q^B K^{B_q} + \frac{h^3}{12}K^{D_0} + \sum_{q=1}^{4} \frac{h^3}{12}\xi_q^D K^{D_q} \tag{205}$$

Here:

- h - the overall thickness of the laminate
- $-1 \leq \xi^A_{[1,2,3,4]} \leq 1$ - governs the pure membrane behavior of the laminate
- $-1 \leq \xi^D_{[1,2,3,4]} \leq 1$ - governs the pure bending behavior of the laminate
- $-1 \leq \xi^B_{[1,2,3,4]} \leq 1$ - governs the coupled membrane-bending behavior of the laminate
- K^{A_0} and K^{D_0} - stiffness matrix contributions that are not paired with lamination parameters
- K^{j_q} $j = \{A, B, D\}$ $q = \{1, 2, 3, 4\}$ - stiffness matrix contributions that are associated with lamination parameters

Due to the use of a balanced and symmetric laminate, we attain certain simplifications. Chiefly, $\xi_q^A = 0,\ \ q = \{3, 4\}$ and $\xi_q^B = 0,\ \ q = \{1, 2, 3, 4\}$. Furthermore, since the problem being studied involves only the membrane deformation under balanced and symmetric laminate assumptions, the affine representation for the stiffness matrix

for each component becomes:

$$K^i = hK^{A_0} + h\xi_1^A K^{A_1} + h\xi_2^A K^{A_2} + \frac{h^3}{12}K^{D_0} \tag{206}$$

Although the three parameters: h, ξ_1^A and ξ_2^A, are sufficient for parametrizing the stiffness matrix associated with the laminate under these restrictions; this does not form the full set of terms that have be considered when online parametric changes are made. The lamination parameters are highly correlated with each other and as such, are not allowed to vary independently. There has been extensive work in the literature to define the interdependencies among the lamination parameters. Bloomfield et al. [158] presented a collection of several of the closed form constraints that were developed in literature for defining the feasible domain for the lamination parameters. It was shown by Grenestedt and Gudmundson [159] that this feasible region is convex. The closed-form lamination parameter constraints summarized by Bloomfield are:

$$\begin{aligned}
2\left(\xi_1^j\right)^2 - 1 - \xi_2^j &\leq 0 && (207)\\
2\left(1+\xi_2^j\right)\left(\xi_3^j\right)^2 - 4\xi_1^j\xi_3^j\xi_4^j + \left(\xi_4^j\right)^2 - \left(\xi_2^j - 2(\xi_1^j)^2 + 1\right)\left(1-\xi_2^j\right) &\leq 0, && (208)\\
\left(\xi_1^j\right)^2 + \left(\xi_3^j\right)^2 - 1 &\leq 0, && (209)\\
\frac{1}{4}\left(\xi_k^A + 1\right)^3 - 1 - \xi_k^D &\leq 0, && (210)\\
-\frac{1}{4}\left(\xi_k^A - 1\right)^3 - 1 + \xi_k^D &\leq 0, && (211)\\
-4\left(\xi_k^A + 1\right)\left(\xi_k^D + 1\right) + \left(\xi_k^A + 1\right)^4 + 3\left(\xi_k^B\right)^2 &\leq 0, && (212)\\
-4\left(\xi_k^A - 1\right)\left(\xi_k^D - 1\right) + \left(\xi_k^A - 1\right)^4 + 3\left(\xi_k^B\right)^2 &\leq 0, && (213)\\
\text{for } j \in \{A, D\},\ \ k = \{1, \ldots, 4\}
\end{aligned}$$

After the simplification provided by the assumptions for the present problem, there are a total of 13 lamination parameter constraints that remain. Notice that there are couplings between in membrane lamination parameters (A) and the out-of-plane (D) parameters. Going forward, the collection of these lamination parameters will be referred to as **lamConstraints**$\left(\xi_{1,2}^A, \xi_{1,2,3,4}^D\right)$. Based on the correlations of the

lamination parameters, the parameters for each component are: $\mu_i = \left\{h, \xi^A_{1,2}, \xi^D_{1,2,3,4}\right\}$.

7.3.4 State-Variable Dependent Constraint For The Problem

The state-variable dependent constraint that was considered is a first-ply failure, material strength constraint. In particular, the Tsai-Wu ply failure constraint was applied to all of the components in the problem domain. The Tsai-Wu failure constraint takes the form:

$$\frac{\sigma_{xx}^2}{X^t X^c}+\frac{\sigma_{yy}^2}{Y^t Y^c}-\sqrt{\frac{1}{X^t X^c}\frac{1}{Y^t Y^c}}\sigma_{xx}\sigma_{yy}+\left(\frac{1}{X^t}-\frac{1}{X^c}\right)\sigma_{xx}+\left(\frac{1}{Y^t}-\frac{1}{Y^c}\right)\sigma_{yy}+\frac{\tau_{xy}^2}{S^2}-1=0 \tag{214}$$

Where:

- σ_{xx}, σ_{yy}, τ_{xy} - The axial, lateral and shear stresses, respectively, in the lamina
- X^t, Y^t - The tensile strength in the axial and lateral directions, respectively, of the lamina
- X^c, Y^c - The compressive strength in the axial and lateral directions, respectively, of the lamina
- S - The shear strength of the lamina

The material strength terms are determined experimentally.

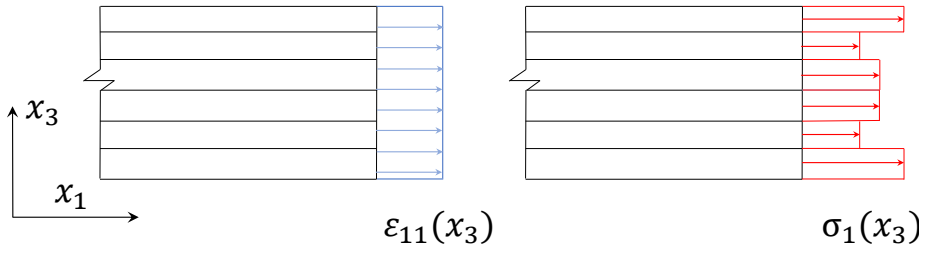

Figure 49: Composite laminate under pure membrane loading. (*Left:*) strain distribution. (*Right:*) stress distribution.

The Tsai-Wu constraint is a type of bound-constraint and must be satisfied at all points in the problem domain. The assumption was made that each component has at least one of each of the following ply angles: $\{0^0, -45^0, 45^0, 90^0\}$. For each of these ply angles, the Tsai Wu constraint is calculated using the local ply stresses developed after applying the boundary conditions to the problem. For pure membrane loading, under the conditions of a symmetric and balanced laminate, the strain field is uniform through the thickness of the laminate. However, when the ply angles vary through the thickness of the laminate, the stress field is not and varies in a piece-wise constant fashion (figure 49). For each component, the Tsai-Wu constraint is evaluated for each ply angle at the Gaussian quadrature sampling locations and then used to determine the associated constraint aggregate functionals over the entire component.

7.4 Chapter Summary

In this chapter, the two variants of the canonical problem were presented. They will be used as the test bed for the numerical experiments described in chapter 8.

Chapter VIII

NUMERICAL EXPERIMENTS

In this chapter, an overview will be given on how the algorithms presented throughout the work were applied to the canonical problem. Additionally, the numerical experiments used to investigate the hypotheses discussed in chapters 5 and 6 are presented.

8.1 Numerical Training Procedures For The Canonical Problem

8.1.1 Generation Of The Parameter Space Samples

For the algorithms used to create the ingredients of the SCRBE and SCRBE-DEIM approaches, samples are needed within the parameter space. The Latin Hypercube sampling [160] technique (LHS) was used to generate these samples. Each component has a parameter space of dimension of seven. The samples were generated within the feasible space prescribed by the function **lamConstraints**$(\cdot)$. During the experimental testing, the author noticed some strange, non-smooth displacement fields for parameter values that are close to the boundary formed by **lamConstraints**$(\cdot)$. To mitigate the effects of these aberrant points, a small constant was added to the estimates produced by **lamConstraints**$(\cdot)$ in order to shift feasible space.

Using the sample set formed on an individual component, the sample set for a larger physical domain consisting of several components was formed by taking the Cartesian product of the local samples. Random permutations of the local samples were combined to form each individual global sample for a problem domain. Due to the prescription of the feasible parameter space in this fashion, it is unlikely that the corners of this design subspace will be explored during the online optimization

procedure. Therefore, no special care is taken to study the behavior of these regions.

8.1.2 SCRBE Training Procedure

8.1.2.1 Edge Mode Training

Using the testing domains built upon the finite element meshes described in section 7.3.2 and the parameter samples mentioned in section 8.1.1, the edge mode training algorithms described in section 5.5.0.6 were performed. A representative set of the edge modes for an interior edge is depicted in figure 50.

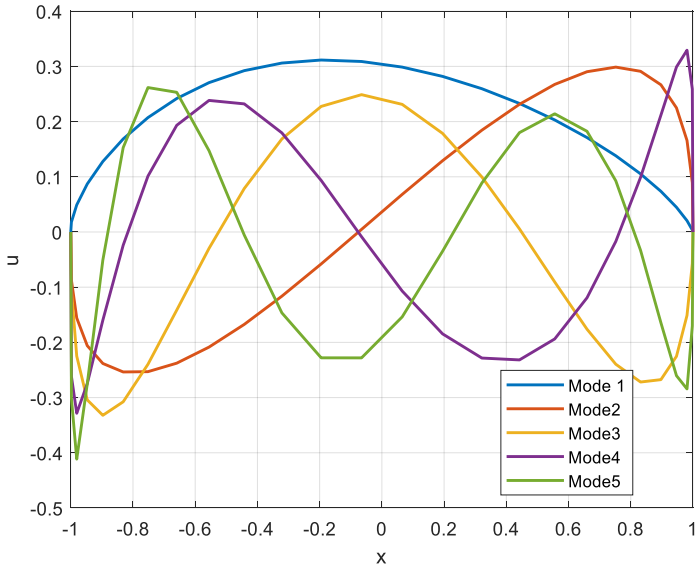

Figure 50: Empirical modes found the solution $u_1(x)$ for a typical interior edge

For the present problem, there are three types of edge modes used in the problem domain: (1) those on the interior; (2) those joining the interior and the periphery of domain; and (3) those used exclusively on the periphery of the domain. However, as described in section 7.3, predetermined, non-empirical modes were selected for the boundaries, for simplicity sake. The edge modes were rotated as necessary and used to form the boundaries of the local archetype components.

8.1.2.2 *Bubble Mode Training*

Leveraging the empirical edge modes and their extensions into the interior of the components, algorithm 5.5.0.7 was used to obtain the corresponding bubble space modes defined on the interior of the adjacent components. Figure 51 illustrates the number of bubble modes that were extracted for each of the first eight modes on a typical interior edge. The bubble space fidelity parameter, η_b, can be used to vary the number of bubble modes used in the approximation and is also illustrated here.

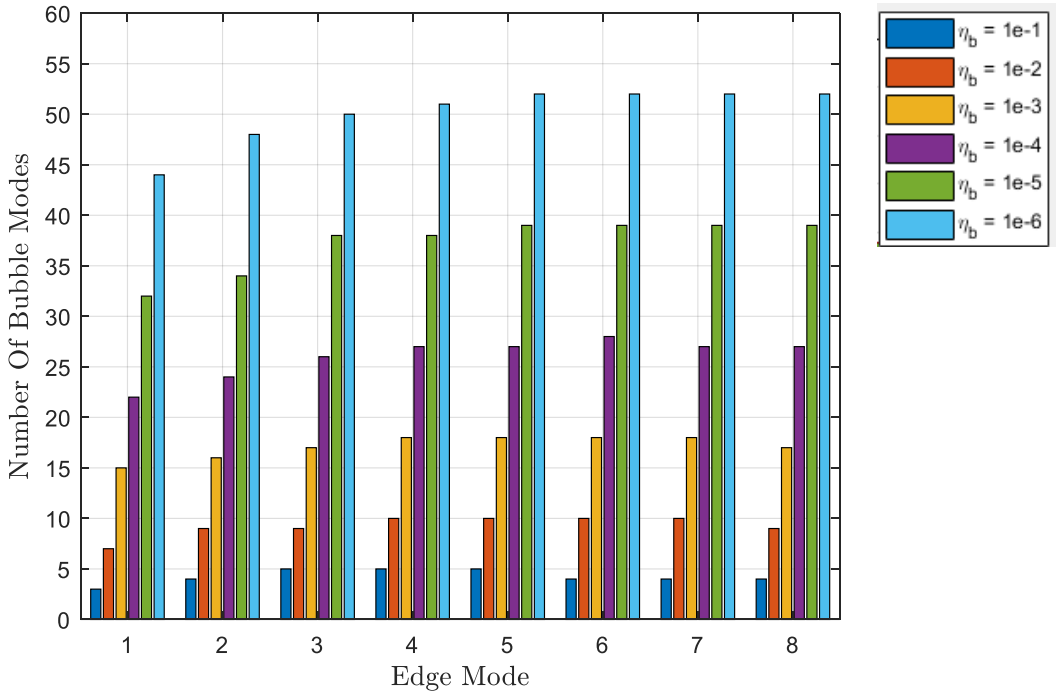

Figure 51: The quantity of empirical bubble modes associated with the first eight interface modes of a typical interior edge

8.1.3 SCRBE-DEIM Training Procedure

Next, the offline elements of the SCRBE-DEIM approach were created. As described in section 6.5.3, this includes the empirical modes required for approximating the operators and mappings; as well as the artificial neural network models that are used to provide estimations for the coefficients in their approximate affine representations.

8.1.3.1 *Stiffness Matrix Approximation*

Using the parameter samples described in section 8.1.1, the symmetric stiffness matrices and their derivatives described in section 5.3.5 were evaluated at the sampling locations. Using the Proper Orthogonal Decomposition (POD) procedure for each stiffness matrix sample set, the empirical modes needed to provide the pseudo-affine relationships were determined. Figure 52 shows the number of empirical modes that were obtained for a POD tolerance of η_{tol}.

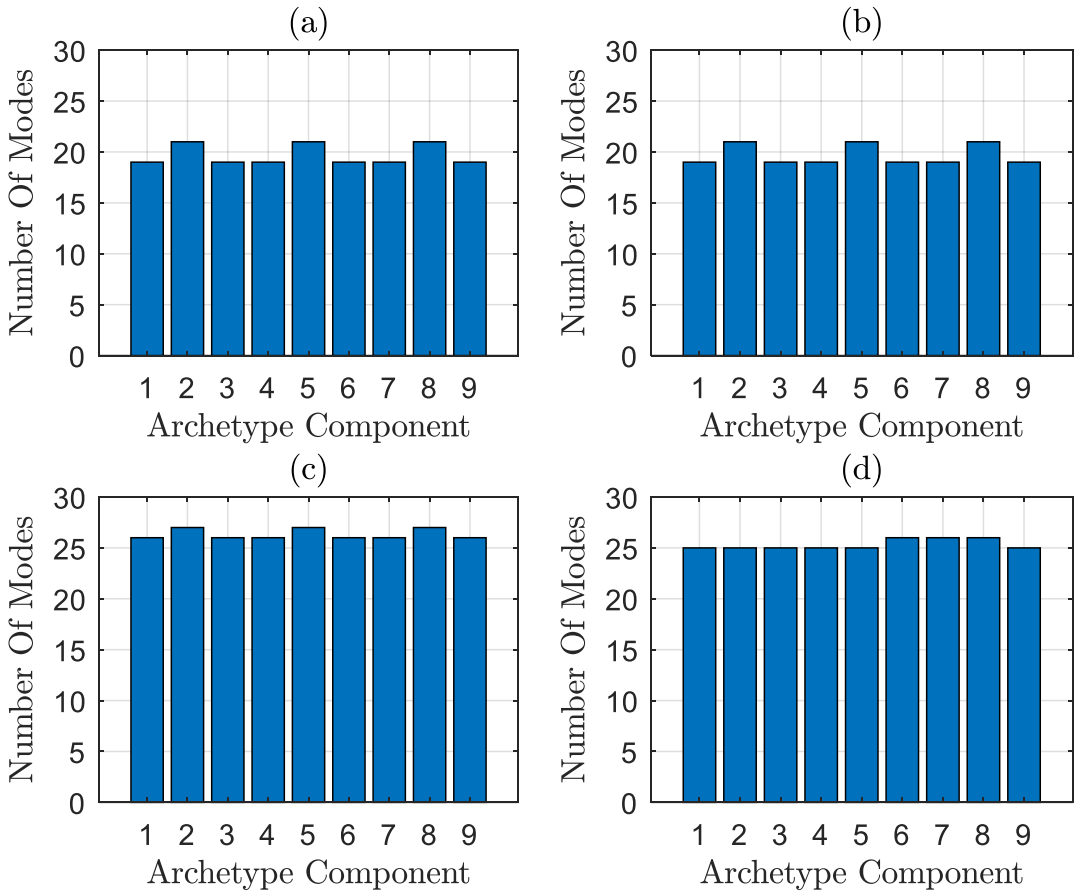

Figure 52: Quantity of empirical modes created for the stiffness matrices of the 9 archetype components. **(a)** State matrix. Derivative with respect to: **(b)** h **(c)** ξ_1^A **(d)** ξ_2^A

(a)

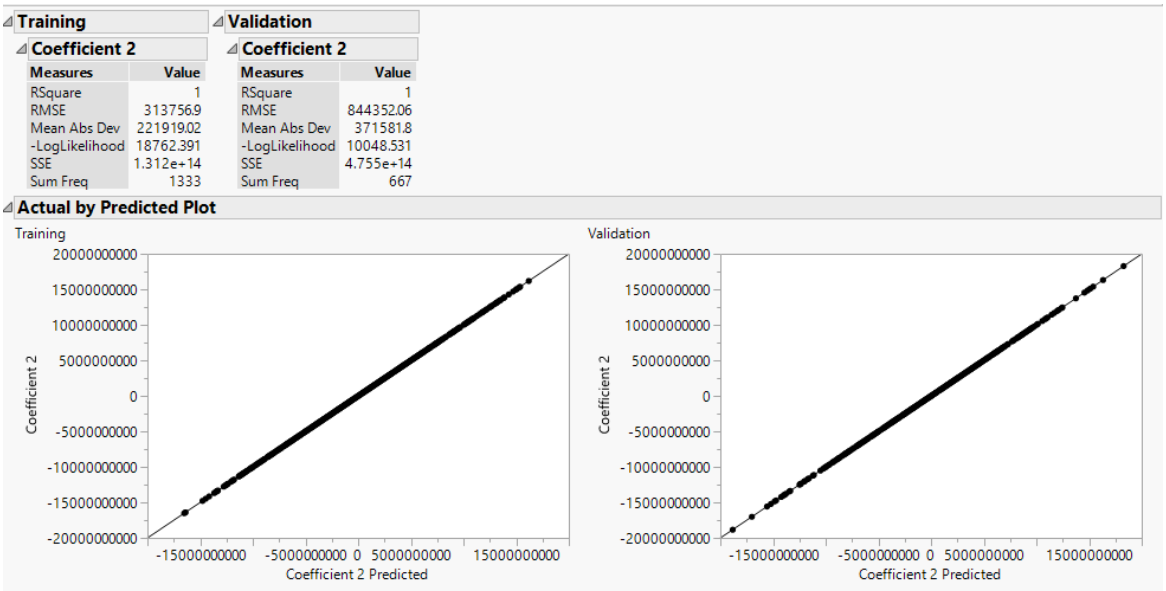

(b)

Figure 53: The training results for the first two coefficients of the stiffness matrix for archetype component 1. Actual vs. predicted results - *Left* training data. *Right* validation data

The artificial neural network (ANN) surrogate models corresponding to the approximation coefficients were created in the statistical software package **JMP** [161] and in the software package **MATLAB** [162]. Two-thirds of the samples generated in the parameter space were used to train the ANN model, whereas the remaining one-third samples were used for validating and testing the performance of each regression. Each ANN was two-layered with 15 nodes in each layer. The activation function selected for each node was the $tanh(\cdot)$ function.

The regression statistics for the first two coefficients of the stiffness matrix of archetype component 1 are shown in figure 53. Judging by the R^2 values and the actual vs. residual plots, it seems that the ANNs capture the functional behavior of the raw data quite well.

8.1.3.2 Parameter-Dependent Mapping Affine Approximation

The parameter domain samples were also used in the estimation of the terms required for affine approximation of the parameter-dependent mappings. First, the empirical modes were created for each unique combination of edge subspace and local edge on the archetype component. In total, there were 14 mappings created for the archetype edges and 8 mappings created for the vertices. The number of modes retained for both type of interface components are shown in figure 54 and 55, respectively.

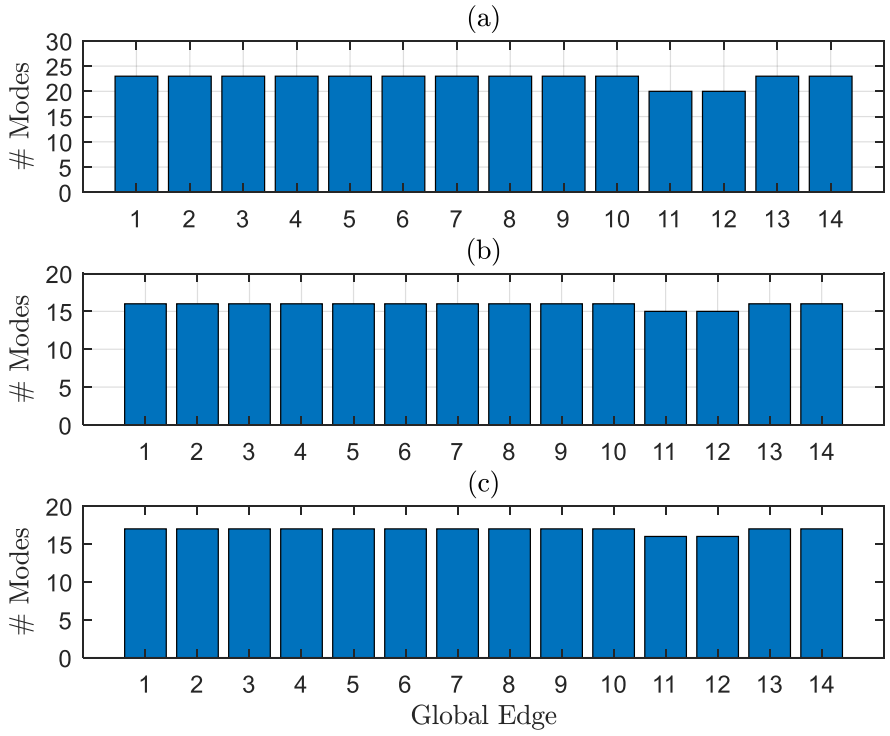

Figure 54: Quantity of empirical modes created for the archetype components edges. **(a)** State matrix. Derivative with respect to: **(b)** ξ_1^A **(c)** ξ_2^A

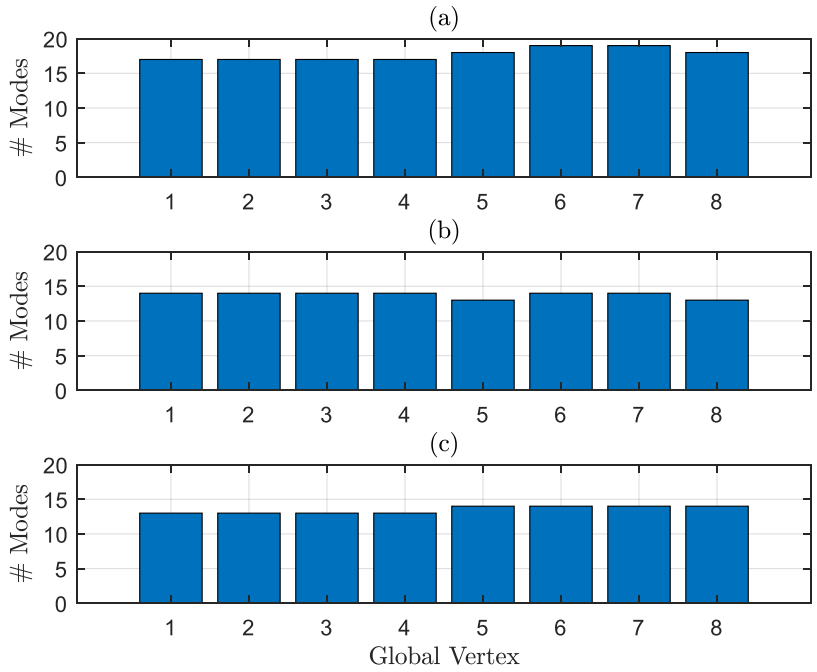

Figure 55: Quantity of empirical modes created for the archetype components vertices. **(a)** State matrix. Derivative with respect to: **(b)** ξ_1^A **(c)** ξ_2^A

Similar to the stiffness matrices, the ANN surrogates were created for each grouping of edge modes and vertices for the state mappings as well as each of their derivatives with respect to the parameters on which they depend.

8.2 Experiment 1: Convergence Behavior Of The SCRBE And SCRBE-DEIM Approximations

Attention is now turned to the first of the two experiments considered in this section. The purpose of the first experiment is to investigate the first two hypotheses that were proposed in this work. The approximation convergence behavior was studied on problem domain variant 1 and the comparison in overhead computation time required was investigated on the middle three rows of problem domain variant 2.

8.2.1 Procedure For Experiment 1(a)

The following procedure was used to generate the results for experiment 1(a).

- **Step 1**: 100 random design points were selected from the feasible region of the domain formed by table 3 i.e. after the constraint set, **lamConstraints** $\left(\xi^A_{1,2}, \xi^D_{1,2,3,4}\right)$, was applied.
- **Step 2**: Problem domain variant 1 was created with the truth finite element model, the SCRBE approach and the SCRBE-DEIM approach. The selected design points in step 1 were applied to each component for the three methods.
- **Step 3**: On the boundary of the problem domain, a parabolic displacement field was applied in the normal direction of the upper and lower boundaries. The magnitude of the displacement was $1mm$ in the center of the field. Furthermore, the left and right boundaries of the problem domain were subjected to homogeneous Dirichlet boundary conditions.
- **Step 4**: Among the Tsai-Wu constraint values that resulted after inducing stresses on the interior of the problem domain for each design point, the most active one (largest non-negative value) evaluated on the truth model was selected for analysis.
- **Step 5**: The derivative of this constraint was also found by evaluating it numerically on the refined truth model.
- **Step 6**: The corresponding Tsai-Wu constraint value and its derivative were evaluated with the SCRBE and SCRBE-DEIM approaches
- **Step 7**: For the SCRBE and SCRBE-DEIM approaches, the fidelity of the interface and bubble space approximations were varied in order to study the convergence behavior of the models. The values of these parameters that were investigated are presented in tables 4, 5 and 6. Tables 4 and 5 also show the correspondence between the selected η_{edge} values and the average number of edge modes per nodal DOF used to form the Schur complement (after the deletion of rows and columns corresponding to the application of the boundary conditions).

- **Step 8**: Similarly, the mesh density of the finite element model was also varied and used to calculate the metrics listed above. This formed the basis of comparison for the speed of convergence.

Table 3: Parameter domain for each archetype component

Parameter	$h(m)$	ξ_1^A	ξ_2^A	ξ_1^D	ξ_2^D	ξ_3^D	ξ_4^D
Lower Limit	1.40e−2	−1	−1	−1	−1	−1	−1
Upper Limit	7.70e−2	1	1	1	1	1	1

Table 4: Correspondence between the interface fidelity parameter setting, η_{edge}, and the average number of edge modes used on the edges per nodal d.o.f. (part 1)

Step	1	2	3	4	5	6	7	8	9
η_{edge}	$10^{-0.50}$	$10^{-1.00}$	$10^{-1.25}$	$10^{-1.50}$	$10^{-2.00}$	$10^{-2.50}$	$10^{-2.75}$	$10^{-3.00}$	$10^{-3.25}$
N	2.00	2.07	3.57	4.00	4.71	6.00	7.00	8.07	9.00

Table 5: Correspondence between the interface fidelity parameter setting, η_{edge}, and the average number of edge modes used on the edges per nodal d.o.f. (part 2)

Step	10	11	12	13	14
η_{edge}	$10^{-3.50}$	$10^{-3.75}$	$10^{-4.00}$	$10^{-4.25}$	$10^{-4.50}$
N	10.07	11.00	12.00	13.43	14.00

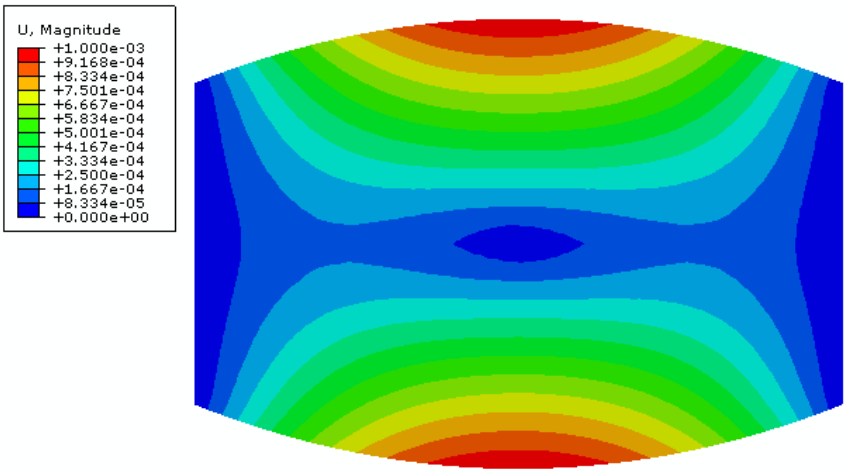

Figure 56: Displacement solution of the problem

Table 6: Values investigated for the bubble space fidelity parameter

Step	1	2	3	4	5	6
η_b	$10^{-1.0}$	$10^{-2.0}$	$10^{-3.0}$	$10^{-4.0}$	$10^{-5.0}$	$10^{-6.0}$

8.2.2 Results From Experiment 1(a)

Figure 56 illustrates the displacement field associated with experiment 1 for one of the investigated design points. As expected, the displacement field on the upper and lower boundaries of the problem domain mimic the applied Dirichlet boundary field, while the displacement vanishes at the interior and on the left and right boundaries.

Figure 57 shows the maximum Tsai-Wu constraint values found for the components in the problem domain for one of the 100 randomly selected design values. For the 90 and 0 degree ply angles, there is symmetry in the stress values found on the components in the problem domain, while for the -45 and 45 degree plies, there is anti-symmetry for the constraint values evaluated on the domain. For the parameter samples evaluated on the problem domain, the most critical constraint value was consistently found on the 90 degree ply closer to boundary of the problem domain.

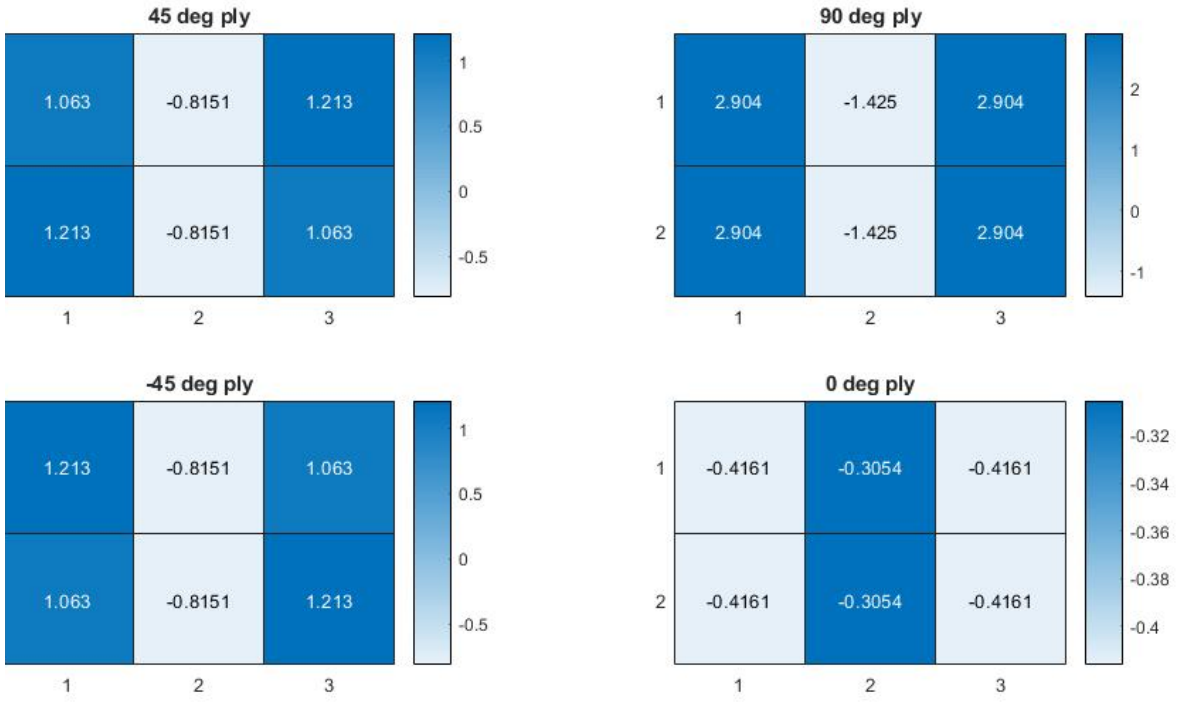

Figure 57: Maximum Tsai-Wu stress constraint values calculated for the various plies in the problem domain

8.2.2.1 Overview Of The Convergence

The observations corresponding to the 100 design points considered were collected. For the same settings (i.e. edge and bubble space refinement parameters or mesh density), the observed metrics of interest were found to be stochastic in nature. As such, the convergence behavior of both the mean of the metrics and their distributions were investigated.

8.2.2.2 Convergence Behavior Of The Mean Of The Metrics With Model Refinement

Figure 58, shows the convergence behavior of the mean of the relative errors for the most active Tsai-Wu constraint values and their derivatives for the 100 design points that were investigated. For the top plot, the absolute value of the relative error between the Tsai-Wu constraint (σ) and its approximation (σ_a) is shown on the ordinate; while the average number edge modes required for each nodal degree

of freedom per edge is shown on the abisca. The refinement of the bubble solution approximation for the SCRBE approach is shown with various trend lines.

For both approximation approaches, there appears to be rapid convergence to the mean of the Tsai Wu constraint values predicted by the truth model relative to the approximations made with FEM mesh refinement. The "edge modes" for the FEM mesh refinement is the finite element basis functions associated with the interior nodes on the edge. Indeed, with the exception of when $\eta_b = 1e-2$, using an average of only 4 edge modes per nodal degree of freedom per edge leads to approximation with less than 1.0% of the truth model's prediction. The refinement of the mesh used on the FEM model leads to comparatively much slower convergence of the constraint prediction. The best approximation achieved by this approach was 1% error in the range of values considered. For the SCRBE method, the influence of the bubble space fidelity parameter, η_b, seems to be more pronounced as the number of global interface modes used increases. For an increasing quantity of edge modes, refinement of η_b leads to an approximation refinement of several orders of magnitude.

The mean of the relative error of the approximations furnished by the SCRBE-DEIM method converges to 0.3%. However, it is clear that the SCRBE approach is superior in its convergence as the model parameters are refined. Both methods are comparable in accuracy in the domain of $\eta_{edge} \in [1e{-}1.50, 1e0]$ or $N \in [2.00, 4.00]$ edge modes per edge per nodal dof. Beyond this domain, further refinement does not appear to have a significant influence on the SCRBE-DEIM approach. Despite this observation, the SCRBE-DEIM still provides an excellent approximation of the constraint.

Regarding the approximation of the constraint derivative (bottom plot in figure 58), both methods display fast convergence as the model parameters are refined. The approximation furnished by the SCRBE-DEIM method appears to be slightly better for the derivative; however, its convergence still stalls beyond a certain level

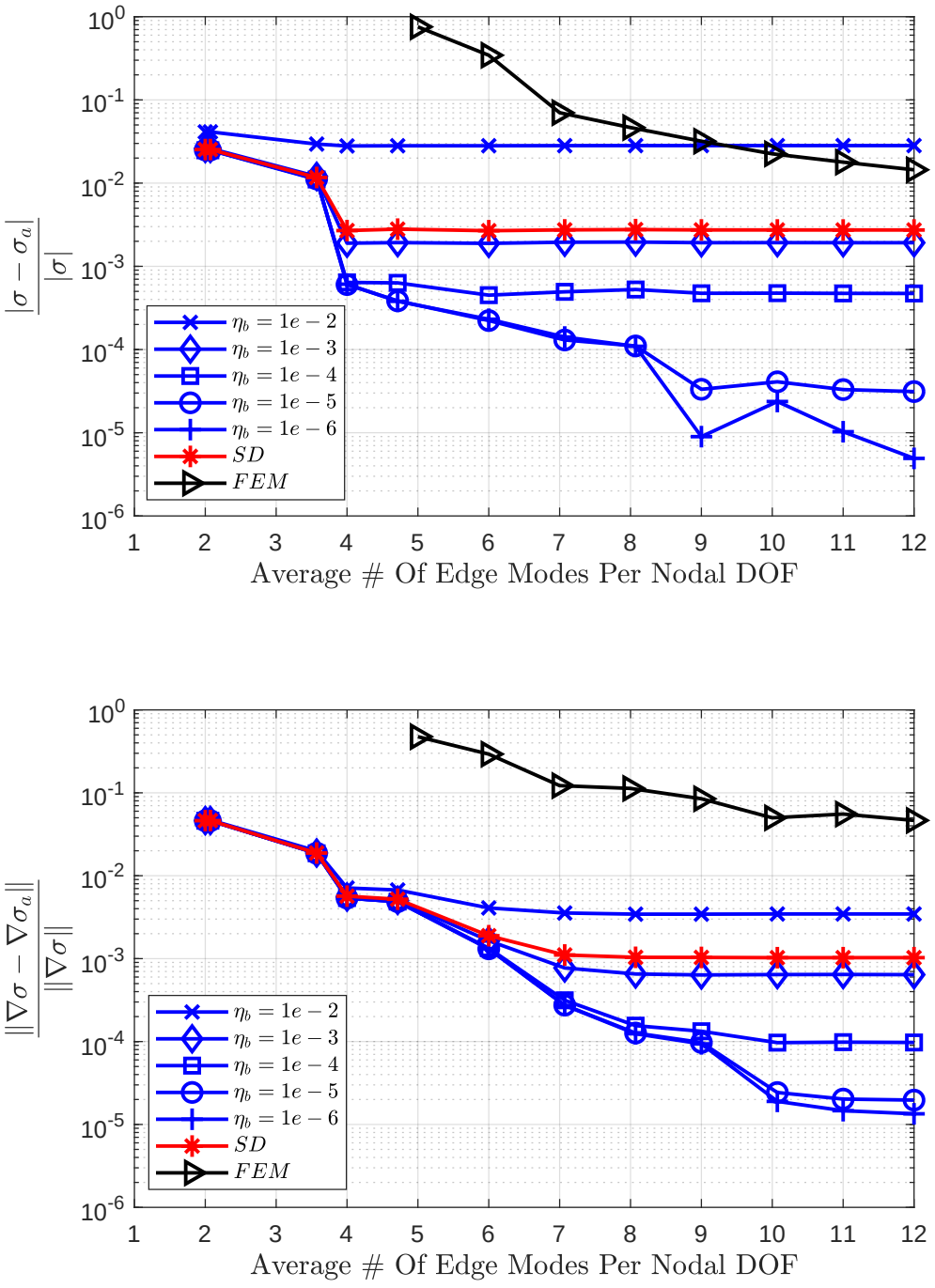

Figure 58: Convergence of the approximation of the most active Tsai-Wu constraint. *Top*: Mean of the observations. *Bottom*: the mean of the observation derivatives

of the refinement. The associated domain extends to $\eta_{edge} \in [1e{-}2.50, 1e0]$ or $N \in [2.00, 6.00]$ edge modes per edge per nodal dof.

8.2.2.3 Distributions Of The Approximation Error With Mesh Refinement

The distributions of the relative error for the maximum constraint values for the various settings of the refinement parameters are shown in three groups of plots i.e. figures 59 to 61. The analogous plots for the derivatives are shown in figures 62 to 64. The distributions are presented in the form of box-plots. Each box in the plots has the following characteristics:

- The red line within the blue box represents the median of the distribution
- The bottom and top lines of the blue box represent the 25^{th} and 75^{th} percentile values of the distribution, respectively
- The whiskers (black lines) denote the extent of the distributed values that are not considered outliers
- Finally, the red data points are those observations that are considered outliers

For the estimates corresponding to the SCRBE approach for the constraint value, (first 5 boxes in each subplot in figures 59 to 61), it can be seen that the simultaneous refinement of the number of edge modes and the bubble modes has the effect of lowering the median value of the residual error, as well as lowering the upper limit of the distributions. On the other hand, for the SCRBE-DEIM method, apart from an initial decrease in these terms for smaller values of the number of edge modes used (roughly $N = 2$ to $N = 4$), further refinement does not appear to have a significant impact on the quality of the approximation produced. In fact, the upper limits of the error distributions do not appear to get better than $1e-2$, i.e. an upper limit of error 1%.

Similar behavior can be observed for the derivative of the constraint with refinement of the model parameters. However, for the SCRBE-DEIM approach, the upper

limit of the error distribution for the derivatives becomes lower than 1%.

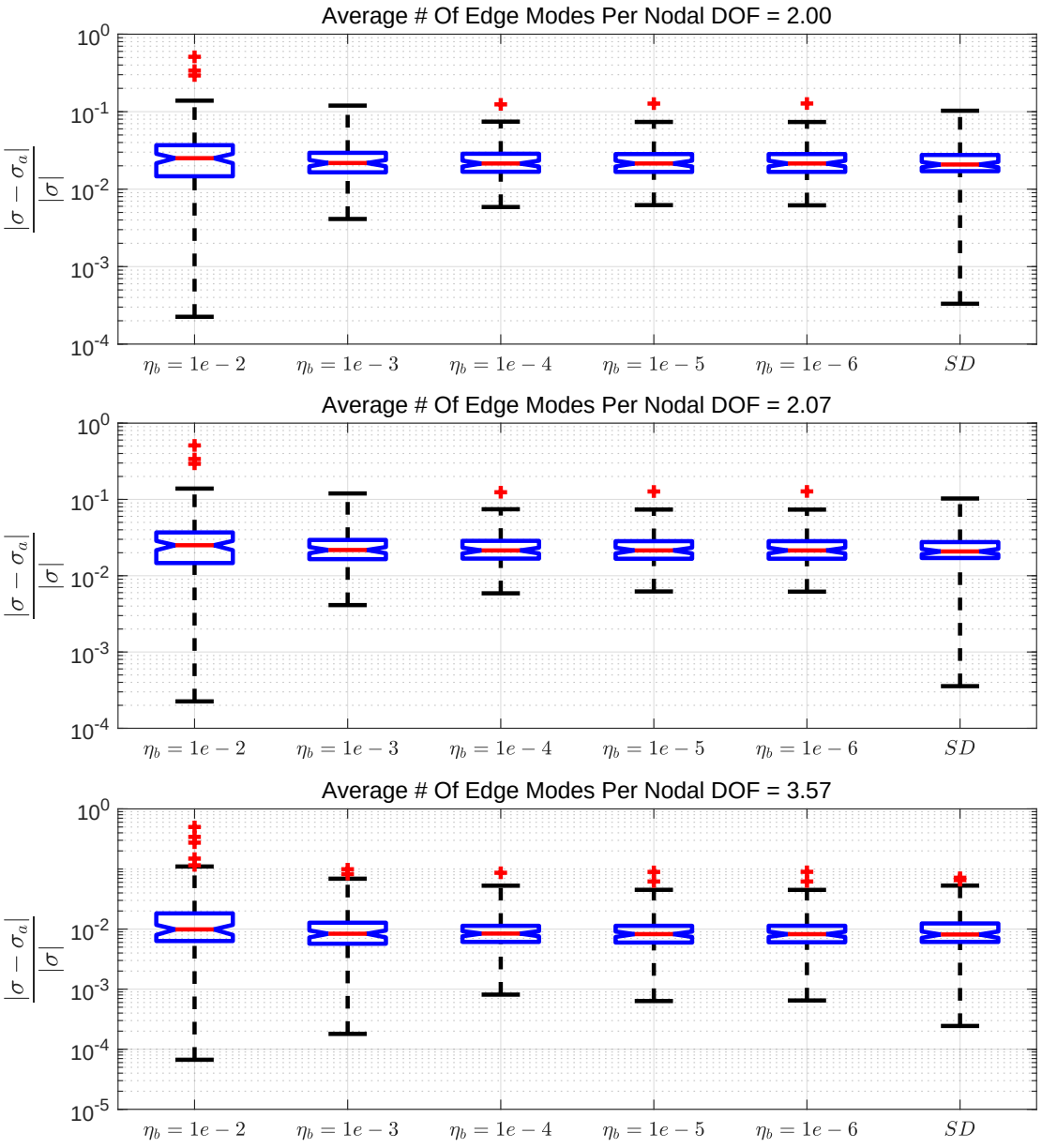

Figure 59: Box plots for the maximum Tsai-Wu approximations - Group 1

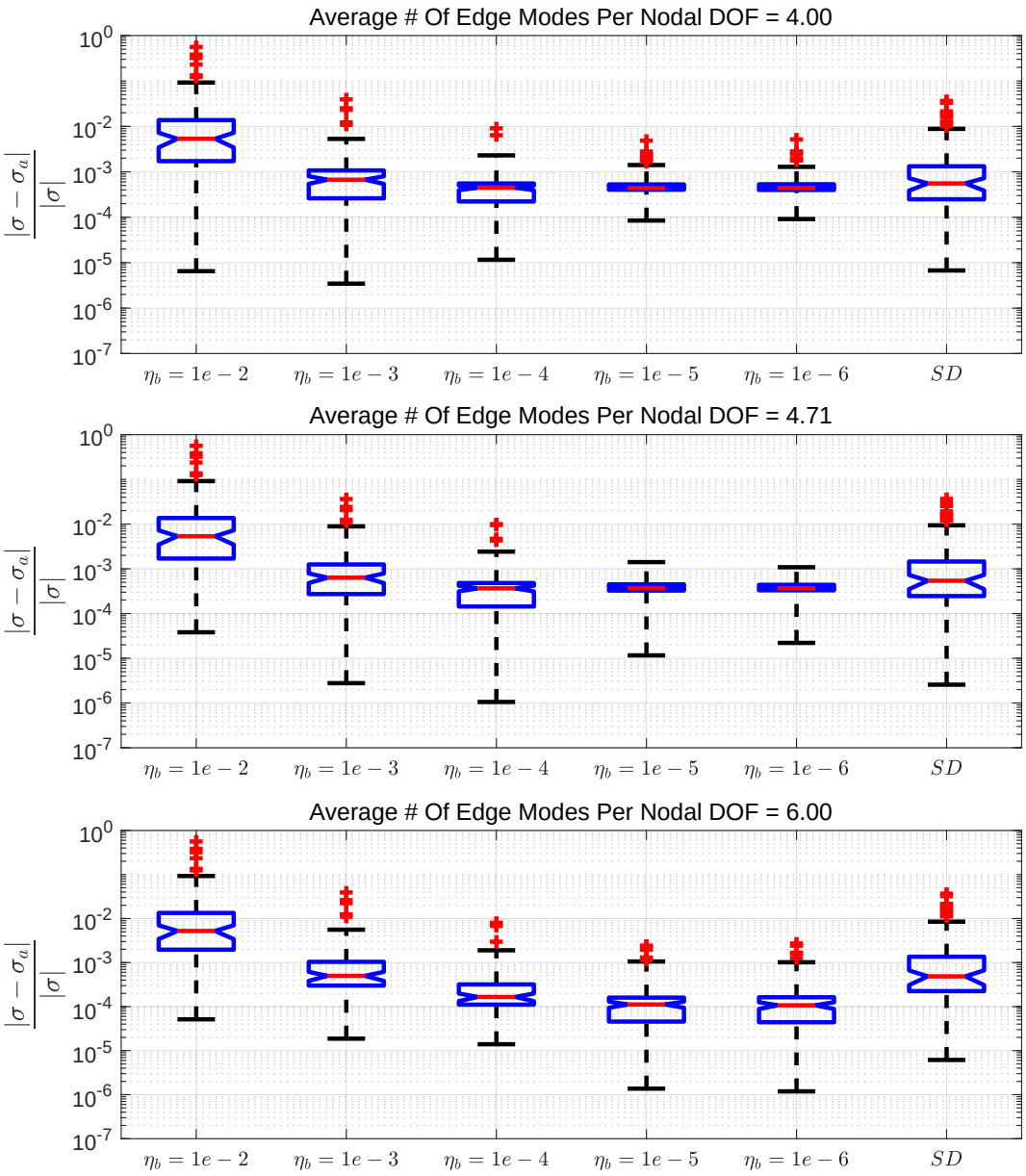

Figure 60: Box plots for the maximum Tsai-Wu approximations - Group 2

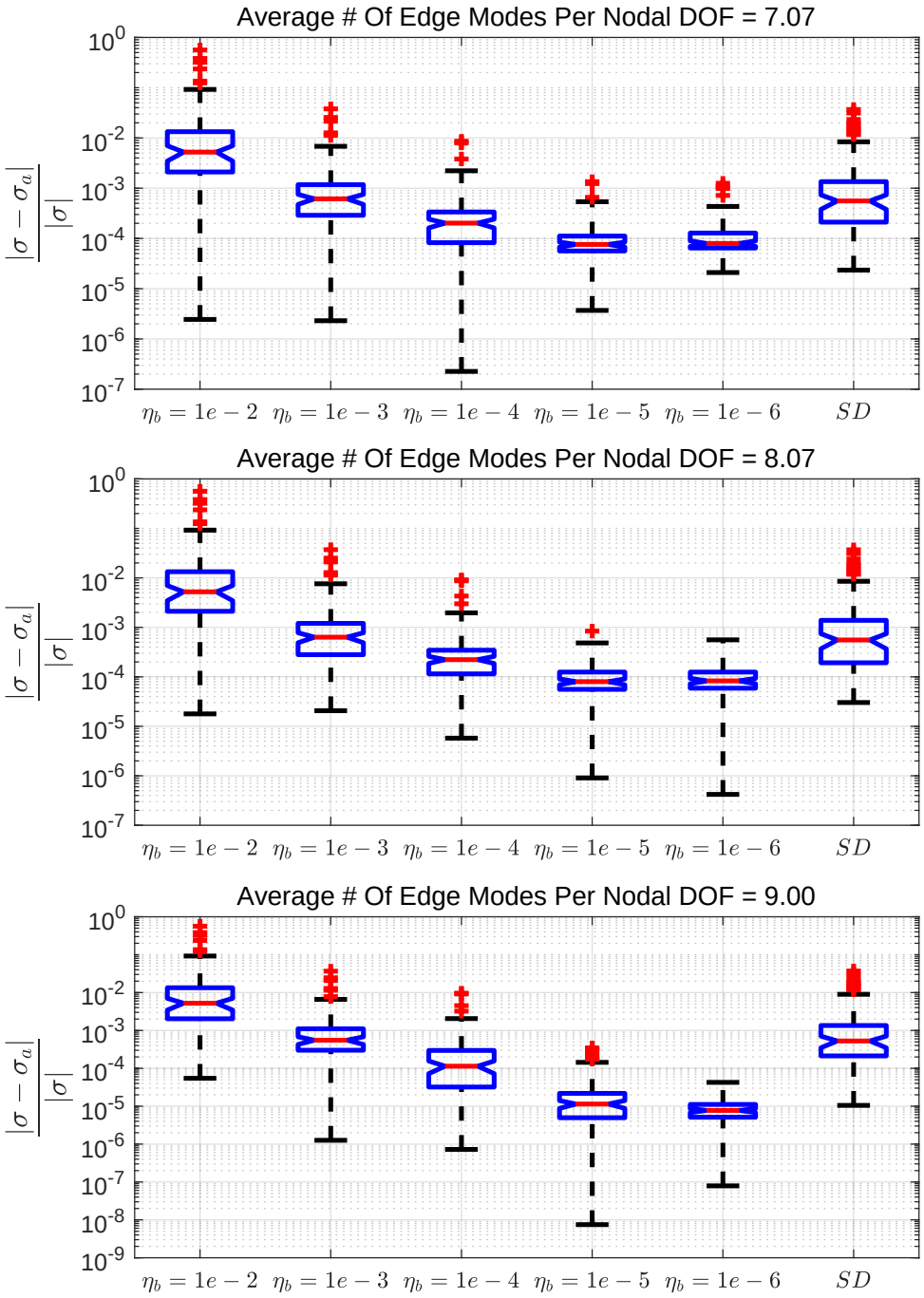

Figure 61: Box plots for the maximum Tsai-Wu approximations - Group 3

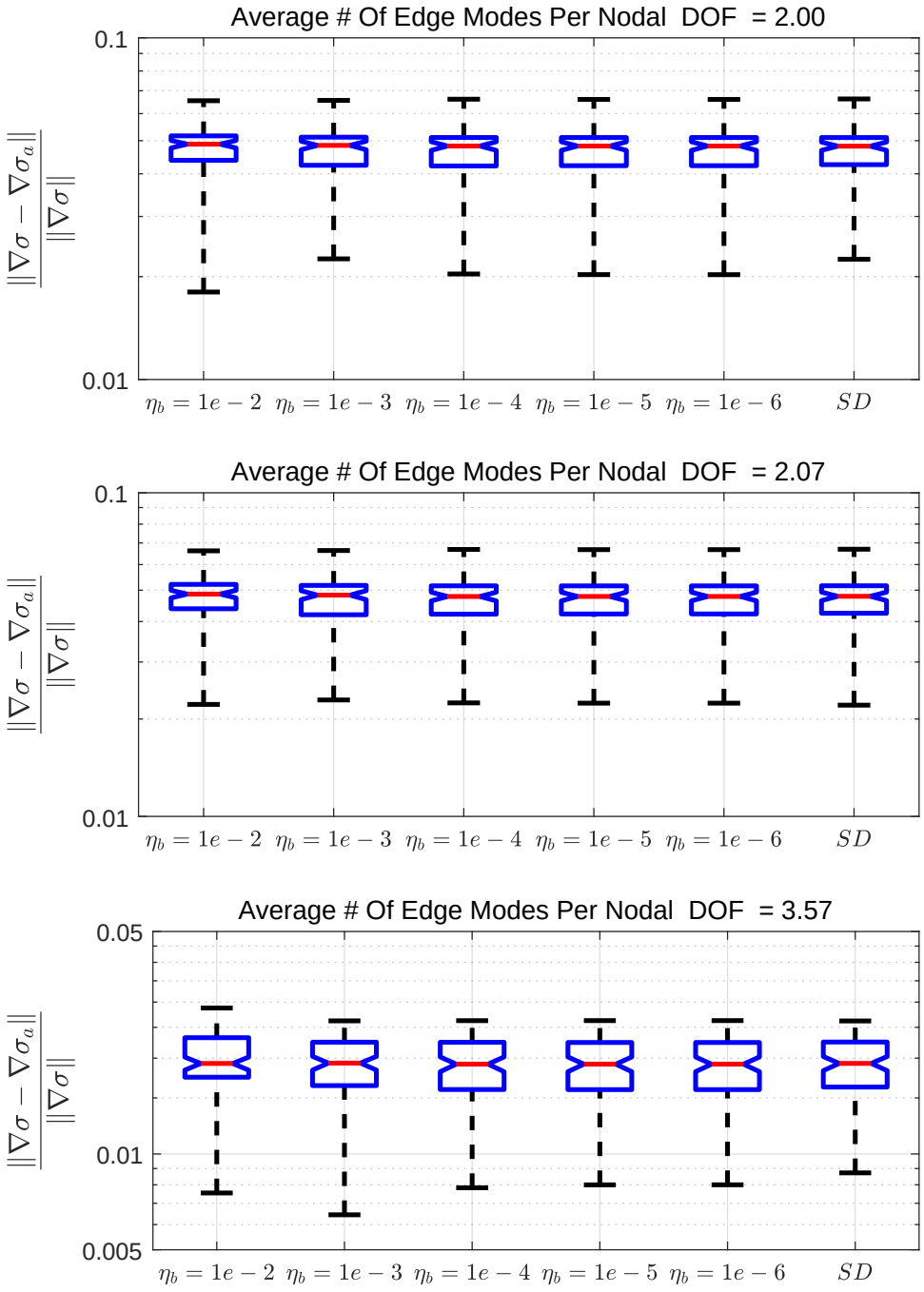

Figure 62: Box plots for the maximum Tsai-Wu derivative approximations - Group 1

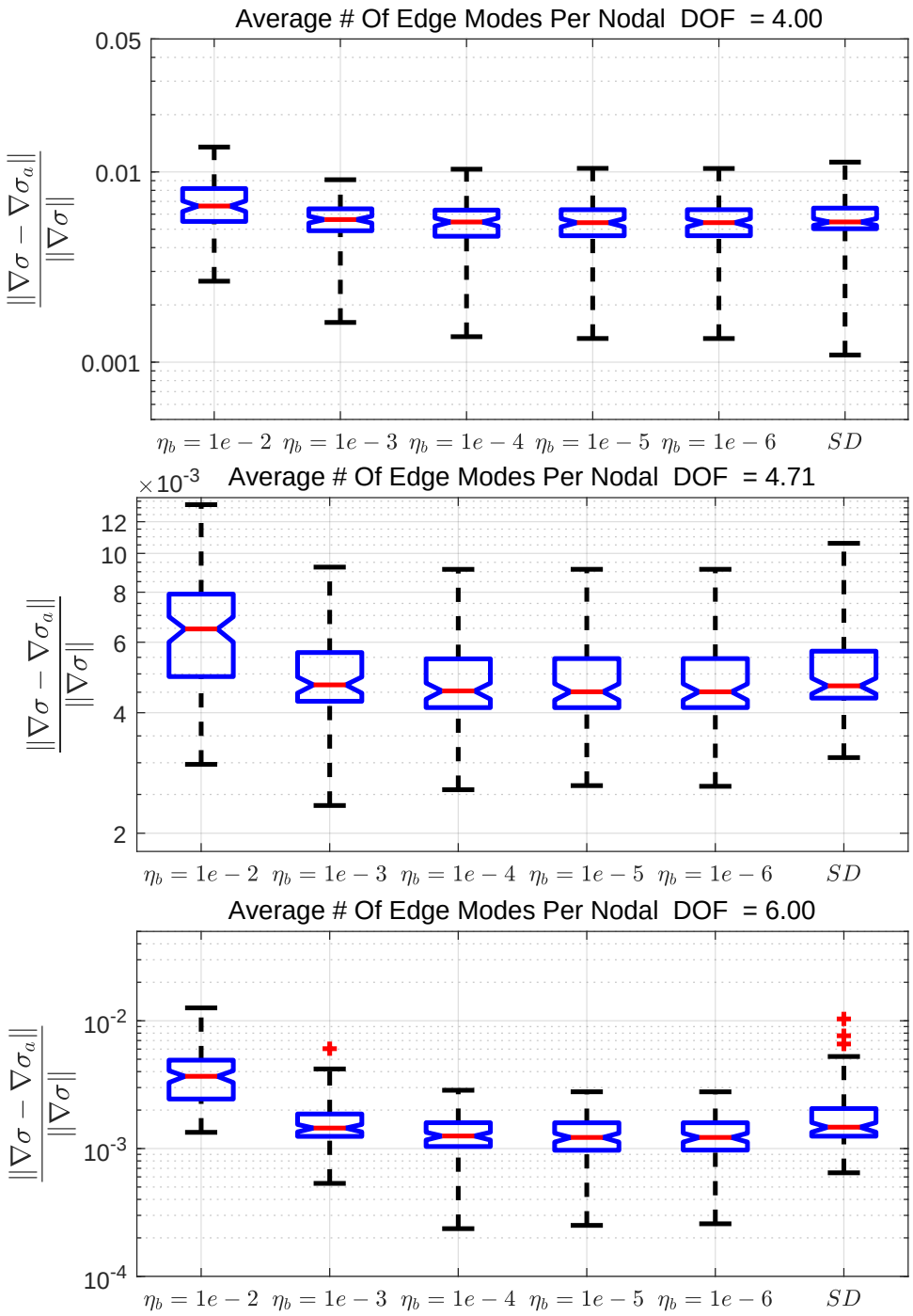

Figure 63: Box plots for the maximum Tsai-Wu derivative approximations - Group 2

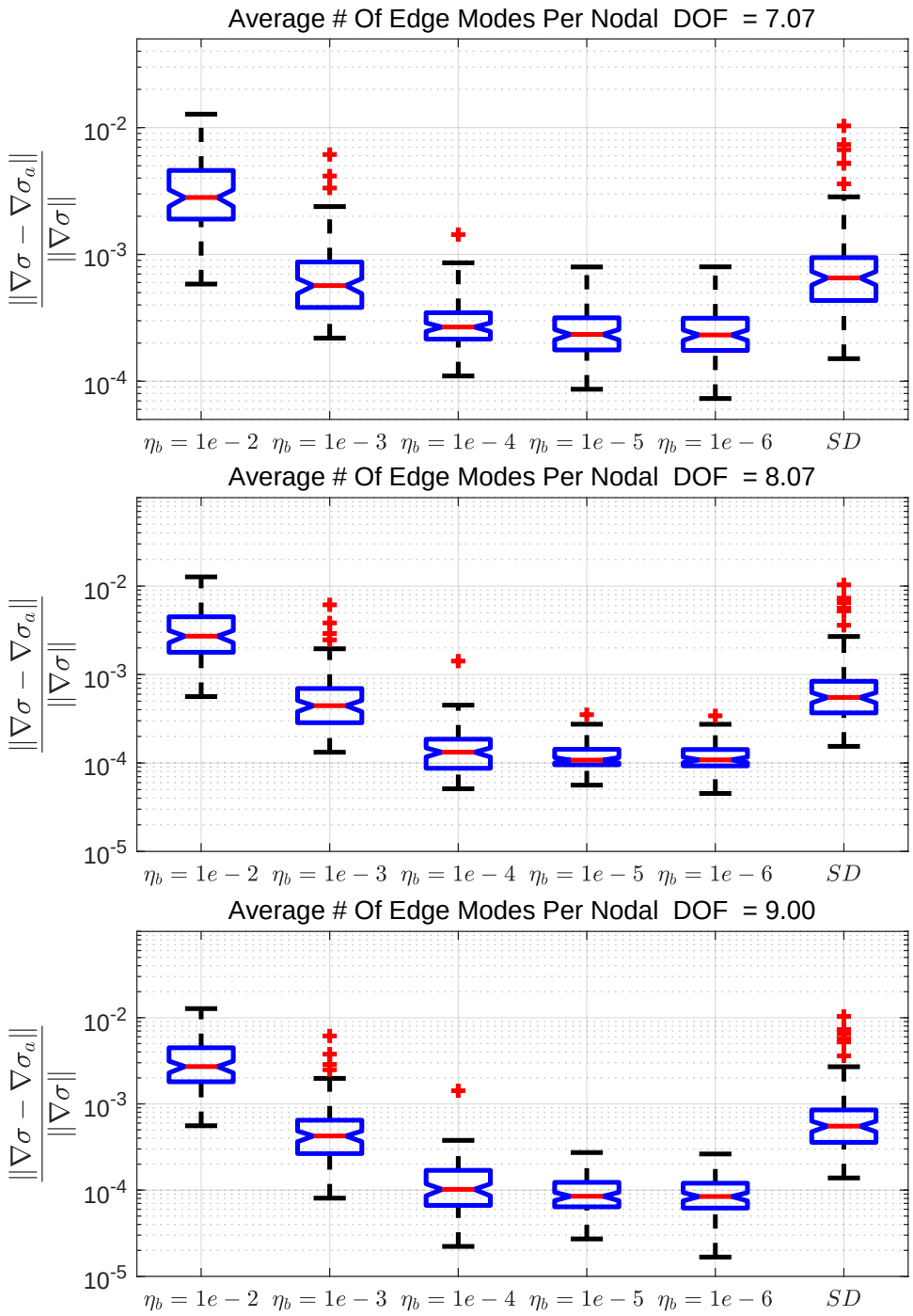

Figure 64: Box plots for the maximum Tsai-Wu derivative approximations - Group 3

8.2.3 Experiment 1(b): Timing Analysis Of The Approaches

The following procedure was followed for the timing analysis

- **Step 1**: A random point was selected within the feasible space of the parameter domain associated with problem domain variant 2. Its physical domain was constructed with both the SCRBE and SCRBE-DEIM approaches.
- **Step 2**: The time required to assemble the contributions to the Schur complement, the outputs and their derivatives from the middle three rows of components were measured and averaged over 15 repetitions.
- **Step 3**: The average times were recorded as both the SCRBE and SCRBE-DEIM models were refined

Figure 65 shows the average serial computational time required to compute the ingredients of the SCRBE and SCRBE-DEIM approximations. This includes the local Schur stiffness matrices, the parameter-dependent, solution recovery mappings and their derivatives. The computational time required to solve for the state solution and its derivative with respect to all of the parameters of the problem was at most $0.15s$. This value corresponds to the maximum number of global interface modes considered. This observation is consistent with the expectations from literature; in that, the formation of the ingredients of the Schur complement and the problem outputs accounts for the majority of the computational time required by the method.

As revealed by the analysis in section 8.2.2.2, the two methods are comparable in accuracy in the lower end of the domain of edge modes, i.e. N (i.e. $2 \leq N \leq 4$). In this region, the speed-ups afforded by the SCRBE-DEIM method over the SCRBE method ranges from $2.91 - 5.73$ times. As discussed in section 2.5.2, the task of computing the ingredients to these approximations is embarrassingly parallel. This implies that the computational time scales linearly with the number of components that are being evaluated at any one time, whether serially or on a single processor in a parallel computing architecture. Due to this linear growth, the time difference between the methods should become especially significant when a large number of components are being considered.

It is also noteworthy that the computational time required for the SCRBE-DEIM method appears to the insensitive to the number of global interface modes used in the approximation in the lower end of the domain considered. This indicates that the dominant factor in the computation is the time required to evaluate the underlying surrogate models. In the present implementation, the number of surrogate models used does not vary with the refinement parameters of the model and presents the same computational overhead for all of the values that are considered.

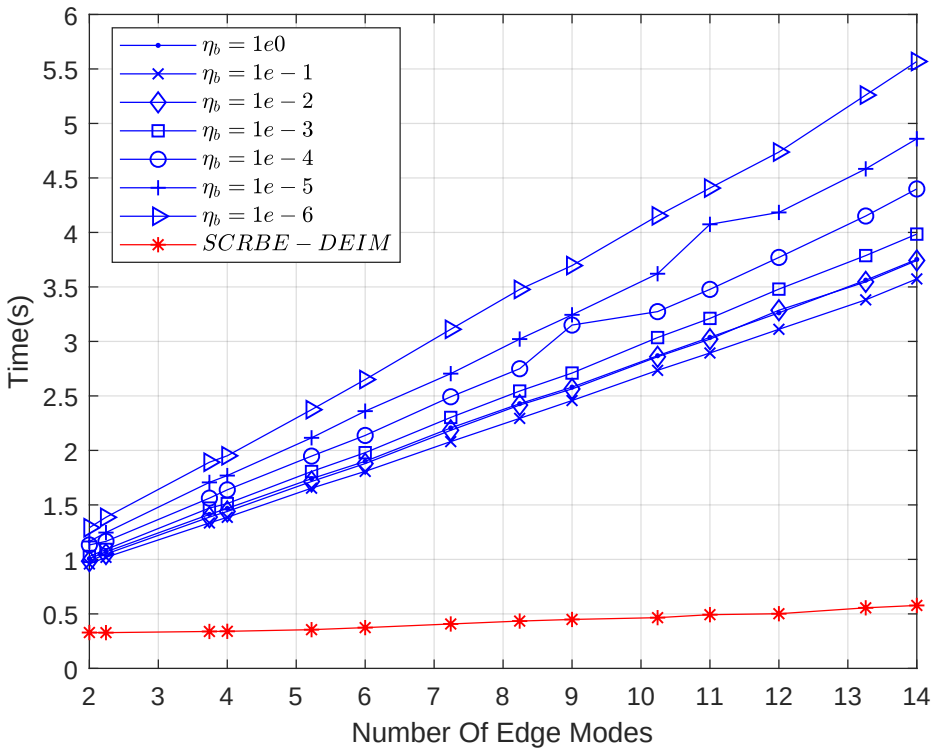

Figure 65: Average computational time required to form the local Schur stiffness matrices, the strain approximation matrices and their derivatives

8.3 Experiment 2: Optimization Study

The purpose of the second experiment is to determine if the SCRBE-DEIM approach is a suitable substitute for the SCRBE method as a means of providing estimates of the constraints and their derivatives in a gradient-based optimization context.

8.3.1 Procedure For Experiment 2

The following procedure was used to generate results for experiment 2

- **Step 1:** In a similar fashion to experiment #1, a truth model and the two SCRBE variants were constructed for problem domain variant 2.
- **Step 2:** As described in section 7.3, the region of the domain being optimized corresponds to the middle three rows of the domain. The top and bottom row of components are used to determine the reaction forces applied the boundary of the domain of interest after Dirichlet boundary conditions are applied. A single design point is chosen in the feasible space of the parameter domain of the archetype component and is replicated for all the components in the top and bottom regions of the problem domain.
- **Step 3:** Using the associated stiffness matrices and the boundary displacement fields, the reactions forces on the periphery of the interior domain of interest are calculated and fixed. For this problem, the magnitude of the displacement is $6mm$.
- **Step 4:** For the interior domain, three random design points within the feasible region of the parameter space for the problem domain were selected as the initial points of the optimization procedure.
- **Step 5:** The interior-point optimization algorithm [163] was used to optimize the two SCRBE variants of the problem with various settings of η_{edge} and η_b. In order to foster an "apples-to-apples" comparison, the same parameters and tolerances were used for the optimizer in all cases.
- **Step 6:** For the optimal solutions furnished by the optimization procedures, the truth model was used to validate the results.

Correspondingly, the optimization problem is:

$$\text{Optimize :} \qquad m(\mu) \tag{215}$$

$$\text{w.r.t :} \qquad \mu \in \mathcal{D}, \;\; x \in \Omega \tag{216}$$

$$\text{Subject to :} \qquad \mathcal{R}\left(u_s(\mu), \mu\right) = \mathbb{K}_{uu}(\mu) u_s - \mathbb{K}_{u0}(\bar{\mu}) u_0 = 0 \tag{217}$$

$$\sigma_j^{\text{TW}}\left(u_s(\mu, x), \mu\right) \leq 0, \quad \text{for } \; 1 \leq j \leq 72 \tag{218}$$

$$\textbf{lamConstraints}\left(\mu\right) + c_0 \leq 0 \tag{219}$$

Here:

- μ - the parameter vector (design variables) for the inner three rows of components
- $\bar{\mu}$ - the fixed parameter vector used for the outer rows of components
- x - the location in the physical domain Ω
- u_s, u_0 - the state solution on the internal global interfaces and boundaries, respectively
- m - the total mass associated with the inner three rows of components
- $\mathcal{R}\left(u_s(\mu), \mu\right)$ - the residual of the discretized, weak form of the PDE
- $\mathbb{K}_{uu}$, $\mathbb{K}_{u0}$ - the global Schur complement stiffness matrices.
- σ_j^{TW} - the j^{th} Tsai-Wu constraints
- c_0 - the heuristic constant chosen to curtail the lamination parameter design space

8.3.2 Results From Experiment 2

The main results of experiment 2 are presented in this section. A typical distribution of the component masses (kg) that results after the convergence of the optimization procedures is shown in figure 66.

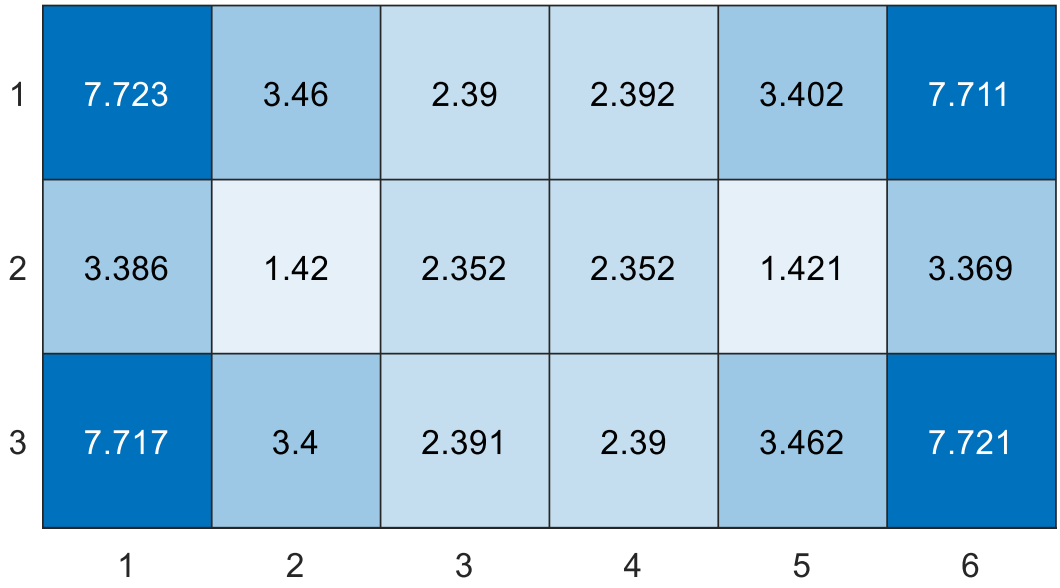

Figure 66: Mass distribution (kg) on the component plates in the domain

It can be seen here that based on the local masses, the components in the corners of the problem domain tend to require more reinforcement compared to those on the interior. This observation can perhaps be attributed to the large reaction stresses that develop from constraining both the displacements on the left and right boundaries of the problem domain. These stresses tend to become less pronounced as one moves away from the corners of the problem domain.

Figure 67 shows the optimal (total) masses found by the various optimization procedures. In each subplot, the optimal masses found by the SCRBE method correspond to the first four columns in the groupings. The final column in each grouping corresponds to the optimum found by the SCRBE-DEIM approach. It can be seen here that the optimal values found by these procedures are fairly close to each other. The optimal masses found fall into the range of $67 - 70kg$. The mass values found seems to be stochastic and appear to not only be affected by the accuracy of the constraint approximations, but also by termination criteria specified for the optimization

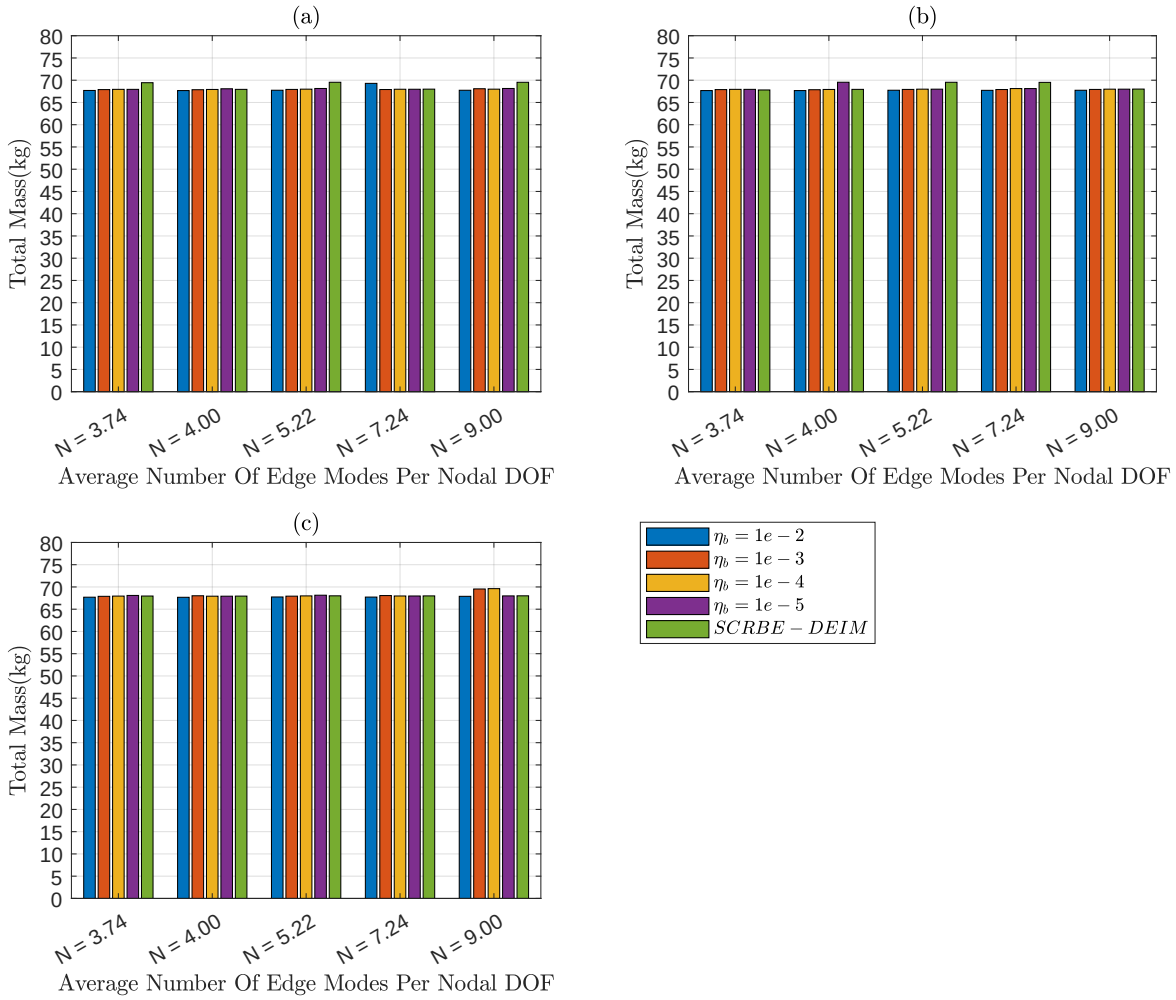

Figure 67: Optimal masses found by the optimization procedures for the three initial design points

algorithm. Among the observations for the three initial design points, there are places were the SCRBE-DEIM approach yields higher masses than its SCRBE counterpart. However, the maximum difference is roughly 2%.

8.3.2.1 Convergence Results For The Tsai-Wu Constraint Values

The form of the Tsai-Wu constraint is such that very small values can be observed at various design points in the parameter domain. This would lead to badly scaled problem when the relative error is calculated and would render the estimates to be ineffective when assessing the suitability of the methods. As an alternative, the

measure of effectiveness that will be used is how well the SCRBE and SCRBE-DEIM methods are able to provide optimal solutions that do not violate the constraints of the problem when they are evaluated by the truth model.

The most active constraint values - as evaluated by the truth model - for the various refinement settings and initial points are presented in figure 68. The constraint tolerance set for the optimizer was $1e-4$. For the SCRBE approach, the most active constraint values tend to decrease with refinement of both η_{edge} and η_b for the three initial points considered. On the other hand, the value predicted by SCRBE-DEIM approach decreases initially and then asymptotes to values of at most $8e-3$ as the model is refined. Since the Tsai-Wu constraint is normalized, this value represents a 0.8% violation outside the feasible region of the design space. These results and the results presented in section 8.2.2.2 indicate that with adequate refinement, the SCRBE gives the better chance between the two approaches of finding a candidate design point that satisfies the constraints of the problem.

8.3.2.2 Computational Overhead Analysis For The Approaches

The final analysis in this section is the comparison of the computational overhead required by the SCRBE and SCRBE-DEIM in performing the optimization. Figure 70 shows the number of function and derivative calls required by the optimization procedures. In one call to either model, the function value, constraint values and their derivatives are all supplied simultaneously. The number of function and derivative calls seem to vary somewhat across optimization run; with no clear distinction as to which method and setting requires the least functions calls in the optimization procedure.

Using this data plus the timing data presented in figure 65, the overhead required to assemble the ingredients to the Schur complement systems and outputs was estimated. These data are presented in figure 71. It is clear that the SCRBE-DEIM

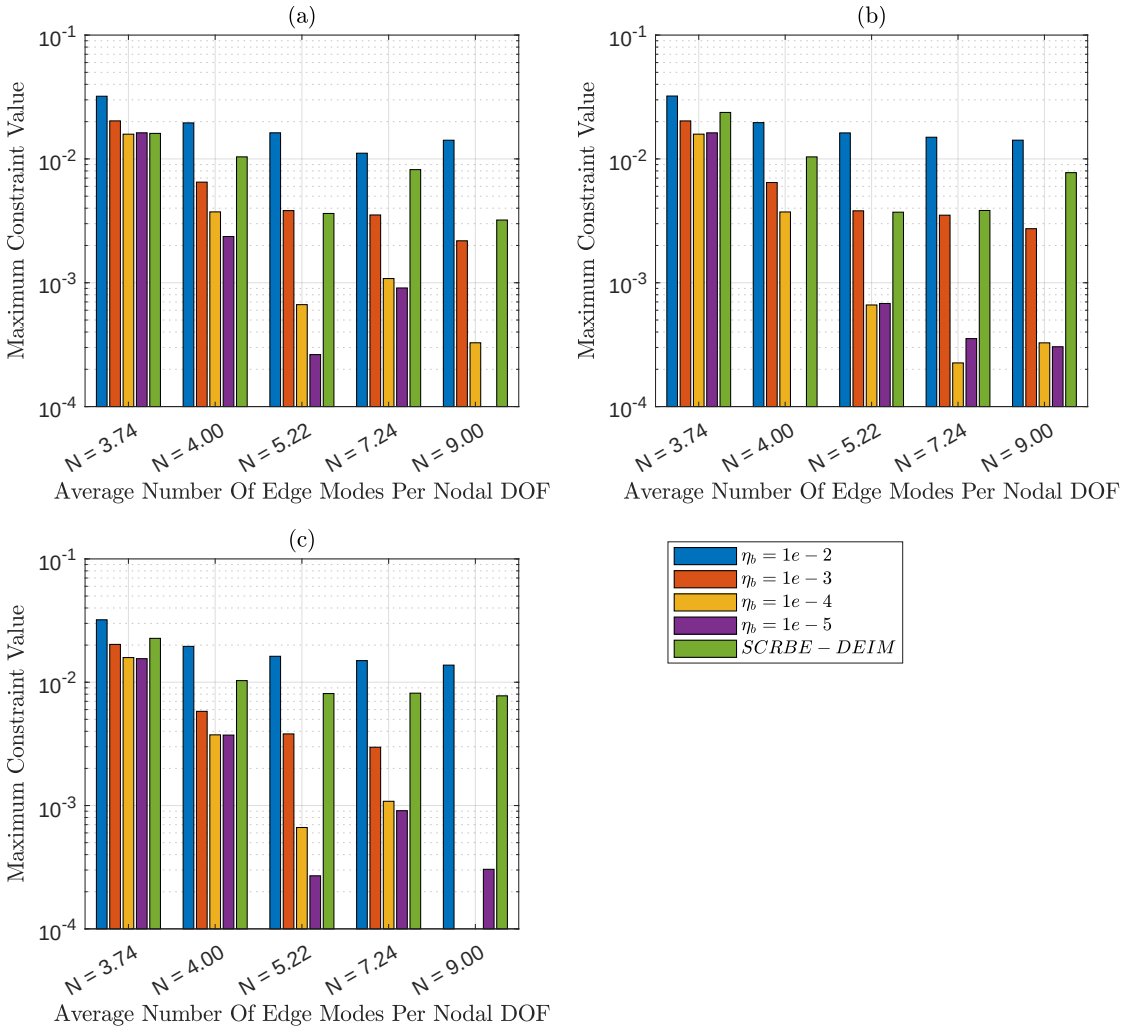

Figure 68: The most active constraints when the optimal solutions are evaluated by the truth model for the three initial design points

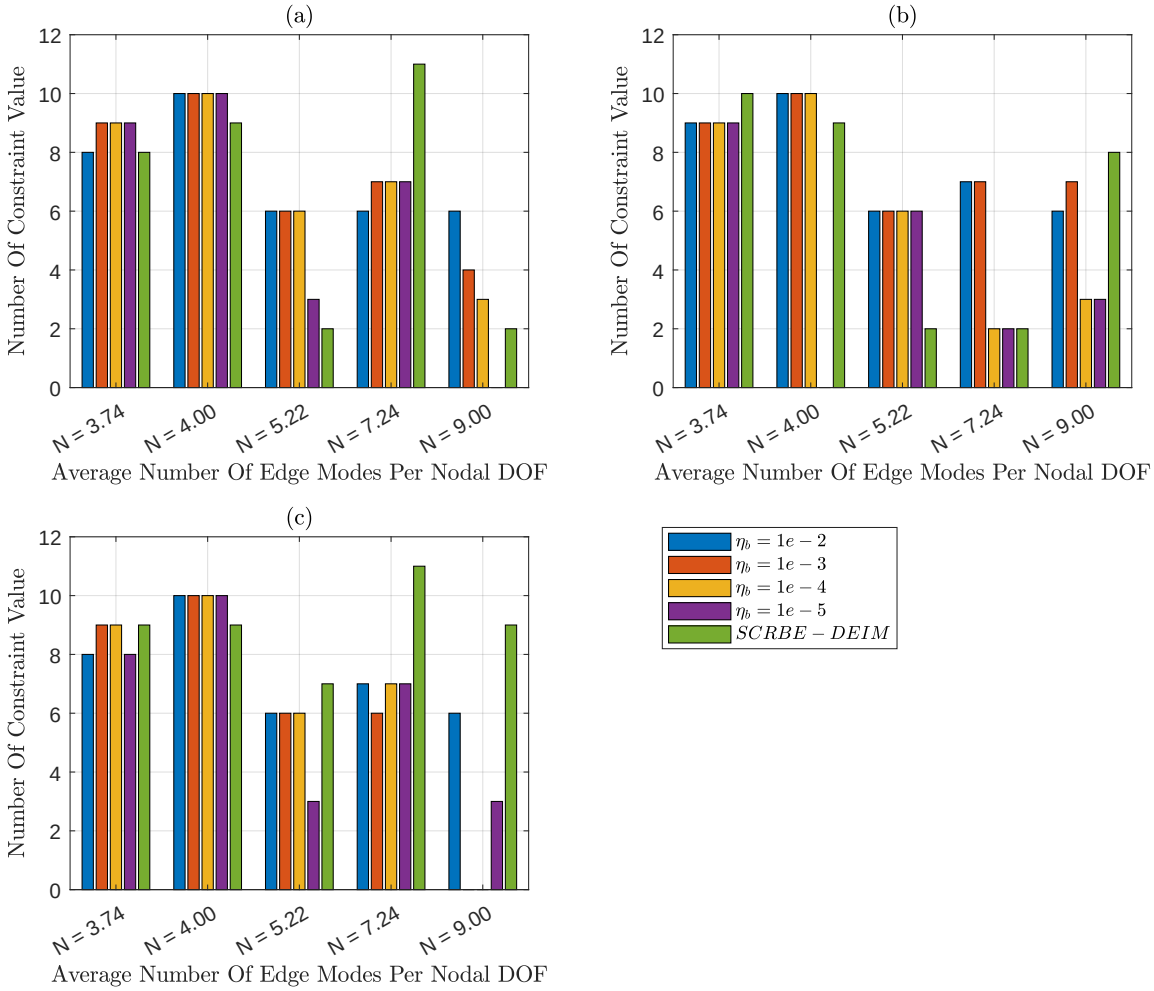

Figure 69: Number of active constraints when the optimal solutions are evaluated by the truth model for the three initial design points

approach provides considerable savings in the computational overhead time relative to the SCRBE approach. This becomes especially significant when the number of global interface modes increases. However, as discussed in section 8.2.2.2, the accuracy of the two methods is comparable only in the lower end of the domain for the number of edge modes considered. For the lowest number of edge modes considered (i.e. $N = 3.74$), the savings afforded by the SCRBE-DEIM approach was approximately $75 - 85\%$. The savings is computational time is more significant as the model is refined; however, this becomes meaningless beyond after a while due to the limitation in accuracy. Therefore, it is incumbent on the designer to establish this point where further refinement is pointless.

8.4 Chapter Summary

In this chapter, results were presented for the numerical experiments performed on the canonical problem. The results indicate that both the SCRBE and SCRBE-DEIM methods achieve relatively fast convergence as the fidelity parameters are refined ($< 1\%$ error). However, the SCRBE method is superior in its convergence beyond this threshold, while the SCRBE-DEIM somewhat stalls. When compared in an optimization framework, it is apparent that the SCRBE-DEIM approach achieves a significant saving in the computational overhead but with a smaller chance of satisfying all of the constraints on the problem as evaluated by the truth model. However, the associated error level is not overbearing and invites further examination.

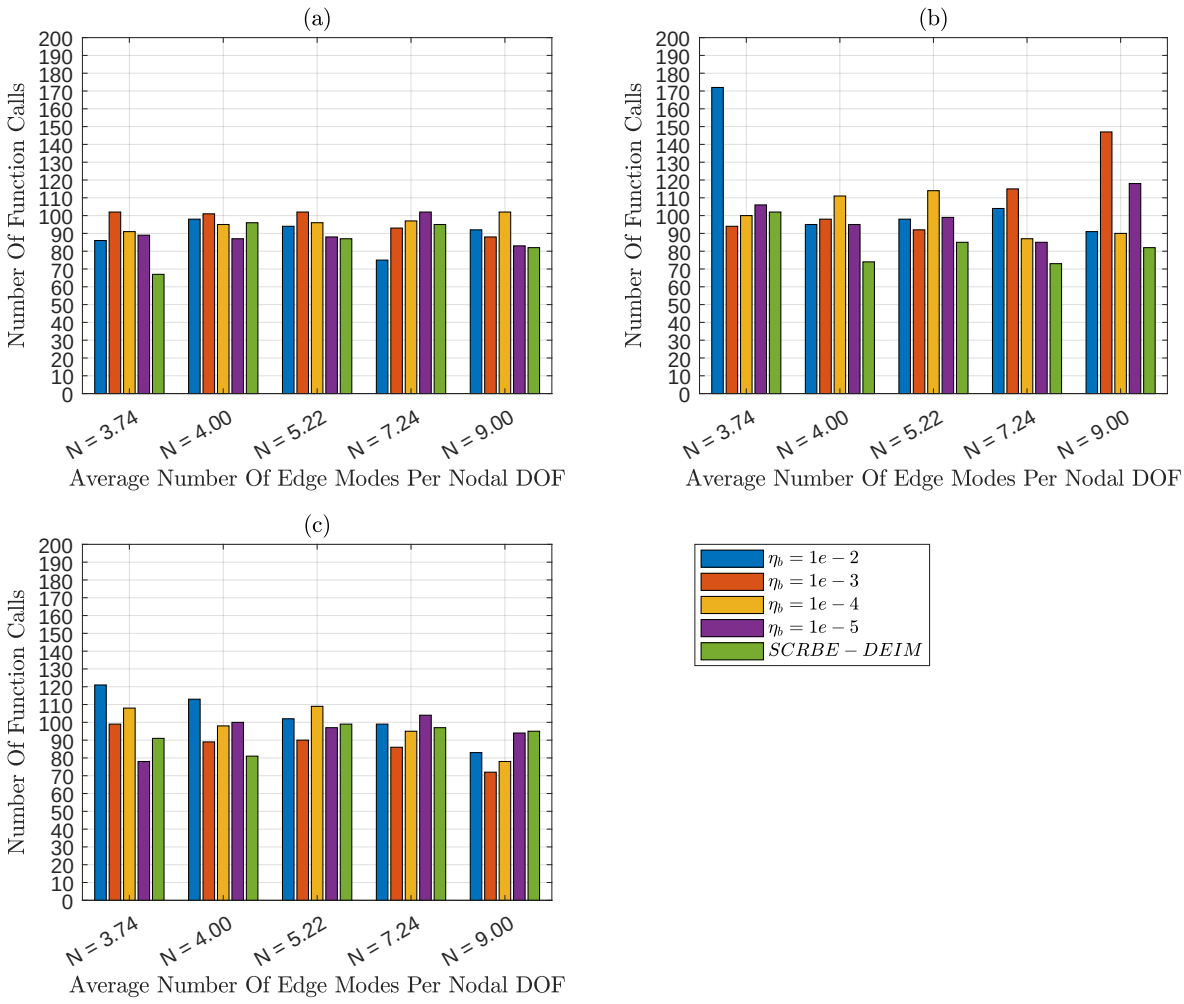

Figure 70: The number of function and derivative calls made by the optimization procedures

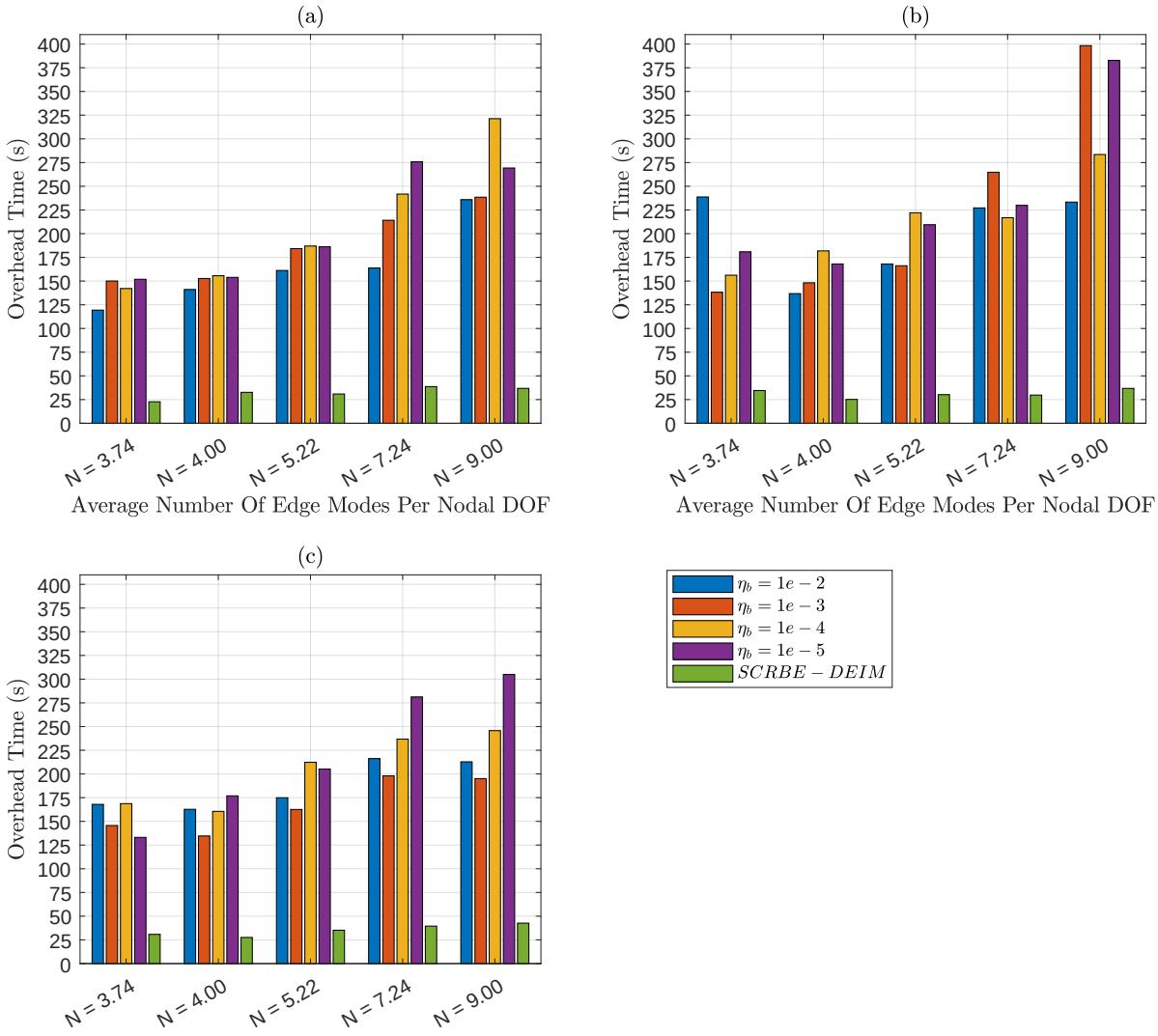

Figure 71: Estimated total computational overhead time required to perform the optimization procedures

Chapter IX

CONCLUSIONS AND FUTURE WORK

In light of the expected environmental challenges associated with increased air traffic over the years to come, the aviation industry has sought to incorporate a wide range of technologies in the design of new vehicles. Among these technologies are a set of structural technologies that are expected to reduce the weight of the airframe of these new concepts. It is imperative that the impact of these new technologies be considered at the conceptual level of aerospace design. Although the conceptual level tools for weight estimation and structural design have been suitable in their function for traditional aircraft, they may be unsuitable for newer, unconventional materials, structural concepts and vehicles. The finite element method has been highlighted by literature as the most accurate method available for numerical structural analysis and as a result for determining the weight of the airframe. Unfortunately, its use in early design has been restricted due to its associated computational expense. A class of techniques, known collectively as Reduced Basis Approximation, has arisen in applied mathematics for the expedient numerical solution of partial differential equations. Specifically, the Static Condensation Reduced Basis Element (SCRBE) method is promising for large-scale airframe structural design, due to its versatility and its computational expediency.

The focus on this research is to identify an approach with which the SCRBE method could be applied for the purpose of conceptual-level, linear-static, aircraft structural design; primarily as a means of enabling weight estimation. This included identifying ways in which common conceptual level structural constraints and their derivatives could be included into the framework, and a way that the framework

itself could be expedited. This process was illustrated on a simple design problem to first foster and understanding of the presented methods. In the following sections, the research questions and hypotheses will be addressed based on the experimental results; as well as: the main limitations; avenues for improvement; and proposed future work will be identified.

9.1 Research Questions And Hypotheses

9.1.1 RQ1 And HYP1

RQ 1.0: What is a suitable approach for determining empirical interface subspaces that can concisely represent the constraints and their derivatives as the fidelity of the model is refined?

HYP 1.0: Relative to the underlying finite element mesh, the use of the empirical edge subspaces and the associated empirical bubble spaces should lead to fast convergence of the estimated constraints and their derivatives as the model is refined.

Based on the results presented in section 8.2.2.2 for a domain featuring homogeneous parameter values, the use of the empirical edge modes and the empirical bubble spaces lead to fairly fast convergence to the evaluated constraint and its derivative when compared to the finite element mesh of the truth model. Indeed, for the same level of accuracy, both the SCRBE and SRBE-DEIM approaches were shown to lead to Schur complements with smaller sizes relative to problem formulated with the approximation space of the FEM. While these results are promising, in a similar manner to the conclusions drawn by Eftang [99] in his initial proposal for empirical *port mode* training, he noted that the use of empirical modes becomes even more impressive when two dimensional interfaces are used. It is desirable to eventually evaluate this procedure on two dimensional interfaces, such as stringer-stiffened panels or perhaps

even full sections in aircraft design.

9.1.2 RQ2 And HYP2

RQ 2.0: What is an alternative approach for generating the ingredients of the SCRBE procedure that will help to alleviate the computational overhead, while not drastically increasing the approximation error?

HYP 2.0: Based on a time complexity analysis, the SCRBE-DEIM approach should help to alleviate some of the computational overhead of the SCRBE approach. However, a reduction is accuracy is expected due to the use of interpolation techniques in multiple places

Based on the results presented in section 8.2.2.2, it can be seen that the SCRBE-DEIM approach achieves a similar rate of convergence as the SCRBE method to about an accuracy level of 0.3% mean relative error. However, after this point, further refinement to the model does not have significant influence on the accuracy provided. On the other hand, the speed-ups afforded by the SCRBE-DEIM model are rather significant relative to the SCRBE model and led to a significant reduction in overhead required to produce the elements for the static condensation and the constraint outputs.

9.1.3 RQ3 And HYP3

RQ 3.0: How do the SCRBE method and its surrogate compare in an optimization setting?

HYP 3.0: The SCRBE-DEIM approach should help to alleviate some of the computational overhead during the optimization procedure. However, its suitability as a replacement to the SCRBE method is contingent on its accuracy along the optimization paths.

Based on the results presented in section 8.3.2, it is clear that the SCRBE-DEIM approach offers an advantage relative to the SCRBE method in overcoming the overhead associated with the SCRBE approach. However, as expected the SCRBE-DEIM approach somewhat stalls in its ability to approximate the constraints. In spite of this, it is fairly accurate based on the stipulations by Elham [43] for a conceptual level design tool (section 1.3.1.1). Here it was stated that a conceptual level tool needs to have an error of less than 5%. The SCRBE-DEIM method was able to furnish objective values to within 2.0% and constraint values that are within 1% of the more refined SCRBE models, but at a fraction of the overhead cost.

9.2 Limitations In The Proposed Method And Suggestions For Improvement

In this section, some of the limitations identified by the author are examined; along with suggestions as to how they can be addressed. This is performed for each of the major levels of the work presented.

9.2.0.1 Overall Limitations

- **Snapshot Sampling Procedures:** In the edge mode training algorithms presented in section 5.5.0.6, a combination of random sampling and Latin-Hypercube sampling was used to generate samples in the parameter domain for the testing problems. While sampling approaches of this kind are common in the SCRBE literature, there are optimization-based, goal-oriented, greedy sampling approaches in the general reduced order modeling literature that are

aimed at addressing high-dimensional problems [83]. For the problems considered in this work, the parameter spaces associated with the testing domains are formed from the Cartesian product of the parameter spaces of the individual components and the polynomial coefficients for the displacement approximations on the boundaries. Depending on the problem, this has the potential to form high-dimensional parameter spaces. The use of this alternate type of greedy sampling method, has been shown to provide even more concise empirical subspaces relative to other sampling methods for such high-dimensional problems. This is an area for improvement for future work

9.2.0.2 SCRBE-DEIM Approach

- **Surrogate Modeling Approach:** Artificial neural network surrogate models were selected for interpolating in the coefficients in the SCRBE-DEIM approach. It is clear from the results in section 8.2.3 that the computational time did not vary for the lower number of edge modes considered. This indicates that the overhead required to evaluate the underlying surrogate models formed the bottleneck in the procedure at this point. There were over 1500 surrogate models used for the nine archetype components. For each of the surrogates associated with the stiffness matrices, the author just blanketly used 15 neurons in each of the two hidden layers of the network. While for the parameter dependent solution recovery matrices, 5 neurons were used in the hidden layers for the coefficients with more influence and 8 and 6 neurons were used for the first and second layers, respectively, of the remaining coefficients. It was evident in many cases that the level of refinement was unnecessary, but it provided robustness in other cases where the nonlinear functional relationship of the coefficient being modeled was a bit more challenging. This is a big area for improvement in future work. The following are alternative strategies that can perhaps be used

to create more parsimonious models:

  - ***Network Pruning:*** In the literature for machine learning, there are a set of techniques known as *pruning algorithms* that are aimed at reducing the complexity of the neural network in an automated fashion. In general, these algorithms train the initially prescribed network using the given data; then, it identifies certain networks connections that are less essential than others and edits the model as necessary. Examples of this type of approach include: Hanson et al. [164], Ström et al. [165], and Han et al. [166].
  - ***Multiple Regression Techniques:*** The approximations for the coefficients of the pseudo-affine relationships are independent of each other. This implies that the choice of regression technique can be chosen specifically based on the nonlinear behavior of the particular coefficient. For those coefficients that have simpler functional relationships, simpler regression models such as *response surface equations* can perhaps be used. The neural network models should perhaps be used when the functional relationship of the coefficient becomes more challenging to approximate. If successful, the overall number of operations should be reduced. However, this has to take place in an automated fashion, as performing manual model selection is not pragmatic for the scale of the problem considered here. Such automated selection approaches were investigated by Couckuyt et al. [167], Mehmani et al. [168]; among others.

- **Inclusion Of More Empirical Modes For The Pseudo-Affine Approximations:** In the offline procedure for the SCRBE-DEIM approach described in section 6.5.3, it was stated that the cardinality of the empirical subspaces used to represent the nonlinear operators and mappings would be kept fixed. However, these bases are hierarchical and the inclusion of more modes could

potentially lead to more accurate predictions by the SCRBE-DEIM approach. The author avoided adding these empirical modes with less "energy" due to fact that their associated coefficients were highly nonlinear relatively to the first few used in the affine representations. This happened for all of the operators and mappings considered. Thus, the decision was made to not include the number of modes beyond a certain tolerance, as this would necessitate more complex surrogate models to capture the nonlinear functional behavior and further add to the overhead required. If the strategies suggested above regarding creating parsimonious surrogate models prove successful, perhaps simpler models could be used for some of the earlier coefficients with simpler functional relationships, while the more adaptable models could be reserved for later, more nonlinear coefficients. This approach has the potential to include more empirical modes into the approximations so as to improve the accuracy; while, not terribly exacerbating the computational overhead required.

9.3 Recommendations For A Conceptual-Level Design Framework

Based on the results presented in the literature, the SCRBE approach provides the opportunity to significantly expedite the familiar static condensation method. This is achieved by reducing the approximation spaces on the interior of the components comprising the model; as well as, reducing the sizes of the interfaces between the components and providing smaller systems to solve. Traditionally, this method has been applied with serial computation with special approaches to ensure efficiency relative to the full finite element approach. For large systems where there are parameter changes to all of the components at each major iteration of an optimization procedure, a parallel implementation is needed. The use of model reduction and parallel computation should lead to very efficient computation of the metrics of interest.

For conceptual level structural design, the author recommends using the SCRBE-DEIM approach to furnish the quantities of interest. This recommendation is primarily due to reduction in overhead when solving for the constraints of the problem. This speed-up is expected to be even more significant in cases where serial computation is used or when the number of components being evaluated on a single processor grows. As discussed in section 9.1.3, the SCRBE-DEIM approach does not achieve the level of accuracy that the SCRBE approach does with model refinement. However, for comparable error levels, the speedups afforded by the SCRBE-DEIM method are rather significant. Furthermore, these errors values are not exacerbating and fall within the threshold for a conceptual level tool.

Finally, a major limitation in the author's implementation of the SCRBE-DEIM approach is the training of the artificial neural networks. If the methods discussed in section 9.2 are applied to remedy this situation, the author is confident that the speedups that will be afforded by the SCRBE-DEIM method will be even more significant than what were presented in this work.

9.4 Contributions Of This Thesis

The main contributions of this thesis are:

- A framework was proposed to perform conceptual level, linear-static structural optimization using the SCRBE method. This framework considered how to account for common conceptual level constraints and how to find their sensitivities with respect to the model parameters.
- A method was proposed to find empirical edge subspaces that approximate both the state variable and its derivatives on the interfaces of the problem domain
- An alternative approach to furnish the ingredients of the SCRBE method was proposed. This is referred to as the SCRBE-DEIM approach. It was shown to reduce the overhead associated with the SCRBE approach, but with a trade-off

in accuracy. However, the error values reported were not overbearing and fall within the acceptable range for a conceptual level tool.

9.5 Future Work

There are many exciting avenues for future work; some of which will be investigated by the author, but could form the potential for work by others. These include:

- **Aposteriori Error Estimation:** An important feature of reduced basis approximation techniques is the prescription of an *aposteriori error certification* framework. This provides the capability of prescribing an upper-bound to the error associated with the outputs of the model at any point in the parameter space. This is particularly useful for giving confidence in the estimates by the model, as well as providing a means of refining the quality of the model in a structured, mathematically manner, rather than in a heuristic fashion. For the present work, there are several additional challenges that are presented. For the SCRBE approach, there is an additional error that is included with the use of bound constraints, as described in section 3.2.2.1. This additional error has to be accounted for. In the associated papers, there does not appear to be a way to calculate this additional error term. For the SCRBE-DEIM, there are aposteriori error estimation techniques presented in the literature as well. For the approach considered, the error associated with the used of surrogate models has to also be included in the estimate.

- **More Complex, Large-Scale Problems** Consistent with the other works in the SCRBE literature, a simple, yet representative problem was investigated in order to study the behavior of the method. For future problem, it is desirable to look at much larger problems that are representative of the subsystems in aerospace construction. This includes commercial aircraft wing-boxes and fuselages. Furthermore, it is desirable to investigate the use of the proposed

empirical edge mode training algorithms to components that feature two dimensional interfaces. In particular, investigating the behavior with stringer stiffened panels that are rife in aerospace construction.

- **Parallel Implementation:** The opportunities to parallelize the computations the calculations associated with the SCRBE and SCRBE-DEIM methods have been consistently highlighted throughout this work. For the test problems considered, they were implemented in the software package **MATLAB** [162] in a serial fashion. It is desirable to implement the work presented in this thesis in parallel, taking full advantage of multi-threading and multi-processing to even further expedite the methods for large scale problems.

Appendices

Appendix I

.

A.1 Shell Formulation, Composite Laminate Constitutive Relationship And Affine Representation

If the composite laminate being modeled is sufficiently thin, it can be modeled by the use of shell theory. This is a form of *operational model order reduction* that conveniently helps to reduce the size of the systems that need to be solved. Here, the displacement behavior through the thickness of the laminate is simplified. The development for the composite laminate is presented below.

A.1.0.1 Displacement And Strain Fields

Consider a shell that is described in a Cartesian reference frame. Any point in its domain can be represented as $\mathbf{x} = \{\hat{x}_1, \hat{x}_2, \hat{x}_3\} \in \hat{\Omega}^h \subset \mathbb{R}^3$ (figure 72). The coordinates $(\hat{x}_1, \hat{x}_2)$ describe the in-plane positions of the shell, while $\hat{x}_3$ is the out of plane coordinate, through which the kinematic behavior is approximated. As per the stipulations of general plate/flat shell theory, the mid-plane of the shell is used as reference for its kinematics. Using the Mindlin-Reissner theory, the displacement field, $u^h = \{\hat{u}_1, \hat{u}_2, \hat{u}_3\}$, can be described mathematically as

$$\begin{aligned}
\hat{u}_1(\hat{x}_1, \hat{x}_2, \hat{x}_3) &= \hat{u}_1^0(\hat{x}_1, \hat{x}_2) + \hat{x}_3\hat{\beta}_{\hat{x}_1}(\hat{x}_1, \hat{x}_2) \\
\hat{u}_2(\hat{x}_1, \hat{x}_2, \hat{x}_3) &= \hat{u}_2^0(\hat{x}_1, \hat{x}_2) - \hat{x}_3\hat{\beta}_{\hat{x}_2}(\hat{x}_1, \hat{x}_2) \\
\hat{u}_3(\hat{x}_1, \hat{x}_2, \hat{x}_3) &= \hat{u}_3^0(\hat{x}_1, \hat{x}_2)
\end{aligned} \tag{220}$$

where $\hat{u}_1^0, \hat{u}_2^0$, and $\hat{u}_3^0$ represent the orthogonal displacements of any point in the shell's mid-plane; while $\hat{\beta}_{x_1}$ and $\hat{\beta}_{x_2}$ represent the rotation of an infinitely rigid, transverse material line about the $\hat{x}_2$ and $\hat{x}_1$ axes, respectively. According to the prescription

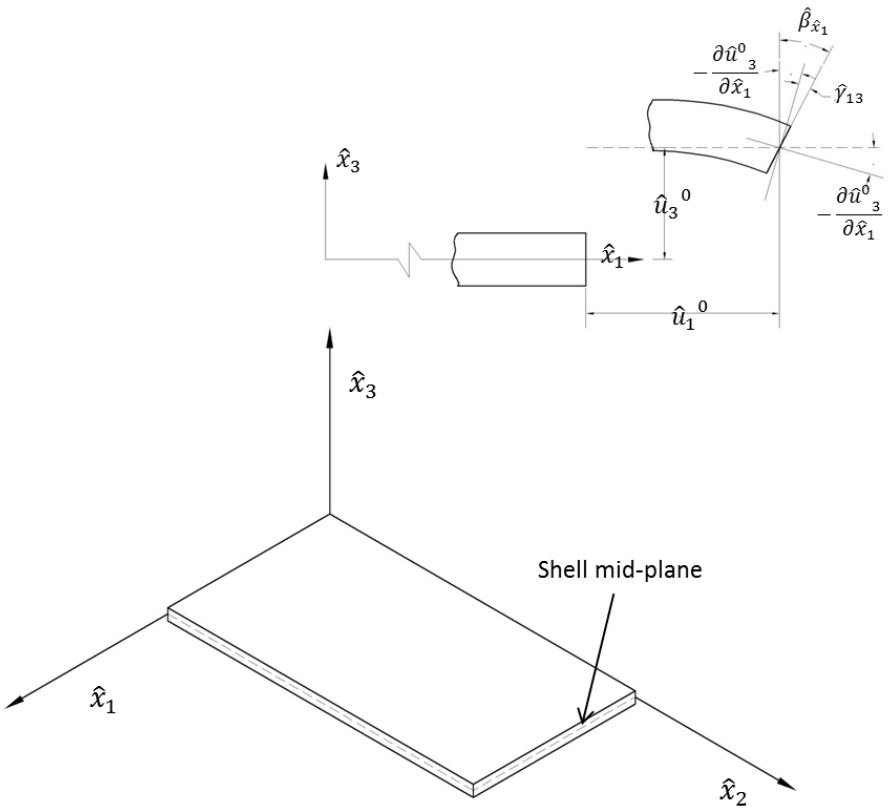

Figure 72: Deformation behavior of a shell under the first order shear deformation theory

of the Mindlin-Reissner plate theory, this arbitrary material line does not have to remain normal to the mid-plane after it rotates.

The strain field can be derived from the displacement field (220) using (36)

$$
\begin{aligned}
\hat{\varepsilon}_{11} = \quad & \frac{\partial \hat{u}_1}{\partial \hat{x}_1} = \quad \frac{\partial \hat{u}_1^0}{\partial \hat{x}_1} + \hat{x}_3 \frac{\partial \hat{\beta}_{x_1}}{\partial \hat{x}_1} \\
\hat{\varepsilon}_{22} = \quad & \frac{\partial \hat{u}_2}{\partial \hat{x}_2} = \quad \frac{\partial \hat{u}_2^0}{\partial \hat{x}_2} - \hat{x}_3 \frac{\partial \hat{\beta}_{x_2}}{\partial \hat{x}_2} \\
\hat{\gamma}_{12} = 2\hat{\varepsilon}_{12} \quad = \quad & \frac{\partial \hat{u}_1}{\partial \hat{x}_2} + \frac{\partial \hat{u}_2}{\partial \hat{x}_1} = \quad \frac{\partial \hat{u}_1^0}{\partial \hat{x}_2} + \frac{\partial \hat{u}_2^0}{\partial \hat{x}_1} + \hat{x}_3 \left(\frac{\partial \beta_{\hat{x}_1}}{\partial \hat{x}_2} - \frac{\partial \hat{\beta}_{x_2}}{\partial \hat{x}_1} \right) \\
\hat{\gamma}_{13} = 2\hat{\varepsilon}_{13} \quad = \quad & \frac{\partial \hat{u}_1}{\partial \hat{x}_3} + \frac{\partial \hat{u}_3}{\partial \hat{x}_1} = \quad \hat{\beta}_{\hat{x}_1} + \frac{\partial \hat{u}_3^0}{\partial \hat{x}_1} \\
\hat{\gamma}_{23} = 2\hat{\varepsilon}_{23} \quad = \quad & \frac{\partial \hat{u}_2}{\partial \hat{x}_3} + \frac{\partial \hat{u}_3}{\partial \hat{x}_2} = \quad -\hat{\beta}_{\hat{x}_2} + \frac{\partial \hat{u}_3^0}{\partial \hat{x}_2}
\end{aligned}
\tag{221}
$$

Here $\hat{\gamma}_{ij}$ represents *engineering shear strain*, which can easily be related to mathematical shear strain, $\hat{\varepsilon}_{ij}$, as shown. As a result of the infinitely rigid material line assumption, the direct strain component through the thickness vanishes; thus $\hat{\varepsilon}_{33} = 0$. The derivatives of the mid-plane displacements and rotations can be represented more concisely by use of the following relationships

$$\hat{\varepsilon}_i^0 = \frac{\partial \hat{u}_i^0}{\partial \hat{x}_i}, \qquad \hat{\varepsilon}_{12}^0 = \frac{\partial \hat{u}_1^0}{\partial \hat{x}_2} + \frac{\partial \hat{u}_2^0}{\partial \hat{x}_1}, \qquad i \in \{1,2\}$$
$$\hat{\kappa}_i = (-1)^{i+1}\frac{\partial \hat{\beta}_{\hat{x}_i}}{\partial \hat{x}_i}, \qquad \hat{\kappa}_{12} = \frac{\partial \hat{\beta}_{\hat{x}_1}}{\partial \hat{x}_2} - \frac{\partial \hat{\beta}_{\hat{x}_2}}{\partial \hat{x}_1}, \qquad \hat{\gamma}_{i3}^0 = (-1)^{i+1}\hat{\beta}_{\hat{x}_i} + \frac{\partial \hat{u}_3^0}{\partial \hat{x}_i}, \tag{222}$$

A.1.0.2 Stress Resultants

The stress tensor is described in further detail in appendix 4.2.1. To be consistent with engineering literature, the shear stresses will be represented with $\hat{\tau}_{ij}$ instead of $\hat{\sigma}_{ij}$. In the flat shell formulation, instead of working with the stress tensor components, $\hat{\sigma}_{ij}$, it is more common to work with cross-sectional quantities known as *stress resultants*. These stress resultants include three in-plane forces, three moments and two shear forces, each defined per unit span. The in-plane forces are defined as

$$\hat{N}_1(\hat{x}_1,\hat{x}_2) = \int_h \hat{\sigma}_1 \mathrm{d}\hat{x}_3, \quad \hat{N}_2(\hat{x}_1,\hat{x}_2) = \int_h \hat{\sigma}_2 \mathrm{d}\hat{x}_3, \quad \hat{N}_{12}(\hat{x}_1,\hat{x}_2) = \int_h \hat{\tau}_{12} \mathrm{d}\hat{x}_3 \tag{223}$$

Where $\hat{N}_1$ and $\hat{N}_2$ are direct forces and $\hat{N}_{12}$ is a shear force. Note also that $\int_h(\cdot)\mathrm{d}\hat{x}_3$ represents the integration of a quantity through the thickness i.e. $\int_{-h/2}^{h/2}(\cdot)\mathrm{d}\hat{x}_3$. The transverse shear forces per unit span, $\hat{Q}_1$ and $\hat{Q}_2$, are defined as

$$\hat{Q}_1(x_1,x_2) = \int_h \hat{\tau}_{13} \mathrm{d}x_3, \quad \hat{Q}_2(x_1,x_2) = \int_h \hat{\tau}_{23} \mathrm{d}x_3, \tag{224}$$

These shear forces both act out of plane, but the subscript denotes the orientation of the cross-sectional face upon which they act. Finally, the bending moments, $\hat{M}_1$ and $\hat{M}_2$, and the twisting moment, $\hat{M}_{12}$, are defined as

$$M_1(x_1,x_2) = \int_h x_3\sigma_1 \mathrm{d}x_3, \quad M_2(x_1,x_2) = \int_h x_3\sigma_2 \mathrm{d}x_3, \quad M_{12}(x_1,x_2) = \int_h x_3\tau_{12} \mathrm{d}x_3 \tag{225}$$

A.1.0.3 Constitutive Relationships

As presented in section 4.2.1, the constitutive relationship between stress and strain in a linear elastic case is given by the relationship, $\hat{\sigma}_{ij} = \hat{C}_{ijkl}\hat{\epsilon}_{kl}$ (30). In the case of composite materials, the constitutive relationship for a single orthotropic composite lamina can be represented in its local coordinate system as [1]

$$\begin{Bmatrix} \hat{\sigma}_{xx} \\ \hat{\sigma}_{yy} \\ \hat{\tau}_{yz} \\ \hat{\tau}_{zx} \\ \hat{\tau}_{xy} \end{Bmatrix} = \begin{bmatrix} Q_{11} & Q_{12} & 0 & 0 & 0 \\ Q_{12} & Q_{22} & 0 & 0 & 0 \\ 0 & 0 & Q_{44} & 0 & 0 \\ 0 & 0 & 0 & Q_{55} & 0 \\ 0 & 0 & 0 & 0 & Q_{66} \end{bmatrix} \begin{Bmatrix} \hat{\varepsilon}_{xx} \\ \hat{\varepsilon}_{yy} \\ \hat{\gamma}_{yz} \\ \hat{\gamma}_{zx} \\ \hat{\gamma}_{xy} \end{Bmatrix} \tag{226}$$

Recall that each ply can be oriented at different angles relative to the global x_1 direction of the laminate. Consequently, the elastic tensor for a single ply has to be transformed into to a representation in the global coordinate system as

$$\begin{Bmatrix} \hat{\sigma}_{1} \\ \hat{\sigma}_{2} \\ \hat{\tau}_{23} \\ \hat{\tau}_{31} \\ \hat{\tau}_{12} \end{Bmatrix} = \begin{bmatrix} \bar{Q}_{11} & \bar{Q}_{12} & 0 & 0 & \bar{Q}_{16} \\ \bar{Q}_{12} & \bar{Q}_{22} & 0 & 0 & \bar{Q}_{26} \\ 0 & 0 & \bar{Q}_{44} & \bar{Q}_{45} & 0 \\ 0 & 0 & \bar{Q}_{45} & \bar{Q}_{55} & 0 \\ \bar{Q}_{16} & \bar{Q}_{26} & 0 & 0 & \bar{Q}_{66} \end{bmatrix} \begin{Bmatrix} \hat{\varepsilon}_{11} \\ \hat{\varepsilon}_{22} \\ \hat{\gamma}_{23} \\ \hat{\gamma}_{31} \\ \hat{\gamma}_{12} \end{Bmatrix} \tag{227}$$

The quantities describing the material's physical properties , Q_{ij} for $i, j \in \{1, 2, 4, 5, 6\}$, are

$$\begin{aligned} Q_{11} &= E_{11}/(1 - \nu_{12}\nu_{21}), & Q_{22} &= E_{22}/(1 - \nu_{12}\nu_{21}), \\ Q_{12} &= Q_{21} = \nu_{12}E_{22}/(1 - \nu_{12}\nu_{21}), & Q_{44} &= G_{23}, \\ Q_{55} &= G_{31}, & Q_{66} &= G_{12} = G_{31} \end{aligned} \tag{228}$$

Where E_{ii}, G_{ij} and ν_{ij} are the direct stiffness, shear stiffness and Poison's ratio, respectively, of the lamina in the specified directions. Consider a laminate consisting

[1] In this document, the coordinates of a single lamina are represented as $\{x, y, z\}$, while the coordinate system of the entire laminate is $\{x_1, x_2, x_3\}$

of N plies as shown in figure 73. The distance from the mid-plane to the upper (lower) edge of the k^{th} ply located below (above) the mid-plane is denoted by h_k. The stiffness of the entire laminate - based on the stacking of the constituent laminae - can be determined by integrating the piecewise constant constitutive relationship through the thickness of the laminate. An example of this for the direct, in-plane force per unit span, N_1, will now be derived. Using (221), (223) and (227)

$$N_1(x_1,x_2) = \int_h \bar{Q}_{11}\left(\frac{\partial \hat{u}_1^0}{\partial \hat{x}_1} + \hat{x}_3\frac{\partial \hat{\beta}_{x_1}}{\partial \hat{x}_1}\right) + \bar{Q}_{12}\left(\frac{\partial \hat{u}_2^0}{\partial \hat{x}_2} - \hat{x}_3\frac{\partial \hat{\beta}_{x_2}}{\partial \hat{x}_2}\right) + \bar{Q}_{16}\left(\frac{\partial \hat{u}_1^0}{\partial \hat{x}_2} + \frac{\partial \hat{u}_2^0}{\partial \hat{x}_1} + \hat{x}_3\left(\frac{\partial \beta_{\hat{x}_1}}{\partial \hat{x}_2} - \frac{\partial \hat{\beta}_{x_2}}{\partial \hat{x}_1}\right)\right) \mathrm{d}x_3, \quad (229)$$

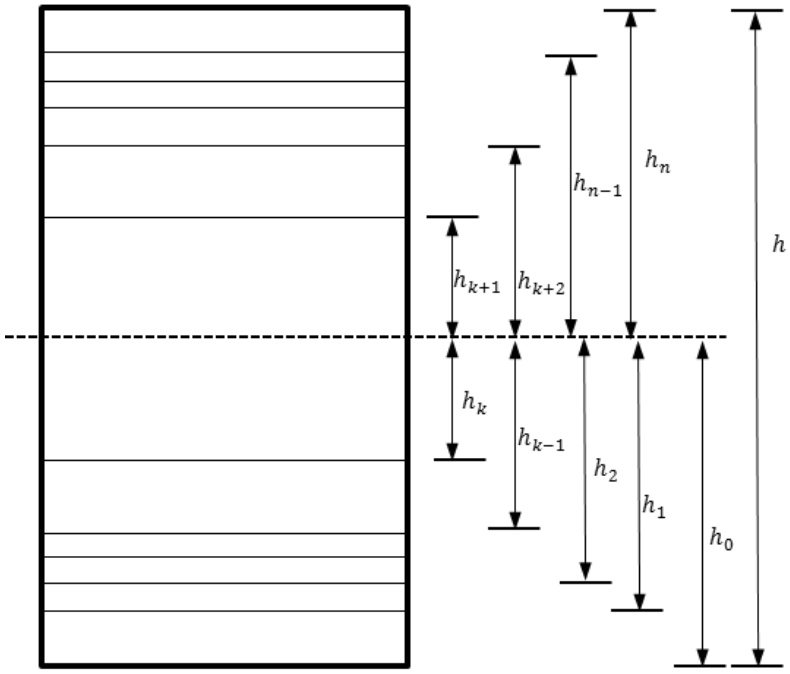

Figure 73: A general composite laminate with N plies

Using the fact that the kinematic terms are independent of x_3 and that the material quantities, Q_{ij}, are piece-wise constant, (229) takes the form

$$N_1(x_1,x_2) = A_{11}\frac{\partial \hat{u}_1^0}{\partial \hat{x}_1} + B_{11}\frac{\partial \hat{\beta}_{x_1}}{\partial \hat{x}_1} + A_{12}\frac{\partial \hat{u}_2^0}{\partial \hat{x}_2} - B_{12}\frac{\partial \hat{\beta}_{x_2}}{\partial \hat{x}_2} + A_{16}\left(\frac{\partial \hat{u}_1^0}{\partial \hat{x}_2} + \frac{\partial \hat{u}_2^0}{\partial \hat{x}_1}\right) + B_{16}\left(\frac{\partial \beta_{\hat{x}_1}}{\partial \hat{x}_2} - \frac{\partial \hat{\beta}_{x_2}}{\partial \hat{x}_1}\right), \quad (230)$$

Where $A_{ij} = \sum_{k=1}^{N} Q_{ij}(h_k - h_{k-1})$ and $B_{ij} = \sum_{k=1}^{N} \frac{Q_{ij}}{2}(h_k^2 - h_{k-1}^2)$ are the in-plane and coupling stiffness terms, respectively. As shown, the sum is carried out over the N plies constituting the laminate. Performing the same operation for the other stress resultants, the following cross-sectional constitutive relationship results

$$\begin{Bmatrix} \hat{N}_1 \\ \hat{N}_2 \\ \hat{N}_{12} \\ \hat{M}_1 \\ \hat{M}_2 \\ \hat{M}_{12} \\ \hat{Q}_1 \\ \hat{Q}_2 \end{Bmatrix} = \begin{bmatrix} A_{11} & A_{12} & A_{16} & B_{11} & B_{12} & B_{16} & 0 & 0 \\ A_{12} & A_{22} & A_{26} & B_{12} & B_{22} & B_{26} & 0 & 0 \\ A_{16} & A_{26} & A_{66} & B_{16} & B_{26} & B_{66} & 0 & 0 \\ B_{11} & B_{12} & B_{16} & D_{11} & D_{12} & D_{16} & 0 & 0 \\ B_{12} & B_{22} & B_{26} & D_{12} & D_{22} & D_{26} & 0 & 0 \\ B_{16} & B_{26} & B_{66} & D_{16} & D_{26} & D_{66} & 0 & 0 \\ 0 & 0 & 0 & 0 & 0 & 0 & \bar{A}_{44} & \bar{A}_{45} \\ 0 & 0 & 0 & 0 & 0 & 0 & \bar{A}_{45} & \bar{A}_{55} \end{bmatrix} \begin{Bmatrix} \hat{\varepsilon}_1^0 \\ \hat{\varepsilon}_2^0 \\ \hat{\varepsilon}_{12}^0 \\ \hat{\kappa}_1 \\ \hat{\kappa}_2 \\ \hat{\kappa}_{12} \\ \hat{\gamma}_{13}^0 \\ \hat{\gamma}_{23}^0 \end{Bmatrix} \tag{231}$$

or more concisely with the block matrix and vector representation

$$\begin{Bmatrix} \hat{N} \\ \hat{M} \\ \hat{Q} \end{Bmatrix} = \begin{bmatrix} A & B & 0 \\ B & D & 0 \\ 0 & 0 & \bar{A} \end{bmatrix} \begin{Bmatrix} \hat{\varepsilon}^0 \\ \hat{\kappa} \\ \hat{\gamma}^0 \end{Bmatrix} \tag{232}$$

Here: $D_{ij} = \sum_{k=1}^{n} \frac{Q_{ij}}{3}\left[h_k^3 - h_{k-1}^3\right]$, $i,j \in \{1,2,6\}$, and $\bar{A}_{ij} = \sum_{k=1}^{n} \bar{Q}_{ij}\left[h_k - h_{k-1}\right]$, $i,j \in \{4,5\}$ are the laminate bending stiffnesses and the out-of-plane shear stiffnesses, respectively. Additionally, the strain terms can be represented more concisely as: mid-plane strains, $\hat{\varepsilon}^0 = \{\hat{\varepsilon}_1^0, \hat{\varepsilon}_2^0, \hat{\varepsilon}_{12}^0\}$; curvatures, $\hat{\kappa} = \{\hat{\kappa}_1, \hat{\kappa}_2, \hat{\kappa}_{12}\}$; and out of plane shear strains, $\hat{\gamma}^0 = \{\hat{\gamma}_{13}^0, \hat{\gamma}_{23}^0\}$.

The constitutive relationship, (232), represents a fully anisotropic composite laminate. For certain stacking sequences, the stiffness matrix can be simplified. When the stacking sequence is *symmetric* about the mid-plane, the coupling matrix vanishes, i.e. $B = 0$. Furthermore, if for every ply oriented at an angle $-\theta$ there is a corresponding one oriented at an angle $+\theta$, the laminate is said to be *balanced* and the terms A_{16}, A_{26}, and A_{45} all vanish.

A.1.0.4 Lamination Parameters

For the composite laminate, a rather convenient parametrization of the constitutive matrix is by the use of *lamination parameters* and *material dependent matrices*. The favorable decomposition afforded by laminate parametrization is especially useful for a concise affine representation of the finite element stiffness matrix. This parametrization approach will be briefly described here. A more detailed presentation of the laminate parametrization for a plate or shell featuring the Mindlin-Reissner plate theory can be found in Grenestedt [169] and Foldager [170].

In order to calculate the sub-components of the laminate constitutive matrix, $\mathbf{A}$, $\mathbf{B}$, $\mathbf{D}$ and $\bar{\mathbf{A}}$, the following material independent and dependent matrices are defined:

$$\begin{pmatrix} A_{11} \\ A_{22} \\ A_{12} \\ A_{66} \\ A_{16} \\ A_{26} \end{pmatrix} = h \begin{bmatrix} 1 & \xi_1^A & \xi_2^A & 0 & 0 \\ 1 & -\xi_1^A & \xi_2^A & 0 & 0 \\ 0 & 0 & -\xi_2^A & 1 & 0 \\ 0 & 0 & -\xi_2^A & 0 & 1 \\ 0 & \xi_3^A/2 & \xi_4^A & 0 & 0 \\ 0 & \xi_3^A/2 & -\xi_4^A & 0 & 0 \end{bmatrix} \begin{pmatrix} U_1 \\ U_2 \\ U_3 \\ U_4 \\ U_5 \end{pmatrix} \tag{233}$$

$$\begin{pmatrix} B_{11} \\ B_{22} \\ B_{12} \\ B_{66} \\ B_{16} \\ B_{26} \end{pmatrix} = \frac{h^2}{4} \begin{bmatrix} 0 & \xi_1^B & \xi_2^B & 0 & 0 \\ 0 & -\xi_1^B & \xi_2^B & 0 & 0 \\ 0 & 0 & -\xi_2^B & 0 & 0 \\ 0 & 0 & -\xi_2^B & 0 & 0 \\ 0 & \xi_3^B/2 & \xi_4^B & 0 & 0 \\ 0 & \xi_3^B/2 & -\xi_4^B & 0 & 0 \end{bmatrix} \begin{pmatrix} U_1 \\ U_2 \\ U_3 \\ U_4 \\ U_5 \end{pmatrix} \tag{234}$$

$$\begin{pmatrix} D_{11} \\ D_{22} \\ D_{12} \\ D_{66} \\ D_{16} \\ D_{26} \end{pmatrix} = \frac{h^3}{12} \begin{bmatrix} 1 & \xi_1^D & \xi_2^D & 0 & 0 \\ 1 & -\xi_1^D & \xi_2^D & 0 & 0 \\ 0 & 0 & -\xi_2^D & 1 & 0 \\ 0 & 0 & -\xi_2^D & 0 & 1 \\ 0 & \xi_3^D/2 & \xi_4^D & 0 & 0 \\ 0 & \xi_3^D/2 & -\xi_4^D & 0 & 0 \end{bmatrix} \begin{pmatrix} U_1 \\ U_2 \\ U_3 \\ U_4 \\ U_5 \end{pmatrix} \tag{235}$$

and finally,

$$\begin{pmatrix} \bar{A}_{44} \\ \bar{A}_{55} \\ \bar{A}_{45} \end{pmatrix} = h \begin{bmatrix} 1 & \xi_1^A \\ 1 & -\xi_1^A \\ 0 & -\xi_2^A \end{bmatrix} \begin{pmatrix} U_6 \\ U_7 \end{pmatrix} \tag{236}$$

The parameter dependent terms or "lamination parameters" are defined as:

$$\xi_{[}^A 1,2,3,4] = {}^1\!/_2 \int_{-1}^{1} [cos2\theta(z), cos4\theta(z), sin2\theta(z), sin4\theta(z)]\, dz, \tag{237}$$

$$\xi_{[}^B 1,2,3,4] = \int_{-1}^{1} [cos2\theta(z), cos4\theta(z), sin2\theta(z), sin4\theta(z)]\, z dz, \tag{238}$$

$$\xi_{[}^D 1,2,3,4] = {}^3\!/_2 \int_{-1}^{1} [cos2\theta(z), cos4\theta(z), sin2\theta(z), sin4\theta(z)]\, z^2 dz, \tag{239}$$

where $\theta(z)$ is the distribution of the ply orientations through the normalized thickness coordinate $\bar{z} = (2/h)\, z$. They represent the moments of the trigonometric functions entering in the rotation formula for the stiffness matrices relative to the plate/shell

mid-plane. The parameter independent terms are:

$$
\begin{aligned}
U_1 &= (3Q_{11} + 3Q_{22} + 2Q_{12} + 4Q_{66})/8, \\
U_2 &= (Q_{11} - Q_{22})/2, \\
U_3 &= (Q_{11} + Q_{22} - 2Q_{12} - 4Q_{66})/8, \qquad (240) \\
U_4 &= (Q_{11} + Q_{22} + 6Q_{12} - 4Q_{66})/8, \\
U_5 &= (Q_{11} + Q_{22} - 2Q_{12} + 4Q_{66})/8 \qquad (241) \\
U_6 &= (Q_{44} + Q_{55})/2 \\
U_7 &= (Q_{44} - Q_{55})/2
\end{aligned}
$$

The U_i terms are referred to as *lamina invariants* because they depend only on the material properties of a given lamina and not on its orientation.

All 12 lamination parameters satisfy $-1 \leq \xi^{A,B,D}_{[1,2,3,4]} \leq 1$. There are certain simplifications that occur with the lamination parameters for particular types of laminate lay-ups. For symmetric layups, the terms $\xi^{B}_{[1,2,3,4]}$ all vanish. For the case of a balanced and symmetric laminate, the terms $\xi^{A}_{[3,4]}$ and $\xi^{B}_{[1,2,3,4]}$ all go to zero. Thus, a symmetric and balanced laminate can be described by 6 lamination parameters and the overall thickness of the plate, h. The remaining lamination parameters are $\xi^{A}_{[1,2]}$ and $\xi^{D}_{[1,2,3,4]}$. Note that there are only two lamination parameters describing the membrane behavior, while there are four describing the bending behavior.

In addition to the side constraints, there a several feasibility constraints that must be prescribed for the space of lamination parameters

A.2 Domain Partitioning With Quadrilateral Finite Elements

This section provides a description of the discretization of the reference domain, $\hat{\Omega}$, as well as a description of the weak form (106) associated with finite element subspace, $\hat{X}^h$, used for the flat shell problem. It is assumed that the finite element partitioning,

$\hat{\mathcal{P}}$, of the domain by quadrilateral finite elements $\{\hat{K}\}$ satisfy the following properties

- The domain is partitioned by the elements such that: $\bar{\hat{\Omega}} = \bigcup_{K \in \mathcal{P}} \bar{\hat{K}}$
- The nonempty intersection of the closure of any two or more distinct elements is either a single common edge or a single common vertex of both elements

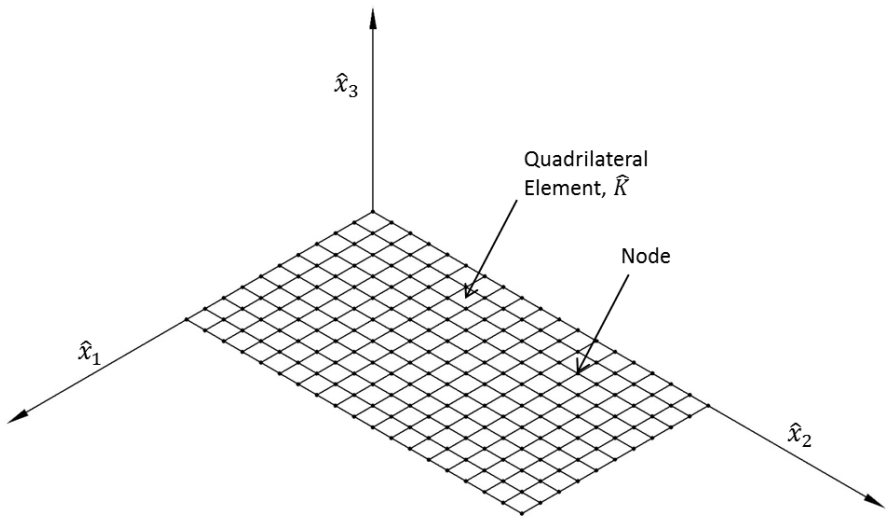

Figure 74: A flat shell discretized with quadrilateral elements

Figure 74 shows a simple flat shell that is discretized with quadrilateral elements. It is assumed that the partitioning is *regular*. The reference domain for each quadrilateral element, $\hat{K}$, can be represented within its plane by *natural coordinates*,

$$\hat{K} = \{(\eta, \xi) : -1 \leq \eta, \xi \leq 1\} \tag{242}$$

Recall from section 5.3.1 that the reference domain can be related to the actual problem domain by use of a geometric map of the form, $\mathcal{T} : \hat{\Omega} \to \Omega$. The mapping can be applied here to transform a quadrilateral element on the reference domain to its representation on the problem domain.

A.2.0.1 Finite Element Subspace on Quadrilaterals

The finite element subspace, $\hat{X}^h$, is built upon the lower order polynomial approximations of the mid-plane displacements and slopes of the shell, defined on $\hat{\mathcal{P}}$. Correspondingly, each of these terms is built upon the polynomial space, $\mathbb{Q}_p$, which consists of polynomials of degree at most p in each variable,

$$\mathbb{Q}_p = \text{span}\left\{x^l y^m, 0 \leq l, m \leq p\right\} \tag{243}$$

Let $\hat{v}^{h_0}$ represent the vector consisting of the d' arbitrary mid-plane displacements and slopes[2] prescribed over the entire problem domain. The finite element subspace, $\hat{X}^{h_0}$, of order p on the regular, reference quadrilateral mesh prescribed on the reference domain can now be defined as

$$\hat{X}^{h_0} = \left\{\hat{v}^{h_0} \in \left(C(\bar{\hat{\Omega}})\right)^{d'} : \forall \hat{K} \in \hat{\mathcal{P}},\ \ \hat{v}^{h_0}|_{\hat{K}} \in (\mathbb{Q}_p)^{d'}\right\} \tag{244}$$

The finite element space, $\hat{X}^h$, corresponding to the arbitrary displacements in the three orthogonal directions associated with the Cartesian reference frame, i.e. $\hat{v}^h = \{\hat{v}_1, \hat{v}_2, \hat{v}_3\}$, can then be approximated by (see (220))

$$\hat{X}^h = \left\{\hat{v}^h \in \left(C(\bar{\hat{\Omega}})\right)^3 : \hat{v}^h = [\hat{x}_3]\hat{v}^{h_0};\ \ \hat{v}^{h_0} \in \hat{X}^{h_0}\right\} \tag{245}$$

where for $d' = 5$

$$[\hat{x}_3] = \begin{bmatrix} 1 & 0 & 0 & \hat{x}_3 & 0 \\ 0 & 1 & 0 & 0 & \hat{x}_3 \\ 0 & 0 & 1 & 0 & 0 \end{bmatrix} \tag{246}$$

The corresponding subspace when the reference domain is mapped to the problem domain is

$$X^h = \left\{v^h \in \left(C(\bar{\Omega})\right)^3 :\ \ v^h = \hat{v}^h \circ \mathcal{T}^{-1};\ \ \hat{v}^h \in \hat{X}^h\right\} \tag{247}$$

The degrees of freedom associated with the subspace X^h consist of function values of the mid-plane displacements and slopes of the shell at the *nodes* of the quadrilateral mesh, $\{f(x_k) : k \in \underline{\mathcal{N}}\}$, where $\underline{\mathcal{N}}$ is the total number of nodes.[3] These nodal values

[2] $d' = 5$ or 6 terms depending on the shell FEM formulation

[3] The nodes are the vertices of all the elements used in the mesh.

are used with a Lagrangian or *nodal basis*, $\{\vartheta_k : k \in \underline{\mathcal{N}}\}$, to represent the associated function in the subspace. Each basis element satisfies the following conditions:

1. $\vartheta \in \hat{X}^h, \ \ \forall k \in \underline{\mathcal{N}}$
2. $\vartheta_k(x_l) = \delta_{kl}, \ \ \forall k, l \in \underline{\mathcal{N}}$

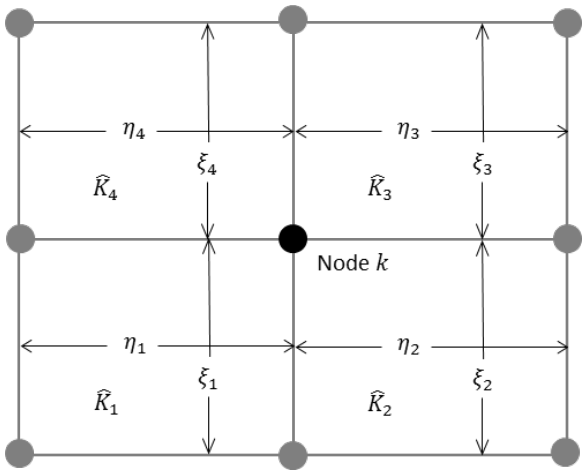

Figure 75: A Langrange basis function about an arbitrary node

Figure 75 shows an arbitrary node that represents the intersection of four quadrilateral elements, each consisting of four nodes. The Lagrangian basis function at this node is

$$\vartheta_k = \begin{cases} \frac{(1+\eta_1)(1+\xi_1)}{4}, & \text{in } \bar{\hat{K}}_1, \\ \frac{(1-\eta_2)(1+\xi_2)}{4}, & \text{in } \bar{\hat{K}}_2, \\ \frac{(1-\eta_3)(1-\xi_3)}{4}, & \text{in } \bar{\hat{K}}_3, \\ \frac{(1+\eta_4)(1-\xi_4)}{4}, & \text{in } \bar{\hat{K}}_4, \\ 0, & \text{in } \bar{\hat{\mathcal{P}}} \setminus (\bigcup_{i=1}^{4} \bar{\hat{K}}_i) \end{cases} \tag{248}$$

This expression can be easily modified when more or less elements intersect at the k^{th} node.

A.2.0.2 Weak Form

Let the degrees of freedom for all the nodes on the quadrilateral partitioning, $\hat{\mathcal{P}}$, be collected into the column vector $q \in \mathbb{R}^{\mathcal{N}'}$, where $\mathcal{N}'$ is total number of degrees of

freedom. The interpolation of these nodal values to any point within the domain is performed by using the shape function matrix, $[N] \in \mathbb{R}^{d' \times \mathcal{N}'}$. $[N]$ consists of the Langrangian basis functions, ϑ_k, in the appropriate element locations. Thus, to obtain the mid-plane displacements and slopes at any point $\hat{\mathbf{x}} = \{\hat{x}_1, \hat{x}_2\}$, the following relationship is used

$$\left\{\hat{u}_1^0,\ \hat{u}_2^0,\ \hat{u}_3^0,\ \hat{\beta}_{x_1},\ \hat{\beta}_{x_2}\right\}^T = [N]\{q\} \tag{249}$$

The mid-plane strains and curvatures (222) can be determined by pre-multiplying (249) by the differential operator matrix, $[\partial]$. $[\partial]$ consist of partial derivatives in appropriate element locations, which collectively transform the displacement field to the (222). Thus

$$\left\{\hat{\varepsilon}^0,\ \hat{\kappa},\ \hat{\gamma}^0\right\}^T = [\partial]\left\{\hat{u}_1^0,\ \hat{u}_2^0,\ \hat{u}_3^0,\ \hat{\beta}_{x_1},\ \hat{\beta}_{x_2}\right\}^T = [\partial][N]\{q\} \tag{250}$$

Finally, to obtain the stain field associated with the entire domain, as prescribed by (221), the matrix $[\hat{x}_3]_\partial$ can be introduced. In a similar fashion to (246), its non-zero elements are simply 1 or x_3 and it facilitates the relationship between the mid-plane strains and curvatures to the strain field defined on $\hat{\Omega}_m^h$. Therefore

$$\{\hat{\epsilon}_{11},\ \hat{\epsilon}_{22},\ \hat{\gamma}_{12},\ \hat{\gamma}_{13},\ \hat{\gamma}_{23}\}^T = [\hat{x}_3]_\partial\left\{\hat{\varepsilon}^0,\ \hat{\kappa},\ \hat{\gamma}^0\right\}^T = [\hat{x}_3]_\partial[\partial][N]\{q\} \tag{251}$$

The billinear form and linear functional for the linear elastostatic governing differential equation are presented in appendix 4.2.3. For convenience, they are restated here. For $i, j, k, l \in \{1, 2, 3\}$

$$\hat{a}(\hat{v}, \hat{w}; \mu) = \int_{\hat{\Omega}} \frac{\partial \hat{w}_i}{\partial \hat{x}_j} C_{ijkl} \frac{\partial \hat{v}_k}{\partial \hat{x}_l} \mathrm{d}\hat{\Omega}, \quad \forall \hat{v}, \hat{w} \in (H^1(\hat{\Omega}))^d \tag{252}$$

$$\hat{f}(\hat{w}; \mu) = \int_{\Omega} \hat{w}_i \hat{f}_i \mathrm{d}\hat{\Omega} + \int_{\hat{\Gamma}} \hat{w}_i \hat{g}_N^n \hat{e}_i^n \mathrm{d}\hat{\Gamma} + \int_{\hat{\Gamma}} \hat{w}_i \hat{g}_N^t \hat{e}_i^t \mathrm{d}\hat{\Gamma} \tag{253}$$

To enable the finite element approximation, the trial space for the unknown displacement vector, $\hat{u}^h$, is restricted to $\hat{X}^h \subset \left(H^1(\hat{\Omega}_m)\right)^d$. The strain field, $\dfrac{\partial \hat{u}_k}{\partial \hat{x}_l}$, was derived

for the shell formulation and is presented in (251). For the test functions, the Lagrangian basis functions associated with each degree of freedom for each node are used. These can be obtained by setting all but the r$^{\text{th}}$ column of the shape function matrix to zero. This is designated as $[N]_r$. The gradient associated with each test function, $\hat{w}^r$, is given by

$$\nabla \hat{w}^r = [\hat{x}_3]_\partial \, [\partial] \, [N]_r \,, \quad r \in \mathcal{N}' \tag{254}$$

The constitutive relationship, $C_{ijkl}\dfrac{\partial \hat{u}_k}{\partial \hat{x}_l}$, for an orthotropic lamina was presented in (226). The bilinear form can be derived by inserting this constitutive relationship along with (251) and (254) into (252). Using the relationship $\mathrm{d}\hat{\Omega} = \mathrm{d}\hat{x}_3 \mathrm{d}\hat{A}$, the integration can be performed through the thickness of the shell, resulting in the linear algebraic system associated with the weak form

$$[\mathbb{A}(\mu)]\{q(\mu)\} = \{f(\mu)\} \tag{255}$$

of size $\mathcal{N}'$. The r$^{\text{th}}$ row of $\mathbb{A}(\mu)$ and the r$^{\text{th}}$ element of $\{f(\mu)\}$ are given by

$$[\mathbb{A}(\mu)]_{r,:} = \int_{\hat{A}_m} \left([\partial] \, [N]_r\right)^T [C]_{cs} \left([\partial] \, [N]\right) \mathrm{d}\hat{A}_m \tag{256}$$

$$\begin{aligned} \{f(\mu)\}_r = & \int_{\hat{A}_m} [N]_r^T \left(\int_{\hat{h}} [\hat{x}_3] \hat{f} \mathrm{d}\hat{x}_3 \right) \mathrm{d}\hat{A}_m + \int_{\hat{A}_m} [N]_r^T \, \hat{g}_N \cdot \hat{e}^n \mathrm{d}\hat{A}_m \\ & + \int_{\hat{A}_m} [N]_r^T \, \hat{g}_N \cdot \hat{e}^t \mathrm{d}\hat{A}_m \end{aligned} \tag{257}$$

The matrix $[C]_{cs}$ is the cross-sectional constitutive relationship given by (232) for a composite laminate. The remaining integrals are with respect to the in-plane coordinates of the shell, i.e. $\mathrm{d}\hat{x}_2$ and $\mathrm{d}\hat{x}_3 : \mathrm{d}\hat{x}_2 \mathrm{d}\hat{x}_3 = \mathrm{d}\hat{A}_m$. f is a body force acting within the domain and $\hat{g}_N$ represent traction forces acting on the boundary of the domain.

The uniqueness of the flat shell formulation comes from performing the integration of the bending and membrane stiffness matrix terms on the boundaries of smoothing cells defined within the finite elements; while the shear terms are approximated by independent interpolation functions in natural coordinates. This removes the issue of locking and furthermore, it is robust and computationally inexpensive.

A.3 Wing-Box Design

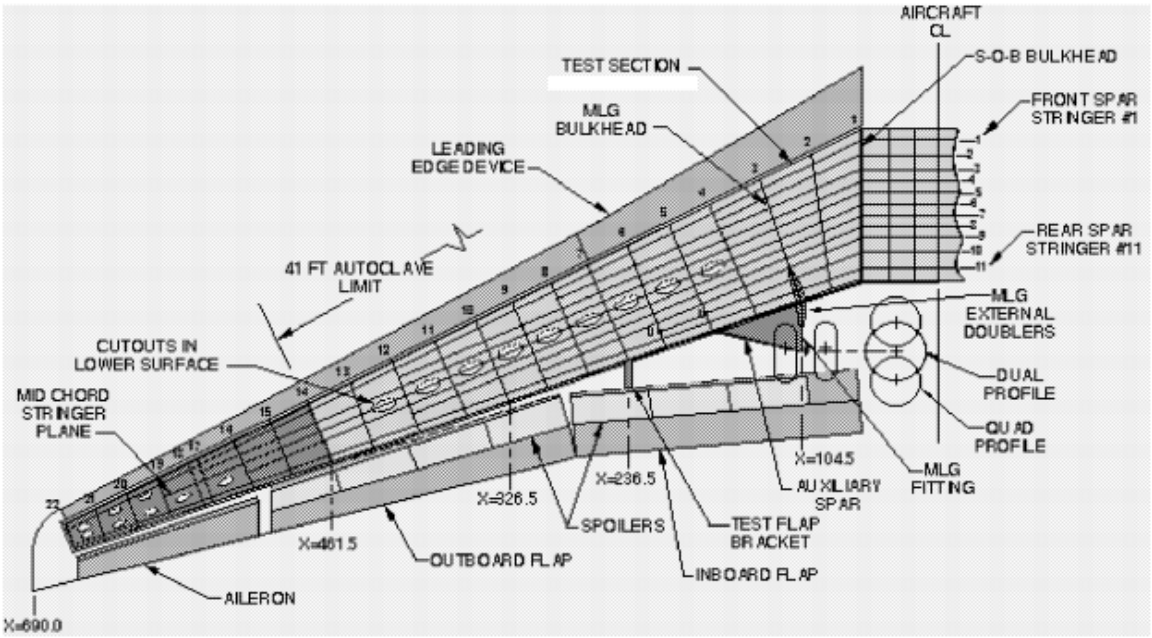

Figure 76: A conventional transport aircraft wing [118]

Figure 76 shows a typical wing for a commercial transport aircraft. In addition to the wing-box, the entire wing assembly consists of high-lift devices, control surfaces, landing gear system etc. In the chord-wise direction of a typical wing, the wing-box starts at about 15% of the chord and terminates at approximately $55 - 60\%$ [11]. In the span-wise direction, extending from the center-body section contained in the fuselage, it commences at the wing-fuselage intersection and extends to the wing tip. Its main purpose is to provide the flexural and torsional rigidity needed by the wing when it is subjected to a variety of external loads. The primary external loads that the wing-box experiences are due to air loads. These loads are generated by the pressure difference between the upper and lower surfaces of the wing when the aircraft produces lift. Air loads experienced during maneuvers or gusts often tend to be most critical from a structural perspective. In normal, positive-g flight, this pressure differential induces upward flexure (bending) of the wing, and also torsion

in the case of swept wings. In addition to air loads, the wing is subjected to a variety of other loads, including inertia from its own weight; pressure loads from the fuel stored within it; concentrated loads from attachments (engine nacelle support, high-lift devices, and control devices); landing gear impact loads; etc. The wing-box achieves the requisite structural rigidity by means of its specially designed constituent parts. Figure 77 shows an exploded isometric view of the components of the wing box. The components shown include wing-box covers, spars, and ribs.

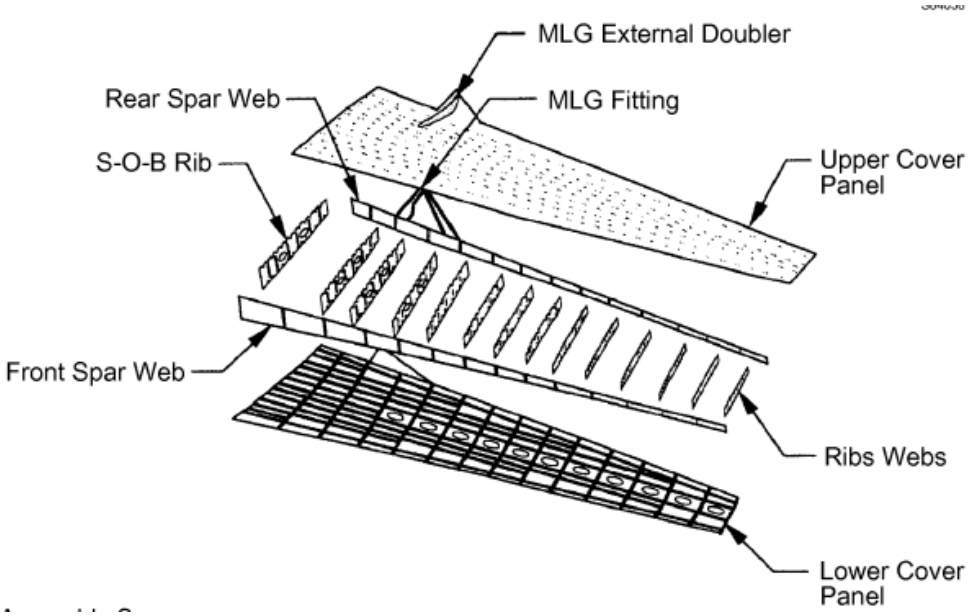

Figure 77: Exploded isometric view of a conventional transport aircraft wing [118]

A.3.0.1 Wing-box Covers

The wing-box covers are the only parts of the wing-box exposed to the flow-field external to the aircraft. The upper and lower covers are composed of skins (thin shells) reinforced by longitudinal stringers (stiffeners). These covers provide the majority of the bending stiffness needed by the wing. Additionally, the enclosed cross-section formed by the wing-covers and the spars resist torsion; which is especially prominent on swept winged aircraft. As it relates to the influence of air loads, the lower wing-box cover is loaded primarily by the tension produced by the upward bending of the

wing while the aircraft is in flight, as well as by direct and torsional shear stresses. When only static loading is being considered, this combination of loads may be the most critical in determining the thicknesses necessary to obviate failure of the wing-cover. In general, however, due to the significant variation in load direction tension during upright, positive-g flight and compression while the aircraft is on the ground or during negative-g flight there is a potential for failure due to fatigue. Thus, material selection is critical and not only involves strength and stiffness considerations, but also the inclusion of suitable damage tolerance properties. On the other hand, the upper wing cover is primarily loaded in compression and the most critical issue is the structural stability (buckling and crippling) within the bays formed by the intersection of the upper wing-cover with the spars and two consecutive ribs. The use of stiffener reinforced skins allow for a structurally efficient design with high bending stiffness with low weight. Due to the fact that the compressive loads experienced by the upper wing-box cover panels are greater than those in the lower-skin, the stiffeners on the former are normally more densely arranged than those on the latter. There is a wide variety of stiffener cross-sections available for use on stiffened panels. A few options are shown in figure 78. The shape of the cross-section of these stiffeners aid in the stability behavior of the panels onto which they are incorporated. As such, some stiffeners allow for more structurally stable panels than others. Niu [48] provides a quantitative comparison of the efficiency of common stiffeners used on stiffened panels in the aerospace context. In practice, the final choice of stiffeners to be used depends on additional factors such as manufacturability and ease of access for fatigue crack inspection.

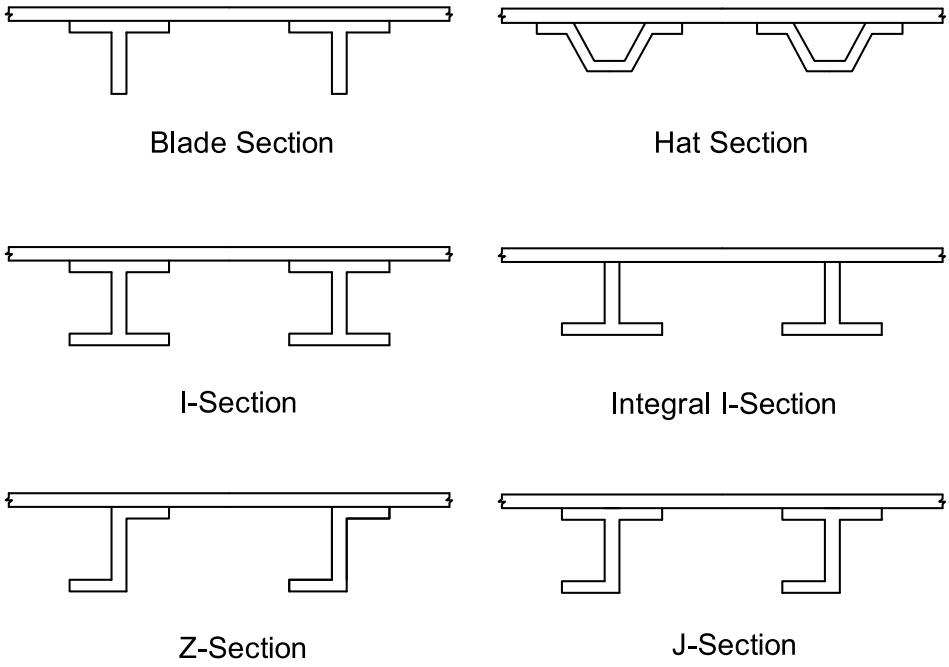

Figure 78: Examples of stiffened panels used in the wingbox

A.3.0.2 Wing Ribs

The ribs are structures discretely placed along the span of the wing. The main purposes of the ribs are to maintain the contour shape of the wing-box's externally exposed surfaces and to limit the unsupported spans of the cover panels. Additionally, the ribs may be used for the introduction of discrete load sources into the wing-box assembly. Examples include, the engine nacelle support and flap track support. These loads are distributed to the wing-box covers and spars. A typical wing rib is composed of caps, stiffeners and webs. The spacing between the ribs is an important consideration. The distance in between adjacent ribs directly affects the panel distances of the upper and lower wing-covers situated in between them. With all other factors being unchanged, the greater the aspect ratio of the wing-cover panels in between adjacent ribs, the more susceptible they are to structural stability issues. In order

to compensate for this, the wing-cover panels have to be reinforced, thereby adding weight. Thus, for an optimum weight wing-box assembly, there is a trade-off that has to be considered between increasing rib spacing (decreasing the number of ribs and thus rib weight) and the resulting increase in the weight of the wing-covers necessary to maintain structural stability.

A.3.0.3 Wing Spars

The wing spars are long beams that span the wing-box. In transport aircraft there may be two or three spars used in the wing-box's construction and the volume in between them is normally reserved for fuel storage. Each spar is normally composed of beam caps, shear webs and stiffeners. The beams caps assist the wing-covers in providing flexural rigidity of the wing, while the shear webs resist direct and torsional shear loads. As stated before, the external air loads act of the wing covers. In turn these loads are directed to the ribs and then to the spar webs in the form of shear loads. There is a variety of cross-sectional shapes available for the spars, including I-beam, C-channel, sinusoidal etc.

A.3.0.4 Stiffened Panel Failure Mechanisms

The components of the wing-box highlighted thus far, all feature stiffened panels. When stiffened panels are loaded, they are vulnerable to certain types of failures which render their use limited or even results in catastrophic failure. Kassapoglou [12] provides a detailed description of these potential failure mechanisms. They can be categorized into two types of failures; these are material failure and structural instability. In the former category, the constituent materials of both the skins or stiffeners of the components may fail when loaded beyond their strengths. In the case of composite laminates, failure is typically signified when any one of constituent lamina fails. The second category of failures involve either the structural instability of each stiffened panel as a whole or the localized instability of any of its constituents.

Localized instability includes, skin buckling between stiffeners; stiffener crippling; skin-stiffener separation; stiffener inter-rivet buckling; and stiffener column buckling. It is incumbent on the structural designer to not only ensure that all these failure modes are precluded during aircraft operation, but to also sequence them such that if one should occur, it is one that will not result in catastrophic failure of the entire aircraft.

REFERENCES

[1] Negri, F., Manzoni, A., and Amsallem, D., "Efficient model reduction of parametrized systems by matrix discrete empirical interpolation," *Journal of Computational Physics*, Vol. 303, 2015, pp. 431–454.

[2] Bonomi, D., Manzoni, A., and Quarteroni, A., "A matrix discrete empirical interpolation method for the efficient model reduction of parametrized nonlinear PDEs: application to nonlinear elasticity problems," *MATHICSE, École Polytechn. Fédérale de Lausanne, Lausanne, Switzerland, Tech. Rep*, Vol. 14, 2016, pp. 2016.

[3] "IATA - New IATA Passenger Forecast Reveals Fast-Growing Markets of the Future," .

[4] on Climate Change. Working Group 3, I. P., Metz, B., Davidson, O., Bosch, P., Dave, R., and Meyer, L., *Climate Change 2007: Mitigation: Contribution of Working Group III to the Fourth Assessment Report of the Intergovernmental Panel on Climate Change: Summary for Policymakers and Technical Summary*, Cambridge University Press, 2007.

[5] Watanabe, R. and Robinson, G., "The European union emissions trading scheme (EU ETS)," *Climate Policy*, Vol. 5, No. 1, 2005, pp. 10–14.

[6] I.A.T.A, *The IATA Technology Roadmap Report*, International Air Transport Association (IATA), 2013.

[7] "ICAO: 37th Assembly Working Papers, A37-WP/402, Montreal, July 2010," .

[8] "ENVIRONMENTALLY RESPONSIBLE AVIATION (ERA) PROJECT," .

[9] Guynn, M. D., Berton, J. J., Tong, M. J., and Haller, W. J., "Advanced Single-Aisle Transport Propulsion Design Options Revisited," *2013 Aviation Technology, Integration, and Operations Conference*, AIAA Paper 2013-4330, 2013.

[10] Nicolais, L., Meo, M., and Milella, E., *Composite materials: a vision for the future*, Springer Science & Business Media, 2011.

[11] Niu, C., *Airframe structural design: practical design information and data on aircraft structures*, Conmilit Press, 1988.

[12] Kassapoglou, C., *Design and analysis of composite structures: with applications to aerospace structures*, John Wiley & Sons, 2013.

[13] Tenney, D. R., Davis Jr, J. G., Johnston, N. J., Pipes, R. B., and McGuire, J. F., "Structural Framework for Flight: NASA's Role in Development of Advanced Composite Materials for Aircraft and Space Structures," 2011.

[14] Taminger, K., "Technical Challenges to Reducing Subsonic Transport Weight," *AIAA Aerospace Sciences Meeting*, 2012.

[15] Hyer, M. and Lee, H., "The use of curvilinear fiber format to improve buckling resistance of composite plates with central circular holes," *Composite structures*, Vol. 18, No. 3, 1991, pp. 239–261.

[16] Gurdal, Z. and Olmedo, R., "In-plane response of laminates with spatially varying fiber orientations-variable stiffness concept," *AIAA journal*, Vol. 31, No. 4, 1993, pp. 751–758.

[17] Setoodeh, S., Abdalla, M. M., and Gürdal, Z., "Design of variable–stiffness laminates using lamination parameters," *Composites Part B: Engineering*, Vol. 37, No. 4, 2006, pp. 301–309.

[18] Lopes, C. S., Camanho, P. P., Gürdal, Z., and Tatting, B. F., "Progressive failure analysis of tow-placed, variable-stiffness composite panels," *International Journal of Solids and Structures*, Vol. 44, No. 25, 2007, pp. 8493–8516.

[19] Alhajahmad, A., Abdalla, M. M., and Gürdal, Z., "Design tailoring for pressure pillowing using tow-placed steered fibers," *Journal of Aircraft*, Vol. 45, No. 2, 2008, pp. 630–640.

[20] Wu, K. C., Tatting, B. F., Smith, B. H., Stevens, R. S., Occhipinti, G. P., Swift, J. B., Achary, D. C., and Thornburgh, R. P., "Design and manufacturing of tow-steered composite shells using fiber placement," *Proceedings of the 50th AIAA/ASME/ASCE/AHS/ASC Structures, Structural Dynamics and Materials Conference. Palm Springs, California*, 2009.

[21] Tatting, B. F. and Gürdal, Z., *Design and manufacture of elastically tailored tow placed plates*, Citeseer, 2002.

[22] Tatting, B. F. and Gürdal, Z., "Automated finite element analysis of elastically-tailored plates," *NASA contractor report no NASA/CR-2003-212679*, 2003.

[23] Li, V. and Velicki, A., "Advanced PRSEUS structural concept design and optimization," *12th AIAA/ISSMO Multidisciplinary Analysis and Optimization Conference*, 2008, pp. 10–12.

[24] Velecki, A. and Jegley, D., "PRSEUS Structural Concept Development," *52nd AIAA Aerospace Sciences Meeting*, 2014.

[25] Bergan, A., Bakuckas, J., Lovejoy, A., Jegley, D., Linton, K., Korkosz, G., Awerbuch, J., and Tan, T.-M., "Full-scale test and analysis of a PRSEUS fuselage panel to assess damage-containment features," *Proceedings of the 2011 Aircraft Airworthiness and Sustainment Conference, San Diego, CA*, 2011, pp. 18–21.

[26] Bergan, A., Bakuckas, J., Lovejoy, A., Jegley, D., Linton, K., Neal, A., Korkosz, G., Awerbuch, J., and Tan, T.-M., "Full-Scale Test and Analysis Results of a PRSEUS Fuselage Panel to Assess Damage-Containment Features," *Aircraft Airworthiness and Sustainment Conference*, 2012.

[27] Bergan, A. C., Bakuckas, J., Lovejoy, A. E., Jegley, D. C., Awerbuch, J., and Tan, T.-M., "Assessment of Damage Containment Features of a Full-Scale PRSEUS Fuselage Panel through Test and Teardown," *Proceedings of the American Society for Composites, 27th Technical Conference, Arlington, TX*, 2012, pp. 1–3.

[28] Jegley, D. C., Velicki, A., and Hansen, D., "Structural efficiency of stitched rod-stiffened composite panels with stiffener crippling," *49 th AIAA/ASME/ASCE/AHS/ASC Structures, Structural Dynamics and Materials Conference*, 2008, pp. 7–10.

[29] Yovanof, N. P. and Jegley, D., "Compressive behavior of frame-stiffened composite panels," *52nd AIAA Structures Dynamics and Materials Conference, paper number AIAA-2011-1913*, 2011.

[30] Jegley, D. C. and Velicki, A., "Development of the PRSEUS Multi-Bay Pressure Box for a Hybrid Wing Body Vehicle," .

[31] Velicki, A., Thrash, P., and Jegley, D., "Airframe development for the hybrid wing body aircraft," *47th AIAA Aerospace Sciences Meeting Including The New Horizons Forum and Aerospace Exposition, Paper AIAA 2009*, Vol. 932, 2009.

[32] Laughlin, T. W., Corman, J., and Mavris, D., *A parametric and physics-based approach to structural weight estimation of the hybrid wing body aircraft*, Ph.D. thesis, Georgia Institute of Technology, 2013.

[33] "HyperSizer - Capabilities," .

[34] Velicki, A. and Jegley, D., "PRSEUS development for the hybrid wing body aircraft," *Proceedings of the AIAA Centennial of Naval Aviation Forum 100 Years of Achievement and Progress*, 2011.

[35] H. Slemp, W. C., Bird, R. K., Kapania, R. K., Havens, D., Norris, A., and Olliffe, R., "Design, Optimization, and Evaluation of Integrally Stiffened Al-7050 Panel with Curved Stiffeners," *Journal of Aircraft*, Vol. 48, No. 4, 2011, pp. 1163–1175.

[36] "NASA - Blended Wing Body Fact Sheet," .

[37] Gipson, L., "In Future Aircraft Designs We "Truss"," feb 2015.

[38] Gur, O., Schetz, J. A., and Mason, W. H., "Aerodynamic Considerations in the Design of Truss-Braced-Wing Aircraft," *Journal of Aircraft*, Vol. 48, No. 3, 2011, pp. 919–939.

[39] Liebeck, R. H., "Design of the blended wing body subsonic transport," *Journal of aircraft*, Vol. 41, No. 1, 2004, pp. 10–25.

[40] Raymer, D. P., "Aircraft Design: A Conceptual Approach, American Institute of Aeronautics and Astronautics," *Inc., Reston, VA*, 1999.

[41] Mavris, D. N., DeLaurentis, D. A., Bandte, O., and Hale, M. A., "A stochastic approach to multi-disciplinary aircraft analysis and design," *36th Aerospace Sciences Meeting & Exhibit, Reno, NV*, 1998.

[42] Mavris, D. N. and Garcia, E., "Affordability assessment for a subsonic transport," 1999.

[43] Elham, A., La Rocca, G., and van Tooren, M., "Development and implementation of an advanced, design-sensitive method for wing weight estimation," *Aerospace Science and Technology*, Vol. 29, No. 1, 2013, pp. 100–113.

[44] Roskam, J., "Rapid sizing method for airplanes," *Journal of Aircraft*, Vol. 23, No. 7, 1986, pp. 554–560.

[45] Torenbeek, E., "Synthesis of subsonic aircraft design," *Student edition, Delft University of Technology/Martinus Nijhoff*, 1982.

[46] Howe, D., *Aircraft conceptual design synthesis*, Vol. 5, Wiley, 2000.

[47] Schilders, W. H., Van der Vorst, H. A., and Rommes, J., *Model order reduction: theory, research aspects and applications*, Vol. 13, Springer, 2008.

[48] Niu, M. C.-Y., *Airframe stress analysis and sizing*, Vol. 2, Conmilit Press Hong Kong, 1997.

[49] Ardema, M. D., Chambers, M. C., Patron, A. P., Hahn, A. S., Miura, H., and Moore, M. D., "Analytical fuselage and wing weight estimation of transport aircraft," *NASA Technical Memorandum*, Vol. 110392, 1996.

[50] Hajela, P. and Chen, J. L., "Preliminary weight estimation of conventional and joined wings usingequivalent beam models," *Journal of Aircraft*, Vol. 25, No. 6, 1988, pp. 574–576.

[51] Gallman, J. W., Smith, S. C., and Kroo, I. M., "Optimization of joined-wing aircraft," *Journal of Aircraft*, Vol. 30, No. 6, 1993, pp. 897–905.

[52] Giles, G. L., "Equivalent plate analysis of aircraft wing box structures with general planform geometry," *Journal of Aircraft*, Vol. 23, No. 11, 1986, pp. 859–864.

[53] GILES, G., "Equivalent plate modeling for conceptual design of aircraft wing structures," 1995.

[54] Giles, G. L., "Further generalization of an equivalent plate representation for aircraft structural analysis," *Journal of Aircraft*, Vol. 26, No. 1, 1989, pp. 67–74.

[55] Livne, E., "Analytic sensitivities for shape optimization in equivalent plate structural wing models," *Journal of aircraft*, Vol. 31, No. 4, 1994, pp. 961–969.

[56] Livne, E., "Equivalent plate structural modeling for wing shape optimization including transverse shear," *AIAA journal*, Vol. 32, No. 6, 1994, pp. 1278–1288.

[57] Livne, E., Sels, R. A., and Bhatia, K. G., "Lessons from application of equivalent plate structural molding to an HSCT wing," *Journal of aircraft*, Vol. 31, No. 4, 1994, pp. 953–960.

[58] Livne, E. and Milosavljevic, R., "Analytic sensitivity and approximation of skin buckling constraints in wing-shape synthesis," *Journal of aircraft*, Vol. 32, No. 5, 1995, pp. 1102–1113.

[59] Livne, E. and Navarro, I., "Nonlinear equivalent plate modeling of wing-box structures," *Journal of Aircraft*, Vol. 36, No. 5, 1999, pp. 851–865.

[60] Liu, Y. and Kapania, R. K., "Equivalent skin analysis of wing structures using neural networks," *AIAA journal*, Vol. 39, No. 7, 2001, pp. 1390–1399.

[61] Liew, K., Xiang, Y., Kitipornchai, S., and Wang, C., *Vibration of Mindlin plates: programming the p-version Ritz method*, Elsevier, 1998.

[62] Gerard, G. and Becker, H., "Handbook of Structural Stability. Part I. Buckling of Flat Plates," Tech. rep., New York Univ., New York, 1957.

[63] Becker, H., "HANDBOOK OF STRUCTURAL STABILITY. PART II. BUCKLING OF COMPOSITE ELEMENTS," Tech. rep., New York Univ., New York, 1957.

[64] Gerard, G. and Becker, H., *Handbook of structural stability part III: buckling of curved plates and shells*, National Advisory Committee for Aeronautics, 1957.

[65] Gerard, G., "HANDBOOK OF STRUCTURAL STABILITY. PART IV. FAILURE OF PLATES AND COMPOSITE ELEMENTS," Tech. rep., New York Univ., New York, 1957.

[66] Gerard, G., "HANDBOOK OF STRUCTURAL STABILITY. PART V. COMPRESSIVE STRENGTH OF FLAT STIFFENED PANELS," Tech. rep., New York Univ., New York, 1957.

[67] Hickman, W. A. and Dow, N. F., "Data on the Compressive Strength of 75S-T6 Aluminum-Alloy Flat Panels With Longitudinal Extruded Z-Section Stiffeners," Tech. rep., DTIC Document, 1949.

[68] Hickman, W. A. and Dow, N. F., "Data on the Compressive Strength of 75S-T6 Aluminum-Alloy Flat Panels Having Small, Thin, Widely Spaced, Longitudinal Extruded Z-Section Stiffeners," 1949.

[69] Niles, A. S., "Tests of Flat Panels with Four Types of Stiffeners," Tech. rep., DTIC Document, 1943.

[70] Wrenn, G. A. and Dovi, A. R., "Multilevel decomposition approach to the preliminary sizing of a transport aircraft wing," *Journal of Aircraft*, Vol. 25, No. 7, 1988, pp. 632–638.

[71] Rohl, P. J., Mavris, D. N., and Schrage, D. P., "A Multilevel Decomposition Procedure for the Preliminary Wing Design of High-Speed Civil Transport Aircraft," 1994.

[72] Bindolino, G., Ghiringhelli, G., Ricci, S., and Terraneo, M., "Multilevel structural optimization for preliminary wing-box weight estimation," *Journal of Aircraft*, Vol. 47, No. 2, 2010, pp. 475–489.

[73] Walsh, J. L., *Application of mathematical optimization procedures to a structural model of a large finite-element wing*, Vol. 87597, National Aeronautics and Space Administration, Scientific and Technical Information Branch, 1986.

[74] Ragon, S., Gürdal, Z., Haftka, R., and Tzong, T., "Global/local structural wing design using response surface techniques," *AIAA Paper*, , No. 97-1051, 1997.

[75] Balabanov, V., Haftka, R. T., Grossman, B., Mason, W. H., and Watson, L. T., "Multifidelity response surface model for HSCT wing bending material weight," *Proc. 7th. AIAA/USAF/NASA/ISSMO Symposium on Multidisiplinary Analysis and Optimization*, 1998, pp. 2–4.

[76] Schneider, W., "A procedure for calculating the weight of wing structures with increased life: for presentation at the 33rd Annual Conference of the Society of Allied Weight Engineers, Inc., Fort Worth, Texas, 6-8 May, 1974," 1974.

[77] Burt, M., "Weight prediction for wings of box construction," Tech. rep., Ministry of Supply, Royal Aircraft Establishment, RAE Farnborough, 1955.

[78] Shanley, F. R., *Weight-strength analysis of aircraft structures*, Dover Publications, 1960.

[79] Hazra, S. B., *Large-scale PDE-constrained Optimization in Applications*, Vol. 49, Springer Science & Business Media, 2009.

[80] "NASA - High-Fidelity Aeroelastic Simulations of Future Airplane Concepts," .

[81] Eftang, J. L. and Patera, A. T., "Port reduction in parametrized component static condensation: approximation and a posteriori error estimation," *International Journal for Numerical Methods in Engineering*, Vol. 96, No. 5, 2013, pp. 269–302.

[82] "NASA Unveils Future Aircraft Designs: Stunning Models," .

[83] Bui-Thanh, T., Willcox, K., and Ghattas, O., "Model reduction for large-scale systems with high-dimensional parametric input space," *SIAM Journal on Scientific Computing*, Vol. 30, No. 6, 2008, pp. 3270–3288.

[84] Wilson, E. L., "The static condensation algorithm," *International Journal for Numerical Methods in Engineering*, Vol. 8, No. 1, 1974, pp. 198–203.

[85] Manzoni, A., Quarteroni, A., and Rozza, G., "Shape optimization for viscous flows by reduced basis methods and free-form deformation," *International Journal for Numerical Methods in Fluids*, Vol. 70, No. 5, 2012, pp. 646–670.

[86] Rozza, G., Lassila, T., and Manzoni, A., "Reduced basis approximation for shape optimization in thermal flows with a parametrized polynomial geometric map," *Spectral and high order methods for partial differential equations*, Springer, 2011, pp. 307–315.

[87] Rozza, G. and Manzoni, A., "Model order reduction by geometrical parametrization for shape optimization in computational fluid dynamics," *Proceedings of the ECCOMAS CFD 2010, V European Conference on Computational Fluid Dynamics*, No. CONF, 2010.

[88] Lassila, T., Manzoni, A., Quarteroni, A., and Rozza, G., "Boundary control and shape optimization for the robust design of bypass anastomoses under uncertainty," *ESAIM: Mathematical Modelling and Numerical Analysis*, Vol. 47, No. 4, 2013, pp. 1107–1131.

[89] Lassila, T., Manzoni, A., Quarteroni, A., and Rozza, G., "A reduced computational and geometrical framework for inverse problems in hemodynamics," *International journal for numerical methods in biomedical engineering*, Vol. 29, No. 7, 2013, pp. 741–776.

[90] Cuong, N. N., *Reduced-basis approximations and a posteriori error bounds for nonaffine and nonlinear partial differential equations: Application to inverse analysis*, Ph.D. thesis, Citeseer, 2005.

[91] Iapichino, L., Ulbrich, S., and Volkwein, S., "Multiobjective PDE-constrained optimization using the reduced-basis method," 2013.

[92] Arian, E., Fahl, M., and Sachs, E., "Trust-Region Proper Orthogonal Decomposition for Flow Control," Vol. 2000-2101, 02 2001.

[93] Kunisch, K. and Volkwein, S., "Proper orthogonal decomposition for optimality systems," Vol. 42, 01 2008.

[94] Qian, E., Grepl, M., Veroy, K., and E Willcox, K., "A Certified Trust Region Reduced Basis Approach to PDE-Constrained Optimization," Vol. 39, 02 2017.

[95] Zahr, M. and Farhat, C., "Progressive construction of a parametric reduced-order model for PDE-constrained optimization," Vol. 102, 12 2014.

[96] Carlberg, K. and Farhat, C., "A low-cost, goal-oriented compact proper orthogonal decomposition basis for model reduction of static systems," Vol. 86, 04 2011, pp. 381 – 402.

[97] Carlberg, K. and Farhat, C., "A Compact Proper Orthogonal Decomposition Basis for Optimization-Oriented Reduced-Order Models," 09 2008.

[98] Raddum, H. and Semaev, I., "Solving Multiple Right Hand Sides linear equations," Vol. 49, 12 2008, pp. 147–160.

[99] Eftang, J., Huynh, D., Knezevic, D., Rønquist, E., and Patera, A., "Adaptive port reduction in static condensation," *Proceedings of 7th Vienna Conference on Mathematical Modelling–MATHMOD*, 2012.

[100] Saad, Y., *Iterative methods for sparse linear systems*, Vol. 82, siam, 2003.

[101] Løvgren, A. E., Maday, Y., and Rønquist, E. M., "A reduced basis element method for the steady Stokes problem," *ESAIM: Mathematical Modelling and Numerical Analysis-Modélisation Mathématique et Analyse Numérique*, Vol. 40, No. 3, 2006, pp. 529–552.

[102] Løvgren, A. E., Maday, Y., and Rønquist, E. M., "A reduced basis element method for the steady Stokes problem: Application to hierarchical flow systems," *Modeling, identification and control*, Vol. 27, No. 2, 2006, pp. 79–94.

[103] Løvgren, A. E., Maday, Y., and Rønquist, E. M., "The reduced basis element method for fluid flows," *Analysis and simulation of fluid dynamics*, Springer, 2007, pp. 129–154.

[104] Phuong Huynh, D. B., Knezevic, D. J., and Patera, A. T., "A static condensation reduced basis element method: approximation and a posteriori error estimation," *ESAIM: Mathematical Modelling and Numerical Analysis*, Vol. 47, No. 01, 2013, pp. 213–251.

[105] Huynh, D., Knezevic, D., and Patera, A., "A static condensation reduced basis element method: Complex problems," *Computer Methods in Applied Mechanics and Engineering*, Vol. 259, 2013, pp. 197–216.

[106] Smetana, K., "A new certification framework for the port reduced static condensation reduced basis element method," *Computer Methods in Applied Mechanics and Engineering*, Vol. 283, 2015, pp. 352–383.

[107] DeVore, R., Petrova, G., and Wojtaszczyk, P., "Greedy algorithms for reduced bases in Banach spaces," *Constructive Approximation*, Vol. 37, No. 3, 2013, pp. 455–466.

[108] Huynh, D., "A static condensation reduced basis element approximation: Application to three-dimensional acoustic muffler analysis," *International Journal of Computational Methods*, Vol. 11, No. 03, 2014, pp. 1343010.

[109] Eftang, J. L. and Patera, A. T., "A port-reduced static condensation reduced basis element method for large component-synthesized structures: approximation and A posteriori error estimation," *Advanced Modeling and Simulation in Engineering Sciences*, Vol. 1, No. 1, 2014, pp. 3.

[110] Smetana, K. and Patera, A. T., "Optimal local approximation spaces for component-based static condensation procedures," *SIAM Journal on Scientific Computing*, Vol. 38, No. 5, 2016, pp. A3318–A3356.

[111] Vallaghé, S. and Patera, A. T., "The static condensation reduced basis element method for a mixed-mean conjugate heat exchanger model," *SIAM Journal on Scientific Computing*, Vol. 36, No. 3, 2014, pp. B294–B320.

[112] Vallaghé, S., Huynh, P., Knezevic, D. J., Nguyen, L., and Patera, A. T., "Component-based reduced basis for parametrized symmetric eigenproblems," *Advanced Modeling and Simulation in Engineering Sciences*, Vol. 2, No. 1, 2015, pp. 7.

[113] Vallaghé, S., "The static condensation reduced basis element method for parabolic problems," *M3AS: Math Models Methods Appl Sci*, 2013.

[114] Bader, E., Grepl, M. A., and Müller, S., "A Static Condensation Reduced Basis Element Approach for the Reynolds Lubrication Equation," *Communications in Computational Physics*, Vol. 21, No. 1, 2017, pp. 126–148.

[115] Buhr, A., Engwer, C., Ohlberger, M., and Rave, S., "ArbiLoMod, a simulation technique designed for arbitrary local modifications," *SIAM Journal on Scientific Computing*, Vol. 39, No. 4, 2017, pp. A1435–A1465.

[116] Vidal-Codina, F., Saa-Seoane, J., Nguyen, N.-C., and Peraire, J., "A multiscale continuous Galerkin method for stochastic simulation and robust design of wave propagation through heterogeneous materials," *arXiv preprint arXiv:1610.00625*, 2016.

[117] Iapichino, L., Quarteroni, A., and Rozza, G., "Reduced basis method and domain decomposition for elliptic problems in networks and complex parametrized geometries," *Computers & Mathematics with Applications*, Vol. 71, No. 1, 2016, pp. 408–430.

[118] Michael, K., "AST Composite Wing Program—Executive Summary," 2001.

[119] Wrenn, G. A., "An indirect method for numerical optimization using the Kreisselmeir-Steinhauser function," 1989.

[120] Kennedy, G. J. and Hicken, J. E., "Improved constraint-aggregation methods," *Computer Methods in Applied Mechanics and Engineering*, Vol. 289, 2015, pp. 332–354.

[121] Kennedy, G. J., "Strategies for adaptive optimization with aggregation constraints using interior-point methods," *Computers & Structures*, Vol. 153, 2015, pp. 217–229.

[122] Plank, R. and Wittrick, W., "Buckling under combined loading of thin, flat-walled structures by a complex finite strip method," *International Journal for Numerical Methods in Engineering*, Vol. 8, No. 2, 1974, pp. 323–339.

[123] Byklum, E., Steen, E., and Amdahl, J., "A semi-analytical model for global buckling and postbuckling analysis of stiffened panels," *Thin-Walled Structures*, Vol. 42, No. 5, 2004, pp. 701–717.

[124] Kidane, S., Li, G., Helms, J., Pang, S.-S., and Woldesenbet, E., "Buckling load analysis of grid stiffened composite cylinders," *Composites Part B: Engineering*, Vol. 34, No. 1, 2003, pp. 1–9.

[125] Wang, D. and Abdalla, M. M., "Global and local buckling analysis of grid-stiffened composite panels," *Composite Structures*, Vol. 119, 2015, pp. 767–776.

[126] Przemieniecki, J., "Finite element structural analysis of local instability," *AIAA Journal*, Vol. 11, No. 1, 1973, pp. 33–39.

[127] Fenner, P. E. and Watson, A., "Finite element buckling analysis of stiffened plates with filleted junctions," *Thin-Walled Structures*, Vol. 59, 2012, pp. 171–180.

[128] Rackliffe, M. E., Jensen, D. W., and Lucas, W. K., "Local and global buckling of ultra-lightweight IsoTruss® structures," *Composites science and technology*, Vol. 66, No. 2, 2006, pp. 283–288.

[129] Orifici, A. C., de Zarate Alberdi, I. O., Thomson, R. S., and Bayandor, J., "Compression and post-buckling damage growth and collapse analysis of flat composite stiffened panels," *Composites science and technology*, Vol. 68, No. 15-16, 2008, pp. 3150–3160.

[130] Degenhardt, R., Kling, A., Klein, H., Hillger, W., Goetting, H. C., Zimmermann, R., Rohwer, K., and Gleiter, A., "Experiments on buckling and postbuckling of thin-walled CFRP structures using advanced measurement systems," *International Journal of Structural Stability and Dynamics*, Vol. 7, No. 02, 2007, pp. 337–358.

[131] Horger, T., Wohlmuth, B., and Dickopf, T., "Simultaneous reduced basis approximation of parameterized elliptic eigenvalue problems," *ESAIM: Mathematical Modelling and Numerical Analysis*, Vol. 51, No. 2, 2017, pp. 443–465.

[132] Bengzon, F. and Larson, M., "The Finite Element Method: Theory, Implementation, and Applications," 2013.

[133] Veroy, K., *Reduced-basis methods applied to problems in elasticity: Analysis and applications*, Ph.D. thesis, Massachusetts Institute of Technology, 2003.

[134] Chaturantabut, S. and Sorensen, D. C., "Discrete empirical interpolation for nonlinear model reduction," *Decision and Control, 2009 held jointly with the 2009 28th Chinese Control Conference. CDC/CCC 2009. Proceedings of the 48th IEEE Conference on*, IEEE, 2009, pp. 4316–4321.

[135] Trefethen, L. N. and Bau III, D., *Numerical linear algebra*, Vol. 50, Siam, 1997.

[136] Hetmaniuk, U. L. and Lehoucq, R. B., "A special finite element method based on component mode synthesis," *ESAIM: Mathematical Modelling and Numerical Analysis*, Vol. 44, No. 03, 2010, pp. 401–420.

[137] JONES, R. E., "A generalization of the direct-stiffness method of structural analysis," *AIAA Journal*, Vol. 2, No. 5, 1964, pp. 821–826.

[138] Schmidt, A., Potschka, A., Korkel, S., and Bock, H. G., "Derivative-extended POD reduced-order modeling for parameter estimation," *SIAM Journal on Scientific Computing*, Vol. 35, No. 6, 2013, pp. A2696–A2717.

[139] Zahr, M. J. and Farhat, C., "Progressive construction of a parametric reduced-order model for PDE-constrained optimization," *International Journal for Numerical Methods in Engineering*, Vol. 102, No. 5, 2015, pp. 1111–1135.

[140] Diana Alina, B. and Resiga, R., "Weighted Proper Orthogonal Decomposition of the swirling flow exiting the hydraulic turbine runner," Vol. doi:10.1016/j.apm.2015.11.015, 11 2015.

[141] Degroote, J., Vierendeels, J., and Willcox, K., "Interpolation among reduced-order matrices to obtain parameterized models for design, optimization and probabilistic analysis," *International Journal for Numerical Methods in Fluids*, Vol. 63, No. 2, 2010, pp. 207–230.

[142] Amsallem, D., Cortial, J., Carlberg, K., and Farhat, C., "A method for interpolating on manifolds structural dynamics reduced-order models," *International journal for numerical methods in engineering*, Vol. 80, No. 9, 2009, pp. 1241–1258.

[143] Amsallem, D. and Farhat, C., "An online method for interpolating linear parametric reduced-order models," *SIAM Journal on Scientific Computing*, Vol. 33, No. 5, 2011, pp. 2169–2198.

[144] Moler, C. and Van Loan, C., "Nineteen dubious ways to compute the exponential of a matrix, twenty-five years later," *SIAM review*, Vol. 45, No. 1, 2003, pp. 3–49.

[145] Barrault, M., Maday, Y., Nguyen, N. C., and Patera, A. T., "An empirical interpolationmethod: application to efficient reduced-basis discretization of partial differential equations," *Comptes Rendus Mathematique*, Vol. 339, No. 9, 2004, pp. 667–672.

[146] Grepl, M. A., Maday, Y., Nguyen, N. C., and Patera, A. T., "Efficient reduced-basis treatment of nonaffine and nonlinear partial differential equations," *ESAIM: Mathematical Modelling and Numerical Analysis*, Vol. 41, No. 3, 2007, pp. 575–605.

[147] Antil, H., Heinkenschloss, M., and Sorensen, D. C., "Application of the discrete empirical interpolation method to reduced order modeling of nonlinear and parametric systems," *Reduced order methods for modeling and computational reduction*, Springer, 2014, pp. 101–136.

[148] Carlberg, K., Tuminaro, R., and Boggs, P., "Efficient structure-preserving model reduction for nonlinear mechanical systems with application to structural dynamics," *53rd AIAA/ASME/ASCE/AHS/ASC Structures, Structural Dynamics and Materials Conference 20th AIAA/ASME/AHS Adaptive Structures Conference 14th AIAA*, 2012, p. 1969.

[149] Carlberg, K., Tuminaro, R., and Boggs, P., "Preserving Lagrangian structure in nonlinear model reduction with application to structural dynamics," *SIAM Journal on Scientific Computing*, Vol. 37, No. 2, 2015, pp. B153–B184.

[150] Astrid, P., Weiland, S., Willcox, K., and Backx, T., "Missing point estimation in models described by proper orthogonal decomposition," *IEEE Transactions on Automatic Control*, Vol. 53, No. 10, 2008, pp. 2237–2251.

[151] Everson, R. and Sirovich, L., "Karhunen–Loeve procedure for gappy data," *JOSA A*, Vol. 12, No. 8, 1995, pp. 1657–1664.

[152] Hagan, M. T., Demuth, H. B., Beale, M. H., and De Jesús, O., *Neural network design*, Vol. 20, Pws Pub. Boston, 1996.

[153] Ghiasi, H., Fayazbakhsh, K., Pasini, D., and Lessard, L., "Optimum stacking sequence design of composite materials Part II: Variable stiffness design," *Composite Structures*, Vol. 93, No. 1, 2010, pp. 1–13.

[154] Kennedy, G. J. and Martins, J. R., "A laminate parametrization technique for discrete ply-angle problems with manufacturing constraints," *Structural and Multidisciplinary Optimization*, Vol. 48, No. 2, 2013, pp. 379–393.

[155] Tsai, S. W. and Pagano, N. J., "Invariant properties of composite materials." Tech. rep., AIR FORCE MATERIALS LAB WRIGHT-PATTERSON AFB OHIO, 1968.

[156] Nguyen-Thanh, N., Rabczuk, T., Nguyen-Xuan, H., and Bordas, S. P., "A smoothed finite element method for shell analysis," *Computer Methods in Applied Mechanics and Engineering*, Vol. 198, No. 2, 2008, pp. 165–177.

[157] Smith, M., *ABAQUS/Standard User's Manual, Version 6.9*, Simulia, 2009.

[158] Bloomfield, M., Diaconu, C., and Weaver, P., "On feasible regions of lamination parameters for lay-up optimization of laminated composites," *Proceedings of the Royal Society of London A: Mathematical, Physical and Engineering Sciences*, The Royal Society, 2008, pp. rspa–2008.

[159] Grenestedt, J. and Gudmundson, P., "Layup optimization of composite material structures," *Optimal design with advanced materials*, Elsevier, 1993, pp. 311–336.

[160] McKay, M. D., Beckman, R. J., and Conover, W. J., "A comparison of three methods for selecting values of input variables in the analysis of output from a computer code," *Technometrics*, Vol. 42, No. 1, 2000, pp. 55–61.

[161] *JMP, Version 13.1.0. SAS Institute Inc., Cary, NC, 1989-2007.*.

[162] MATLAB, *version 9.3.0 (R2017b*, The MathWorks Inc., Natick, Massachusetts, 2017.

[163] Zhang, Y., "Interior Point Algorithms: Theory and Analysis," 1999.

[164] Hanson, S. J. and Pratt, L. Y., "Comparing biases for minimal network construction with back-propagation," *Advances in neural information processing systems*, 1989, pp. 177–185.

[165] Ström, N., "Phoneme probability estimation with dynamic sparsely connected artificial neural networks," *The Free Speech Journal*, Vol. 5, No. 1-41, 1997, pp. 2.

[166] Han, S., Pool, J., Tran, J., and Dally, W., "Learning both weights and connections for efficient neural network," *Advances in neural information processing systems*, 2015, pp. 1135–1143.

[167] Couckuyt, I., De Turck, F., Dhaene, T., and Gorissen, D., "Automatic surrogate model type selection during the optimization of expensive black-box problems," *Proceedings of the Winter Simulation Conference*, Winter Simulation Conference, 2011, pp. 4274–4284.

[168] Mehmani, A., Chowdhury, S., Meinrenken, C., and Messac, A., "Concurrent surrogate model selection (COSMOS): optimizing model type, kernel function, and hyper-parameters," *Structural and Multidisciplinary Optimization*, Vol. 57, No. 3, 2018, pp. 1093–1114.

[169] Grenestedt, J. L., "Lamination parameters for Reissner-Mindlin plates," *AIAA journal*, Vol. 32, No. 11, 1994, pp. 2328–2331.

[170] Foldager, J., Hansen, J., and Olhoff, N., "A general approach forcing convexity of ply angle optimization in composite laminates," *Structural optimization*, Vol. 16, No. 2-3, 1998, pp. 201–211.